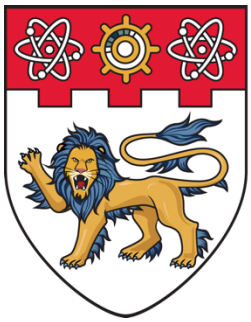

NANYANG TECHNOLOGICAL UNIVERSITY
SINGAPORE

SINGLE PHOTON DETECTION AND MANIPULATION IN PHOTONIC INTEGRATED CIRCUITS

SALIH YANIKGONUL
SCHOOL OF ELECTRICAL & ELECTRONIC ENGINEERING
2021

SINGLE PHOTON DETECTION AND MANIPULATION IN PHOTONIC INTEGRATED CIRCUITS

SALIH YANIKGONUL

School of Electrical & Electronic Engineering

A thesis submitted to the Nanyang Technological University
in partial fulfilment of the requirement for the degree of
Doctor of Philosophy

2021

Statement of Originality

I hereby certify that the work embodied in this thesis is the result of original research, is free of plagiarized materials, and has not been submitted for a higher degree to any other University or Institution.

29/06/2021	
Date	Salih Yanıkgönül

Supervisor Declaration Statement

I have reviewed the content and presentation style of this thesis and declare it is free of plagiarism and of sufficient grammatical clarity to be examined. To the best of my knowledge, the research and writing are those of the candidate except as acknowledged in the Author Attribution Statement. I confirm that the investigations were conducted in accord with the ethics policies and integrity standards of Nanyang Technological University and that the research data are presented honestly and without prejudice.

29/06/2021

Date

Cesare Soci

Authorship Attribution Statement

This thesis contains material from five papers published in the following peer-reviewed journals / from papers accepted at conferences in which I am listed as the first author.

In Chapter 2, § 2.3 is published as **S. Yanikgonul**, V. Leong, J. R. Ong, C. E. Png, and Leonid Krivitsky, "2D Monte Carlo simulation of a silicon waveguide-based single-photon avalanche diode for visible wavelengths," *Optics Express* **26**, 15232-15246 (2018). DOI: 10.1364/OE.26.015232.

The contributions of the co-authors are as follows:

- I developed the 2D Monte Carlo device simulator with assistance from Dr. Leong and Dr. Ong.
- I designed the devices with Dr. Leong and Dr. Ong.
- I performed the device simulations and analyzed the data.
- Dr. Ong contributed to the DC electrical and 3D FDTD simulations.
- Dr. Png and Dr. Krivitsky supervised the project.
- All co-authors contributed to writing and proofreading the manuscript.

In Chapter 2, § 2.4 is published as **S. Yanikgonul**, V. Leong, J. R. Ong, C. E. Png, and L. Krivitsky, "Simulation of silicon waveguide-based single-photon avalanche detectors for integrated photonic applications," *IEEE Journal of Selected Topics in Quantum Electronics* **26**, 2 (2020). DOI: 10.1109/JSTQE.2019.2938439.

The contributions of the co-authors are as follows:

- I designed the devices with Dr. Leong and Dr. Ong.
- I optimized the device simulator and added dark count rate simulation capability.

- I performed the device simulations and analyzed the data.
- Dr. Ong contributed to the DC electrical and 3D FDTD simulations.
- Dr. Png and Dr. Krivitsky supervised the project.
- All co-authors contributed to writing and proofreading the manuscript.

Chapter 4 is published as **S. Yanikgonul**, V. Leong, J. R. Ong, T. Hu, S. Y. Siew, C. E. Png, and L. Krivitsky, "Integrated Avalanche Photodetectors for Visible Light," *Nature Communications* **12**, 1834 (2021). DOI: 10.1038/s41467-021-22046-x.

The contributions of the co-authors are as follows:

- I designed the devices with Dr. Leong and Dr. Ong.
- I designed and performed the experiments with assistance from Dr. Leong and Dr. Siew. I also analyzed the data.
- Dr. Hu contributed to the device fabrication.
- Dr. Png and Dr. Krivitsky supervised the work.
- All co-authors contributed to writing and proofreading the manuscript.

Chapter 6 and Chapter 7 are published as **S. Yanikgonul**, R. Guo, A. Xomalis, A. N. Vetlugin, G. Adamo, C. Soci, and N. I. Zheludev, "Phase stabilization of a coherent fiber network by single-photon counting," *Optics Letters* **45**, 2740-2743 (2020). DOI: 10.1364/OL.381388.

The contributions of the co-authors are as follows:

- I developed the phase stabilization method by single-photon counting.
- I implemented the phase stabilization technique in a fiber network set up by Dr. Guo.
- I designed and performed the experiments with Dr. Guo and Dr. Vetlugin.
- I analyzed the time-correlated single-photon counting data.
- Dr. Xomalis contributed to the fabrication of the plasmonic metamaterial sample.
- Prof. Zheludev and Prof. Soci supervised the project.
- All co-authors contributed to writing and proofreading the manuscript.

Chapter 8 is published as **S. Yanikgonul**, A. N. Vetlugin, R. Guo, A. Xomalis, G. Adamo, C. Soci, and N. I. Zheludev. Quantum State Filtering of Dual-rail Photons with Fiberized Plasmonic Metamaterial. *Conference on Lasers and Electro-Optics (CLEO)*, San Jose, CA, USA (2019). DOI: 10.1364/CLEO_QELS.2019.FTu3D.7.

The contributions of the co-authors are as follows:

- I implemented our method to phase stabilize the interferometer.
- I designed and performed the experiments with Dr. Guo and Dr. Vetlugin.
- I analyzed the data and interpreted the results with assistance from Dr. Vetlugin.
- Dr. Xomalis contributed to the fabrication of the plasmonic metamaterial sample.
- Prof. Zheludev and Prof. Soci supervised the project.
- All co-authors contributed to writing and proofreading the manuscript.

Moreover, we gratefully acknowledge Prof. Christian Kurtsiefer for providing us with the APD detector module that we used in the verification of our testbed. By the same token, we acknowledge Prithvi Gundlapalli, who is a member of our research group, for his assistance in acquiring the measurement data presented in § 5.4 as well as Dr. Charles Altuzarra for developing the heralded single-photon source setup used in § 7.4.1. We also thank Prof. Mingbin Yu and Dr. Shiyang Zhu for their inputs at the initial stage of the waveguide-integrated APD project.

29/06/2021

Date

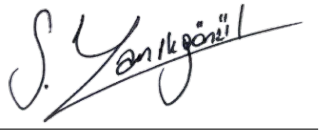

Salih Yanıkgönül

Acknowledgments

First and foremost, I would like to express my appreciation to my supervisors, Prof. Cesare Soci and Dr. Leonid Krivitsky, for their invaluable leadership and continuous support throughout my doctoral degree. Your guidance and support in all means have made working with you a memorable experience. I will always be grateful to you for your visionary mentorship and kindness. In addition, I would like to thank Agency for Science, Technology and Research (A*STAR) of Singapore and Turkish Educational Foundation (TEV) for the support of the Singapore International Graduate Award (SINGA).

I am immensely grateful for having the opportunity to work with Dr. Victor Leong, who has always been a true mentor and exemplary companion for me. It would be impossible to count all the ways that you have helped me in my studies. I have learned a lot from your constructive feedback and scientific rigor. You have taught me how to welcome challenges of any sort and made me feel empowered while tackling them. I am indebted to you for all your invaluable teachings and mentorship which helped me to grow as a researcher.

Lots of gratitude to Dr. Jun Rong Ong for being a great collaborator and having me on board when I started my PhD. Our long and fruitful discussions at scenic Infuse have always provided me with valuable insights for my research on single-photon detectors. I also extend my thanks to Dr. Aravind Padath Anthur for answering my never-ending questions during our lunch breaks. Having conducted experiments at neighbor labs, you have been a colleague from whom I can always seek advice.

By the same token, I am grateful to work with Dr. Ruixiang Guo and Dr. Anton Vetlugin at Centre for Disruptive Photonic Technologies (CDPT). Thanks to Ruixiang, for enduring with me while setting up our experiments and acquiring data till late at night, and always being supportive; and Anton, for introducing me into the second quantization picture and providing me with new insights into our single-photon interference experiments.

Doing a PhD is more pleasing when you are surrounded with nurturing and affable team members. I am grateful to the rest of the group members for their cherished friendships. To Dmitry Kalashnikov, Zhang Haizhong, Anna Paterova, Jibo Dai, Jun Yi Lee, Hongzhi

Yang, Desmond Toa Zi Siang, Prithvi Gundlapalli, and Sumin Choi: thanks for giving me the pleasure of sharing our lunch breaks, afternoon teas with delicious Russian chocolates and sweet Turkish delights, BBQs with Russian caviar, and many more such moments.

Many thanks to all of my friends here for adding joy and happiness in my life on this beautiful tropical island.

Most importantly, I am immensely grateful to my parents for their endless love, encouragement, and support all the time. I left you for my education when I was in my teens, and our separation has yet to finish. For the last few years, I could barely visit you once a year. Although missing my little brothers and nephew growing up makes being far from home even harder, your patience and understanding have given me the strength and motivation that I need to pursue my PhD.

My dear wife Sena... I cannot express how I am grateful for everything you have done. Coming to Singapore without you was the hardest thing throughout of my whole PhD life. We were separated for the first 1.5 years of my PhD, but fortunately our yearning for each other led to our marriage. I am deeply thankful to you for helping me find peace when I get overwhelmed, supporting me for every step I have taken, and for being patient when you get exposed to my endless speeches about my experiments (*I think you should be awarded a minor in Physics at least!*). I am so blessed to share the life with you, and I love you.

Table of contents

Summary

One way to achieve a scalable quantum computing and communication platform is to construct a network of quantum systems. Building a quantum network with photonic integrated circuits (PICs) is a promising avenue as they provide a platform on which quantum information can be generated and manipulated via integrated photonic structures. One such example would be a hybrid PIC with quantum light sources, modulators, interferometers, and single-photon detectors for complete on-chip single-photon processing.

To date, reports of waveguide-coupled single-photon detectors have been limited to operation at infrared telecommunication wavelengths. However, many relevant quantum systems operate in the visible spectrum, which makes efficient, low-noise integrated single-photon detectors for visible wavelengths highly desirable.

In addition to on-chip detection, coherent modulation of photon states is of paramount importance for integrated quantum information processing. In this regard, the novel concept of coherent perfect absorption (CPA) provides new ways of controlling quantum states of light in hybrid quantum systems. Compared to conventional Mach-Zehnder intensity modulators which only redistribute photons between two outputs, interferometric modulators based on CPA can deterministically prevent the propagation of residual photons in complex networks and eliminate undesired interference or crosstalk at other network arms. Such a hybrid platform holds the promise of performing linear optical quantum computing (LOQC) protocols in a scalable architecture with on-chip readout of quantum information. This thesis focuses on manipulation and detection of photons in its two parts.

In the first part, a new class of silicon waveguide-integrated avalanche photodiodes (APDs) on silicon-on-insulator photonic platform for visible wavelengths are designed, fabricated, and characterized. The devices with p-n^+ and p-i-n^+ junction structures and various geometries are investigated, and 2D Monte Carlo simulations are performed in order to optimize device performance. Operated in linear mode at 685 nm, we achieved a gain-bandwidth product exceeding 200 GHz along with a sub-μA dark current, which are on par or even superior to state-of-the-art similar devices. Operated in Geiger mode, it turns out that

our devices are affected by high dark count rate for which we provide in-depth analysis and propose solutions.

The second part of the thesis focuses on single photon manipulation experiments performed by phase-stabilized interferometers with CPA capability. With the end goal of an integrated CPA interferometer, we tested our ideas of coherent control of single photons via CPA on a coherent optical fiber network and proved their applicability. Besides serving as an easily accessible testbed, such optical fiber networks are also indispensable for long haul distribution and exchange of quantum information.

Regardless of being integrated or fiberized, a fundamental challenge to any interferometer operation is phase noise; its elimination without degrading the efficiency of quantum channels is of the upmost importance to protect quantum coherence. To deal with the phase noise, fiberized quantum optics experiments often employ resource demanding stabilization techniques, which cause additional losses and possible interference on the quantum channel. Here, first, we develop an active phase stabilization scheme by single-photon counting, and then apply it to a quantum network operating at the single-photon level. Our method can overcome the phase noise with no need for auxiliary laser and additional optical components required in conventional approaches, and it achieved a competitive phase stability while preserving the efficiency of quantum channels.

Next, we show that a phase-stabilized interferometric modulator based on CPA can be used to control the absorption probability of single photons via phase modulation. We demonstrate that CPA at the single-photon level can be used for all-optical dissipative single-photon switching, which provides increased functionalities over nonlinear approaches for all-optical signal processing. Moreover, by utilizing different optical response of our CPA interferometer to symmetric and anti-symmetric wavefunctions of photons, we showed an application of our coherent network in filtering quantum states of photons where quantum information is encoded in superposition of two spatial modes. Our work may find applications in quantum information protocols such as in dual-rail encoding.

Harnessing the functionality of different physical systems for storage, processing, and readout of quantum information, hybrid photonics approach described in this thesis provides a viable path towards scalable quantum information processing. In this thesis, we reported the first integrated avalanche photodetection at visible wavelengths, and by tailoring optical properties of designer materials, we achieved two successful demonstrations of quantum light manipulation in coherent optical networks stabilized by our phase stabilization method. Overcoming hybrid integration and device engineering challenges would pave the way for performing on-chip LOQC with integrated readout capability.

List of Figures

List of Tables

Chapter 1

Introduction

Quantum information technologies have been rapidly developing in recent years, and efforts are shifting from conceptual laboratory demonstrations to scalable real-world devices. Relying on the principles of quantum mechanics, especially quantum entanglement and quantum superposition, new quantum technologies are emerging. Quantum computers hold the promise of performing computations that are beyond the reach of classical computers [12–16]. Quantum cryptography secures communication channels with unhackable encryption methods [17–21]. Quantum simulators allow us to investigate quantum many-body systems that are hard to investigate in laboratory settings or not feasible to model with classical computers [22–25]. Quantum sensing and metrology enable us to measure various quantities with better sensitivity beyond the standard quantum limit [26–29].

Scalability challenge

Ambitious quantum flagship initiatives [30–34] have been launched with the aim to spearhead the quantum computational advantage or supremacy race [35]. Google has recently claimed that it achieved quantum advantage with its 53-qubit programmable superconductor-based processor [16]. There is yet to be any demonstration of otherwise intractable real-world computing problem that has been solved with this chip. Nonetheless, the field takes a huge leap forward and promises to achieve a practical quantum computer in the near future.

To be practically useful, however, a quantum chip needs to be scaled beyond these 53 qubits [36]. One clear approach is to increase the number of qubits on the same chip but doing so makes the preservation of the coherence between qubits and quantum error correction extremely challenging [37]. Moreover, engineering challenges emerge in connecting and

controlling large number of qubits on the same device, and consequently, scaling up to hundreds to thousands of qubits on a single chip is presently not easily accessible.

Photonic quantum networks

A viable approach to overcome the challenge of building a scalable universal quantum computer is to utilize modularity approach. Modularity allows us to construct large architectures from smaller subsystems while keeping the individual system complexity at an easily manageable level. Motivated by how computational tasks are executed on a contemporary supercomputer that consists of CPUs, RAM, and other peripheral electronics in a modular fashion, a network of separate quantum systems can be interconnected to achieve a scalable quantum computing and communication platform [38–40]. Within such networks, separate quantum systems constitute individual network nodes which process and store quantum information as stationary qubits. Photons, serving as flying qubits, exchange quantum information between these nodes with high fidelity and communication rates. Promising progress has been made for many suitable candidates for quantum nodes, including superconducting circuits [16, 41–44], quantum dots [45–47], color centers [48–50], trapped ions [51–53], rare-earth-doped materials [54, 55], and neutral atoms [56–58].

Photonic quantum systems are prominent candidates for the realization of a quantum network [59, 60] because photons are low-noise carriers of quantum information. Superposition and entanglement of quantum states can be generated, distributed, and detected using photons. Moreover, photons are currently the only feasible candidate to connect nodes of a distributed quantum information network and quantum communication system.

In the KLM protocol [59] described in the linear optical quantum computing (LOQC) approach, simple linear optical elements are used to perform unitary quantum gate operations on qubits while quantum memories and single-photon detectors are used to store and read-out quantum information. This protocol makes it possible to realize a universal quantum computation platform via a network of linear optical elements along with single-photon sources and detectors.[1]

Most of components required for a photonic quantum network can be monolithically integrated on a photonic chip. Such photonic integrated circuits (PICs) provide the possibility of incorporating a lot of functionalities including phase and intensity modulators, interferometers, phase shifters, resonators, and detectors while maintaining a very small device

[1] Not all the LOQC protocols allow for universal quantum computing though. KLM protocol is suitable for this purpose, whereas boson sampling [61], for instance, constitutes a restricted model where its applicability is not universal.

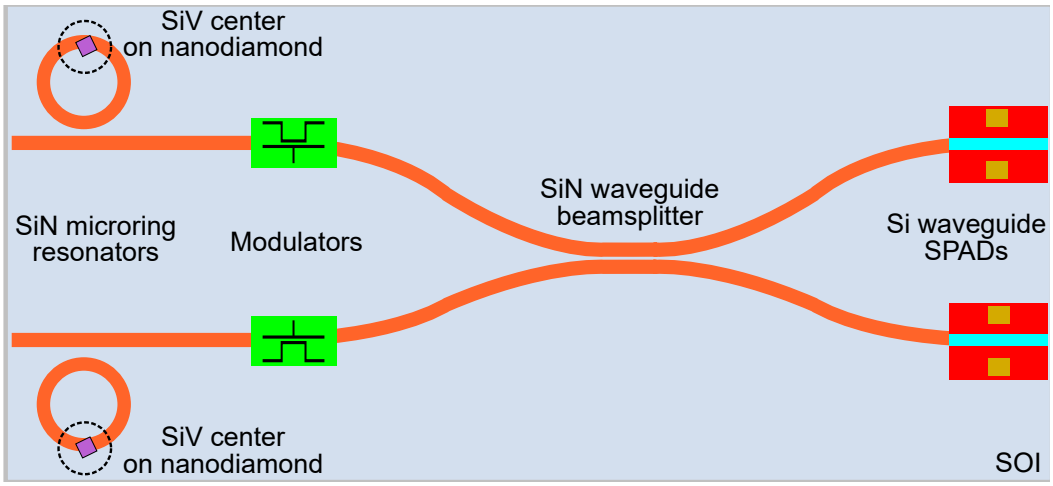

Figure 1.1: Simplified schematic of our photonic integrated circuit which consists of high Q-factor silicon nitride (SiN) microring resonators with silicon-vacancy (SiV) color centers in nanodiamonds as quantum light sources, SiN waveguide beamsplitter, phase modulators, and silicon waveguide-integrated single-photon avalanche diodes (SPADs) on silicon-on-insulator (SOI) platform. This circuit is configured as a Hong-Ou-Mandel (HOM) interferometer, where HOM effect can be observed via coincidence measurements between the on-chip detectors.

footprint. This component miniaturization brings about scalability and ease of operation. Furthermore, PICs provide advantages of cost reduction, standardization, and precision compared to bulk implementations. Quantum communication [62–66], quantum computation [67–73], quantum simulation [74–81], and quantum metrology [82] have all been reported with PICs, proving its versatility and viability for on-chip implementations of different quantum technologies.

One example of a multi-functional PIC combination comprises of a photonic platform where photons are generated, manipulated, and detected via on-chip quantum light sources, modulators, interferometers, and single-photon detectors as shown in Fig. 1.1. This platform can be reconfigured to accommodate other photonic components to extend functionalities for on-chip single-photon processing. One such example utilizes interferometers with coherent perfect absorption capability. This type of interferometers has been implemented to quantum states of light including single-photon Fock states [83], entangled states [84], and NOON states [85]. They have also been used for controlling coupling of photons to other light-matter eigenstates [86–88], and they have potential applications in quantum communication and LOQC protocols such as dual-rail encoding.

In the first part of this thesis, we present our work towards monolithically integrated single-photon detectors for visible wavelengths, which lacks in the literature. The second

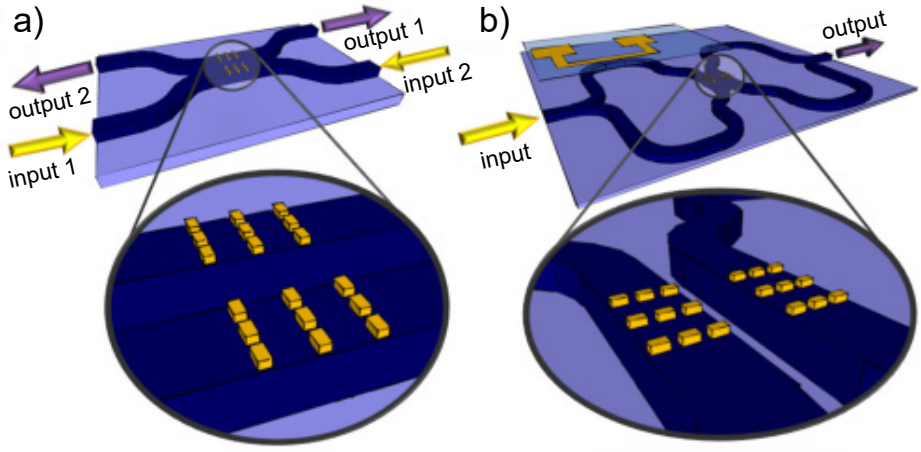

Figure 1.2: Schematic of integrated CPA interferometers. Concept of a) all-optical single-photon switch and b) single-photon absorption control via plasmonic nanoantennas on top of the waveguides as coherent absorbers in the middle of the beamsplitter structure. An electro-optic or thermo-optic actuator for phase modulation is depicted for b). The image is taken from [1].

part focuses on single photon manipulation experiments performed by phase-stabilized interferometers with coherent perfect absorption (CPA) capability. An integrated CPA interferometer as shown in Fig. 1.2 depicts our end goal, and the efforts are geared towards developing the integrated metamaterial part to achieve on-chip CPA (see § 9 for numerical studies). While pursuing that end goal, in Part II, we used a coherent optical fiber network with a coherent perfect absorber as a prototype to prove the applicability of our single photon manipulation concepts.

Apart from serving as an easily accessible testbed, fiber networks comprising of numerous interferometers constitute a prominent building block of long-haul quantum information and communication systems. Quantum computation based on dual-rail qubit encoding [89, 90], quantum key distribution [91, 92], entanglement swapping and distribution [92, 93], and high-dimensional quantum state transmission [94] have already been demonstrated in fiber-based quantum networks, showing the viability of the approach. In addition to being stand-alone platforms, PICs and optical fiber networks can also work together as complementary platforms. For instance, an optical fiber network can be used for lang haul connection of distant quantum nodes realized on PICs; a modular system that utilizes the benefits of both photonic platforms.

Whether it is integrated or fiberized, an important challenge pertaining to interferometers originates from phase noise. If it is not eliminated, phase noise destroys quantum coherence, which subsequently prevents quantum superposition and quantum entanglement. Therefore,

stabilization of interferometers without degrading quantum channel efficiency is of the upmost importance for realizing quantum optics applications. In the second part, we address this issue and present our experimental results on phase stabilization of coherent optical networks and coherent control of single photons.

On-chip detection of single photons at visible wavelengths (Part I) and coherent manipulation of quantum states of light via CPA phenomenon in phase stabilized optical networks (Part II) are fundamental to the development of our integrated photonics platform. Extended functionalities for quantum light manipulations together with on-chip readout of quantum information with single-photon detectors would potentially make our platform an important device for on-chip LOQC applications.

Part-1: Integrated single photon detection at visible wavelengths

Recent developments based on complementary metal-oxide semiconductor (CMOS) compatible material platforms highlight the remarkable promise of a compact, low-cost, and mass-manufacturable quantum photonics device technology [95–97]. Currently, many current PICs still rely on coupling of light to external bulk photodetectors [62, 69]. Major improvements in device footprint and scalability could be achieved if these photodetectors reside on the same photonic chip and couple directly to waveguides [98]; therefore, on-chip waveguide-coupled single-photon detectors would be one of the key building blocks of a scalable integrated quantum photonics platform.

Superconducting nanowire single-photon detectors (SNSPDs) are a state-of-the-art solution, featuring waveguide integrability, near-unity quantum efficiencies, low dark count rate of a few counts per second (cps), and low timing jitter down to $< 20\,\mathrm{ps}$ [99–101]. However, they require cryogenic operating temperatures of a few degrees Kelvin, which is expensive and prohibitive for large-scale deployment.

A practical alternative can be found in single-photon avalanche diodes (SPADs)[2]. A single photon that is incident on a SPAD can trigger a macroscopic avalanche current via a cascade of impact ionizations, and the resultant avalanche current is used for detection. In contrast to SNSPDs, SPADs typically only require thermoelectric cooling and can operate even at room temperature [102–104]. Moreover, SPADs can be easily incorporated into silicon photonics platforms and benefit from mature CMOS fabrication technologies [105–107], making them a promising candidate for scalable manufacturing. To date, reports of

[2] The term single-photon avalanche diode (SPAD) is used to describe avalanche photodiodes (APDs) that are specifically designed to operate at reverse bias voltages beyond breakdown voltage to achieve single-photon sensitivity. Therefore, the term SPAD is used interchangeably with Geiger-mode APDs in this thesis.

waveguide-coupled SPADs have been limited to operation at infrared wavelengths [108, 109]. However, many relevant quantum systems, including trapped ions [110–112] and color centers in diamond [49, 113], operate in the visible spectrum, which makes efficient and low-noise SPADs for visible wavelengths highly desirable.

Apart from integrated quantum photonics devices, a high detection efficiency and low timing jitter waveguide-integrated single-photon detector is desirable in a wide range of photon-starved applications such as LIDAR [114, 115], non-line-of-sight imaging [116], 3D time-of-flight imaging [117], fluorescence medical imaging [118, 119], optical time domain reflectometry [120, 121], STED microscopy [122], and astronomy [123–125], to name a few.

When operated at a bias voltage that is below breakdown voltage, APDs can achieve a finite and stable gain for a given applied voltage. This is in contrast with Geiger-mode operation for which the concept of gain is not applicable in the strict sense due to divergent nature of the avalanche breakdown. In this linear-mode regime, APDs work as linear amplifiers such that an incident optical signal is converted into an amplified photocurrent signal with internal gain. APDs in linear-mode operation are mostly utilized to achieve up-front amplification of low-intensity optical signals. Linear-mode APDs are extensively used in numerous applications including high-speed receivers of optical interconnects [126–130], LIDAR [131, 132], biomedical imaging [119, 133], and scintillation detection [134–136] which require high bandwidth and high sensitivity.

In this part of the thesis, we report on the design, simulation, and characterization of silicon waveguide-integrated avalanche photodiodes (APDs) on a silicon-on-insulator (SOI) photonic chip for visible wavelengths. Our waveguide-integrated APDs are end-fire coupled to silicon nitride (Si_3N_4, hereinafter denoted as SiN) photonic waveguides (see Fig. 1.1). SiN is a suitable material for scalable quantum photonics applications because it is CMOS compatible [105, 137, 138] and has a large transparency window for many quantum emitters that emit at visible wavelengths [49, 110]. Moreover, χ^3 nonlinearity of SiN has been recently utilized to demonstrate quantum frequency conversion of single-photons and photon pairs emitted from quantum dots [139, 140]. Therefore, silicon SPADs which are waveguide-coupled to SiN waveguides on the same photonic chip constitutes an important milestone on the road towards scalable quantum information network.

We design two classes of silicon waveguide-integrated APDs for Geiger-mode operation at visible wavelengths. We develop a 2D Monte Carlo device model that is suitable with the stochastic nature of impact ionization process and subsequently simulate photon detection efficiency and timing jitter of devices. Compared to previous SPAD simulation works which are aimed at simulating free-space devices by considering electric field only along

photon propagation axis, our 2D Monte Carlo simulator is better suited for SPADs in small waveguide geometries where the electric field distribution is highly non-uniform. We study the effect of different doping configurations and device geometries on device performance in Geiger-mode operation by performing numerical simulations.

Next, we fabricated our devices and characterized them in both linear-mode and Geiger-mode operation. We investigated the effect of different design parameters and operating conditions on device performance. Operated in linear mode, our APDs show competitive performance in terms of dark current, primary responsivity, gain, and bandwidth. This demonstration is the first report on the monolithically integrated avalanche photodiodes for visible light in the literature.

Operated in Geiger mode, we investigated avalanche breakdown dynamics and noise performance of our devices . We characterized the breakdown voltage, avalanche pulse characteristics, and dark count rate along with their temperature and excess bias dependence. The effect of peripheral quenching electronics on device performance is discussed, and various methods to reduce dark count rate are presented.

Part-2: Integrated single photon manipulation via CPA

LOQC schemes extensively use interferometers to encode, exchange, and process quantum information of multiple photons. Various interferometric methods have been used to coherently control quantum states of light, however conventional interferometers operate probabilistically. Extended functionalities are achievable with interferometric modulator systems based on novel coherent perfect absorption (CPA) phenomenon, which brings the advantage of deterministically controlling light propagation. When implemented in complex optical networks, such interferometric modulators with CPA capability allows for deterministic prevention of residual photon propagation into other network arms, eliminating undesired interference or crosstalk elsewhere.

However, whether it is equipped with CPA functionality or not, phase noise poses an important challenge to any interferometer operation. Interferometers, particularly if built on a fiber network, suffer from phase noise due to environmental factors such as thermal, mechanical, and acoustic noise. The phase information between photons propagating through different interferometer arms must be preserved for quantum superposition and quantum entanglement, for which quantum interference plays a vital role.

Many experiments on optical fiber networks use either resource-demanding stabilization or elaborate data post-selection techniques to eliminate the effect of phase noise [6–8, 141]. Conventional approaches that form a feedback loop for active phase stabilization use an

auxiliary laser with a distinct degree of freedom (e.g., wavelength, polarization, or temporal mode) probing the same optical path traversed by quantum light. However, any optical components introduced for multiplexing (demultiplexing) auxiliary laser into (out of) an interferometer increase optical losses in the quantum channel. Furthermore, scattering-induced photons and crosstalk of the auxiliary laser interfere with the quantum signal.

In this part of the thesis, we developed an active phase stabilization scheme for coherent optical networks operating at the single-photon level. Our method relies on a digital feedback controller which monitors single-photon counts sampled directly from the quantum channel. Compared to other phase stabilization schemes which use dedicated auxiliary lasers, multiplexers, and additional photodetectors, our method utilizes existing single-photon detectors and modulators on the network, and hence, it is less resource demanding and potentially improve the efficiency of the quantum channel.

We first implemented our method in a coherent optical network represented by a fully-fiberized Mach-Zehnder interferometer (MZI) operating at the single-photon level. We demonstrated a phase stability that is comparable to those demonstrated in conventional stabilization schemes. We further applied this technique to an optical network with a coherent perfect absorber, and subsequently demonstrated deterministic control of single-photon absorption probability.

Next, we showed all-optical switching by driving the coherent network between its coherent perfect absorption and transmission regimes. Unlike conventional approaches based on nonlinear optical processes requiring high light intensity, the interferometric nature of coherent perfect absorption allows us to demonstrate all-optical switching down to the single-photon level. Moreover, our demonstration allows for complete light dissipation, unlike a standard Mach–Zehnder intensity modulator which only redistributes light between its two output ports. CPA switches, therefore, are useful for building complex quantum networks where photon propagation can be deterministically controlled by dissipating photon energy through coherent interactions.

Lastly, we demonstrated quantum state filtering of single photons whose quantum information is encoded in superposition of two spatial modes, i.e., dual-rail photons. Here, we extended our setup to a cascaded Mach-Zehnder interferometer for input state preparation and output state measurement and utilize different optical responses of the metamaterial to symmetric and anti-symmetric wavefunctions of spatial wave function. Our work may find use cases in optical quantum information protocols such as dual-rail encoding.

To summarize, the work presented here adopts a hybrid approach for building an integrated photonics platform with on-chip photon generation, manipulation, and detection

capabilities. We report on the first demonstration of waveguide-integrated APDs for visible wavelengths. Operated in linear mode, the gain-bandwidth product exceeding 200 GHz and sub-microampere dark current makes our devices very competitive when benchmarked against other integrated APDs operating in the telecommunication wavelengths. Operated in Geiger mode, our devices are affected by high dark count rate for which we provide in-depth analysis and recommendations for future work to overcome this issue. The other key ingredient of our hybrid integrated platform is the ability of coherent control of photons to perform on-chip LOQC protocols. Coherent control of single photons is achieved by using interferometric modulator systems equipped with coherent perfect absorbers. Since eliminating phase noise is vital to any interferometer operation, we developed a method of active phase stabilization for coherent optical networks operating at the single-photon level. Finally, we demonstrated two successful examples of coherent control of single photons, single-photon switching and quantum state filtering of dual-rail photons, to prove the applicability of our concepts for future on-chip LOQC applications.

Thesis structure

The content of the thesis is structured in the following chapters.

- **Chapter 2** presents a brief literature review of solid-state single photon detectors compatible with monolithic integration and outlines the physics of Geiger-mode APD operation. This is followed by our design and simulation study for silicon waveguide-integrated Geiger-mode APDs on silicon-on-insulator platform to achieve single-photon detection at visible wavelengths.

- **Chapter 3** describes the method to fabricate silicon waveguide-integrated APDs which are end-fire coupled to silicon nitride waveguides on silicon-on-insulator platform.

- **Chapter 4** presents the experimental results on characterization of fabricated APDs in linear-mode operation. It investigates the effect of different device geometries and doping profiles on optical coupling, device responsivity, dark current, and electro-optical bandwidth performance.

- **Chapter 5** first describes the performance metrics of an APD in Geiger-mode operation together with their dependence on operating conditions. Next, it introduces our test setup and quenching electronics for Geiger-mode operation, and reports on the experimental results on characterization of a commercial APD to verify the operation of our test setup. Experimental results on characterization of fabricated APDs in

Geiger-mode operation are then presented. Lastly, it provides a discussion on the physical mechanism of excessive dark count rate and suggests methods to prevent device saturation.

- **Chapter 6** introduces our method for active phase stabilization of coherent optical networks operating at the single-photon level, and reports on the experimental results obtained from its implementation in a quantum network represented by a fully-fiberized Mach-Zehnder interferometer.

- **Chapter 7** briefly reviews the coherent perfect absorption phenomenon in plasmonic metamaterials. Then, it presents a practical application of CPA, which is all-optical single-photon switching, in a phase-stabilized coherent optical network with heralded single photons.

- **Chapter 8** extends the application realm of our phase-stabilized quantum network and presents our experimental results on filtering quantum states of photons whose quantum information is encoded in superpositions of spatial wave functions.

- **Chapter 9** concludes the thesis and outlines the future work towards the development of a photonic platform incorporating waveguide-integrated Geiger-mode APDs and waveguide-based coherent perfect absorbers for on-chip LOQC applications with integrated quantum information readout capability.

Part I

Integrated Single Photon Detection at Visible Wavelengths

Chapter 2

Design and Simulation of Integrated SPADs

2.1 Introduction

Here, we first briefly overview various single-photon detector technologies that are suitable for photonic integration. Next, we present our design and simulation results for silicon waveguide-integrated SPADs on a silicon-on-insulator platform. Our devices are designed to detect single photons at visible wavelengths where many relevant quantum systems, including trapped ions [110–112] and color centers in diamond [49, 113], operate.

Here, we first investigated a SPAD which consists of a p-n^+ junction implemented in a doped silicon waveguide and couples to an input silicon nitride waveguide on the same layer. We developed a 2D Monte Carlo model to simulate the stochastic avalanche multiplication process of charge carriers following absorption of an input photon, and calculated photon detection efficiency (PDE) and timing jitter. We simulated device performance for different device dimensions and doping configurations at 640 nm input light. The temperature in our simulations is set to 243 K, which is achievable by thermoelectric cooling.

In the second half of the chapter, we extended this first simulation study. Specifically, we improved the device simulator, added dark count rate (DCR) calculations, and then investigated p-i-n^+ junction-based devices together with new design variations of p-n^+ junction-based devices. Here, we explored various waveguide structures and doping profiles to maximize photon detection efficiency while keeping timing jitter and dark count rate at acceptable levels. Our simulation study shows that p-i-n^+ SPADs have the highest PDE and the lowest DCR while attaining low timing jitters.

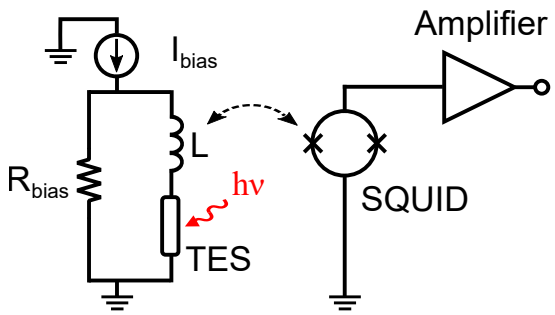

Figure 2.1: Operation principle of TES-SQUID circuit. Driving I_{bias} through R_{bias} results in a voltage bias on the transition edge sensor such that the device operates on its self-biased region where the dissipated power is constant with the applied voltage. A photon absorption leads to a negative electrothermal effect and drops the device current. The SQUID, which is inductively coupled to the input coil L, picks up this change in the device current, and subsequently outputs a detection signal.

2.2 Single-photon Detector Technologies

Integrated quantum photonics is recognized as a key enabling technology on the road towards scalable quantum networking schemes. However, many state-of-the-art integrated quantum photonics demonstrations still require coupling of light to external photodetectors. On-chip silicon single-photon avalanche diodes (SPADs) provide a viable solution as they can be seamlessly integrated with photonic components and operated with high efficiencies and low dark counts at temperatures achievable with thermoelectric cooling.

Besides their use in quantum-enabled technologies, such devices would also find numerous applications in other important realms, including LIDAR [114, 115, 142], non-line-of-sight imaging [116, 143], fluorescence medical imaging [118, 144], and STED microscopy [122].

Many such applications employ solid-state detectors due to their advantages of having a miniature size, lower voltage operation, and high quantum efficiency. Their compatibility for monolithic integration with photonic integrated circuits motivates research on transition edge sensors, superconducting nanowire single-photon detectors, and single-photon avalanche diodes. Next, we review the state-of-the-art solid-state single-photon detectors that can be suitable for integrated photonic architectures.

2.2.1 Transition Edge Sensors

A transition edge sensor (TES) is a class of single-photon detector based on superconductivity [145, 146]. A TES operates as an extremely sensitive calorimeter, a device used to measure heat generated during a physical process. TES operation strongly relies on temperature-dependent resistance of superconducting phase transition; therefore, they are operated at cryogenic temperatures. On-chip implementations of transition edge sensors have already been demonstrated [147–149].

During its operation, a TES detector is cooled below its superconducting transition temperature [150]. The device is voltage-biased by driving a current source I_{bias} through a bias resistor R_{bias} as shown in Fig. 2.1. The bias voltage is chosen to put the TES in its "self-biased region" at which the power dissipated in the device is constant with the applied voltage. The excess heat caused by a photon absorption is removed by negative electrothermal effect: the increase in the absorber's temperature increases the TES resistance, and subsequently results in a drop in the TES current. This leads to a reduction in the Joule power dissipated, which in turn cools the device back to its equilibrium state in the self-biased region. The relatively weak electron-photon coupling at these low temperatures allows for low thermal conductance between the TES and its surrounding thermal bath, ensuring that most of the incident photon energy is captured by the TES rather than lost through thermal conduction to the thermal bath. To read-out the detection signal, a TES is typically connected in series with an input coil L, which is inductively coupled to a superconducting quantum-interference device (SQUID) [151]. The change in the TES current is coupled to the SQUID, whose output is further amplified and read by room-temperature electronics.

TES detectors offer very high photon detection efficiency that can be tailored to different operation wavelengths ranging from the millimeter regime to gamma rays [152, 153]. In addition to their very low dark count rates, they also offer photon number resolving capability [150]. However, TES detectors suffer from poor timing attributes, e.g., approximately 100 ns FWHM timing jitter [154]. Their operating temperature at around 100 mK necessitates cooling through an adiabatic de-magnetization refrigerator, which is an energy-intensive and costly process for scaled system implementations [155].

2.2.2 Superconducting Nanowire Single-photon Detectors

Superconducting nanowire single-photon detectors (SNSPDs) are a versatile class of photodetectors exhibiting near-unity photon detection efficiencies ($> 90\%$), fast response times, low timing jitter (< 20ps), and very low dark counts over a broad range of wavelengths [156].

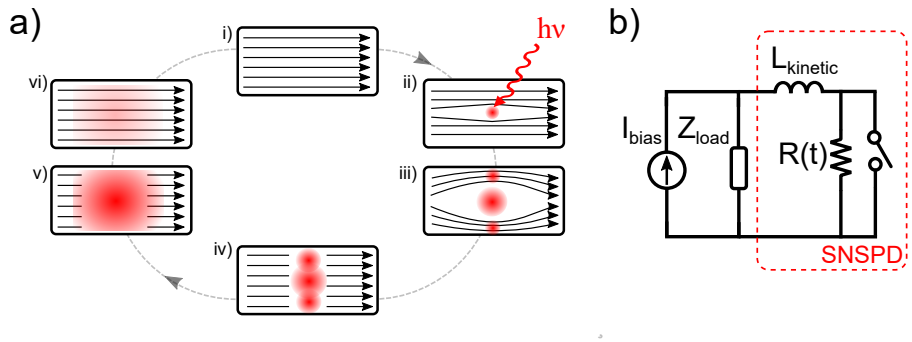

Figure 2.2: a) Operation principle of SNSPD. (i) A DC current biases the SNSPD. (ii) The photon absorption creates a localized hotpot. (iii) The local current density around the hotspot exceeds the superconducting critical current density. (iv) A resistive barrier across the width of the nanowire is formed. (v) Joule heating extends the resistive region until the current shunts through load resistance of the read-out amplifier. (vi) Finally, the non-superconducting region cools down and returns to the superconducting state. b) Equivalent circuit model. I_{bias}: bias current, Z_{load}: input impedance of the read-out amplifier, L_{kinetic}: kinetic inductance, $R(t)$: hotspot resistance. Photon absorption corresponds to the switch opening. Images are adapted from [2].

Their waveguide-integrated implementations also attain performance metrics similar to that of their free-space counterparts [99–101, 157, 158].

SNSPDs are based on a superconducting nanowire which is cooled below its superconducting critical temperature. A DC current that is close to but less than the superconducting critical current of the nanowire is applied to bias the photodetector. A photon incident on the nanowire breaks Cooper pairs and reduces the local critical current at that point below that of the bias current (see Fig. 2.2(a)). This leads to a formation of a localized non-superconducting region called a hotspot with a finite electrical resistance. If a readout amplifier having an input resistance less than that of the hotspot is used, then most of the bias current shunts to the input impedance Z_{load} of the readout amplifier and generates a measurable voltage for detection (Fig. 2.2(b)). With most of the bias current diverted to the amplifier, the non-superconducting region cools and returns to the superconducting state, and the device becomes ready for the next photon detection.

Despite having performance metrics that are desired from a good single-photon detector, the maintenance of cryogenic temperatures on the order of a few Kelvins is an energy-consuming and expensive task, which limits the implementation of SNSPDs in scalable architectures.

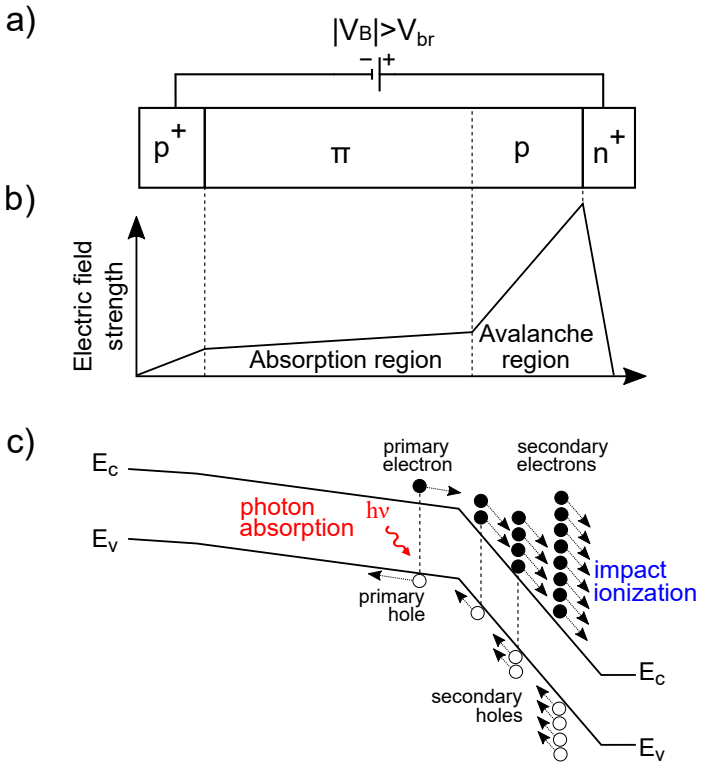

Figure 2.3: A descriptive illustration showing the avalanche multiplication process in SPADs.

2.2.3 Single-photon Avalanche Diodes

Single-photon avalanche diodes (SPADs) are a type of solid-state single-photon detectors based in a reverse biased diode structure. SPADs typically only require thermoelectric cooling and can even operate at room temperature [102, 104]; this offers many practical advantages in system implementation.

Figure 2.3 depicts the avalanche multiplication process in SPADs. Photogenerated charge carriers trigger an avalanche of subsequent charge carrier generation due to the impact ionization process. This avalanche generation then leads to a macroscopic current on the order of a few milliamperes to flow across the device. If the primary charge carrier is generated by photon absorption, then the leading edge of the avalanche pulse heralds the arrival of the photon. The details pertaining to device physics are explained in detail in the next sections.

SPADs are preferred due to their ease of use, as cryogenic temperature is not required, and competitive performance metrics in single photon detections. SPADs can be fabricated with mature standard CMOS fabrication techniques, enabling their utilization in scalable architectures in a cost-effective way with high yields [159–162]. In addition to these advan-

tages, SPADs have competitive figures of merit for their photon detection efficiency, dark count rate and timing jitter performance.

Waveguide-coupled photodetectors have gained increasing attention in recent years; compared to traditional free-space devices, waveguide devices can achieve higher speeds and responsivities thanks to perpendicular directions of light absorption and current collection [163, 164].

In waveguide-based devices, long penetration depths to have high photon absorption efficiency can be achieved simultaneously while keeping the transport time of photogenerated charge carriers low. The reason is that the carrier collection path in waveguide-integrated detectors, unlike free-space devices, is orthogonal to the light propagation direction. Moreover, the optical mode confinement provided by waveguides can allow for further reducing the required depletion width that should be overlapped with the mode profile. Therefore, such devices can attain higher transit-time-limited bandwidth and timing jitter performance.

In conventional free-space coupled reach-through devices, the depletion region is formed along the propagation direction of light. Therefore, the generated charge carriers are swept across the device thickness, which is usually large to achieve high photon absorption efficiency at target wavelengths. This eventually limits the device bandwidth due to longer transit time, and potentially leads to degradation of the timing jitter performance.

Besides, the active device volume is considerably smaller for waveguide-based devices compared to their free-space counterparts. For a given light penetration depth, such a device has orders of magnitude higher active device volume compared to a waveguide-based device having a cross-section of submicron dimensions. A smaller active device volume provides for low-noise operation because shot noise, Johnson noise, and generation-recombination noise all scale with the detector active volume [165]. Reduced junction capacitance enabled by a smaller active device volume would also improve the RC-limited bandwidth at low bias voltages.

Another advantage of waveguide-based devices is that they are suitable for planar monolithic integration with other photonics components [108, 166]. For instance, they can lead to miniaturized devices for biomedical imaging [119, 133], molecular sensing [167] and underwater imaging [168]. Combined with nanophotonic phased arrays [169, 170], they can be used in visible light communication [127, 130, 171] and bathymetric LIDAR systems [172]. Integrated APDs are also advantageous for developing scalable systems for quantum information processing, such as the recently demonstrated 100-mode photonic quantum computer [173]. Integrated visible-light APDs will enable the photonic integration of various quantum systems operating at visible wavelengths, such as trapped ions, color centers

in diamond, quantum dots, and 2D materials [174]. For the scaled systems, the challenges pertaining to interconnects between photonic chips and readout detectors can be overcome by using monolithically integrated detectors. However, the waveguide-integrated SPAD technology is still in its infancy compared to traditional free-space coupled reach-through SPADs which have been developed over the course of decades and are now commercially available. Table 2.1 compares the features of waveguide-based SPADs with that of such reach-through APDs. For the sake of a quantitative comparison, we compared the widely used C30902SH series avalanche photodiodes from Excelitas (formerly Perkin Elmer) [175][1] with our waveguide-integrated APD (see Chapter 4 and 5) since there is no other prior work on waveguide-integrated APDs for visible wavelengths.

The reports of waveguide-coupled SPADs to date have been limited to operation at infrared wavelengths [177]. However, many relevant quantum systems such as trapped ions [110] and color centers in diamond [49], operate in the visible spectrum, which makes efficient, low-noise SPADs for visible wavelengths highly desirable. In the following sections, we present our research on design and simulation of silicon waveguide-integrated SPAD for visible wavelengths.

2.3 First Study: Symmetric Rib Waveguide APDs

Here, we present our first design and simulation study for silicon waveguide-integrated avalanche photodiodes (APDs) in Geiger-mode operation. Operated in Geiger mode, APDs can detect single photons, and hence, they are commonly referred to as single-photon avalanche diodes (SPADs). Our silicon waveguide-integrated SPADs are waveguide-coupled to input silicon nitride (Si_3N_4) waveguides on silicon-on-insulator (SOI) platform, and they are suitable for quantum photonics applications at visible wavelengths. Moreover, they use CMOS-compatible materials so that they can be readily incorporated into more complex silicon photonic integrated circuits, leveraging on mature fabrication techniques and an optimized set of component devices [105, 178, 179].

To model the SPAD operation, we first perform a DC electrical simulation to extract the relevant electrical parameters, e.g., electric field, carrier mobilities, ionization coefficients,

[1] It also offers single photon counting modules (SPCM-AQRH series) that contain a silicon APD with super low k factor (SLiK™), where k is the ratio of hole to electron ionization coefficients. Compared to the k factor of 0.02 of its reach-through APDs, the k factor of 0.002 of SLiK™ APDs leads to a smaller excess noise factor at typical gain and makes these detectors more suitable for photon counting applications [176]. Equipped with active quenching circuit and temperature controller, these self-contained modules are intended only for Geiger-mode operation. Thus, the comparison is made with reach-through APDs whose specifications are provided for operation both in linear mode and Geiger mode (see 5.2 for characterization in Geiger mode).

Table 2.1: Comparison of waveguide-integrated and conventional reach-through APDs.

Feature	**Waveguide-integrated** $W = 900$ nm (Chapter 4, 5)	**Reach-through** Excelitas C30902SH [175]
Structure		
Light coupling	End-fire	Free-space
Spatial light profile	Confined mode	Unconfined
Carrier collection path vs. light propagation direction	Orthogonal	Parallel
Photosensitive area (mm^2)	2.25×10^{-7}[a]	0.2
Linear-mode operation		
Dark current (nA)	<0.01 – 120[b]	1 –15[c]
Primary responsivity (A/W)	0.8	∼0.4[d]
Typical linear gain	12.3[e]	250
Bandwidth (GHz)	19.1[e]	0.7[f]
Geiger-mode operation		
Breakdown voltage (V)	15	185
Typical DCR (kcps)	>100	0.25 – 5[g]
PDE (%)	N/A	∼50

[a] The light is confined within a 900-nm-wide and 250-nm-thick waveguide core.
[b] Depending on the bias voltage, it varies from <10 pA to 120 nA at room temperature.
[c] It varies from 1 nA (−20 °C) to 15 nA (room temperature).
[d] The spectral responsivity curve at 685 nm is divided by the typical gain of 250.
[e] The values are for the operation with maximum gain-bandwidth product.
[f] The 3 dB bandwidth $f_{3\text{dB}}$ is calculated from the rise time τ_r of 0.5 ns with $f_{3\text{dB}} \approx 0.35/\tau_r$.
[g] It varies from 0.25 (−20 °C) to 5 kcps (room temperature) for a PDE of 5% at 830 nm.

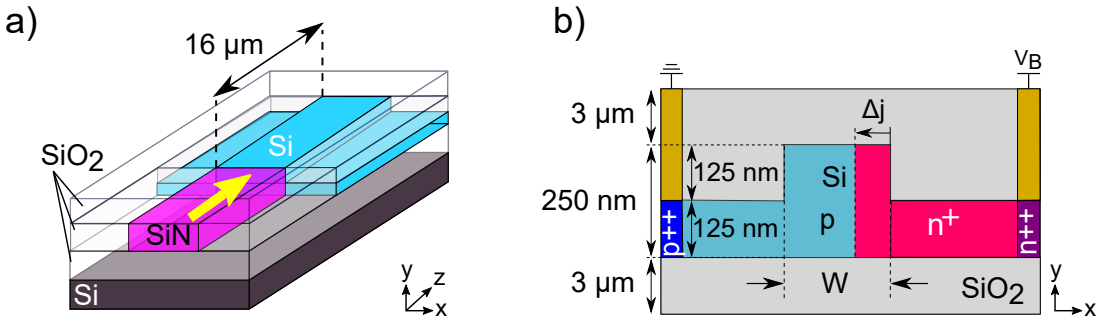

Figure 2.4: (a) SPAD structure, consisting of a silicon rib waveguide end-fire coupled to an input Si_3N_4 waveguide. (b) SPAD doping profile, with an asymmetric placement of the p-n^+ junction. The cross section is constant along the length of the waveguide.

and breakdown voltage. We use a Monte Carlo technique based on a random path length (RPL) model [180–183] to simulate the avalanche process in the SPAD, and subsequently obtain the photon detection efficiency (PDE) and timing jitter. Here, we study a series of devices with variations of waveguide width and doping levels.

2.3.1 Device Description

2.3.1.1 Device structure

The SPAD is based on a SOI platform, and it consists of a symmetric silicon rib waveguide end-fire coupled to an input Si_3N_4 rectangular waveguide (see Fig. 2.4). Silicon is a suitable photodetector material in the visible range due its high absorptivity, while Si_3N_4 has high transmittivity and a moderately high refractive index [105]. The structure is cladded with 3 µm of silicon dioxide SiO_2 above and below. The length of the silicon waveguide is 16 µm, with an absorption of >99% at 640 nm. For ease of fabrication, we fix the height of the silicon and Si_3N_4 waveguide layers at 250 nm and the rib height at 125 nm; and vary the width W between 450–900 nm in our study.

2.3.1.2 Doping profile

The choice of doping profile is essential in determining the performance characteristics of the SPAD. In surface illuminated configurations, the location and orientation of the diode junction, as well as the presence of a thick intrinsic region, is used to enhance the absorption length and to target specific wavelengths of light. This often comes at the cost of a reduced wavelength detection range or increased timing jitter [184, 185].

To mitigate this trade-off between the increased timing jitter and enhanced absorption, we design our SPAD to consist of a p-n$^+$ diode with a single continuous depletion region along the length of the waveguide (see Fig. 2.4(b)). In this waveguide geometry, absorption is given by the waveguide length. On the other hand, the timing jitter is largely dependent only on the waveguide width, and not its length.[2]

In silicon, electrons have a higher ionization coefficient than holes; this results in a more efficient avalanche multiplication process for electrons [186]. We hence aim to have photo-generated electrons (rather than holes) drift into the avalanche region of the diode in order to increase the PDE. In a p-n$^+$ junction, the depletion region extends largely into the p-doped side, where the dominant charge carriers are electrons. To maximize the spatial overlap between the large depletion region on the p-doped side and the optical waveguide mode, the p-n$^+$ junction is placed asymmetrically within the waveguide, with p- and n$^+$-doped regions having a width ratio of roughly to 5:1.

We choose a nominal n$^+$ (p) doping concentration of 1×10^{19} (2×10^{17}) dopants/cm^3, drawing on experience from previously published literature [160, 184, 187]. The depletion width within a 1D approximation is

$$W_{\text{dep}} \approx \left[\frac{2\varepsilon_r\varepsilon_0}{q}\left(\frac{N_A+N_D}{N_AN_D}\right)(V_{\text{bi}}-V_A)\right]^{1/2}, \tag{2.1}$$

where ε_r is the relative dielectric permittivity of the semiconductor, ε_0 is the permittivity of free space, q is the elementary charge, N_A and N_D are the number of ionized acceptors and donors, respectively, V_{bi} is the built-in voltage, and V_A is the applied bias. The chosen doping levels ensure that the depletion region covers a large part of the waveguide width. We also explore other doping levels in this work and assess their effect on SPAD performance.

Electrical connections to the device are made via metal contacts deposited on top of heavily-doped p^{++} and n^{++} regions.

2.3.1.3 Optical coupling

State-of-the-art integrated photodetectors for infrared wavelengths typically use a phase-matched interlayer transition to couple light from the input waveguide to the detector [109, 178, 188–190]. However, this is difficult to achieve at shorter wavelengths due to the large

[2]The length of the waveguide could affect the timing jitter due to the timing uncertainty of photon absorption during its propagation along the waveguide. Since the propagation time along the full 16 µm length is very short, its contribution to timing jitter is negligible (see § 2.3.4.2).

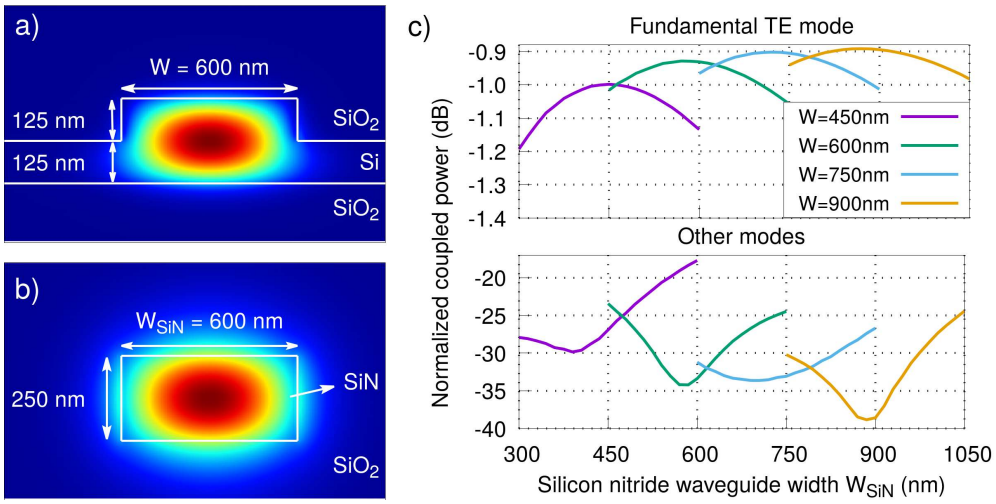

Figure 2.5: (a), (b) Optical mode profiles at 640 nm for the fundamental (quasi-)TE modes of 600 nm wide silicon and Si_3N_4 waveguides, respectively. (c) 3D FDTD simulations of end-fire coupling efficiency from the fundamental TE mode of the Si_3N_4 waveguide to the fundamental TE (top) and other modes (bottom) of the silicon waveguide. In both plots, each curve shows the coupled power for a fixed silicon waveguide width W, normalized to the input power.

difference in refractive indices for silicon ($n = 3.8$) and Si_3N_4 ($n = 2.1$). Thus, we choose to end-fire couple the input Si_3N_4 waveguide to the silicon rib waveguide in the same layer.

The optical modes in the silicon and Si_3N_4 waveguides have different shapes (see Fig. 2.5(a) and 2.5(b)). To investigate the dependence of optical coupling on the widths of the silicon waveguide W and the Si_3N_4 waveguide W_{SiN}, we perform 3D Finite Difference Time Domain (FDTD) simulations using Lumerical software (see Fig. 2.5(c)).

For a fundamental (quasi-)TE mode at 640 nm in the input Si_3N_4 waveguide, near-optimal coupling to the fundamental TE mode of the silicon waveguide can be obtained by choosing $W = W_{SiN}$, with coupling loss <1 dB for widths below 1 µm. Choosing the two waveguides to be of the same width also simplifies device fabrication. The remaining power is mostly reflected, with minimal excitation of other waveguide modes (< 25 dB for $W = W_{SiN}$). As such, we only consider the fundamental TE mode of the silicon waveguide at 640 nm for subsequent Monte Carlo simulations.

2.3.2 DC Electrical Analysis

Using the device dimensions and doping profile, we perform a DC electrical analysis of the SPAD (ATLAS device simulator, Silvaco Inc.) to obtain the electric field $\mathbf{F}$ and the charge carrier mobilities (μ_e, μ_h), drift velocities ($\mathbf{v}_e, \mathbf{v}_h$), and ionization coefficients (α_e, α_h),

where the subscripts e, h denote electron and hole, respectively. These position-dependent parameters are required for the Monte Carlo simulation of the avalanche process. We also obtain the breakdown voltage V_{br} by analyzing the current-voltage characteristics and identifying V_{br} as the reverse bias voltage at which the current increases sharply.

As the geometry and doping profile are constant along the length of the silicon waveguide, a full 3D simulation is not necessary, and we simplify the calculations by considering only the 2D waveguide cross-section. We use ATLAS's built-in graduated meshing system with a maximum element size of 5×5 nm in the waveguide core region (given by the width W and the 250 nm height) and minimum element size of 1×1 nm in a $\sim$200 nm region around the diode junction.

Within ATLAS, we use the Masetti [191] model with the phosphorus parameter set in conjunction with the Canali [192] model to obtain doping- and field-dependent mobilities and drift velocities. Amongst the available mobility models in ATLAS, we use the Masetti model as it is built upon the most updated empirical mobility data and provides more detailed information at high dopant concentrations (we simulate devices with up to 10^{19} dopants/cm^3) [191]. Ionization coefficients are obtained from the Selberherr impact ionization model [193], which only considers local electric fields; the dead space effect of impact ionization modeling is taken into account within the RPL model in the Monte Carlo simulator. The implementation details of these models can be found in the ATLAS manual [194].

2.3.3 2D Monte Carlo Simulator

2.3.3.1 Initial motivations

In addition to photon detection efficiency, timing jitter is another critical performance indicator of single photon detectors for applications such as quantum key distribution (QKD) [195], LIDAR [196], and lifetime measurements of single photon sources [197]. Timing jitter arises from the stochastic nature of the impact ionization and avalanche buildup process and cannot be modeled by deterministic simulators [198]. In contrast, Monte Carlo simulators can capture the probabilistic outcome of individual avalanches, and thus can evaluate the timing performance through statistical analysis of repeated simulation runs.

In our Monte Carlo device simulator, the Random Path Length (RPL) model is used to simulate the avalanche multiplication process [180, 182, 183]. Briefly, an absorbed photon gives rise to an electron-hole pair. Each charge carrier is accelerated by the electric field

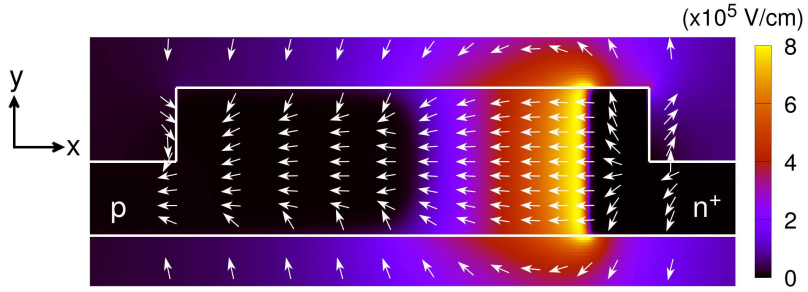

Figure 2.6: Electric field profile for a silicon rib waveguide (outlined in white), showing the waveguide core of width W = 900 nm and the surrounding regions, at a reverse bias voltage of V_B = 21 V. In regions with a lower electric field magnitude, minority charge carriers (electrons and holes in the p and n^+ regions, respectively) near the device edges are accelerated outwards of the silicon waveguide, potentially leading to their loss from the SPAD.

and may cause an impact ionization after traveling a certain path length, creating further electron-hole pairs until the device current crosses a detection threshold.

Given the probabilistic nature of the RPL model, charge carriers under the same conditions may or may not cause an impact ionization; if they do, the path length traversed by these charge carriers until the impact ionization is also random. Overall, this leads to a distribution of random detection times (i.e., time between the initial photon absorption to when the detection threshold is crossed), from which we obtain the detection timing uncertainty, i.e., the timing jitter. The initial photo-generated charge carriers may also fail to cause sufficient impact ionizations to trigger a self-sustaining avalanche process and reach the detection threshold; we thus regard the PDE as the ratio of successful detection events to the total number of simulation runs.

The most efficient way to simulate the RPL model would be to use a 1D simulator, considering only electric fields normal to the p-n^+ junction (F_x), as had been done in previous SPAD simulation work [180, 182, 183]. However, the geometry of the rib waveguide with a shallow height results in significant orthogonal F_y field components (see Fig. 2.6). As such, minority charge carriers (electrons and holes in the p and n^+ regions, respectively) near the device edges are accelerated outwards of the silicon waveguide, potentially leading to their loss from the SPAD. A 1D simulator would not take this into account, and thus likely overestimate the PDE. On the other hand, a full 3D simulation is not necessary, given the symmetry along the length of the silicon waveguide. Therefore, we choose to implement a 2D Monte Carlo simulator.

2.3.3.2 Implementation

While the DC electrical analysis considers the silicon waveguide as well as the surrounding material, we restrict the Monte Carlo simulation to only the waveguide core region, as the contribution of charge carriers is negligible outside this area.

Each simulation run models the absorption of a single input photon, the injection of a photo-generated electron-hole pair at that location, and the subsequent avalanche process. The main steps are:

1. Defining the depletion and quasi-neutral regions.
2. Absorbing an input photon and injecting a photo-generated electron-hole pair.
3. Simulating charge carrier diffusion in the quasi-neutral regions.
4. Simulating avalanche buildup with the RPL model.

For each device setting (device structure, doping levels, and bias voltage), we repeat the simulation runs until we obtain sufficient statistics. The following subsections describe the implementation of the simulator in detail.

Defining the depletion and quasi-neutral regions

The SPAD can be divided into the central depletion region, and the p- and n-type quasi-neutral regions at the sides of the silicon waveguide. The different electric field strengths in these regions give rise to different charge carrier transport dynamics. The strong electric fields in the depletion region result in the drift along the electric field being the dominant transport process, with diffusion being negligible [199]. In the quasi-neutral regions, diffusion governed by Brownian motion must be considered alongside the drift force under the weaker electric fields, while impact ionization can be ignored.

Although the transition between these regions would not be abrupt in an actual device, we follow Ref. [198] and use a threshold electric field to distinguish the high-field depletion region from the low-field quasi-neutral regions. We choose a threshold field of $F_{\text{thr}} = 1\times10^5$ V/cm, on the same order as the breakdown field in silicon [200]. The transport of charge carriers in different regions is simulated differently, as detailed in the following subsections.

Injecting a photo-generated electron-hole pair

The probability of a photon absorption event at any position is proportional to the amplitude of the input optical field. We use the spatial profile of the optical mode as a probability

density map to determine the injection point of the photo-generated electron-hole pair for each simulation run. If the injection point is in the depletion region, the simulation proceeds straight to step 4. For the quasi-neutral regions, we proceed to step 3. These photo-generated charge carriers are injected with zero initial energy.

Simulating charge carrier diffusion in the quasi-neutral regions

For the photo-generated electron-hole pair injected into the quasi-neutral regions, we immediately remove the majority carrier from the simulation as it would travel towards the metal electrodes and not towards the depletion region. Thus, we only consider the movement of the minority charge carrier (electron and hole in p and n^+ regions, respectively) of the photo-generated electron-hole pair. We model its Brownian motion as a series of random walk steps, and additionally factor in the drift due to electric fields at each step. Impact ionization is not considered here.

It is not practical to simulate every collision event; instead, for simulation efficiency, we choose a nominal step size Δd_{rw}, treating each step as a "macrocollision", i.e., a group of true collisions [201],

$$\Delta d_{\text{rw}} = \Delta l_{\text{q-n}}/50, \tag{2.2}$$

where $\Delta l_{\text{q-n}}$ is the shortest of the three relevant length scales: the widths of both quasi-neutral regions and the 250 nm height of the silicon waveguide. In other words, at least 50 steps are required to traverse the full width or height of the quasi-neutral region. The time duration of this Brownian motion displacement is

$$\Delta t_{\text{rw}} = (\Delta d_{\text{rw}})^2/2D, \tag{2.3}$$

where $D = \mu \frac{kT}{q}$ is the diffusion constant given by the mobility μ, Boltzmann constant k, temperature T, and elementary charge q. The total displacement of each random walk step is then

$$d\mathbf{r}_{\text{rw}} = \Delta d_{\text{rw}} \cdot \hat{\mathbf{e}}_{\text{R}} + \mathbf{v}_{\{e,h\}}(\mathbf{r}) \cdot \Delta t_{\text{rw}}, \tag{2.4}$$

where the first term describes the Brownian motion with a randomly chosen direction $\hat{\mathbf{e}}_{\text{R}}$ at each step, and the second term describes the displacement under the drift velocity $\mathbf{v}_e(\mathbf{r})$ or $\mathbf{v}_h(\mathbf{r})$ (depending on charge carrier type) at the current position $\mathbf{r}$.

The simulation continues until the charge carrier reaches the depletion region edge (as defined by the threshold field), where the simulation of the charge carrier continues under

the RPL model described below; or when it is lost from the SPAD through the other edges of the waveguide core, and the simulation run ends.

Simulating avalanche buildup with the RPL model

In the depletion region, charge carriers accumulate energy as they are accelerated by the electric field. Above the ionization energy threshold, they can probabilistically cause an impact ionization, creating a new electron-hole pair. The repetition of this process leads to an avalanche of charge carriers, giving rise to a macroscopic current that indicates a photon detection event.

The simulation is carried out in time steps of duration $\Delta t_{\mathrm{rpl}} = 1$ fs. In every step, we consider individually the evolution of each charge carrier i having an initial position $\mathbf{r}_{i,0}$ and a current position $\mathbf{r}_i$. The displacement under the electric field drift is

$$d\mathbf{r}_i = \mathbf{v}_{\{e,h\}}(\mathbf{r}_i) \cdot \Delta t_{\mathrm{rpl}}, \tag{2.5}$$

and the energy gain is

$$\Delta\varepsilon_i = q \cdot \Delta t_{\mathrm{rpl}} \cdot [\mathbf{F}(\mathbf{r}_i) \cdot \mathbf{v}_{\{e,h\}}(\mathbf{r}_i)], \tag{2.6}$$

where the term within the square brackets is a dot product.

The charge carrier traverses a random ionization path length before causing an impact ionization. To simulate this, each charge carrier is assigned a random number X_i from a uniform distribution between 0 and 1. We define the dead space $d_{s,i}$ as the total distance traveled by the charge carrier $s_i = \int_{\mathbf{r}_{i,0}}^{\mathbf{r}_i} d\mathbf{r}_i$ when its energy ε_i crosses the ionization energy threshold $\varepsilon_{\mathrm{thr},e}$ and $\varepsilon_{\mathrm{thr},h}$ for electrons and holes, respectively (see Table 2.2).

Above the threshold, the charge carrier accumulates an incremental ionization probability along its path with each time step, depending on the ionization coefficients $\alpha_e(\mathbf{r}_i)$ and $\alpha_h(\mathbf{r}_i)$. The cumulative probability that the charge carrier has caused an impact ionization is [182, 202]

$$P_{\mathrm{ion},i} = \begin{cases} 0 & \text{if } s_i < d_{s,i} \\ \int_{\mathbf{r}_{i,0}}^{\mathbf{r}_i} \alpha_{\{e,h\}}(\mathbf{r}'_i)\, e^{-\int_{\mathbf{r}_{i,0}}^{\mathbf{r}'_i} \alpha_{\{e,h\}}(\mathbf{r}''_i)\, d\mathbf{r}''_i}\, d\mathbf{r}'_i & \text{if } s_i \geq d_{s,i} \end{cases}. \tag{2.7}$$

Impact ionization occurs when $P_{\mathrm{ion},i} > X_i$, generating a new electron-hole pair at the current location $\mathbf{r}_i$, and the energy ε_i is redistributed among the three charge carriers as

Table 2.2: Parameters used in the simulations of symmetric rib waveguide SPADs.

Name	Symbol	Value	Reference
Electric field threshold	F_{thr}	1×10^5 V/cm	[200]
Avalanche detection threshold	I_{det}	0.2 mA	[205]
Temperature	T	243 K	-
RPL time step	Δt_{rpl}	1 fs	-
Electron ionization threshold energy	$\varepsilon_{\text{thr},e}$	1.103 eV	[203]
Hole ionization threshold energy	$\varepsilon_{\text{thr},h}$	1.269 eV	[204]
No. of simulations per parameter set	-	$\approx$ 20k	-
Energy redistribution constants:			
— electrons in an electron impact ionization	$\text{a}_{e,e}$	0.29	[203]
	$\text{b}_{e,e}$	-0.32 eV	[203]
— hole in an electron impact ionization	$\text{a}_{h,e}$	-0.31	[203]
	$\text{b}_{h,e}$	-0.92 eV	[203]
— electron in a hole impact ionization	$\text{a}_{e,h}$	-0.314	[204]
	$\text{b}_{e,h}$	-0.86 eV	[204]
— holes in a hole impact ionization	$\text{a}_{h,h}$	0.375	[204]
	$\text{b}_{h,h}$	-0.476 eV	[204]

follows [203, 204]. For an impact ionization caused by an electron, the electron and hole energies are

$$\varepsilon'_{e,e} = \text{a}_{e,e}\varepsilon_i + \text{b}_{e,e} \qquad \text{and} \qquad \varepsilon'_{h,e} = -(\text{a}_{h,e}\varepsilon_i + \text{b}_{h,e}) - \varepsilon_{\text{thr},e}, \tag{2.8}$$

respectively, and the corresponding energies for an impact ionization caused by a hole are

$$\varepsilon'_{e,h} = \text{a}_{e,h}\varepsilon_i + \text{b}_{e,h} \qquad \text{and} \qquad \varepsilon'_{h,h} = -(\text{a}_{h,h}\varepsilon_i + \text{b}_{h,h}) - \varepsilon_{\text{thr},h}. \tag{2.9}$$

The a and b coefficients are listed in Table 2.2.

For simplicity, we do not consider the effects of random walk within the RPL model, even if the charge carriers travel to the quasi-neutral regions as defined previously. Charge carriers that exit the waveguide core are considered to be lost from the SPAD and removed from the simulation. We also assume that the charge carriers are not lost via recombination, as the carrier lifetime is >10 ns for our doping concentrations, while the transport time across the sub-micron depletion width under high electric fields is below 1 ns [198, 206].

We obtain the device current using Ramo's theorem from the contributions of each charge carrier [207]

$$I = \sum_i \frac{q \cdot v_{i,x}}{W_{\text{dep}}}, \tag{2.10}$$

where $v_{i,x}$ is the component of the drift velocity in the x direction (i.e., across the width of the waveguide). We set a detection current threshold $I_{\text{det}} = 0.2$ mA as a reasonable discriminator threshold used in experimental SPAD characterization setups [205]. The simulation ends with a successful detection event when $I > I_{\text{det}}$; otherwise, it ends with a failed avalanche when the number of charge carriers drops to zero, or when the simulated time exceeds 1 ns.

Repeating the simulation to obtain sufficient statistics

For each device setting, we perform $\approx$ 20k simulation runs to obtain adequate statistics for subsequent analysis. In addition, we also performed a separate set of $\approx$ 500k simulation runs for width $W = 900$ nm at $V_{\text{B}} = 19$ V reverse bias. To reduce simulation time, this separate set of simulations are performed with a reduced detection current threshold of 0.02 mA. From the regular simulation runs, we do not observe any case where the device current rises above 0.02 mA but then fail to reach 0.2 mA, thus these results will still predict the PDE correctly. While these reduced-threshold simulations do not capture the full avalanche behavior, they can still provide insight into the diffusion of initial photo-generated charge carriers injected into the quasi-neutral regions, which requires a large number of simulation runs to observe due to low probabilities of occurrence.

2.3.4 Simulation Results

We first investigate the PDE and temporal behavior for devices with a nominal n^+ (p) doping concentration of 1×10^{19} (2×10^{17}) dopants/cm^3, then explore the effects of varying the doping concentrations.

2.3.4.1 Photon detection efficiency

By treating the success and failure outcomes of the simulation runs as a binomial distribution, we obtain the PDE as the ratio of successful detection events to the total number of simulation runs, with an uncertainty given by the standard deviation. For devices with nominal n^+ (p) doping concentration of 1×10^{19} (2×10^{17}) dopants/cm^3, the breakdown voltage $V_{\text{br}} \approx 12.4$ V; PDE increases with reverse bias voltage V_{B} and saturates at about 20 V (see Fig. 2.7(a)). We observe a maximum PDE of 45% for waveguide widths W of 750 nm and 900 nm, with narrower devices being less efficient.

Figure 2.7(b) illustrates the spatial distribution of successful avalanches. At low V_{B}, only photo-generated charge carriers injected in the central depletion region are sufficiently accelerated to cause enough impact ionizations, which leads to successful avalanches. As V_{B}

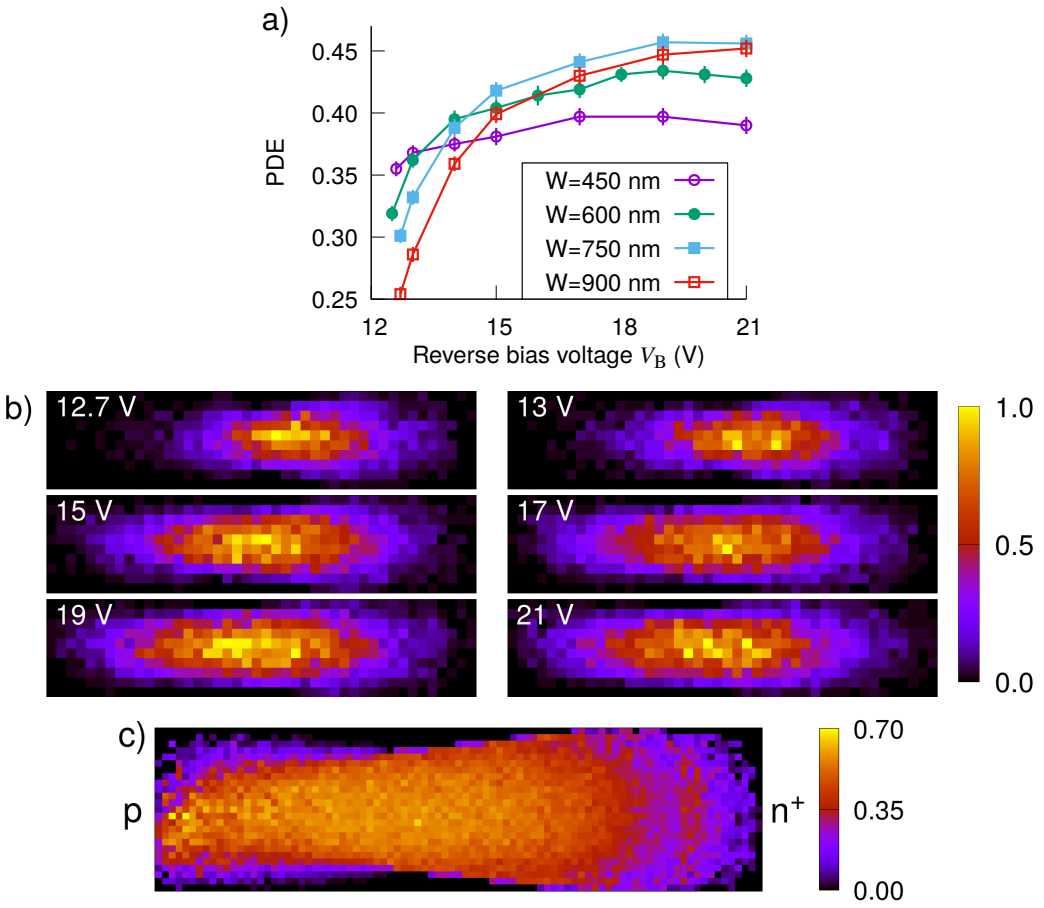

Figure 2.7: (a) Photon detection efficiency (PDE) for different waveguide widths W. Error bars show the uncertainty given by the standard deviation. (b) Maps of successful avalanches at different reverse bias voltages V_B for $W = 900$ nm. The plots show the 900×250 nm waveguide core, with each pixel being $\approx 20 \times 20$ nm. Color scale values indicate the number of successful avalanches caused by initial photo-generated charge carriers injected within that pixel, normalized to the maximum value in each plot. The data in each plot consists of ≈ 20k simulation runs. (c) Map of position-dependent probability of avalanche success for $W = 900$ nm at $V_B = 19$ V over ≈ 500k runs. Each $\approx 10 \times 10$ nm pixel shows the probability of an initial photo-generated electron-hole pair injected within that pixel resulting in a successful avalanche. All devices in this figure have a n^+ (p) doping concentration of 1×10^{19} (2×10^{17}) dopants/cm^3, and a breakdown voltage of $V_{br} \approx 12.4$ V.

increases, the depletion region becomes wider, and the impact ionization rate is enhanced. This results in more successful avalanches caused by photo-generated charge carriers injected nearer the waveguide edges, and an overall higher PDE. However, PDE saturates at high V_B and does not increase above $\sim$45%.

To gain further insight into the saturation behavior, we consider how the probability of generating successful avalanches depends on the injection coordinate of the initial photo-generated electron-hole pair (see Fig. 2.7(c)); this shows the SPAD behavior independent of the optical mode.

In general, as the initial electron-hole pair is injected further away from the junction towards the p-doped side, the avalanche success probability increases as the charge carriers can travel a larger distance over which impact ionizations can occur. However, this probability saturates at $\sim$70% near the middle of the waveguide and does not increase even as the initial injection occurs further towards the p-doped side. This indicates that most of the impact ionizations occur near the p-n$^+$ junction, where the electric fields and ionization coefficients are very high (see Fig. 2.6 and Fig. 2.9(f)). This high-field region does not become significantly wider with further increases in V_B or W; in fact, the peak electric field magnitude $|\mathbf{F}|$ decreases with increasing V_B.

Figure 2.8 plots the electric field profile together with electron and hole ionization coefficients at different reverse bias voltages V_B for $W = 900$ nm p-n$^+$ junction SPAD at the waveguide mid-height, i.e., 125 nm from the bottom. Figure 2.8(c,e) shows that higher V_B widens the part of the depletion region where impact ionization coefficients are greater than unity. However, this increase is offset by a reduction of the ionization coefficients near the junction region as shown in Fig. 2.8(d,f). Their combined effect subsequently results in the saturation of PDE with the reverse bias voltage V_B (see Fig. 2.7(a) and Fig. 2.11(a)).

Injections near the top and bottom edges in the middle section of the waveguide do not lead to successful avalanches. These regions correspond to areas where the electric field has a significant F_y component (see Fig. 2.6), thus we infer that charge carriers are pushed out of the waveguide and are lost from the device. However, within the quasi-neutral regions, it is possible for the random Brownian motion to overcome the F_y field and bring the charge carrier to the depletion region, thus contributing to the overall device PDE.

A large dead space could also suppress the device PDE by limiting the available space for charge carriers to impact ionize. However, the dead space travelled by the initial injected charge carriers is $\sim 0.05\,W$ across all widths, which is a relatively small fraction of the device dimensions.

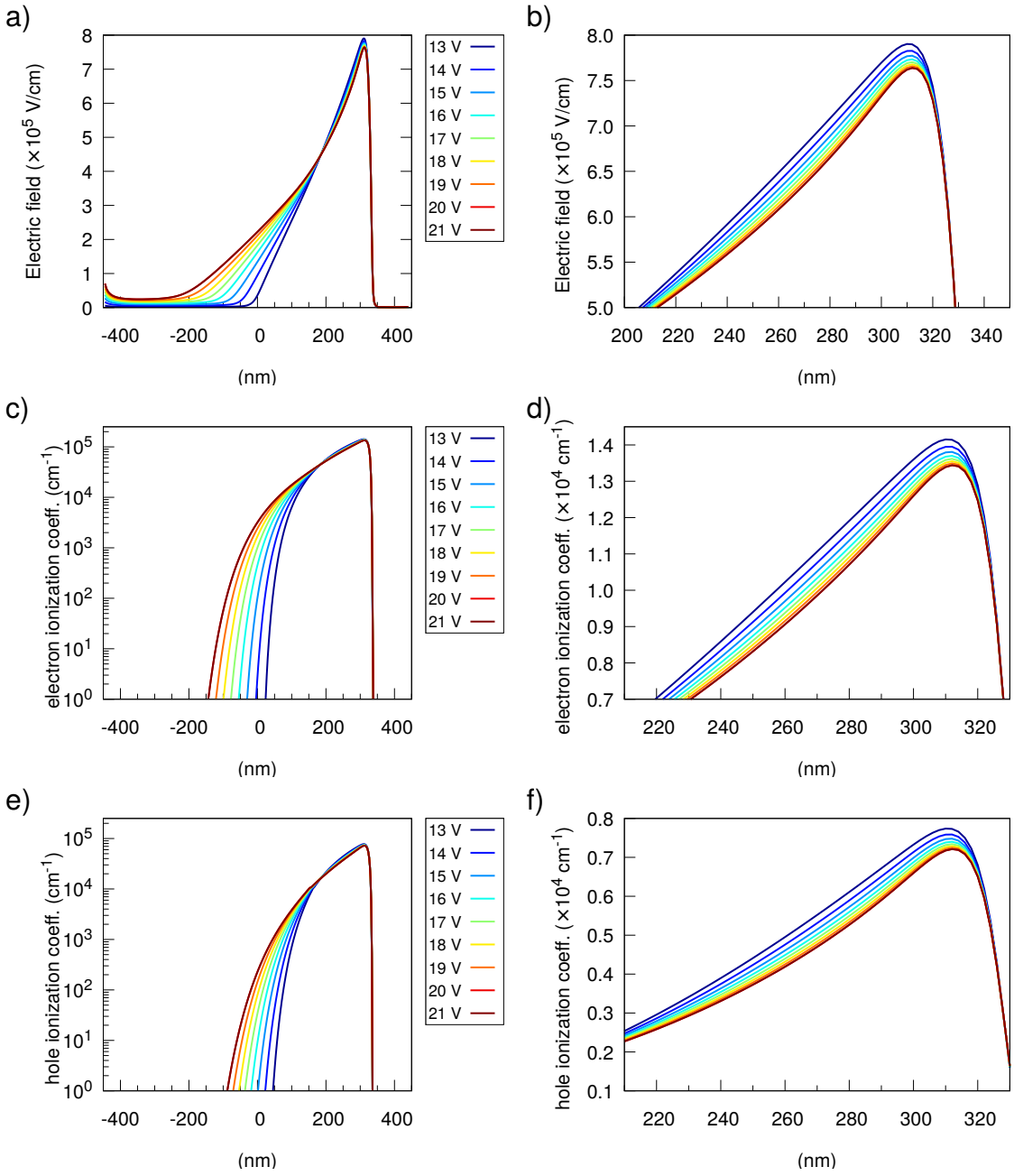

Figure 2.8: Electric field profile and electron and hole ionization coefficients vs. reverse bias voltage V_B for $W = 900$ nm p-n$^+$ junction SPAD along a cut line at the middle of the waveguide rib height. (a) Electric field profile, (c) electron ionization coefficients, (e) hole ionization coefficients with their corresponding zoomed view around the junction region in (b), (d), and (e), respectively.

The highest electric fields are concentrated at the junction separating the p- and n^+-doped regions. Alternative doping profiles, e.g., 'L'- or 'U'-shaped p-n junctions, may be a feasible way of enhancing the device PDE by increasing the overall junction length, and thus the overlap between the optical mode and the high-field regions [208–210].

2.3.4.2 Temporal behavior

The distribution of simulated times t_{ava} taken to reach the detection threshold I_{det} is generally asymmetric, and a typical example is shown in Fig. 2.9(a). Long tails in the timing distribution can adversely affect applications requiring high timing accuracies. Therefore, we extract both the full-width-half-maximum (FWHM) and full-width-tenth-maximum (FWTM) timing jitter from these timing histograms (bin size 0.2 ps). We ignore the effect of finite group velocity of the input light along the input waveguide; the propagation time along the full 16 µm waveguide is ∼0.1 ps, and the actual effect on the timing jitter is expected to be much less significant.

To further investigate the asymmetric distribution, we consider avalanches caused by photo-generated carriers injected into the p-side quasi-neutral region, as well as those injected into the high field region within the depletion width (Fig. 2.9(b) and 2.9(c)). In both cases we still observe an asymmetry, which we attribute to the nature of the impact ionization process. However, the avalanches from the p-side quasi-neutral region show a ∼3 ps longer median t_{ava} and has a larger contribution to the long tail.

Long tails in the timing distribution can be problematic for certain applications, e.g., high-repetition-rate QKD [195]. Such features with long characteristic timescales (∼ns) have been reported in other SPAD work [198, 205, 211], and were attributed to the slow diffusion of charge carriers within the quasi-neutral regions. In our device, the time taken for charge carriers injected into the quasi-neutral regions to diffuse to the depletion region is much faster (∼10 ps, see Fig. 2.9(d) and 2.9(e)), due to the smaller size of the quasi-neutral regions in our waveguide device compared to conventional free-space-coupled SPADs. We also note that the diffusion in the p-side quasi-neutral region is much faster despite its wider width compared to the n-side, due to the higher mobilities of electrons in the p-side region.

To better understand the dynamics of the avalanche process, we divide t_{ava} into an initiation time t_{init} (where the total number of charge carriers <100) and a rapid avalanche buildup time t_{bu}

$$t_{\text{ava}} = t_{\text{init}} + t_{\text{bu}}, \tag{2.11}$$

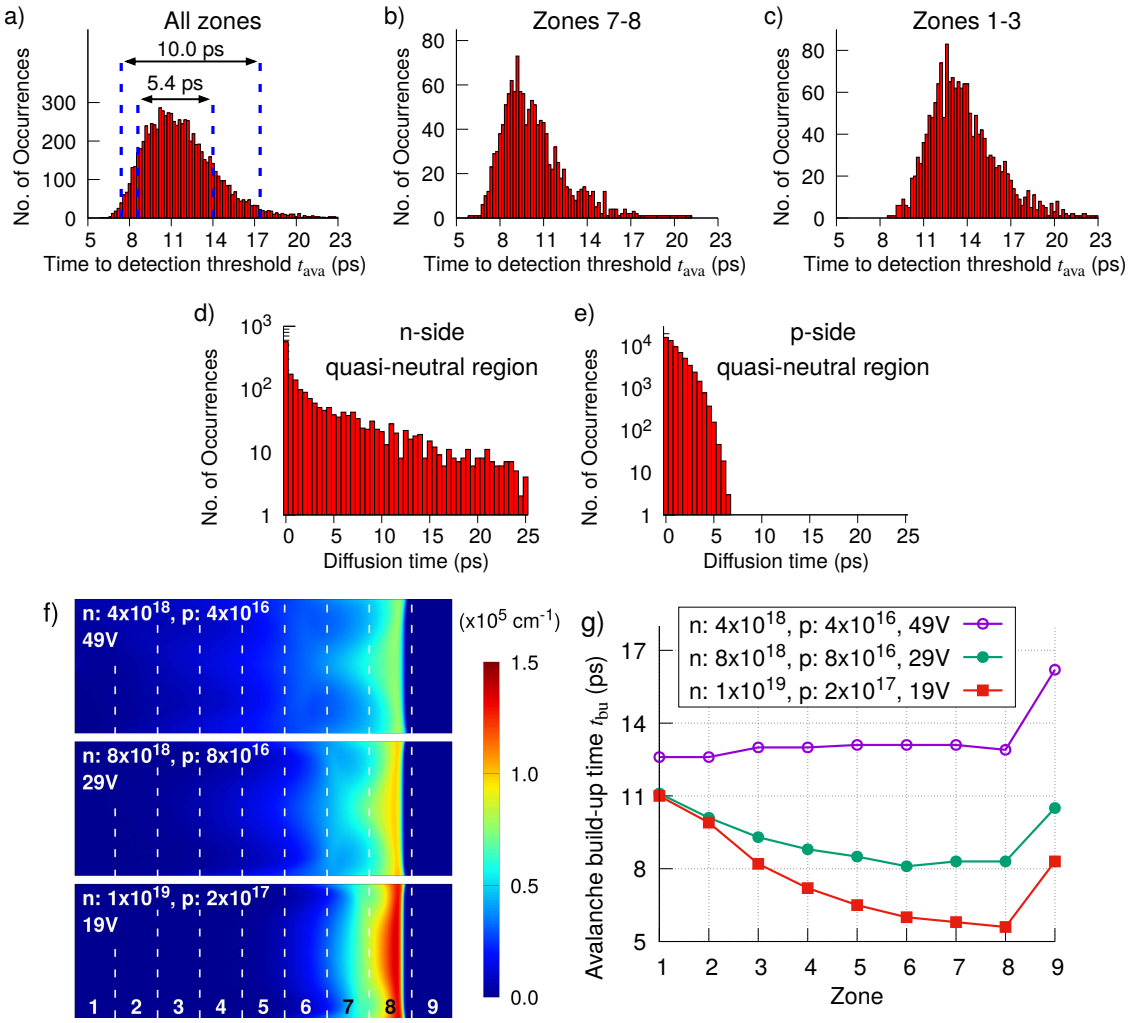

Figure 2.9: (a) Simulated times taken to reach the detection threshold t_{ava} for a device of width W=900 nm and n^+ (p) doping concentration of 1×10^{19} (2×10^{17}) dopants/cm^3, at a reverse bias voltage of V_B=19 V. Histogram bin size is 0.2 ps. The full-width-half-max (FWHM) and full-width-tenth-max (FWTM) ranges are indicated by dashed lines. Total simulation runs $\approx$ 20k. (b) and (c) show the results from the same device, but only for cases with the initial photo-generated charge carriers injected into the high-field region (zones 7 to 8) and the p-side quasi-neutral region (zones 1 to 3), respectively. The zones are as defined in (f). (d),(e) Times taken for initial charge carriers injected into n- and p-side quasi-neutral regions, respectively, to diffuse to the depletion region. Total simulation runs $\approx$ 500k; only results from successful avalanches are included in the histograms. Histogram bin size is 0.5 ps. (f) Electron ionization coefficients α_e within the 900×250 nm waveguide core at different doping levels, with V_B significantly above breakdown. (g) Median avalanche build-up times t_{bu} for charge carriers injected into each zone.

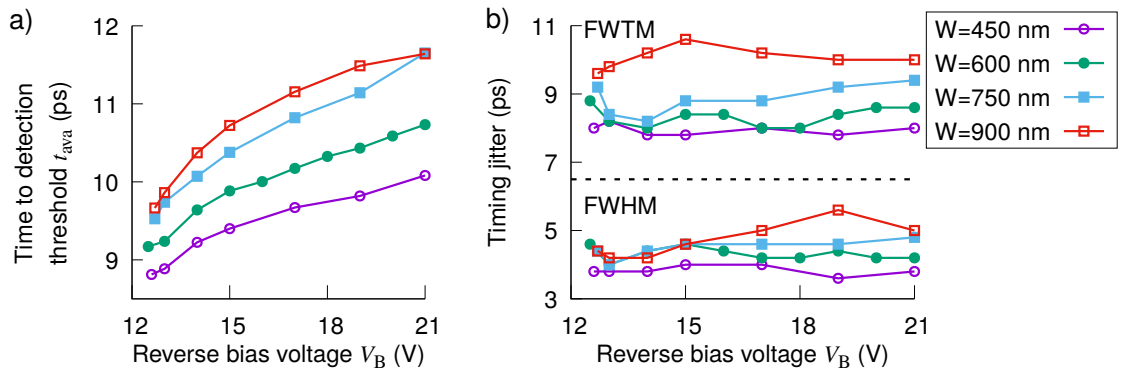

Figure 2.10: (a) Median time taken to reach the detection threshold t_{ava}, and (b) full-width-half-max (FWHM) and full-width-tenth-max (FWTM) timing jitter for different waveguide widths W. All plots share the same legend. All devices in this figure have a n^+ (p) doping concentration of 1×10^{19} (2×10^{17}) dopants/cm^3, and a breakdown voltage of $V_{br} \approx 12.4$ V.

and consider the dependence of both on the initial injection position. We find a median $t_{init} \approx 5$ ps across all regions in our simulated devices. However, there is a significant variation of t_{bu} across some devices. Regions with high ionization coefficients, also indicative of high electric field, show lower t_{bu} due to more rapid impact ionizations (see Fig. 2.9(f) and Fig. 2.9(g)).

In general, t_{ava} increases with the waveguide width W and the reverse bias voltage V_B (see Fig. 2.10(a)). As shown in Fig. 2.7(b), at higher V_B, the depletion region becomes wider, and more avalanches are caused by carriers injected nearer the waveguide edges. The slower avalanche build-up for these charge carriers results in the overall longer t_{ava} but does not significantly alter the timing jitter (see Fig. 2.10(b)). Wider waveguides have a larger spatial distribution of photo-generated charge carriers, which accounts for the longer avalanche times and larger jitter.

2.3.4.3 Varying the doping concentrations

Lower doping concentrations have been shown to increase the multiplication gain in avalanche photodiodes, albeit at a cost of higher breakdown voltages V_{br} (and thus higher operational voltages) [212]. However, for our device the PDE still saturates at about 45% as we decrease the doping levels (see Fig. 2.11). The time taken to reach detection threshold t_{ava} also shows a clear increase with decreased doping, and timing jitter becomes worse. Thus, on all three counts, we do not observe any performance advantage in lowering the doping concentrations.

We note that our results do not capture the sharp change in PDE near V_{br} for n^+ (p) doping concentrations of 4×10^{18} (4×10^{16}) dopants/cm^3; we only run simulations above

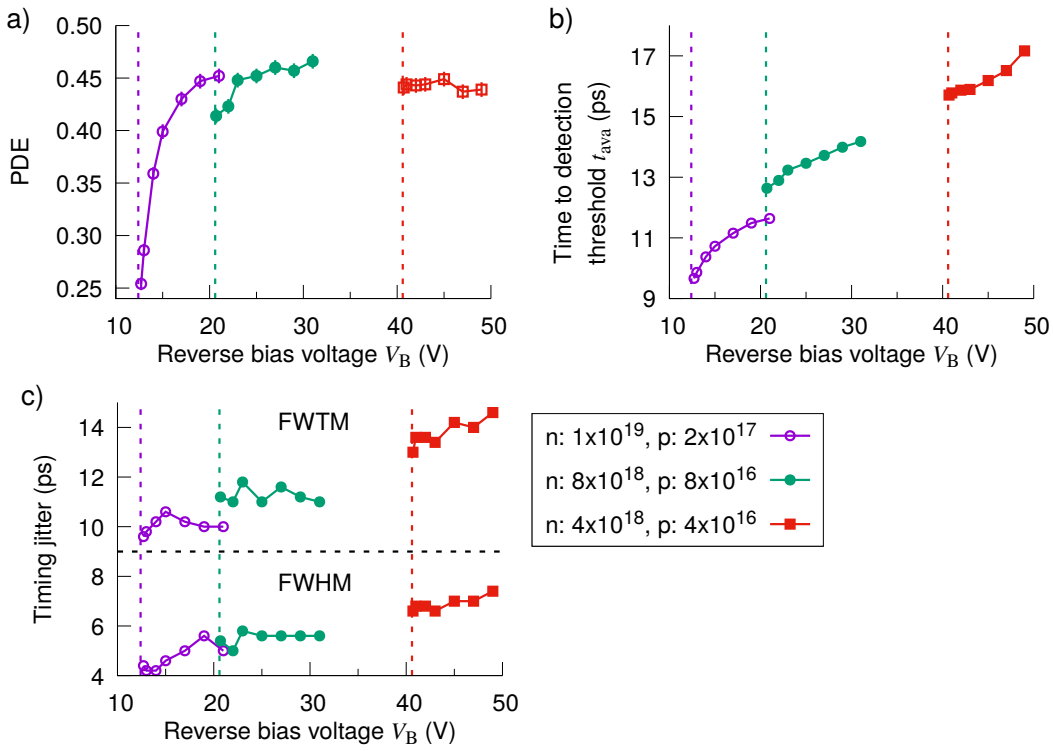

Figure 2.11: (a) Photon detection efficiency (PDE), (b) median time taken to reach the detection threshold t_{ava}, and (c) full-width-half-max (FWHM) and full-width-tenth-max (FWTM) timing jitter at different doping levels (in units of dopants/cm^3) for waveguides of width $W = 900$ nm. Error bars in (a) show the uncertainty given by the standard deviation. Dashed vertical lines indicate breakdown voltages V_{br}. All plots share the same legend.

$V_{\mathrm{br}} \approx 40.6\,\mathrm{V}$ obtained from the DC electrical analysis, but perhaps our simulator would show a significant PDE even below this value.

From our observations, it may be inferred that increasing the doping concentrations (and, in turn, the electric field) further could still yield a high PDE with an even lower operating voltage. However, Zener breakdown becomes dominant at very high electric fields [200, 213], which would then impede the performance of the SPAD.

2.3.5 Discussion

In this section, we performed the first design and simulation study on CMOS-compatible silicon waveguide-integrated SPADs for visible wavelengths. Our devices have symmetric rib waveguide geometry, and our simulated devices show a maximum PDE of 45% at $\sim$20 V reverse bias, which is slightly lower but still competitive compared to commercial large-area free-space SPAD modules with PDEs of up to $\sim$70% [214]. However, typical FWHM timing jitter in our devices is $< 8\,\mathrm{ps}$, significantly better than high-timing-resolution free-space SPADs (jitter $\sim 35\,\mathrm{ps}$).

To simulate a device at a given bias voltage, our simulator (implemented in Python) requires $\sim$24k CPU-hours on two sets of 12-core CPUs (Intel® Xeon® E5-2690 v3). Such a high computation cost limits the variety of SPAD designs we can feasibly study. In the next section, we optimized the simulation parameters to reduce computation time without sacrificing the simulation accuracy and explored more design variations to improve device performance.

2.4 Extended Study: Asymmetric Rib Waveguide APDs

Here, we extended our study on silicon waveguide-integrated SPAD design and enhanced device performance through the optimization of device structure. In our previous study, the p-n$^+$ junction was placed asymmetrically within a symmetric rib waveguide core to maximize the spatial overlap between the large depletion region on the p-doped side and the optical waveguide mode. Following some preliminary studies, here, we designed devices with asymmetric rib waveguides and explored p-n$^+$ junctions placed also outside the waveguide core to find an optimum position that yields a high photon detection efficiency and low timing jitter. Besides, we also investigated p-i-n$^+$ junctions and studied the effect of the intrinsic region width on device performance[3].

[3] We started our research on the asymmetric rib waveguide APDs with p-n$^+$ and p-i-n$^+$ junction profiles after the simulation and tape-out of the symmetric rib waveguide APDs with p-n$^+$ junction profiles.

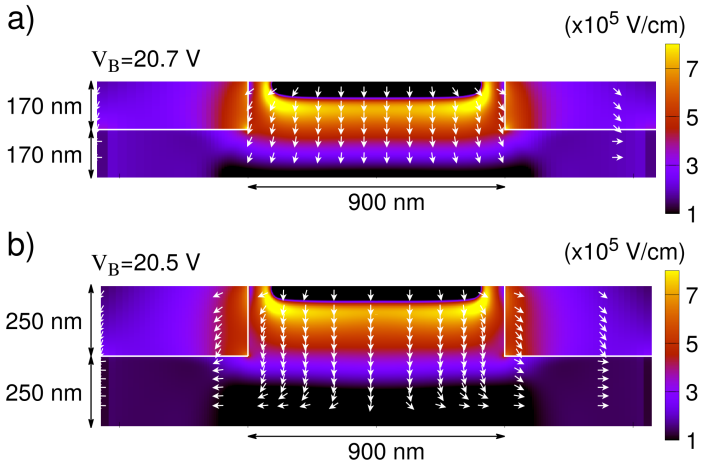

Figure 2.12: Electric field profiles of waveguide-integrated SPADs with p-n$^+$ junctions horizontally placed inside the waveguide core. The devices have symmetric rib waveguides with waveguide thicknesses of a) 340 nm and b) 500 nm. The electric field profiles are obtained at reverse bias voltages V_B at which the devices attain their saturated PDEs.

The required computation time to simulate a device with a set of design parameters was a limiting factor in the previous section; here, we optimized our 2D Monte Carlo simulator to reduce the simulation time without sacrificing the simulation accuracy. We also incorporated dark count rate calculations to compare the noise performance of different designs at room temperature and at $-30\,^{\circ}$C (243 K), which is a typical operating temperature achievable by thermoelectric coolers.

2.4.1 Preliminary Investigations

The photon detection efficiency and timing jitter of devices with waveguide widths W of 750 nm and 900 nm are found to be similar (see § 2.3). Given their similar performance, there are some advantages in choosing a slightly larger width because a wider waveguide allows for greater flexibility in the diode junction design, as well as affording a greater tolerance for device fabrication. For this reason, we fixed the waveguide width to 900 nm in this section.

2.4.1.1 Horizontal junction designs

In the previous section, SPAD designs consist of 250 nm thick symmetric rib waveguides of various widths with p-n$^+$ junctions being placed vertically inside the waveguide core (see Fig. 2.4). The map of the successful avalanches of these devices (see Fig. 2.7) indicates that the injections near the top and bottom edges in the middle section of the waveguide fail to lead to successful avalanches due to significant F_y field components at

these regions (see Fig. 2.6). This led us to explore devices with junctions placed horizontally inside the waveguide core. Unlike the devices having junctions placed vertically inside the waveguide core, the horizontal junction placement results in negligible overlap between the optical mode profile and the field component which may cause charge carrier escape. Here, we first performed a preliminary study to investigate if placing the junction horizontally inside the waveguide core region would improve the PDE.

Motivated by the previous observation that a larger waveguide width increases the distance over which avalanche multiplication of charge carriers can occur, we increased the waveguide thickness to improve the photon detection efficiency of these new set of devices.

Figure 2.12 shows electric field profiles for devices that have different waveguide thickness with p-n^+ junctions placed horizontally inside the symmetric rib waveguide cores. Similar to the devices with vertically oriented p-n^+ junctions, these devices also have similar n^+ (p) doping concentration of 1×10^{19} (2×10^{17}) dopants/cm^3. A 60-nm-thick n^+-doped region is centrally placed on top of the rib waveguide with its sides being 80 nm away from the edges of the rib waveguide. The simulated saturated PDEs of these devices for waveguide thicknesses of 340 nm and 500 nm are 18 % and 36 %, respectively. Therefore, these new designs do not bring any improvements to the photon detection efficiency compared to our previous designs in § 2.3. Increasing the waveguide thickness beyond 500 nm might increase the PDE, however the fabrication of such devices becomes challenging due to the mechanical stress associated by such thick waveguide layers. Consequently, the horizontal doping configuration was not studied any further.

2.4.1.2 Increasing avalanche multiplication path length

Our simulation study in the previous section showed that increasing waveguide core widths (up to 900 nm) could lead to a higher PDE, as charge carriers can travel a larger distance over which avalanche multiplication can occur. Here, we fixed the waveguide width to 900 nm, and alternatively vary the placement of the p-n^+ junction. We investigate the hypothesis that increasing the displacement of the junction beyond the edge of the waveguide core region can enhance this effective distance as well.

Asymmetric rib waveguides

As a preliminary study, we studied two devices which are comprised of p-n^+ junctions that are placed vertically at 200 nm away from the right edge of the waveguide core as shown in Fig. 2.13. Here, the attention should be paid to minimize possible hot carrier injections

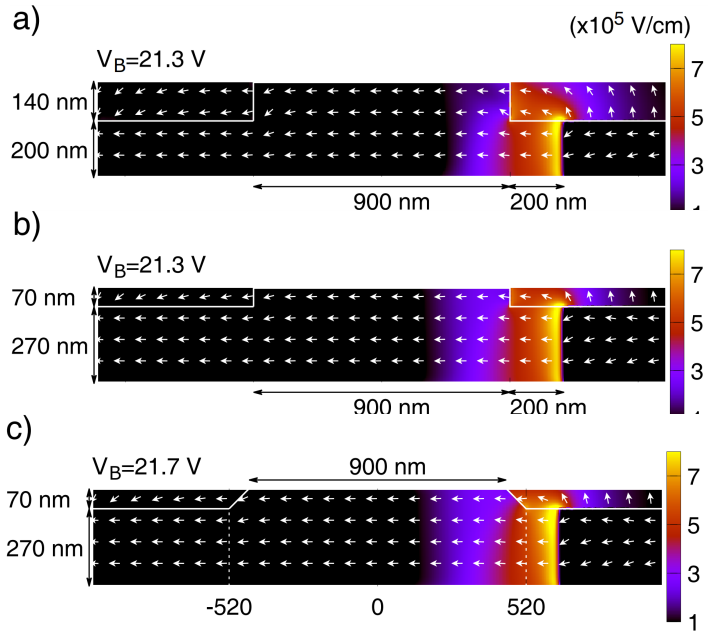

Figure 2.13: Electric field profiles of waveguide-integrated SPADs of 340 nm thick asymmetric rib waveguides. The p-n$^+$ junctions are vertically placed 200 nm away from the right edge of the waveguide core. a) The asymmetric rib waveguide having a rectangular cross section with 140 nm etch depth. The asymmetric rib waveguide having a b) rectangular and c) trapezoid cross section with 70 nm etch depth.

into the interface between the rib waveguide and SiO_2 top cladding, which would otherwise reduce the PDE (see Fig. 2.13). Thus, we design the rib waveguide to be asymmetric via a slightly shallower etch depth. To have more fabrication tolerance and design flexibility in designs with shallower etch depth, we increased the waveguide thickness from 250 nm to 340 nm.

Figure 2.13(a) shows a waveguide-integrated SPAD that is comprised of a 340-nm-thick waveguide with an etch depth of 140 nm. When the device is biased at $V_B = 21.3$ V, at which the device attains its saturated PDE, 4% of hot electrons undergo sidewall collisions at the right edge of the rib waveguide during their drift motion. With the aim of minimizing such sidewall collisions, we increase the rib waveguide asymmetry by designing a device which has even shallower etch depth of 70 nm as shown in Fig. 2.13(b). This design reduces the sidewall collisions from 4% to 0.4%, and subsequently increases the PDE from $29.2 \pm 0.4\%$ to $40.6 \pm 0.6\%$. We note that the increase in PDE is higher than the percentage improvement in the sidewall collisions. This additional increase in PDE is due to the prevention of high electric field leakage into the top SiO_2 cladding. Increasing the asymmetry of the rib waveguide leads to more confinement of the high electric field inside the Si waveguide. SPAD

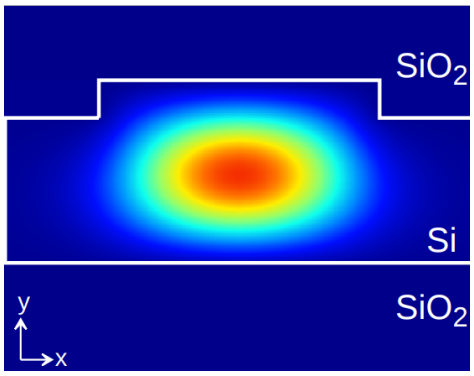

Figure 2.14: The optical mode profile at 640 nm for the fundamental (quasi-)TE mode of our silicon waveguide-integrated SPAD in asymmetric rib waveguide geometry. The 900 nm wide silicon waveguide has a thickness of 340 nm with a shallow etch depth of 70 nm.

designs with shallower etch depths were not investigated because decreasing the etch depth even further causes the optical mode profile to leak from the waveguide core.

Trapezoid waveguide

Lastly, we checked whether an angled interface between the silicon rib waveguide and the top SiO_2 cladding improves the photon detection efficiency by reducing such sidewall collisions. Here, we modified the rectangular asymmetric rib waveguide design with a shallow etch depth of 70 nm in a way that the cross-section of the rib waveguide is now a trapezoid. Figure 2.13(c) shows our trapezoid rib waveguide design with 135° angle between the rib waveguide and the top cladding. The simulated PDE of $39.8 \pm 0.4\%$ is not significantly different from that of its rectangular counterpart (see Fig. 2.13(b)); therefore, we proceed with the rectangular waveguide geometry due to its easier fabrication.

2.4.2 Device Description

Based on our preliminary studies, we fixed the device structure such that the silicon waveguide is 900 nm wide and 340 nm thick with a shallow etch depth of 70 nm, defining the rectangular rib waveguide as shown in Fig. 2.13(b). The optical mode profile at 640 nm for the fundamental (quasi-)TE mode for this geometry is shown in Fig. 2.14.

Doping configurations

Next, we studied p-n^+ and p-i-n^+ doping configurations to maximize the PDE. For both device families, we maintained a constant doping profile along the length of the waveguide.

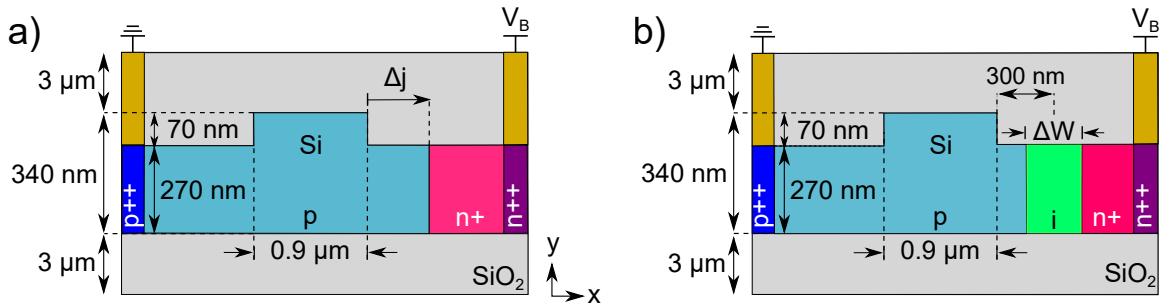

Figure 2.15: (a) p-n$^+$ doping configuration with the junction placed at a distance Δj from the right edge of the waveguide core, (b) p-i-n$^+$ doping configuration with an intrinsic region width ΔW. The cross section is constant along the length of the waveguide. The images are not drawn to scale.

Similar to the previous study, we choose a n$^+$ (p) doping concentration of 1×10^{19} (2×10^{17}) dopants/cm^3, and a lightly p-doped intrinsic region with 1×10^{15} dopants/cm^3.

Exploring optimum junction placement for p-n junctions

As described in § 2.4.1.2, increasing the displacement Δj of the junction beyond the edge of the waveguide core region may enhance the avalanche multiplications. Here, we extend our design study in § 2.3 and explore the optimum position for the p-n$^+$ junction placement as shown in Fig. 2.15(a).

Widening the high-field region with p-i-n junctions

Impact ionizations are most efficient in regions with high electric field strengths (see Figs. 2.16(a)-(c)). Widening a high-field region can enhance the PDE and is achievable by introducing an intrinsic region between the p- and n$^+$-doped areas (Fig. 2.15(b)). However, doing so would also lower the peak electric field strength, and subsequently reduce the impact ionization efficiency (Fig. 2.16(d)). Here, we explore the effectiveness of such p-i-n$^+$ devices and study the optimum width ΔW of the intrinsic region, which is centered at 300 nm from the edge of the waveguide core.

2.4.3 DC Electrical Analysis

Similar to the previous section, for each set of device dimensions and doping configurations, we perform a DC electrical analysis (ATLAS, Silvaco Inc.) by applying a reverse bias voltage V_B across the device electrodes. For each device, the cathode and anode are placed

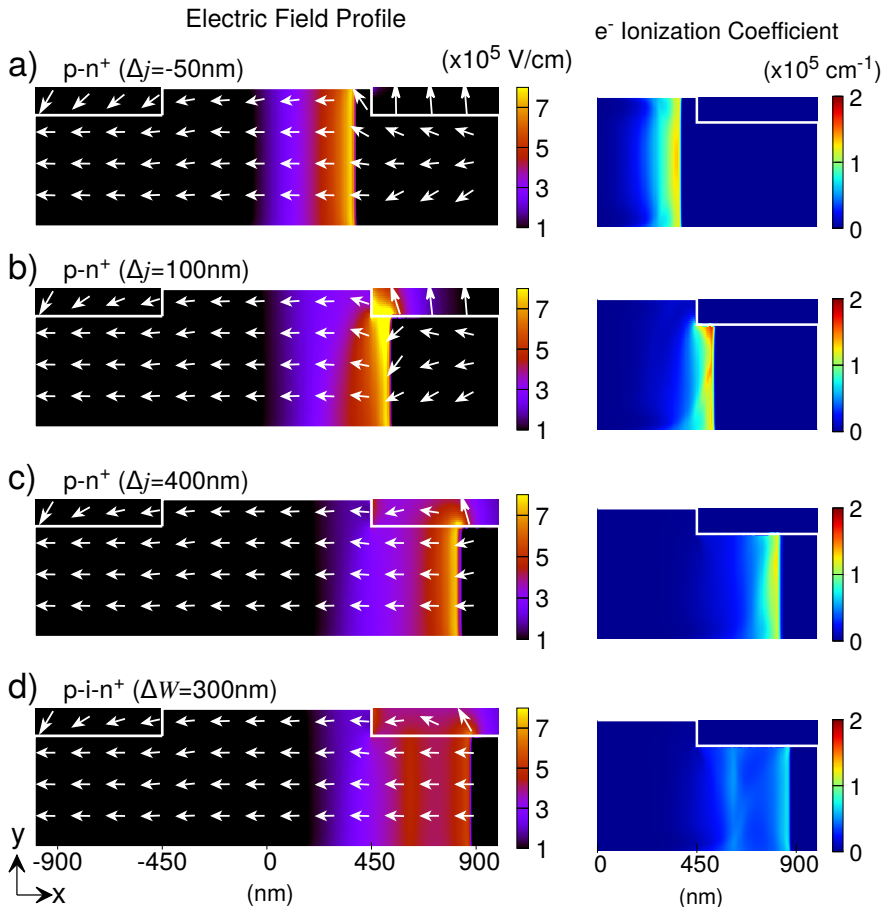

Figure 2.16: Electric field profiles (left) and electron ionization coefficients (right) at reverse bias voltages V_B where the photon detection efficiency (PDE) saturates. a) p-n$^+$ SPAD with Δj = -50 nm at V_B = 18.5 V, b) p-n$^+$ SPAD with Δj = 100 nm at V_B = 23.7 V, c) p-n$^+$ SPAD with Δj = 400 nm at V_B = 26.5 V, and d) p-i-n$^+$ SPAD with ΔW = 300 nm at V_B = 28.2 V. For the electron ionization coefficients, only half the waveguide ($x > 0$) is shown as their values are negligible in the other half.

equidistant from the center of the Si waveguide, with a minimum n$^+$ region width of 45 nm. Thereafter, we obtain the electric field $\mathbf{F}(\mathbf{r})$, ionization coefficients, and other parameters dependent on the 2D position vector $\mathbf{r}$ in the $x-y$ plane; these are required for the Monte Carlo simulation of the avalanche process.

2.4.4 2D Monte Carlo Simulator

2D Monte Carlo simulations are performed with the same simulation steps outlined in § 2.3.3.2. Similar to the previous section, we use the fundamental (quasi-)TE mode profile (Fig. 2.14) as a probability density map to determine the location where the initial

electron-hole pair is injected for each simulation run. If the injection occurs in the quasi-neutral regions, charge carrier transport is simulated using the diffusion model; if the charge carrier crosses over to the depletion region, the simulation continues under the RPL model.

2.4.4.1 Simulator modifications

Unlike the Monte Carlo simulator in the previous section, however, the Monte Carlo simulation in this section considers the entire device area and is not restricted to the waveguide core region as the device designs in this section also include junction placements outside of the waveguide core region.

The other major difference is the calculation of the device current. In the previous section, we calculate the device current using a 1D approximation of Ramo's theorem, which only considers the motion of charge carriers in one direction. However, this would not be suitable here given our SPAD designs and more complex electric field profiles. As such, we use the generalized Shockley-Ramo's current theorem [207, 215], where each charge carrier i at position $\mathbf{r}_i$ contributes to the device current I induced on the cathode via

$$I = \sum_i q_i \cdot \mathbf{v}_i(\mathbf{r}_i) \cdot \mathbf{F}_0(\mathbf{r}_i), \tag{2.12}$$

where q_i is the charge, $\mathbf{v}_i(\mathbf{r}_i)$ is the instantaneous velocity, and $\mathbf{F}_0(\mathbf{r}_i)$ is a weighting electric field calculated in a similar way to $\mathbf{F}(\mathbf{r})$, but under these modified conditions: (i) the cathode is at unit potential, while the anode is grounded; (ii) all charges (including space charges) are removed, i.e., the waveguide is undoped [216].

2.4.4.2 Simulator optimizations

The Monte Carlo simulations are computationally expensive due to the need to keep track of and model individual charge carriers, especially when the number of charge carriers grows exponentially during an avalanche process. In the previous section, long simulation times were a limiting factor for us to study devices with more design variations. Therefore, we optimized our 2D Monte Carlo simulator to reduce the simulation time without sacrificing simulation accuracy to be able to explore more designs.

Here, we use a representative device (p-n$^+$ SPAD with Δj = -50 nm, at V_B = 21.5 V) to perform a series of preliminary studies to optimize the simulation parameters: the detection threshold I_det, RPL time step Δt_rpl, and number of simulation runs per parameter set.

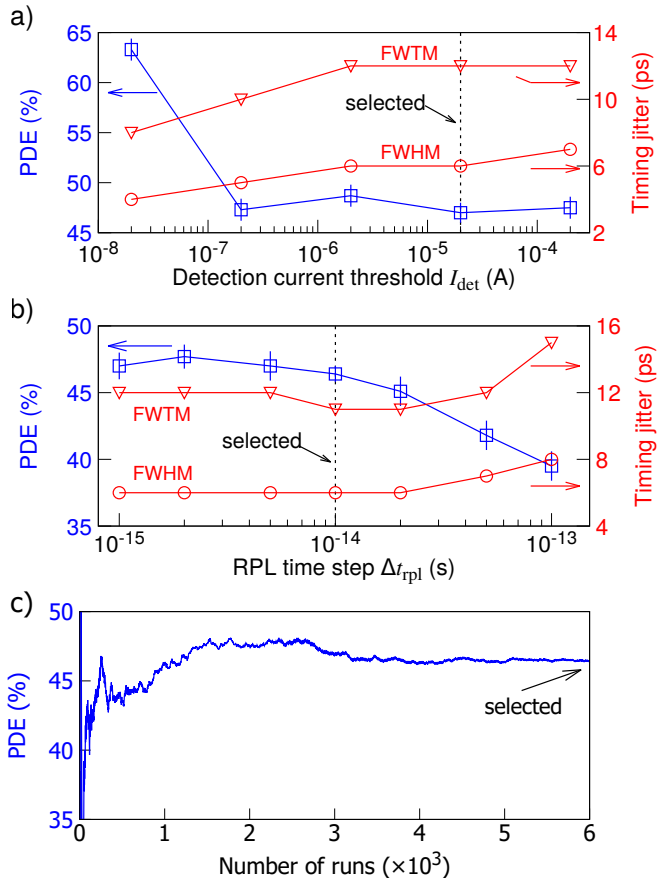

Figure 2.17: Optimization study of varying simulator parameters and their effects on the photon detection efficiency (PDE) and timing jitter (full-width-half-max (FWHM) and full-width-tenth-max (FWTM)), for a p-n$^+$ SPAD with Δj = -50 nm at V_B = 21.5 V. (a) Varying I_{det} with Δt_{rpl} = 1 fs, 2k simulation runs per I_{det} value. (b) Varying Δt_{rpl} with I_{det} = 20 µA, 2k simulation runs per Δt_{rpl} value. (c) Convergence of PDE for Δt_{rpl} = 10 fs and I_{det} = 20 µA after several thousand runs. Error bars for PDE indicate 1 s.d. uncertainty. Selected parameters for subsequent simulations are marked.

Detection current threshold

A reasonable discriminator threshold in experimental SPAD characterization setups is $I_{\text{det}} = 0.2\,\text{mA}$ [205], a value we used in our first design and simulation study in § 2.3. However, it may not be necessary to simulate the multiplication of charge carriers up to that point as the avalanche process might already have passed a self-sustaining threshold at a lower current. On the other hand, a very low I_{det} would overestimate the PDE by falsely identifying small avalanches that would not be self-sustaining and underestimate the timing jitter by not simulating the full avalanche.

By varying I_{det} while fixing $\Delta t_{\text{rpl}} = 1\,\text{fs}$ with 2k simulation runs per I_{det} value (Fig. 2.17(a)), we conclude that we can lower I_{det} to 20 µA without significant deviations in PDE or timing jitter.

RPL time step

A larger RPL time step Δt_{rpl} would speed up simulations but reduces time resolution and hence accuracy. A suitable choice would be just short enough such that the charge carrier environment does not change too significantly between each step, even in the high-field regions with large field gradients.

We vary Δt_{rpl} while fixing $I_{\text{det}} = 20\,\mu\text{A}$ with 2k simulation runs per Δt_{rpl} value (Fig. 2.17(b)). We choose $\Delta t_{\text{rpl}} = 10\,\text{fs}$ as an optimal value; for larger time steps, PDE begins to deviate significantly compared to the previous value of $\Delta t_{\text{rpl}} = 1\,\text{fs}$.

Number of simulation runs

We analyze the PDE over an increasing number of simulation runs for $\Delta t_{\text{rpl}} = 10\,\text{fs}$ and $I_{\text{det}} = 20\,\mu\text{A}$ and observe that the PDE converges to a stable value after several thousand runs. We choose to perform at least 6k runs per parameter set to reduce the relative uncertainty to $\sim 1\%$.

Compared to the previous simulation parameters (i.e., $\Delta t_{\text{rpl}} = 1\,\text{fs}$, $I_{\text{det}} = 0.2\,\text{mA}$, 18k runs), our optimized values ($\Delta t_{\text{rpl}} = 10\,\text{fs}$, $I_{\text{det}} = 20\,\mu\text{A}$, 6k runs) require only ~ 90 CPU-hours per set, indicating an improved timing performance by a factor of ~ 270.

2.4.5 Dark Count Rate Calculations

Even in the absence of light, free charge carriers may be generated, which can probabilistically trigger avalanche events and result in dark counts. Due to the high electric fields in SPADs,

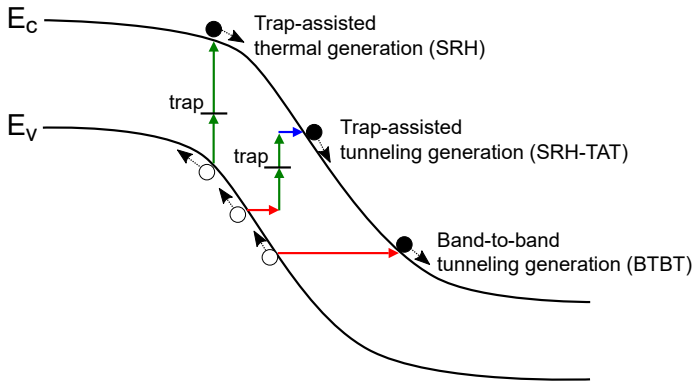

Figure 2.18: Band diagram of various dark count generation mechanisms. Trap-assisted tunneling and band-to-band tunneling are the dominant generation mechanisms for silicon SPADs operated in high electric fields.

the most relevant carrier generation mechanisms are thermal excitation enhanced by trap-assisted tunneling (TAT), and band-to-band tunneling (BTBT) (see Fig. 2.18). We quantify the dark noise by calculating the DCR $R_D(T)$ via [217]

$$R_D(T) = L \cdot \iint P_{\text{trig}}(\mathbf{r}) \cdot \left(G_{\text{TAT}}(\mathbf{r},T) + G_{\text{BTBT}}(\mathbf{r},T)\right)\, \mathrm{d}\mathbf{r}, \tag{2.13}$$

where T is the temperature, $L = 16\,\mu\text{m}$ is the SPAD length, $P_{\text{trig}}(\mathbf{r})$ is the avalanche triggering probability, and $G_{\text{TAT}}(\mathbf{r},T)$, $G_{\text{BTBT}}(\mathbf{r},T)$ are the net generation rates of charge carriers (per unit volume) of their respective mechanisms.

2.4.5.1 Trap-assisted tunneling

The thermal generation rate of carriers can be obtained from the Shockley-Read-Hall (SRH) model, modified to account for TAT [218, 219]

$$G_{\text{TAT}}(\mathbf{r},T) = \frac{n_i(T)}{\tau_g(\mathbf{r},T)}, \tag{2.14}$$

where $n_i(T)$ is the intrinsic carrier concentration and $\tau_g(\mathbf{r},T)$ is the electron-hole pair generation lifetime, which can be expressed in terms of the recombination lifetime $\tau_r(\mathbf{r},T)$ [206]

$$\tau_g(\mathbf{r},T) = \frac{\tau_r(\mathbf{r},T) \cdot e^{|E_t - E_i|/k_B T}}{1 + \Gamma(\mathbf{F}(\mathbf{r}),T)}, \tag{2.15}$$

where the exponential term describes the main temperature dependence in TAT, and the field effect function $\Gamma(\mathbf{F}(\mathbf{r}),T)$ describes the effect of electric fields. E_t and E_i are the energy

levels of the recombination centers (assumed to be equal to that of traps at the Si/SiO_2 interface [220]) and the intrinsic Fermi level, respectively, and k_B is the Boltzmann constant. The field effect function $\Gamma(\mathbf{F}(\mathbf{r}),T)$ is

$$\Gamma(\mathbf{F}(\mathbf{r}),T) = 2\sqrt{3\pi}\cdot\frac{|\mathbf{F}(\mathbf{r})|}{F_\Gamma(T)}\cdot\exp\left(\left(\frac{|\mathbf{F}(\mathbf{r})|}{F_\Gamma(T)}\right)^2\right), \tag{2.16}$$

in which

$$F_\Gamma(T) = \frac{\sqrt{24m_t^*(k_BT)^3}}{q\hbar}, \tag{2.17}$$

where q is the electron charge, and $m_t^* = 0.25\,m_0$ is the effective electron tunneling mass, with m_0 being the electron rest mass [221]. In eq. 2.14, we calculate the intrinsic carrier concentration $n_i(T)$ in silicon via [222]

$$n_i(T) = 5.29\times10^{19}\cdot(T/300)^{2.54}\cdot\exp(-6726/T). \tag{2.18}$$

To obtain the electron-hole pair generation lifetime in $\tau_g(\mathbf{r},T)$ (Eq. 2.15), we obtain the effective recombination lifetime at 243 K as follows: The effective recombination lifetime $\tau_r(T)$ was measured to be 7 ns at room temperature for an undoped Si rib waveguide device with similar sub-µm dimensions [223]. To obtain a suitable value at 243 K, we analyze the temperature dependence of $\tau_r(T)$. For low-level injection in p-type silicon, $\tau_r(T)$ can be approximated as the electron recombination lifetime [206]

$$\tau_r(T) \approx \frac{1}{\sigma_e\cdot\nu_e(T)\cdot N_t}, \tag{2.19}$$

where σ_e is the electron capture cross section, $\nu_e(T)$ is the mean thermal velocity of electrons, and N_t is the trap density. The trap density N_t is assumed to be temperature-independent, while for traps at Si/SiO_2 interface with E_t - E_i = 0.25 eV, σ_e has been shown to be relatively constant over our relevant temperature range (243 – 300 K) [224]. Thus, the temperature dependence comes only from $\nu_e(T)\propto\sqrt{T}$, and we obtain

$$\tau_r(243) = \tau_r(300)\cdot\sqrt{300/243}. \tag{2.20}$$

2.4.5.2 Band-to-band tunneling

The BTBT mechanism has been shown to be important at electric field strengths above 7×10^5 V/cm, where band-bending is sufficiently strong to allow significant tunneling of electrons from the valence band to the conduction band [221]. This rate can be expressed as

Table 2.3: Parameters used in the simulations of asymmetric rib waveguide SPADs.

Name	Symbol	Value	Reference
Electric field threshold	F_{thr}	1×10^5 V cm^{-1}	[200]
Avalanche detection threshold	I_{det}	20 µA	-
RPL time step	Δt_{rpl}	10 fs	-
No. of simulations per parameter set	-	$>$ 6k	-
BTBT parameter	B_A	4×10^{14} cm$^{-0.5}$V$^{-2.5}$s^{-1}	[221]
	B_Γ	2.5	[221]
Recombination energy	E_t-E_i	0.25 eV	[220]
Temperature dependent parameters at 300 (243) K:			
– intrinsic carrier concentration	n_i	9.70×10^9 (2.95×10^7) cm^{-3}	[222]
– Recombination lifetime	τ_r	7.0 (7.8) ns	[220, 223]
– BTBT parameter	B_B	1.90 (1.94) $\times$ 10^7 V cm^{-1}	[221, 225]

$$G_{\text{BTBT}}(\mathbf{r},T) = B_A \cdot |\mathbf{F}(\mathbf{r})|^{B_\Gamma} \cdot \exp\left(\frac{-B_B(T)}{|\mathbf{F}(\mathbf{r})|}\right), \tag{2.21}$$

where B_A, B_B, and B_Γ are model parameters; we use values based on ref [221]. Values for B_A, B_B and B_Γ at room temperature are given in ref. [221]. Both B_A and B_Γ are nominally temperature-insensitive, while $B_B(T) \propto [E_g(T)]^{3/2}$, where $E_g(T)$ is the Si bandgap energy [225]

$$E_g(T) = A + BT + CT^2, \tag{2.22}$$

in which $A = 1.1785$ eV, $B = -9.025 \times 10^{-5}$ eV/K, and $C = -3.05 \times 10^{-7}$ eV/K^2, for 150 K $\leq T \leq$ 300 K. We thus obtain

$$B_B(243) = B_B(300) \cdot \left(\frac{E_g(243)}{E_g(300)}\right)^{(3/2)}. \tag{2.23}$$

The values of the parameters used in our calculations are listed in Table 2.3.

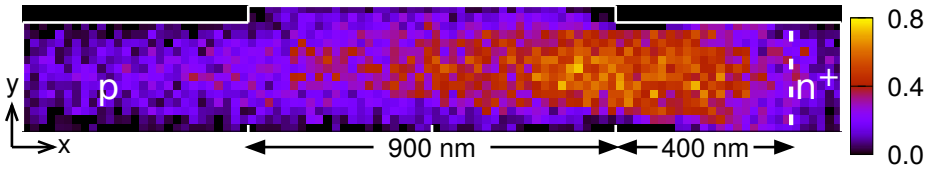

Figure 2.19: Avalanche triggering probability $P_{\text{trig}}(\mathbf{r})$ for a p-n$^+$ SPAD with $\Delta j = 400$ nm at $V_{\text{B}} = 16.5$ V, obtained over >40k Monte Carlo simulation runs. Each 20×20 nm pixel shows the probability of an initial photo-generated electron-hole pair injected within that pixel resulting in a successful detection event. The dashed line indicates the junction position.

2.4.5.3 Avalanche triggering probability

To obtain the avalanche triggering probability $P_{\text{trig}}(\mathbf{r})$ for each device, we perform >40k Monte Carlo simulation runs, with photon absorption positions distributed uniformly across the device. A representative map of $P_{\text{trig}}(\mathbf{r})$ is shown in Fig. 2.19.

2.4.6 Simulation Results

2.4.6.1 Photon detection efficiency and timing jitter

We simulate each device at increasing reverse bias voltages V_{B}, starting from just above its breakdown voltage. For all devices, PDE increases with V_{B} and reaches a saturation level (representative plots shown in Fig. 2.20(a)). We define the saturated bias voltage V_{sat} as the lowest V_{B} value where the obtained PDE values within a ±1 V range agree within their 1 s.d. uncertainty; the PDE at V_{sat} is then the saturated PDE.

The distribution of avalanche times is generally asymmetric, especially for p-i-n$^+$ SPADs with $\Delta W > 600$ nm (see Fig. 2.20(b)). Similar to the previous study, here we present the full-width-half-maximum (FWHM) and full-width-tenth-maximum (FWTM) timing jitter, both extracted from timing histograms with 1 ps bin size, to better describe the timing performance of the SPADs. In general, timing jitter does not vary significantly with V_{B}, except when V_{B} is near the breakdown voltage.

For p-n$^+$ SPADs, we observe a general trend of PDE increasing with the junction displacement Δj (Fig. 2.21(a)). If the junction is placed further away from the waveguide core, charge carriers injected after a photon absorption in the core region travel a longer distance and can undergo more impact ionizations, thus increasing the likelihood of a successful avalanche. The stochastic avalanche process taking place over a larger distance would also explain the increasing timing jitter at higher Δj. However, Δj being too large would weaken the electric field strength in the waveguide core, which would lead to more

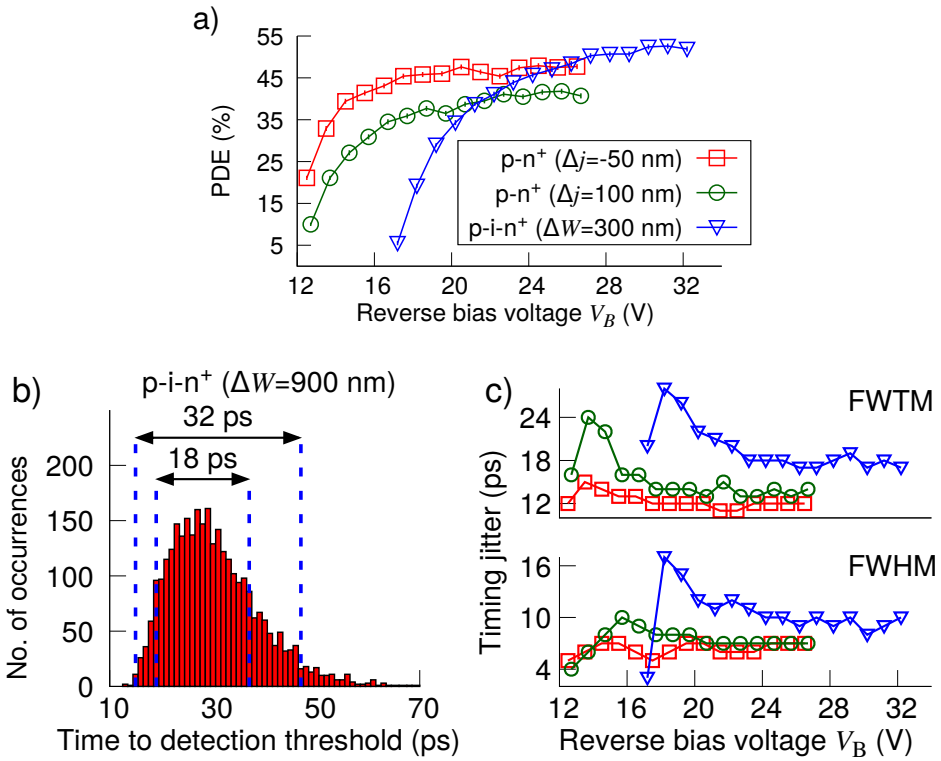

Figure 2.20: (a) Simulated PDE at varying reverse bias voltages V_B for representative devices, showing the saturation behavior as V_B increases. Error bars indicating 1 s.d. uncertainty are much smaller than the symbol size. (b) Distribution of simulated avalanche times (i.e., time between photon absorption and reaching the detection threshold I_{det}) for a p-i-n$^+$ SPAD with $\Delta W = 900$ nm at $V_B = 41$ V. Histogram bin size is 1 ps. The full-width-half-max (FWHM) and full-width-tenth-max (FWTM) timing jitter values are indicated. (c) FWHM and FWTM timing jitter performance for the same devices in (a). (a) and (c) share the same legend.

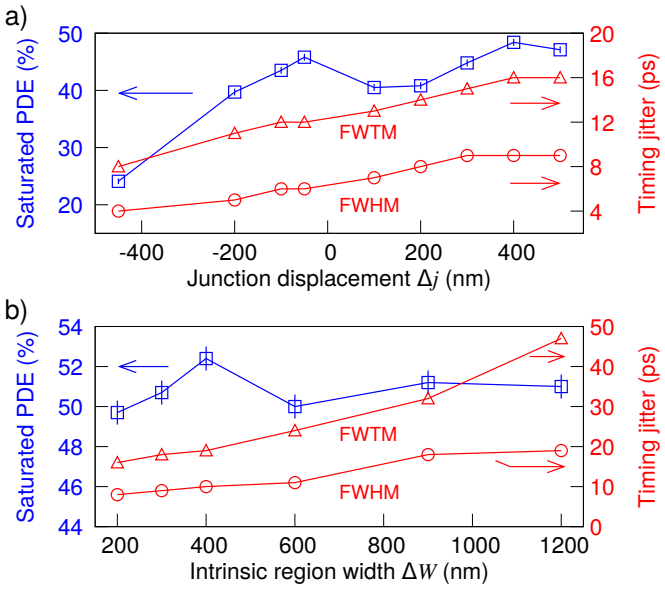

Figure 2.21: Saturated PDE and timing jitter for various (a) p-n$^+$ and (b) p-i-n$^+$ SPADs. Both full-width-half-max (FWHM) and full-width-tenth-max (FWTM) timing jitter values are shown. Error bars for PDE indicate 1 s.d. uncertainty.

charge carriers being lost at the waveguide boundaries due to random walk; this may explain the slight drop in PDE for $\Delta j > 400$ nm.

The observed drop in PDE for $\Delta j = 100$ nm is due to an "edge effect": when the junction is placed in close proximity to the waveguide rib edge, we observe a narrowing of the effective impact ionization region where ionization coefficients are high (Fig. 2.16(b)), which leads to a lower PDE.

The highest saturated PDE obtained for p-n$^+$ SPADs is $48.4 \pm 0.6\%$ at $V_B = 26.5$ V for $\Delta j = 400$ nm, with a FWHM timing jitter of 9 ps.

For p-i-n$^+$ SPADs, the widening of the high-field region has led to a higher PDE than for p-n$^+$ devices (Fig. 2.21(b)). Besides the increased efficiency of impact ionizations, this can also be explained by a lower loss rate of charge carriers under the diffusion model ($<5\%$ for p-i-n$^+$, $\sim 10\%$ for p-n$^+$), which follows a photon absorption event in the quasi-neutral regions. We do not find an obvious dependence of the PDE on the intrinsic region width for $\Delta W > 400$ nm, although timing jitter increases with ΔW.

Based on our analysis, the optimum performance is obtained for $\Delta W = 400$ nm, which gives a saturated PDE of $52.4 \pm 0.6\%$ at $V_B = 31.5$ V, and a FWHM timing jitter of 10 ps.

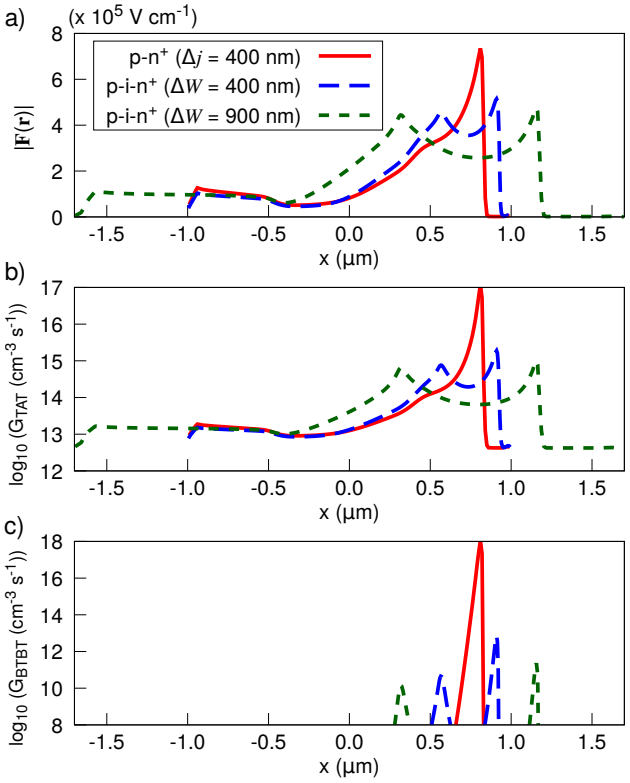

Figure 2.22: (a) Electric field strength $|\mathbf{F}(\mathbf{r})|$, (b) trap-assisted tunneling (TAT) generation rates, and (c) band-to-band tunneling (BTBT) generation rates at the waveguide mid-height (170 nm from the bottom) for SPADs with high saturated PDEs: p-n$^+$ SPAD with $\Delta j = 400$ nm, and p-i-n$^+$ SPADs with $\Delta W = 400$ nm and 900 nm, at reverse bias voltages beyond where their PDE has already saturated ($V_B = 31.5$ V, 34.5 V, and 53 V, respectively).

2.4.6.2 Dark count rate

We also evaluate the dark count rate performance of the SPADs, focusing on devices having high saturated PDEs: p-n$^+$ SPAD with $\Delta j = 400$ nm and p-i-n$^+$ SPADs with $\Delta W = 400$ nm and 900 nm. We calculate the DCR at 243 K, which is in a typical SPAD operating regime readily achieved with thermoelectric cooling, as well as at 300 K to explore the feasibility of room temperature operation.

For our simulated parameters, BTBT shows a greater sensitivity to peak electric field strength than TAT (Fig. 2.22). In p-n$^+$ SPADs, where the peak fields are high, BTBT is the dominant dark carrier generation mechanism. As the bias V_B increases, the depletion region widens, leading to a decrease in the peak field strength and hence the overall DCR, while the TAT contribution stays relatively constant (Fig. 2.23(a)). At an operating bias of $V_B = 31.5$ V (which is above the saturated bias), the DCR is 11k cps and 21k cps at 243 K and 300 K, respectively.

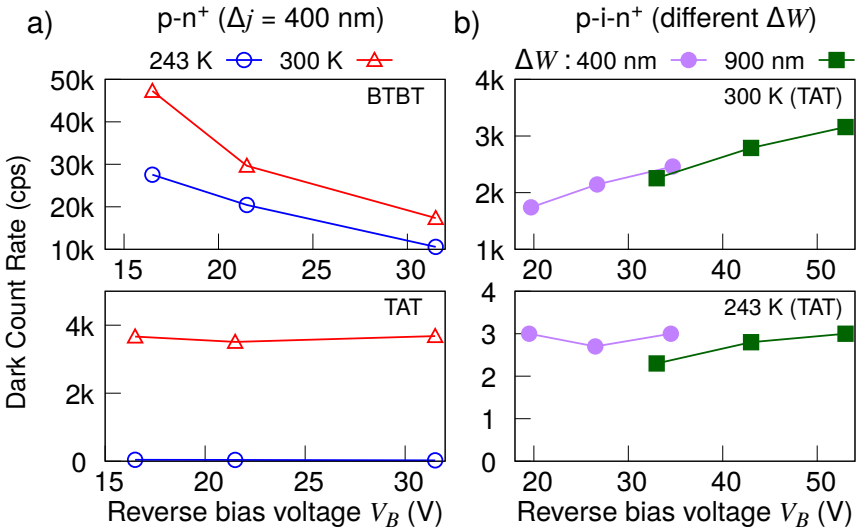

Figure 2.23: Dark count rate (DCR) contributions due to TAT and BTBT mechanisms at varying reverse bias V_B and temperatures. (a) p-n$^+$ SPAD with $\Delta j = 400$ nm. (b) p-i-n$^+$ SPADs with $\Delta W = 400$ nm and 900 nm. The contribution from BTBT is negligible, thus only TAT is shown here.

In p-i-n$^+$ SPADs, due to wider high-field regions with lower peak fields, BTBT becomes negligible compared to TAT. As such, DCR generally increases with V_B, and shows a steeper dependence on temperature (~ 1000 - fold drop between 300 K and 243 K). We observe that while SPADs with wider intrinsic region widths ΔW had lower dark carrier generation rates per unit volume, this was offset by the larger device volume, and could lead to higher DCR compared to narrower ΔW.

Overall, dark count performance for p-i-n$^+$ SPADs is significantly better compared to p-n$^+$ devices, with observed DCR of $<$ 4k cps at 300 K and $<$ 5 cps at 243 K (Fig. 2.23(b)), even at V_B beyond the saturated bias.

The BTBT process that increases the dark carrier generation rate for our silicon junction-based APDs is not a phenomenon that only pertains to the integrated photodetectors. In fact, it is utilized in other types of semiconductor devices such as tunnel field-effect transistors, tunnel diodes (a.k.a. Esaki diode), and Zener diodes. However, we note that the effects of BTBT can be more significant in waveguide geometries because smaller radius of curvature on device edges, if overlaps with the depletion region, leads to further enhancement of the electric field at those regions. For instance, the overlap between the high field depletion region and the corner of the rib waveguide leads to an enhancement of the electric field strength as shown in Fig. 2.16(b). A similar effect is also responsible for higher dark current generation in devices that contain sharp corners between p- and n$^+$-doped regions (see

§ 4.4.2.1 for a detailed discussion). Methods for the mitigation of adverse effects of BTBT include mesa-type junction structures where such sharp curvatures are eliminated by grooving and guard-ring structures at such sharp edges to reduce the electric field at those regions.

In this second design study, p-i-n^+ junction-based devices outperform their p-n^+ counterparts both in terms of photon detection efficiency and dark count rate; we identify the optimum device as a p-i-n^+ SPAD with $\Delta W = 400$ nm, with a saturated PDE of $52.4 \pm 0.6\%$ at a bias of $V_B = 31.5$ V, FWHM timing jitter of 10 ps, and DCR < 5 cps at 243 K. This is an improvement over our previous design described in § 2.3, where the highest PDE obtained was around 45%.

For our simulated devices, the PDE is slightly lower than typical free-space SPAD modules with PDEs of up to $\sim 70\%$ [214]; however, our waveguide devices can offer superior timing performance and dark noise compared to available commercial devices (jitter ~ 35 ps, DCR < 25 cps). We note that even at room temperature, the DCR of a few kcps is acceptable for certain important technologies including LIDAR [226] due to the use of temporal gating, thus indicating the potential applicability of our waveguide SPADs.

2.5 Conclusion

In this chapter, we designed and simulated different silicon waveguide-integrated SPADs for visible wavelengths, which lacks in the literature. Our devices are waveguide-coupled to SiN waveguides on SOI platform, and suitable for on-chip integration with other photonic components. We described a 2D Monte Carlo device simulator based on random path length model of impact ionization to capture the stochastic nature of avalanche breakdown. The simulator enabled us to capture the timing jitter performance of different designs. This is important for quantum applications such as quantum key distribution, where timing jitter is an important performance parameter of single-photon detectors.

In our first design study presented in § 2.3, our simulated devices show a maximum PDE of 45% at $\sim$20 V reverse bias, with a typical FWHM timing jitter of < 8 ps. We optimized our simulation parameters by performing convergence tests and reduced the required computation time by 270 times without deteriorating simulation accuracy in our second design study presented in § 2.4. We also incorporated dark count rate simulation capability into our simulator and investigated devices with more design variations in terms of doping configurations and device structures. Compared to our first study, an intrinsic region between p- and n^+-doped regions improves the PDE to $\sim$52.4% while just increasing

the FWHM timing jitter by only 2 ps. The dark count rate calculations showed that p-i-n^+ junction-based devices have superior DCR performance compared to their p-n^+ counterparts.

In the following chapters, we provide characterization results of our fabricated silicon waveguide-integrated APDs both in linear-mode and Geiger-mode operation.

Chapter 3

Fabrication of Integrated APDs

3.1 Introduction

In this chapter, we present the fabrication steps for the silicon waveguide-integrated APDs. The device fabrication is performed in IME's silicon photonics foundry (later incorporated to Advanced Micro Foundry). Here, the fabrication details are depicted for a p-n^+ junction-based APD with a symmetric rib waveguide structure, and we provide major etching, implantation, and metallization steps, respectively. The fabrication of p-i-n^+ junction-based APDs with an asymmetric rib waveguide structure follows the same procedure.

We note that the etching procedure was pivotal to achieve end-fire coupling between SiN channel waveguide and silicon rib waveguide on the same layer. Compared to conventional interlayer coupling methods, which lead to deteriorations in noise and bandwidth performance due to much longer coupler length required to achieve efficient coupling at visible wavelengths, the novel end-fire input light coupling achieved here has enabled the waveguide-integrated APDs with sub-microampere dark current and superior bandwidth performance as reported in the next chapter.

3.2 Device Fabrication

We start with an 8-inch silicon-on-insulator (SOI) wafer which has a 220-nm-thick p-type silicon device layer on top of 3 μm buried oxide (Fig. 3.1(a)). An epitaxy of 30 nm silicon using plasma enhanced chemical vapor deposition (PECVD) tops up the total silicon thickness to 250 nm (Fig. 3.1(b)). The silicon slab is then defined using 248 nm KrF deep-UV lithography. Inductively coupled plasma (ICP) etch is used to fully etch the silicon layer to form the silicon slab (Fig. 3.1(c)). This is followed by the photoresist stripping.

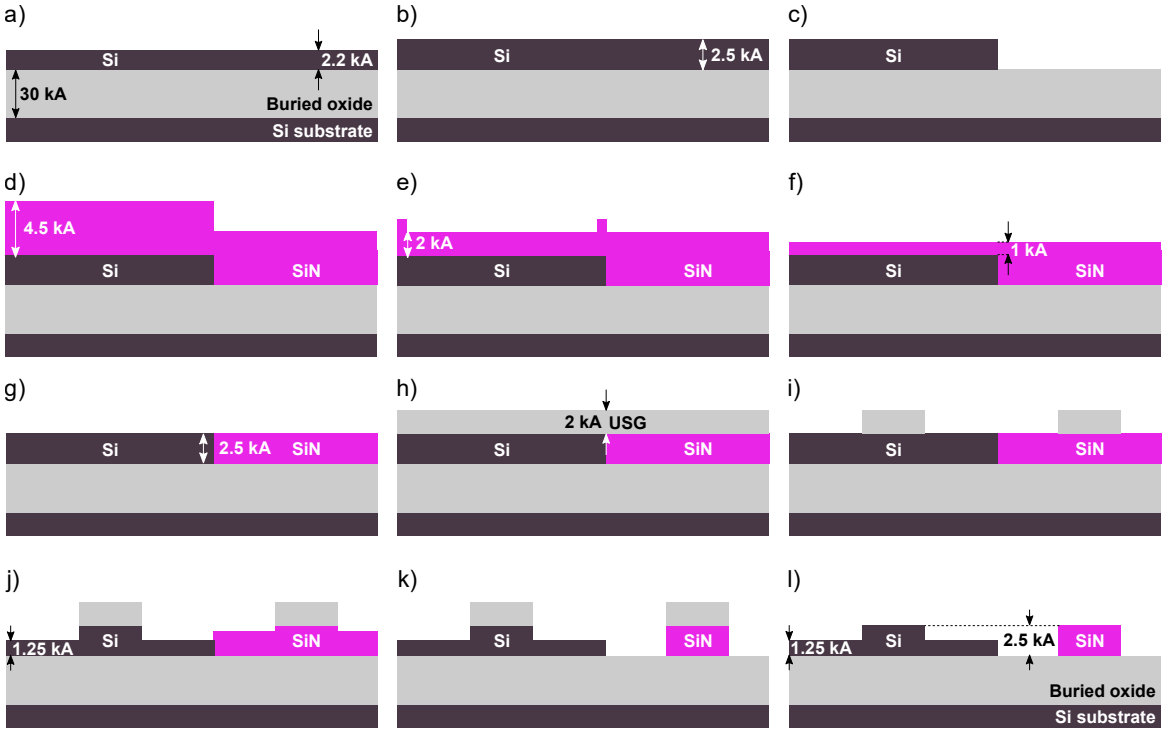

Figure 3.1: Etching steps. (a) Initial 8-inch SOI wafer with 220-nm-thick silicon device layer and 3 µm buried oxide. (b) Epitaxy of 30 nm silicon. (c) Lithography to define silicon slab. (d) 450-nm-thick SiN layer deposition via LPCVD. (e) Reverse etch of SiN by 250 nm. (f) CMP of SiN by 100 nm. (g) Blanket etch of SiN. (h) Hard mask deposition. (i) Hard mask etching to pattern the region for silicon rib and SiN channel waveguides. (j) Silicon rib waveguide formation. (k) SiN channel waveguide formation. (l) Hard mask removal.

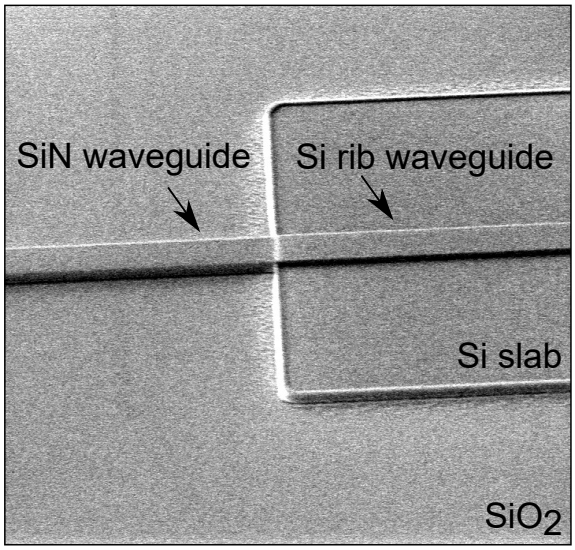

Figure 3.2: Scanning electron microscope (SEM) image of a fabricated device without the top SiO_2 cladding and metal contacts. The inspection window is $10 \times 10\,\mu m$.

Next, a 450-nm-thick silicon nitride (SiN) layer is deposited using low pressure chemical vapor deposition (LPCVD) as shown in Fig. 3.1(d). Reverse etching of SiN reduced the thickness of the SiN layer on top of the silicon slab by 250 nm (Fig. 3.1(e)). The mask used in this etching step was the same mask that defines the silicon slab except that it was 1 µm contracted from the sides; therefore, it results in some unetched SiN on top of the silicon slab edges. The remaining 200 nm SiN layer on top of the silicon slab together with these unetched SiN on the edges is thinned down to 100 nm using chemico-mechanical polishing (CMP) as shown in Fig. 3.1(f). After cleaning and blanket etch steps, the SiN layer is reduced to the same height with the silicon slab, i.e., 250 nm (Fig. 3.1(g)).

Thereafter, a 200-nm-thick undoped silica glass (USG) hard mask layer is deposited and patterned using 248 nm KrF deep-UV lithography to define the silicon rib and SiN channel waveguides (Fig. 3.1(h)). The USG hard mask is defined by a subsequent etch step on top of the silicon and SiN layer (Fig. 3.1(i)). Following the photoresist stripping, the silicon rib waveguide with 125 nm etch depth is formed using ICP etch (Fig. 3.1(j)). The partially etched SiN layer is etched down to the buried oxide layer by a subsequent ICP etch step so that the SiN channel waveguide is formed (Fig. 3.1(k)). The oxide hard mask is finally removed by wet etch (Fig. 3.1(l)). Figure 3.2 shows the scanning electron microscope (SEM) image of a fabricated device without the top SiO_2 cladding and metal contacts.

Next, we proceed to ion implantation steps to define junction regions. A 10-nm-thick pad oxide layer is deposited via PECVD. A lithography step with subsequent Boron implantation

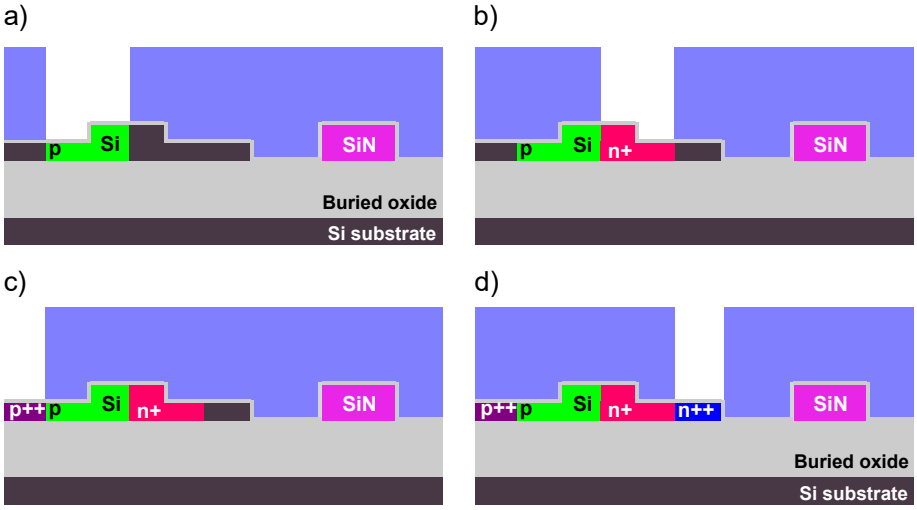

Figure 3.3: Implantation steps. (a), (b), (c), and (d) depict p-, n^{+}-, p^{++}- and n^{++}-type region formation, respectively.

is used to form the p-type region as shown in Fig. 3.3(a), followed by the photoresist stripping. Similar steps are followed to define the n-type region with Phosphorus implantation (Fig. 3.3(b)). After forming p^{++} and n^{++} ohmic contact regions (Fig. 3.3(c, d)), dopant activation is performed by rapid thermal annealing at 1030 °C for 5 s, and the pad oxide is subsequently removed by ICP etch step.

Finally, we proceed to metallization steps to form contact pads on the device as shown in Fig. 3.4. First, 600-nm-thick silicon oxide is deposited as the first interlayer dielectric (ILD) using PECVD (Fig. 3.4(a)). The vias are subsequently formed using lithography and ILD dry etch. After stripping the photoresist and wet cleaning with a hydrofluoric (HF) acid for 10 s, the first metal layer is deposited using a 750-nm-thick aluminum (Al) layer with a 50 nm tantalum nitride (TaN) barrier layer (Fig. 3.4(b)). Next, a 50-nm-thick SiN layer is deposited using PECVD. A lithography together with a subsequent etching step pattern the SiN etch stop layers (ESL) on top of this metal layer. The metal layer is then etched to form the metallization onto the ohmic contact regions formed in the silicon slab. The photoresist is then stripped.

Next, 2.65 µm silicon oxide is deposited using PECVD as the second interlayer dielectric (Fig. 3.4(c)). Lithography is used to define the region for 0.8 µm (i.e., first metal layer thickness) oxide dry etch using CMP reverse etch step. Following photoresist stripping, CMP lowers the total thickness of the top oxide down to 3 µm. To form the vias inside the first interlayer dielectric, ∼1.5 µm of the oxide layer is etched down to the ESL on top of the first

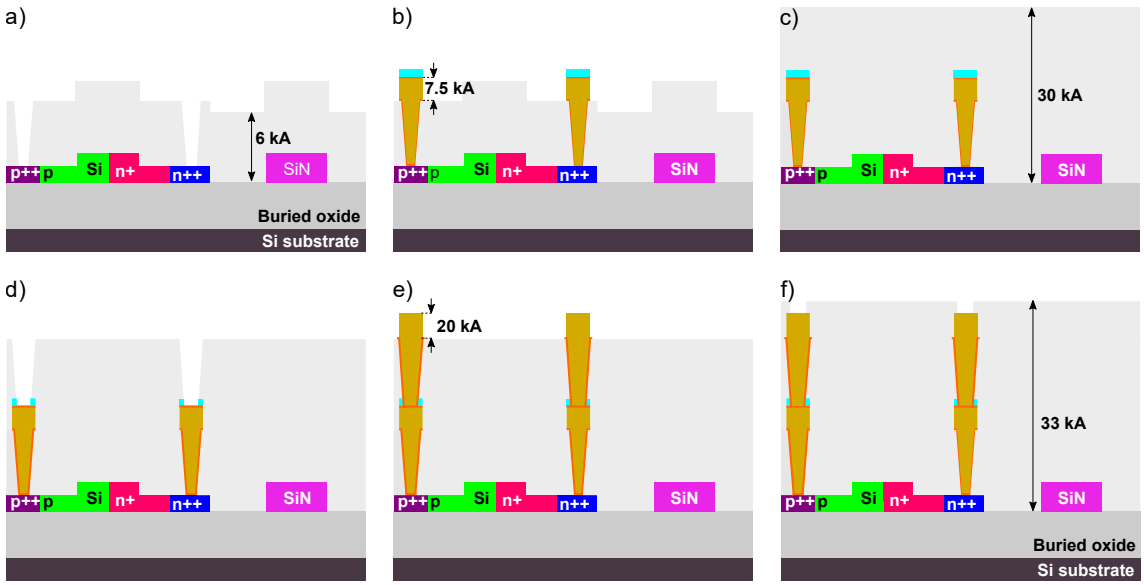

Figure 3.4: Metallization steps. (a) Silicon oxide deposition as the first interlayer dielectric and a subsequent etching step for vias formation. (b) Aluminum deposition as the first metal layer, followed by 50 nm SiN patterning to form the etch stop layer. (c) Silicon oxide deposition and a subsequent CMP step to form the second interlayer dielectric. (d) Silicon oxide etch and a subsequent ESL etch for vias formation. (e) Aluminum deposition as the second metal layer. (f) Silicon oxide deposition as the passivation layer using PECVD, followed by bond pad opening.

metal layer as shown in Fig. 3.4(d). The vias are then formed by subsequent ESL etch down to the first metal layer.

Thereafter, the photoresist is stripped and wet cleaning with a HF acid is performed for 10 s. The second metal layer is deposited using a 2-µm-thick Al layer with a 50-nm-thick TaN barrier layer as shown in Fig. 3.4(e). Similar to the first metal layer formation, the second metal layer is patterned via lithography and etching steps. The photoresist is stripped afterwards.

At the last stage, a 300-nm-thick oxide layer is deposited as the passivation layer using PECVD. The bond pad openings are then formed by etching the passivation layer following a lithography step (Fig. 3.4(f)). The photoresist is then stripped. Finally, the deep trench is formed by etching 6 µm of oxide layer and 100 µm of silicon substrate to form the region for edge coupling with fibers.

Chapter 4

Characterization of Integrated APDs in Linear-mode Operation

4.1 Introduction

In this chapter, we present the experimental results on characterization of silicon waveguide-integrated APDs for linear-mode operation[1]. We investigated dark current, device responsivity, dynamic range, and gain-bandwidth product for 685 nm input light and performed eye diagram measurements. In addition to the devices with lateral doping profile, we also describe an alternative APD design with an interdigitated doping profile. These devices are not significantly affected from junction misalignments as laterally doped devices are, and therefore they are more robust to fabrication tolerances. However, their increased junction lengths lead to higher depletion capacitances and pose a limit on their bandwidth performance. Here, we fabricated these devices together with laterally doped devices and performed a comparative characterization study.

Our experimental results in this chapter reports on the first monolithically integrated avalanche photodetectors for visible light in the literature.

[1] The laterally doped devices presented here are based on p-n^+ junction doping profile with symmetric rib waveguide that is introduced § 2.3. The fabrication of p-i-n^+ junction-based APDs were completed after we performed the experimental studies here, and their characterization in Geiger mode is presented in § 5.4.

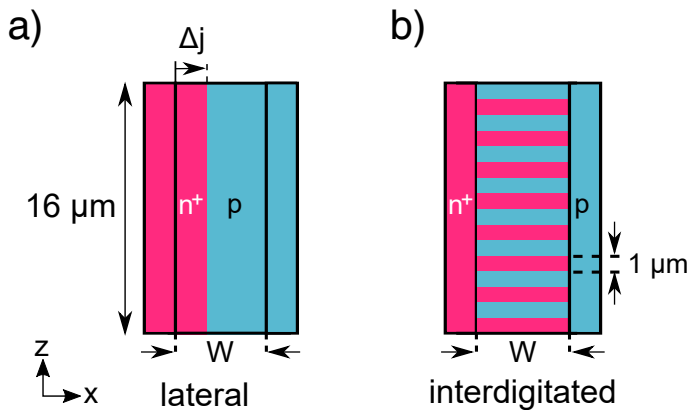

Figure 4.1: Device structure and doping configurations. Top view of the (a) lateral and (b) interdigitated doping profiles. The images are not drawn to scale.

4.2 Device Description

4.2.1 Device Structure

The design of the characterized devices follows our first simulation study in § 2.3.1. The primary photodetector structure is a Si rib waveguide of length 16 µm, which has a high absorptivity at visible wavelengths (>96% at 685 nm). Input light is end-fire coupled from an input SiN rectangular waveguide, which allows for low-loss propagation of visible light [105, 227, 228]. Both the Si APD and SiN input waveguide have the same width W, and we explored waveguide widths of 750 nm and 900 nm here. The height of both the Si APD and SiN waveguide is fixed at 250 nm, and the Si rib height at 125 nm. The structures are fabricated on a SOI substrate on the same device layer and cladded with 3 µm of silicon dioxide (SiO_2) above and below.

To establish electrical connections to the device, metal electrodes are deposited on top of heavily doped p^{++} and n^{++} regions at the far ends of the Si slab along the x axis, 3 µm apart.

4.2.2 Doping Profile

A careful consideration of the doping profile is required to produce high-performance APDs. Here, we design our APDs to consist of a p-n^+ diode in two different doping configurations: lateral and interdigitated (see Fig. 4.1). Both profiles aim to maximize the spatial overlap between the depletion region on the p-doped side and the optical waveguide mode.

In our previous design and simulation studies in Chapter 2, we studied devices with lateral doping profiles. These devices have diode structures with a single continuous depletion region along the waveguide length as shown in Fig. 4.1(a). The design distance between the junction and the n^+ edge of the waveguide Δj is $\{100, 110, 120, 150\}$ nm for waveguide widths $W = \{450, 600, 750, 900\}$ nm. Though conceptually simple, the lateral doping profile requires stringent control during fabrication. A small misalignment of the junction would result in a large mismatch between the optical waveguide mode and the depletion region, and hence, lead to a reduction in photon detection efficiency due to impaired avalanche multiplications of photogenerated charge carriers.

The alternative design uses an interdigitated profile (see Fig. 4.1(b)), which consists of alternating p and n^+ regions, each 1 µm in length. This design is less sensitive to such misalignment errors, but the increased junction lengths could lead to a higher depletion capacitance and hence limit the bandwidth, as is reported for Si modulators [229, 230].

4.2.3 Optical Coupling

From our previous analysis of the optical mode overlap between the waveguide modes, we expect a SiN-Si end-fire coupling loss of $\eta_{\text{SiN-Si}} \leq 1$ dB per facet (see § 2.3.1.3). On our fabricated devices, light is coupled into the SiN waveguides via single-tip inverse tapers at the edge of the waveguide chip.[2] Regardless of the waveguide width, the inverse tapers are designed to have a taper length of 200 µm and a minimum taper width of 180 nm. The edge-coupled devices are suited for interfacing with lensed optical fibers; for a focused spot diameter of 2 µm, the expected coupling loss into the SiN waveguide is $\eta_{\text{f-SiN}} \sim 1.5$ dB per facet.

4.3 Experiment

We test the fabricated devices at room temperature using a custom-built light-tight probe station. The schematic of the electro-optic characterization setup is shown in Figure 4.2. Representative photographs of a device under test are shown in Fig. 4.3.

We establish electrical connections via 100×100 µm contact pads on the chip surface using electrical probes (see Fig. 4.3(b)). We use a 685 nm continuous wave diode laser (Thorlabs LP685-SF15) as the optical source. The laser light is coupled to the SiN waveguide

[2] In addition to this single-tip inverse tapers, we also studied double-tip inverse taper structures with various design parameters and presented their characterization results in Appendix A.

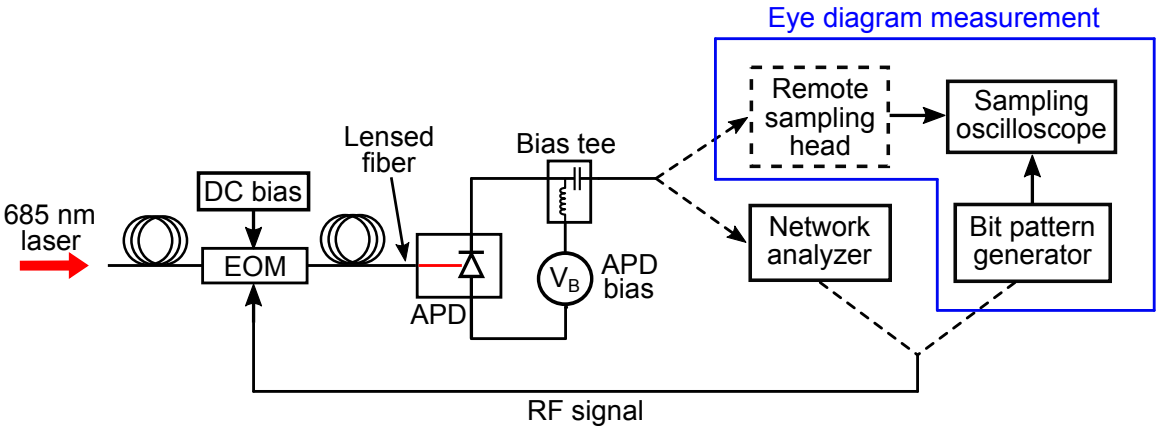

Figure 4.2: Schematic of the characterization setup. Horizontally polarized (TE) 685 nm light, which can be modulated with an RF signal using an electro-optic modulator (EOM), is coupled to the on-chip SiN waveguide with a lensed fiber. Electrical connections to the devices are made via contact pads on the chip surface using electrical probes. A bias tee separates the AC and DC signals from the APDs. The AC signal is sent either to a network analyzer for bandwidth measurements, or to a sampling oscilloscope for eye diagram measurements. An additional remote sampling head was used at 56 Gbps to obtain a clearer signal.

using single-mode tapered lensed fibers (OZ Optics TSMJ-3U-633-4/125-1-30-2-9-1, 2 µm spot diameter).

We maintain a horizontal input polarization, which couples to the fundamental TE mode of the SiN waveguide. Although different input polarizations could lead to some variations in the coupling and propagation losses, the APD response itself is not expected to exhibit any significant polarization dependence.

Over the course of our measurements, we have tested several tens of devices with different device parameters picked from various locations across an 8" wafer. All tested devices show repeatable results, and we did not observe a single failed device. This indicates that the fabrication is robust and has a high device yield.

4.3.1 Coupling and Propagation Loss Measurements

We first systematically characterized the coupling and propagation losses on our devices by performing a series of cutback measurements with test waveguides. The optical transmission T through the device was obtained by measuring the input power P_A and output power P_B with a pair of lensed fibers (see Fig. 4.4(a)). Using SiN cutback waveguides of various lengths l_{SiN} without Si rib waveguide (see Fig. 4.5 for representative micrographs),

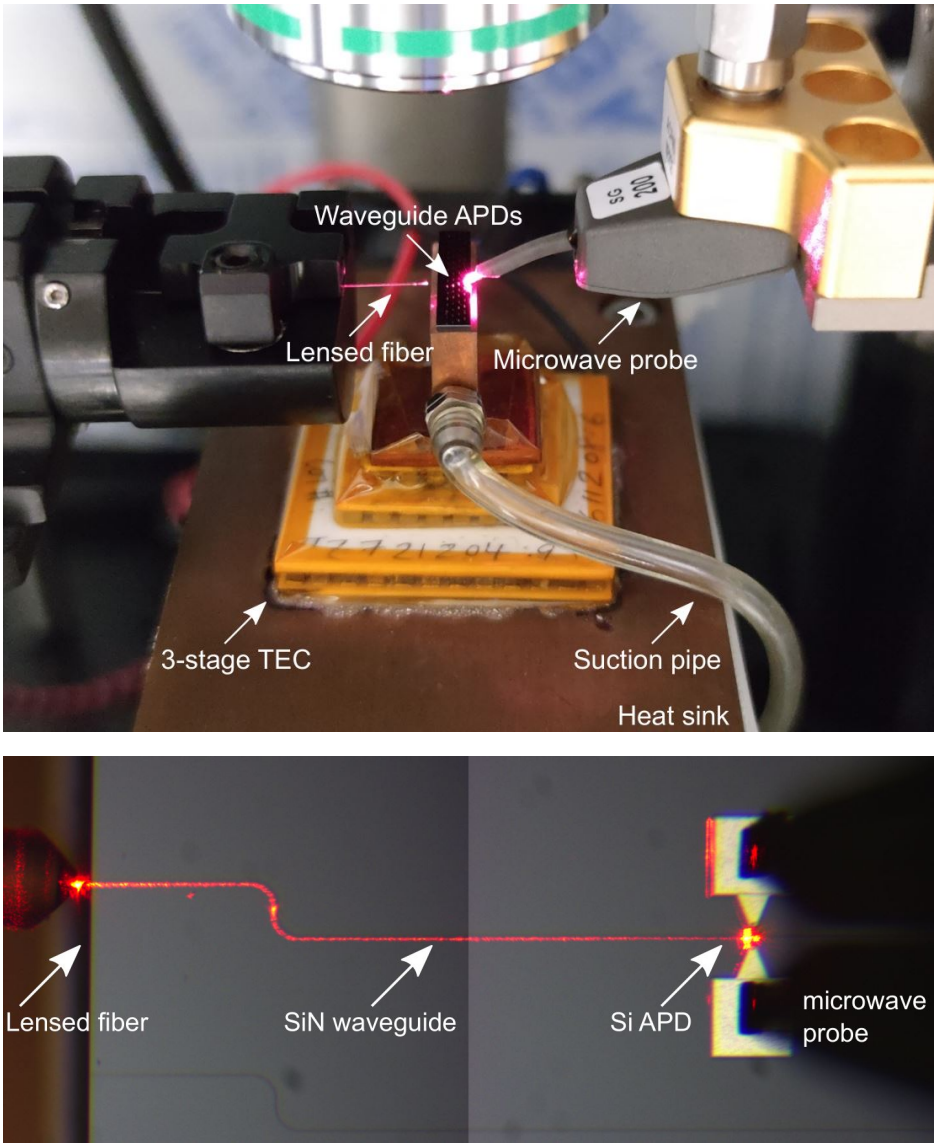

Figure 4.3: Representative photographs of device under test. a) A bare die of silicon waveguide-integrated APDs is under test in our custom probe station. The CW laser light is injected from a lensed fiber into devices. Samples are placed on top of a temperature-controlled sample holder and stabilized with a suction force during probing. b) Fabricated devices are imaged under an optical microscope. Shown here are the optical coupling with lensed optical fibers and Si APD regions. The red glow is due to the scattering of the 685 nm input light.

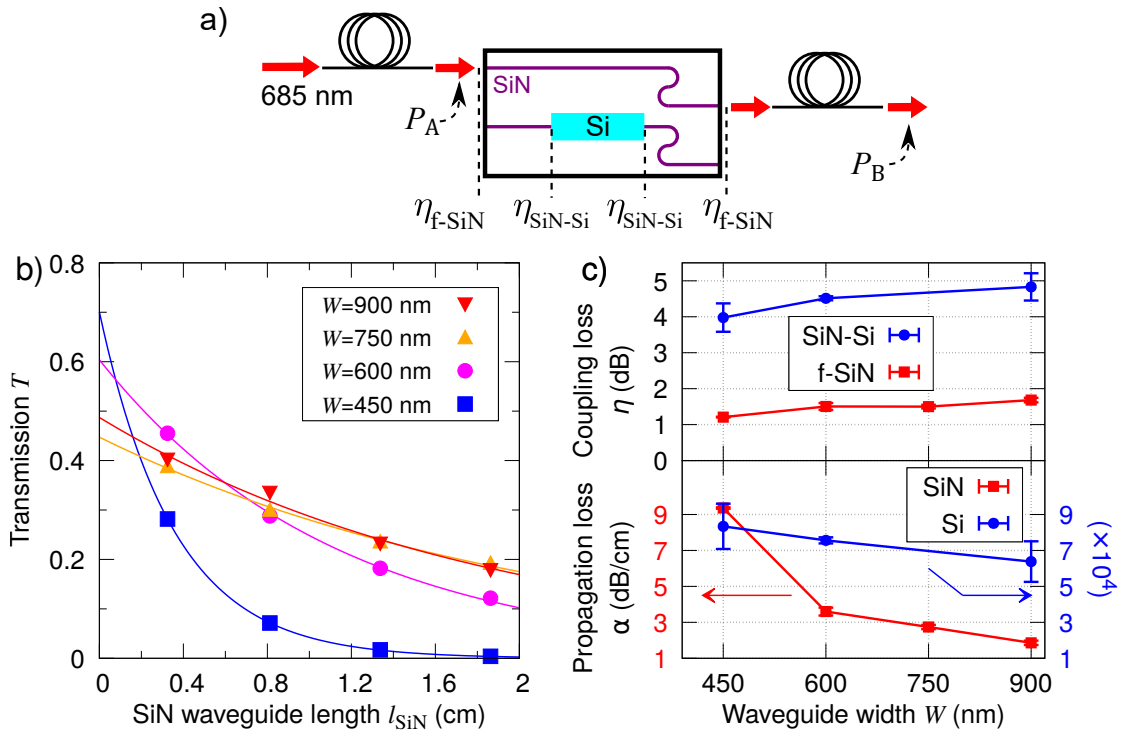

Figure 4.4: Optical coupling loss measurements. (a) Schematic of the experimental setup, depicting the cutback waveguide structures and the various sources of coupling losses. Horizontally polarized 685 nm light is coupled to and from the waveguides via lensed fibers. The optical powers at both ends of the chip (denoted P_A and P_B) are measured. (b) Optical transmission measurements for SiN cutback waveguides of various lengths l_{SiN} and different waveguide widths W. The solid curves are exponential fits, see Eq. 4.1. (c) Measured coupling losses for different waveguide widths W. The results shown in (c) are the averaged measurements across several devices; error bars reflect the standard deviation.

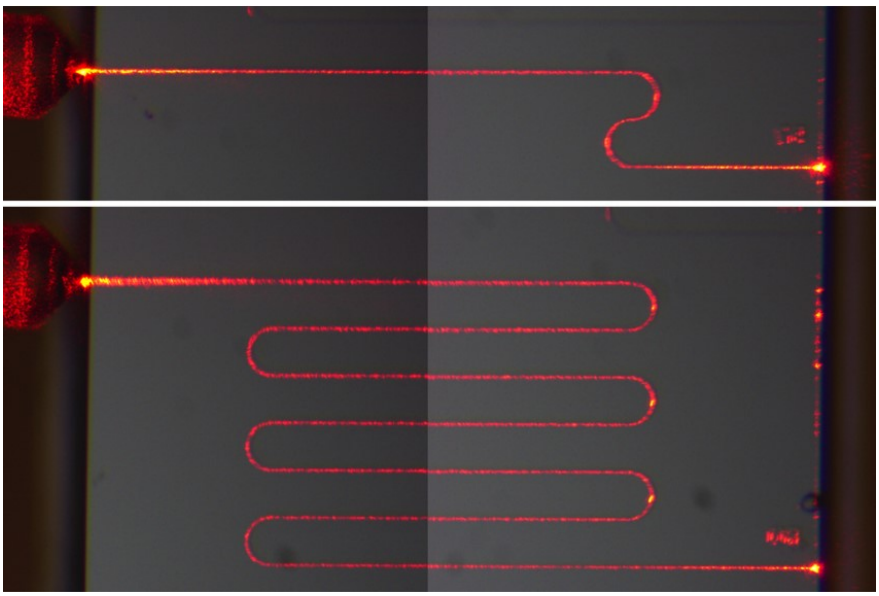

Figure 4.5: Micrographs of SiN cutback waveguides. Shown here are two test structures with shortest and longest waveguide lengths amongst all SiN cutback waveguides. Since our camera was not wide enough to capture both edges of the chip in a single frame, the images are obtained by merging two separate micrographs.

we fitted our results using

$$T = P_{\mathrm{B}}/P_{\mathrm{A}} = \eta_{\text{f-SiN}}^2 \, e^{-(\alpha_{\mathrm{SiN}} \, l_{\mathrm{SiN}})}, \tag{4.1}$$

to obtain the fiber-waveguide coupling loss $\eta_{\text{f-SiN}}$ and the SiN waveguide propagation loss coefficient α_{SiN}. A representative plot is shown in Fig. 4.4(b).

Following this, we measured another series of devices that also included Si waveguides of various lengths l_{Si}. We obtain the SiN-Si end-fire coupling loss $\eta_{\text{SiN-Si}}$ and the Si waveguide propagation loss coefficient α_{Si} by fitting our results to

$$T = P_{\mathrm{B}}/P_{\mathrm{A}} = \eta_{\text{f-SiN}}^2 \, \eta_{\text{SiN-Si}}^2 \, e^{-(\alpha_{\mathrm{SiN}} \, l_{\mathrm{SiN}})} \, e^{-(\alpha_{\mathrm{Si}} \, l_{\mathrm{Si}})}. \tag{4.2}$$

The measured coupling and propagation losses are shown in Fig. 4.4(c). We note that we lack test structures for Si waveguides of width $W = 750\,\mathrm{nm}$; nonetheless we anticipate that the coupling and propagation losses will not significantly deviate from that of the other widths.

The observed fiber-waveguide coupling losses $\eta_{\text{f-SiN}}$ agree with our expected values. The slight increase in $\eta_{\text{f-SiN}}$ with width W is likely due to the larger inverse taper angle, since the taper length and tip width are kept constant for all W. The end-fire coupling loss $\eta_{\text{SiN-Si}}$ is $\sim$3-4 dB larger than mode-matching calculations, which is attributed to fabrication imperfections

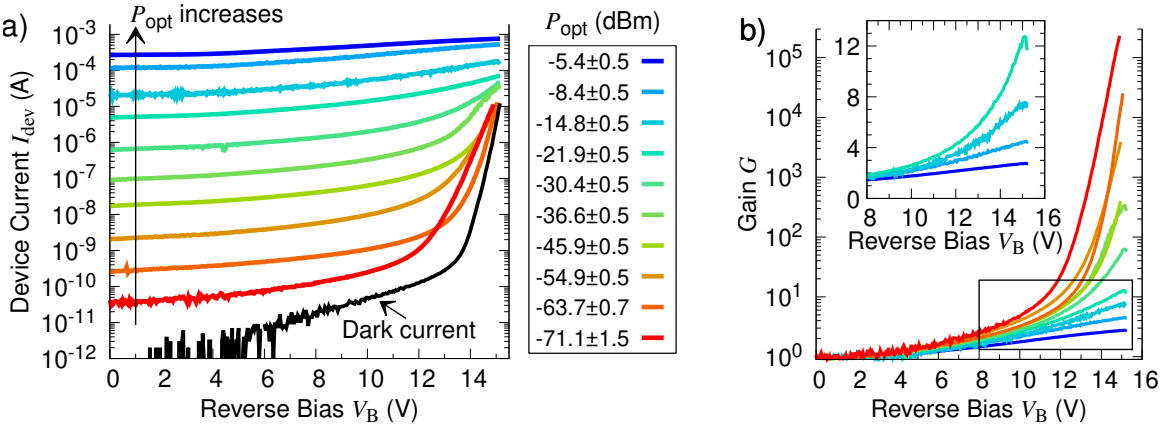

Figure 4.6: DC characteristics of a laterally doped device with width $W = 900$ nm. (a) Current-voltage measurements at different input optical powers P_{opt}. The reverse bias voltage V_B is swept till the avalanche breakdown voltage $V_{br} \approx 15.5$ V, where the dark current I_{dark} reaches 10 µA. Each sweep takes a few seconds; prior to each sweep, the device is reset with the application of a forward bias voltage. (b) The avalanche gain G at different P_{opt}. The inset is a magnified view of the area marked by the rectangle, showing the curves at larger P_{opt} on a linear scale. Both plots in this Figure share the same legend for P_{opt}.

resulting in a non-ideal waveguide interface. We also observe decreasing propagation losses with increasing W.

For APD characterization, the total insertion loss into the active device structure (i.e., the Si rib waveguide) is given by

$$\eta_{total} = \eta_{f\text{-}SiN}\, \eta_{SiN\text{-}Si}\, e^{-(\alpha_{SiN}\, l_{SiN})}, \tag{4.3}$$

where $l_{SiN} = 0.3125$ cm is constant for all characterized devices. For both $W = 750$ nm and 900 nm, this yields $\eta_{total} = 7.1 \pm 0.4$ dB. We decided to focus on devices with lower insertion loss, and only considered devices with these two widths for the rest of this study.

4.3.2 Current-voltage Measurements

We measured the current-voltage (I-V) characteristics of each device up to the breakdown voltage V_{br}, with a series of different input optical powers P_{opt} entering the Si. The values of P_{opt} are reported after accounting for the insertion loss. Here we consider representative results for a $W = 900$ nm laterally doped device, as shown in Fig. 4.6(a). For I-V measurements, the reverse bias voltage V_B is swept from 0 V to the avalanche breakdown voltage V_{br} over a few seconds. We define V_{br} here as the voltage where the dark current I_{dark} (i.e., without input light) reaches 10 µA; this definition follows other reports of APDs in the literature [231, 232].

We note here that V_{br} drifts with time in our devices; as such, to ensure consistent results, it is necessary to reset the device with the application of a forward bias voltage prior to each sweep. More details regarding the drift behavior are discussed in § 4.4.3 and § 4.4.4.

From the I-V data we extract the photocurrent $I_{\mathrm{ph}} = I_{\mathrm{dev}} - I_{\mathrm{dark}}$, where I_{dev} and I_{dark} are the measured device current and dark current, respectively. We then obtain the avalanche gain G as the ratio of the photocurrent I_{ph} at bias V_{B} to that measured at unity gain point of $V_{\mathrm{B}} = 2\,\mathrm{V}$, where we consider the quantum efficiency to be nearly maximized, and the effects of avalanche gain to be insignificant

$$G(V_{\mathrm{B}}) = \frac{I_{\mathrm{ph}}(V_{\mathrm{B}})}{I_{\mathrm{ph}}(2\,\mathrm{V})}. \tag{4.4}$$

A discussion of how we determined the unity gain point is provided in § 4.4.1.

At $V_{\mathrm{B}} > 10\,\mathrm{V}$, both I_{dark} and G increase dramatically due to avalanche multiplication. In this regime, the power dependence of the device response becomes obvious, with G decreasing for higher P_{opt}. This is due to the larger number of multiplied charge carriers causing an increased space charge effect. As a result, the electric field is depressed, leading to saturation of the device current. Thus, while $G \sim 10$ at $V_{\mathrm{B}} = 15\,\mathrm{V}$ for $P_{\mathrm{opt}} = $ -20 dBm, it rises to $G > 10^5$ for a low input power of $P_{\mathrm{opt}} = $ -71 dBm. Power-dependent characteristics have also been studied in other APDs [233, 234].

As such, we will separately compare the device performance in low-gain and high-gain regimes.

4.3.2.1 Performance in the low-gain regime

In the low-gain regime, the APDs can be operated at small bias voltages suited for applications requiring low power consumption. An important example is to monitor optical power levels in integrated photonic circuits, which requires low dark current and wide dynamic range with linear response [233, 235].

We focus on the primary responsivity $R_{\mathrm{p}} = I_{\mathrm{ph}}/P_{\mathrm{opt}}$ measured at unity gain, i.e., at $V_{\mathrm{B}} = 2\,\mathrm{V}$. All device types show linear behavior, with R_{p} within an overall range of 0.65 ± 0.18 A/W over a dynamic range of $> 50\,\mathrm{dB}$ (see Fig. 4.7(a) and Table 4.1). We expect the actual dynamic range to be even larger since we did not explore higher input powers in detail for all devices, and we had not yet observed the device approaching saturation. R_{p} is slightly higher for $W = 900\,\mathrm{nm}$ devices due to the larger absorption volume of a wider waveguide.

The dark current measurements are shown in Fig. 4.7(b). I_{dark} at $V_{\mathrm{B}} = 2\,\mathrm{V}$ is less than 70 pA for all device types. Laterally doped devices with $W = 900\,\mathrm{nm}$ exhibit the lowest $I_{\mathrm{dark}} \sim 1$ pA

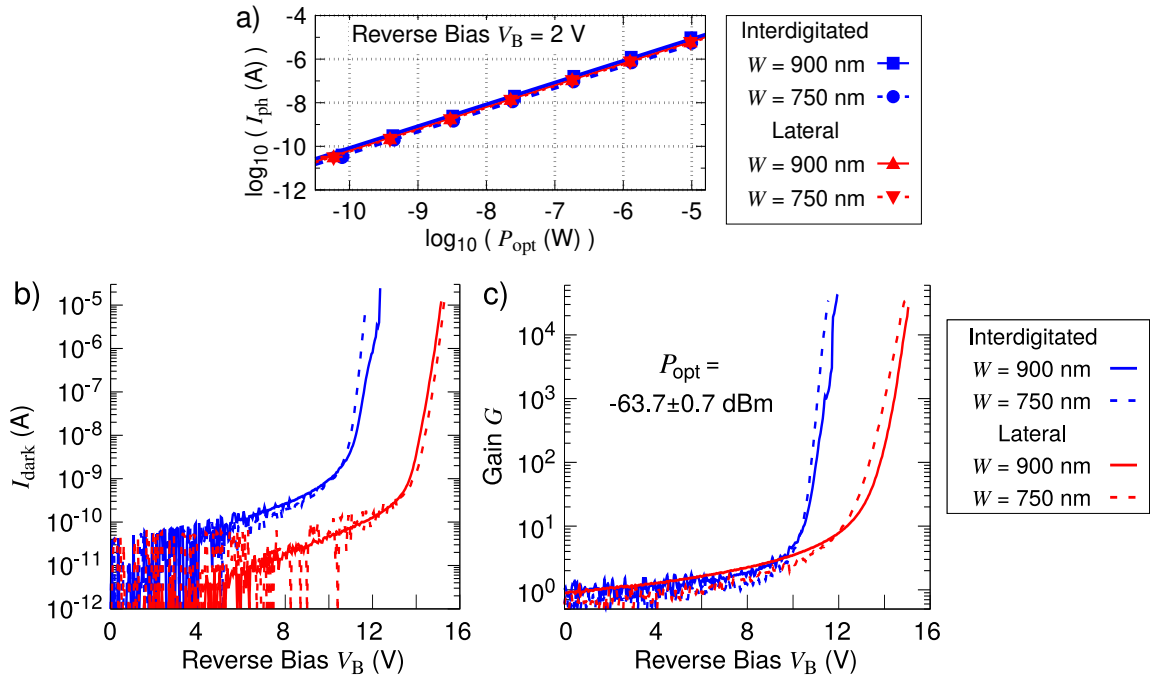

Figure 4.7: Comparison of DC performance for lateral and interdigitated doping profiles with different widths W. (a) Photocurrent I_{ph} versus input power P_{opt} at the unity gain point of reverse bias $V_B = 2$ V. Straight lines are linear fits, from which we extract the primary responsivity R_p, see Table 4.1. (b) Dark current I_{dark} measurements at varying V_B. (c) Avalanche gain G at varying V_B with a fixed input power $P_{opt} = -63.7 \pm 0.7$ dBm. Figures (b) and (c) share the same legend on the right.

(see also Fig. 4.6(a)). We note that in the low bias regime ($V_B < 10$ V), laterally doped devices have about an order of magnitude lower I_{dark} than interdigitated devices. This effect has also been previously reported in other waveguide-based photodetectors [233]. There are two likely reasons for the higher dark current in interdigitated devices. First, high peak electric field strengths associated with the corners of the interdigitated regions can lead to a higher dark carrier generation rate § 4.4.2. Furthermore, the interdigitated devices have a larger depletion volume where dark carriers can undergo avalanche multiplication, compared to their laterally doped counterparts.

4.3.2.2 Performance in the high-gain regime

Fig. 4.7(c) shows the gain G for different device types at a relatively low input power of $P_{opt} = -63.7 \pm 0.7$ dBm, where the devices exhibit high gain. We see that interdigitated devices have a lower breakdown voltage V_{br} and a slightly steeper rise in G with respect to V_B. These effects can likely be attributed to premature breakdown due to high electric fields at

the edges of the interdigitated regions (see § 4.4.2 for details). For both doping profiles, we observe no significant dependence of V_{br} on the device width W. This is consistent with our previous simulations for laterally doped devices in Chapter 2.

Applications in integrated photonics typically require low power consumption, thus both I_{dark} and V_{B} should ideally be low as well [235]. While interdigitated devices achieve similar gain at a lower V_{B} compared to laterally doped devices, I_{dark} tends to be higher. The optimal choice of doping profile in this regime would then require a more in-depth consideration of the operating requirements.

4.3.3 High-Speed Response and Bandwidth

For bandwidth measurements and eye diagram measurements, the device gain is first stabilized by continuously applying a reverse bias over ~ 30 mins; this is necessary due to the drift behavior (see § 4.4.3). The 685 nm input light is modulated with an RF signal using a 40 GHz electro-optic modulator (EOM, Eospace AZ-AV5-40-PFA-PFA-700). The EOM is operated at 65 °C to mitigate the photorefractive effects caused by high optical input powers. The EOM is maintained at its half transmission point, i.e., the DC bias is adjusted such that the EOM output power is at 50% of its maximum value, before RF modulation is added.

The frequency response is measured with an Agilent E8363C network analyzer, which generates the RF signal for the EOM and measures the APD response. For all devices, we use an input power of P_{opt} = -24.5 dBm. The measured data is corrected for the electro-optic S21 response of the EOM and smoothed with a Savitzky–Golay filter with a 3$^{\mathrm{rd}}$ order polynomial fit. The 3 dB bandwidth is extracted from the fit function.

For eye diagram measurements, a bit pattern generator (SHF 12104 A together with Anritsu MG3693C) is used to generate non-return-to-zero on-off-keying (NRZ-OOK) patterns with pseudorandom binary sequences (PRBS) of length $2^7 - 1$. These patterns are then amplified (Centellax OA4MVM3) and used to modulate the RF signal driving the EOM. The eye diagrams are measured with a sampling oscilloscope (Keysight 86100D with 86116C module). An additional remote sampling head (Keysight N1046A) was used at 56 Gbps to obtain a clearer signal.

Fig. 4.8(a) shows the results of a frequency response measurement for a $W = 900$ nm laterally doped device. The 3 dB bandwidth, which we define with respect to the device response at 1 GHz, is obtained via a smoothing fit to the data points. Figs. 4.8(b,c) compare the bandwidth and gain-bandwidth product (GBP) of the different device types. At lower reverse bias V_{B}, the bandwidth generally increases with V_{B} due to a wider depletion region and a lower junction capacitance. However, this effect eventually reaches a limit, beyond

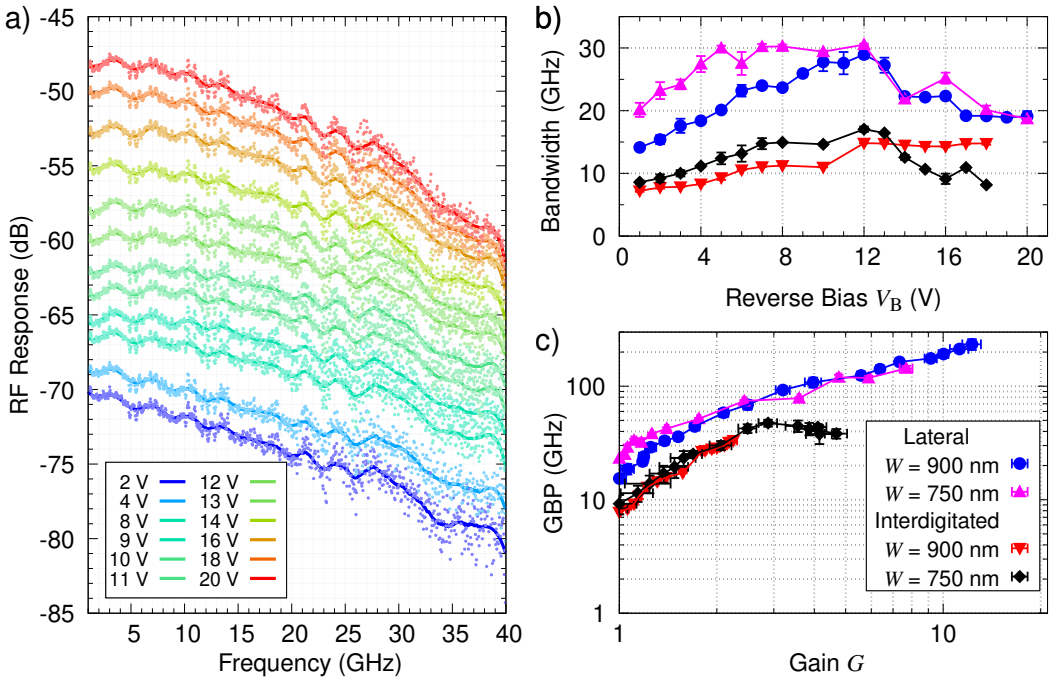

Figure 4.8: Optical-electrical bandwidth measurements. An input power of P_{opt} = -24.5 dBm is used throughout. (a) Frequency response of a W = 900 nm laterally doped device at various bias voltages V_B. The 3 dB bandwidth is obtained from a smoothing fit to the data points (see Methods). (b),(c) 3 dB bandwidth and gain-bandwidth product (GBP), respectively, for different device types. Both plots share the same legend shown in (c). Each data point and error bar in both plots represents the mean and standard deviation, respectively, of several measurements.

which the bandwidth saturates or starts to decrease, due to the device response being limited by avalanche buildup times at large gain [235]; this occurs at $V_B \sim$12 V in our devices.

We find that the bandwidth is indeed lower in interdigitated devices, as expected from the higher capacitance due to its doping profile. Another potential contributing factor is that a larger proportion of photo-generated charge carriers in interdigitated devices are created in n^+-doped regions where the electric field is low, leading to slower carrier diffusion and hence slower device response (see § 4.4.2).

A detailed comparison of the best GBP performance for each device is shown in Table 4.1. The highest observed GBP is 234 $\pm$ 25 GHz for the W = 900 nm laterally doped device, at a reverse bias of V_B = 20 V. Although its W = 750 nm version has a lower maximum GBP, it also has a much lower dark current, as well as higher 3 dB bandwidths of up to 30 GHz at lower V_B. As such, the optimal choice of device parameters might also depend on the specific application and operating conditions.

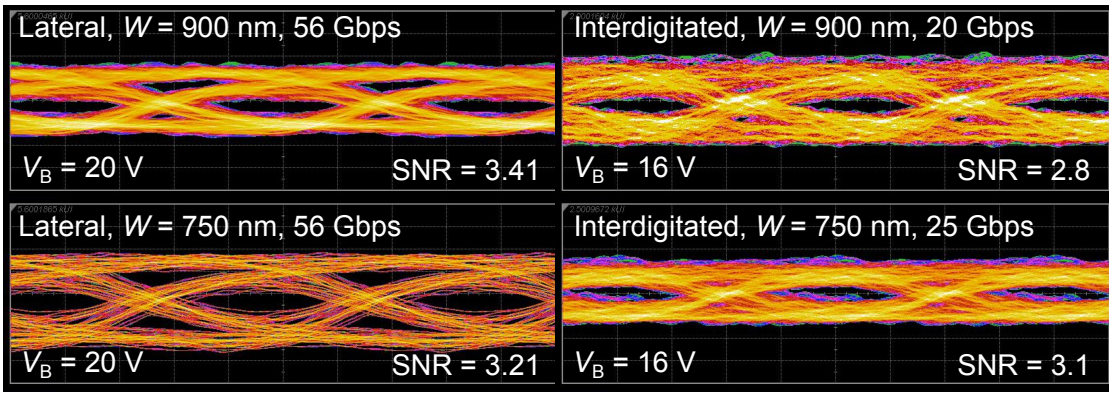

Figure 4.9: Measured eye diagrams for the different device types. Lateral devices show open eyes at data rates of up to 56 Gbps at $V_B = 20$ V, where the maximum GBP is observed. The results for interdigitated devices are obtained at the highest data rate where open eyes could be measured for each device. The signal-to-noise ratio (SNR) is obtained from the sampling oscilloscope.

To demonstrate the performance of our devices in communications systems, we measured eye diagrams of the different device types (see Fig. 4.9). Lateral devices show open eyes at data rates of up to 56 Gbps at $V_B = 20$ V, where the maximum GBP is observed. We note that these devices can potentially support even higher data rates at lower bias, where the 3 dB bandwidth is higher, but our setup is not capable of generating faster bit patterns. Interdigitated devices show open eyes only at lower data rates, with the $W = 750$ nm devices performing slightly better (25 Gbps) than $W = 900$ nm ones (20 Gbps). This is attributed to the narrower devices having a larger gain ($G \sim 4$ at $V_B = 16$ V, while $G \sim 2$ for the wider devices), despite having a slightly lower 3 dB bandwidth as seen in Fig. 4.8(b).

The reference eye diagrams of the EOM output are shown in Figure 4.10(a). We observe clear, open eyes at up to 56 Gbps, indicating that our measurement system performs well at these bit rates. We are unable to measure at higher bit rates due to our limitations in generating faster bit patterns.

The eye diagrams presented in Fig. 4.9 show the open eyes at the highest data rate measured for each device. We note that all devices can be operated at lower data rates with a higher SNR. In general, the signal-to-noise ratio (SNR) obtained from the eye diagram increases with the reverse bias V_B, as the signal amplitude increases with a larger gain. Figure 4.10(b) shows the SNR increase with V_B for laterally doped devices at 25 Gbps. Figures 4.10(c),(d) show additional data obtained at different data rates for lateral and interdigitated devices, respectively.

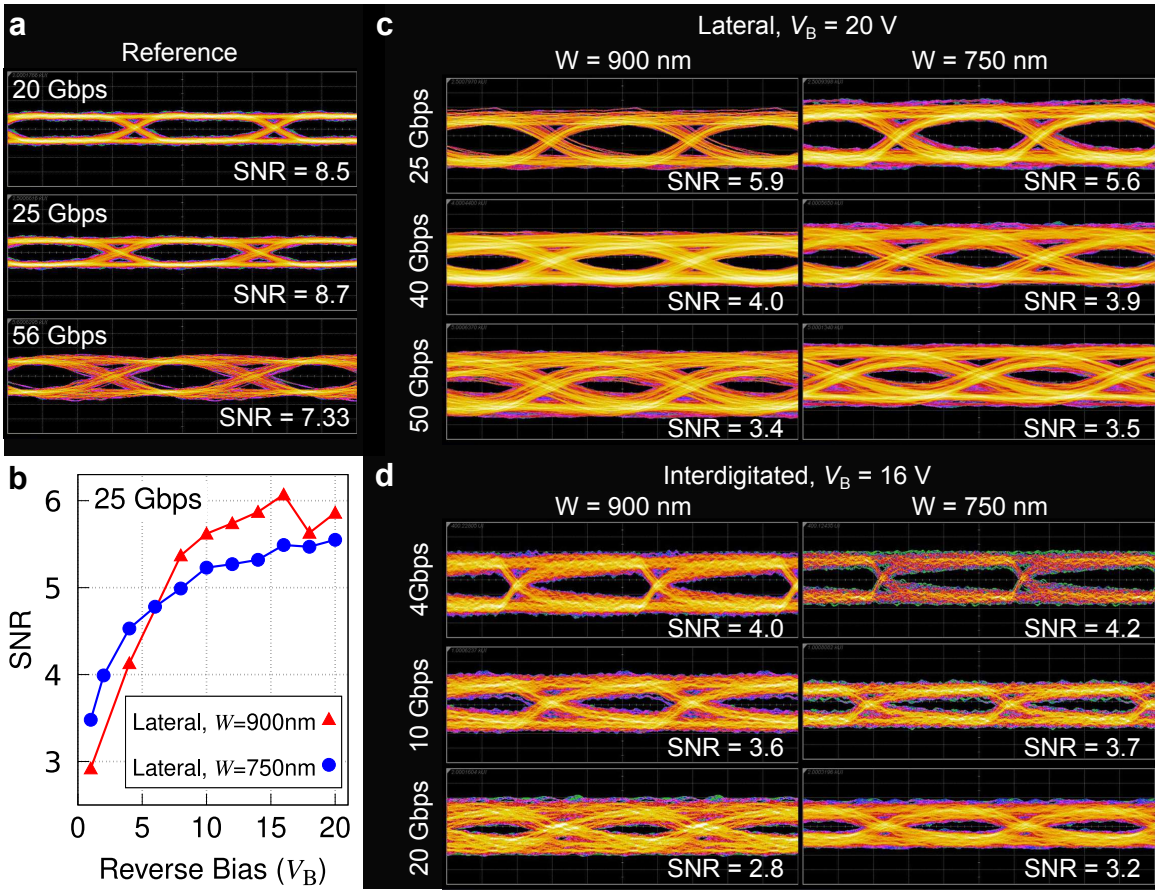

Figure 4.10: Additional eye diagram measurements. (a) Reference eye diagrams of the EOM output at different data rates, measured with a Newport 1004 photodetector (3 dB bandwidth: 40 GHz) and the sampling oscilloscope. (b) Increase in signal-to-noise ratio (SNR) with the reverse bias V_B, obtained from eye diagrams measured for laterally doped devices. (c) Eye diagrams measured for laterally doped devices at $V_B = 20$ V at different data rates. (c) Eye diagrams measured for interdigitated devices at $V_B = 16$ V at different data rates.

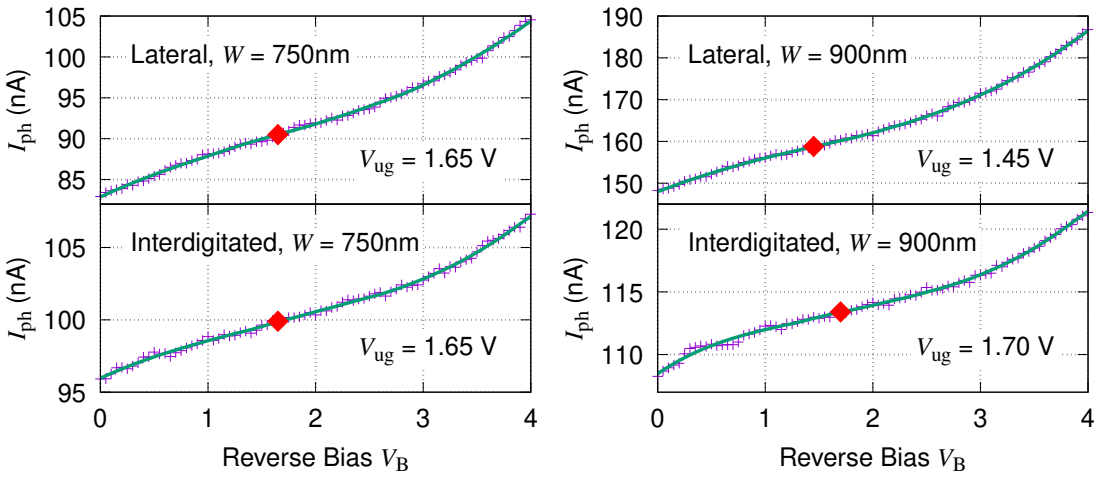

Figure 4.11: Empirical estimates of the unity gain point V_{ug}. Each plot shows the measured photocurrent I_{ph} at an input power of $P_{opt} = 30.2 \pm 0.2$ dBm for a device type. From the data points, we obtain a smoothed curve (solid line), from which we calculate its second derivative with respect to V_B. The red diamonds mark the curves at V_{ug}, the reverse bias value where $\partial^2 I_{ph}/\partial {V_B}^2 = 0$.

We note that the high-speed performance of our devices can be adversely affected by factors such as the size of contact pads, which could be further reduced or removed altogether in future large-scale integration with a photonics platform.

4.4 Detailed Analysis of Device Characteristics

4.4.1 Determination of the Unity Gain Point

To determine the avalanche gain G at a particular reverse bias V_B, the measured photocurrent I_{ph} has to be compared to that measured at a low bias voltage V_{ug} where avalanche effects are negligible, i.e., the APD exhibits unity gain. We can then attribute any further increase in I_{ph} at $V_B > V_{ug}$ solely to the avalanche gain. An implicit assumption here is that the quantum efficiency (QE) — the efficiency of absorbing input photons and converting them into a photocurrent (without multiplication gain) — is saturated and remains essentially constant above V_{ug}.

However, at a low bias, the junction might not be fully depleted yet, and the QE might not have reached saturation. Thus, the increase of the photocurrent I_{ph} with V_B may be caused by both an increase in the QE and G, and it is difficult to distinguish between the two mechanisms. This leads to a difficulty in determining the unity gain bias V_{ug}.

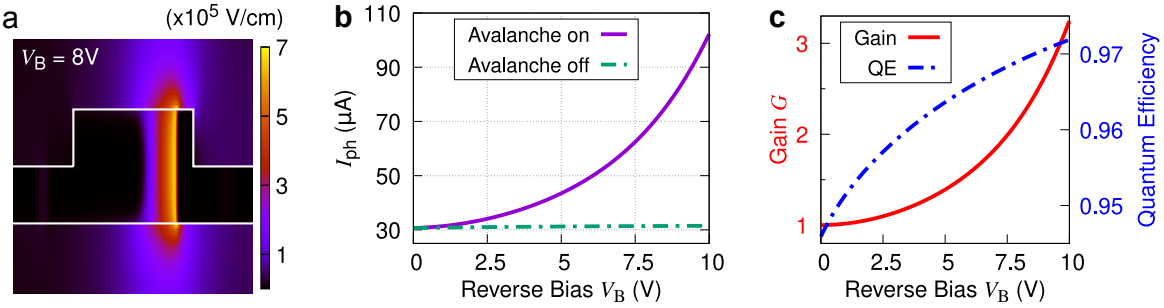

Figure 4.12: Simulations based on a laterally doped device with width $W = 900\,\text{nm}$. (a) Electric field at reverse bias $V_B = 8\,\text{V}$. (b) Photocurrent I_{ph} with and without avalanche effects. (c) Avalanche gain G and quantum efficiency (QE).

In this section, we will present an empirical estimation based on the measured device photocurrent, as well as numerical simulations of the gain G and QE. Finally, we analyze our findings and conclude with our choice of V_{ug}.

4.4.1.1 Empirical estimation: 2nd derivative of the photocurrent with respect to bias

Some reports in the literature rely on a bias-independent photocurrent at low V_B to indicate unity gain [129, 236]. However, we do not observe such a feature in our current-voltage measurements (see Fig. 2(a)). Other reports assume full or nearly full depletion at low V_B [235, 237], but it is not obvious that this assumption is valid for our devices: the increase in 3 dB bandwidth with bias up to $V_B \sim 10\,\text{V}$ suggests that the depletion region might still be widening.

Instead, we estimate the unity gain point by measuring where the second derivative of the photocurrent with respect to bias becomes zero [238, 239], i.e., $\partial^2 I_{ph}/\partial {V_B}^2 = 0$. This yields a reasonable transition point between regimes where the increase in I_{ph} with V_B is likely dominated by a saturation in QE (at lower bias) and an increase in G (at higher bias). For an input optical power of $P_{opt} = 30.2 \pm 0.2\,\text{dBm}$, we obtain V_{ug} of $1.45 - 1.7\,\text{V}$ across all device types (see Figure 4.11).

4.4.1.2 Numerical simulations of gain and quantum efficiency

We simulate the DC electrical performance of laterally doped devices using the ATLAS device simulator (Silvaco Inc.), allowing us to analyze the electric field (an example is shown in Figure 4.12(a)), ionization coefficients, charge carrier drift velocities, etc. Avalanche effects can be simulated by activating the impact ionization model (we choose the Selberherr's model) within ATLAS. By comparing the device photocurrent with and without the impact

ionization model, we can extract a simulated value of the gain G (see Figure 4.12(b),(c)). The gain increases smoothly with the bias V_B, and already starts to deviate from unity gain ($G = 1$) at low bias.

The QE can also be obtained by normalizing the simulated photocurrent to the input optical power (see Figure 4.12(c)). While QE does vary with bias, it is already almost saturated at $V_B \sim 0\,V$ with a high QE of ~ 0.95. We note that the high doping concentrations lead to large built-in electric fields in the APD even without applied bias, which strongly accelerates the photogenerated charge carriers. Coupled with the small device size, this results in the charge carrier transit time being much shorter than the recombination lifetime. Thus, the photogenerated carriers are efficiently collected by the device before they are lost to recombination.

While it is sufficient to just simulate the 2D cross-section for laterally doped devices, interdigitated devices lack a convenient symmetry axis, and thus require full 3D simulations of the whole device. However, we do not have the required computational resources to perform a thorough quantitative analysis of the gain and QE for the interdigitated devices. Nonetheless, we assume the trends in gain and QE for the interdigitated devices will be similar to that of the lateral devices.

4.4.1.3 Analysis

Our empirical estimates of the unity gain point yield $V_{ug} \lesssim 2\,V$. This is consistent with our simulation results, which show that QE is already high and that the gain G is already increasing even at these low bias voltages. Taking these into account, and to avoid overestimating the avalanche gain G and gain-bandwidth product (GBP), we conservatively consider the unity gain point to be $V_{ug} = 2\,V$ for all devices and input powers P_{opt} in our analysis.

4.4.2 Analysis of Simulated Electric Field Profiles

In this section, we will analyze the representative electric field profiles of both laterally doped and interdigitated devices of the same width W and relate their features to the device characteristics we observe in our measurements. The electric field profiles are obtained using the ATLAS device simulator (Silvaco Inc.).

Figure 4.13(a) shows the electric field profile in a laterally doped device, where the high-field regions are found along the p-n^+ junction within the waveguide core. Figure 4.13(b) shows the electric field profile of an interdigitated device. To reduce computation time, we limited the scale of the device to only two periods of alternating p-n^+ regions. Nonetheless,

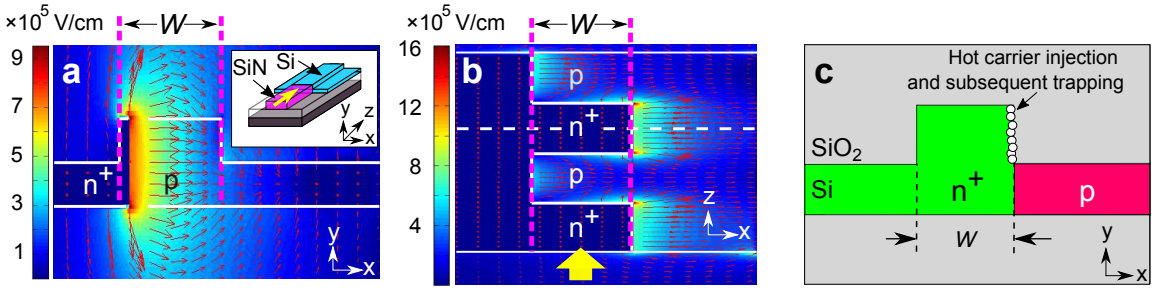

Figure 4.13: Simulated electric field profiles. (a) Electric field profile of a laterally doped device. Inset shows the schematic of the APD structure (top cladding omitted for clarity) and the axis orientations. (b) Electric field profile of an interdigitated device. The highest electric field strengths are concentrated at the corners of the n^+-doped areas. The devices in both (a) and (b) have the same width W and are simulated at just above the breakdown voltage. The yellow arrows indicate the propagation direction of input light. (c) Schematic of the waveguide cross-section along the horizontal white dashed line in (b). We mark the interface where we expect significant injection and subsequent trapping of hot carriers.

we are still able to obtain the necessary features for our analysis. Both figures are simulated at just above the breakdown voltage of the devices.

4.4.2.1 Peak electric field strengths

We observe that the highest electric field strengths in the interdigitated device are concentrated at the corners of the n^+-doped areas, and that their magnitude is significantly higher than that found in the laterally doped device with the same waveguide dimensions. The emergence of these localized high-field regions is likely to have resulted in a lower breakdown voltage V_{br} in interdigitated devices. This could also have contributed to the higher dark current observed in interdigitated devices, due to the exponential dependence of the dark carrier generation rate on higher field strengths.

4.4.2.2 Light absorption in undepleted n^+-doped regions

In a p-n^+ junction, the p-doped regions are fully depleted, but the depletion region only extends minimally into the n^+-doped regions due to their higher doping concentration. For the lateral doping profile, there is a large overlap between the depletion region and optical mode over the full length of the Si rib waveguide. However, for the interdigitated design, a significant amount of light absorption occurs in the undepleted n^+-doped regions, as input light propagates along the alternating p- and n^+-doped "digits".

It is less desirable for light absorption to occur in the undepleted n^+ regions. Due to the weak electric field strengths, the avalanche multiplication of the photo-generated charge carriers is less efficient compared to the high-field depletion region, and thus it is detrimental to the overall device gain and responsivity. This might explain the slightly lower responsivity observed in $W = 900$ nm interdigitated devices compared to laterally doped devices, though we do not observe a significant difference for $W = 750$ nm devices. The slower charge carrier diffusion in the low-field regions (see § 2.3.3.2) would also contribute to the lower device bandwidth observed in our interdigitated devices.

In our devices, input light is first incident on a n^+-doped region. This results in an overall slightly higher absorption (a difference of $\sim$10%) in n^+-doped compared to p-doped regions. Thus, the effect of light absorption in the n^+-doped regions could be slightly reduced by having input light incident on the opposite end of the Si waveguide, such that the light is first incident on a p-doped region.

The dimensions of the interdigitated doping regions can potentially be optimized, e.g., the pitch and length of each doping region, or to have p- and n^+-doped regions of different lengths. However, we foresee a design trade-off as increasing the depletion volume would also likely increase the device capacitance, which could lead to an RC-limited bandwidth.

4.4.2.3 Charge trapping

Charge trapping can occur as hot carriers are injected into the SiO_2 cladding and are subsequently trapped at the interface between the n^+-doped region and the cladding. The trapped charges would change the electrical field distribution inside the depletion region over time [240]. This effect is likely more severe in interdigitated devices, as the high electric fields occur at the edge of the Si rib waveguide (see Figure 4.13(c)). This could lead to drifts in breakdown voltage and device gain over time, which is discussed in detail in the next section.

A potential mitigating strategy is to include guard-ring structures [241] at the Si-SiO_2 interface. In addition, adopting a shallow etch for the Si rib waveguide would also reduce the interface area for charge trapping.

4.4.3 Decaying Gain and Breakdown Voltage Drifts at High Bias

In our devices, the device breakdown voltage V_{br} drifts towards higher values over time as a reverse bias voltage V_{B} is continuously applied. This is accompanied by an observed decay in the photocurrent and dark current from the onset of applying the reverse bias. Representative

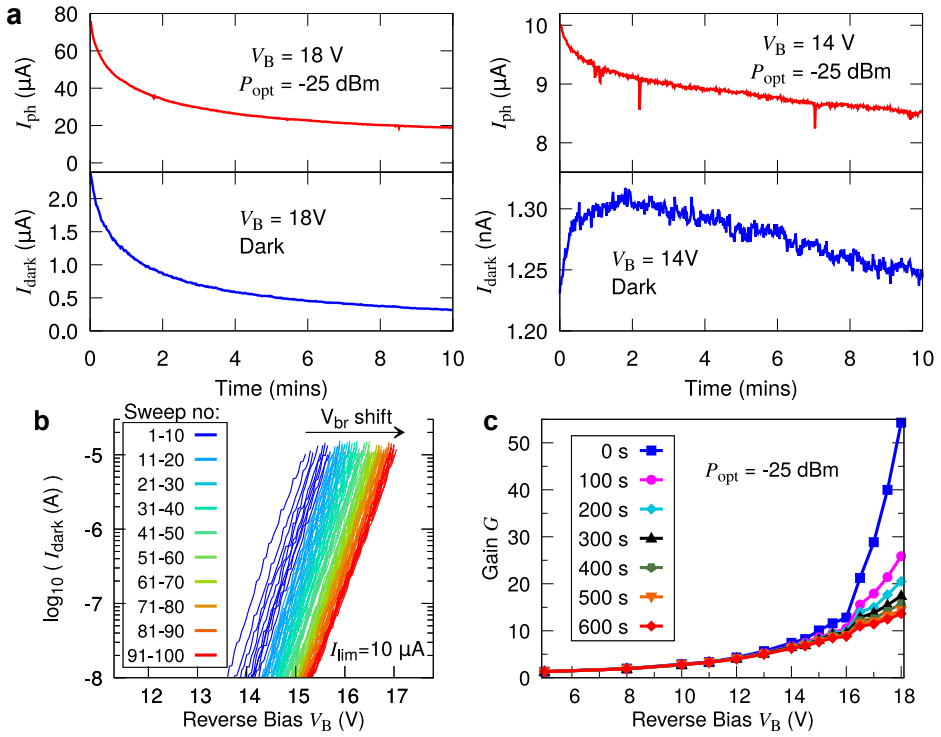

Figure 4.14: Decaying gain and breakdown voltage drifts for a $W = 900$ nm laterally doped device. (a) Photocurrent I_{ph} (measured at $P_{opt} = -25$ dBm) and dark current I_{dark} at reverse bias V_B of 14 V and 18 V. Prior to each measurement, the device is reset with the application of a forward bias voltage. (b) The avalanche breakdown voltage V_{br} increases upon successive voltage sweeps. Each sweep starts from $V_B = 0$ V and is terminated upon the dark current I_{dark} reaching the breakdown current of 10 µA. Here, the device is not reset with a forward bias voltage in between runs. (c) Change in gain G over time at different V_B. Here, the reverse bias is continuously applied.

measurements based on a $W = 900$ nm laterally doped device are shown in Figure 4.14(a),(b). The decrease is more pronounced at higher V_B with a steep decay in the current at the start before gradually leveling off, while at lower V_B the decay is much slower.

There is a corresponding decrease in the gain G with time, as shown in Figure 4.14(c). While the effect is minimal at lower V_B, where G decreases by <10% over 10 mins for V_B <13 V at P_{opt} = -25 dBm, the drop in gain increases sharply at high V_B. The rate of decrease slows down significantly after the first 10 mins, but full stability of G is observed only after $\sim$ 30 mins.

The V_{br} drift has been reported in other APDs [242, 243]. As discussed above, this effect is likely to be more severe in interdigitated devices. This is consistent with our observation of a larger gain reduction over time for interdigitated devices (comparing Table 1 and Fig. 4).

This phenomenon reveals two distinct operating modes for our devices: a gated mode where the APD is operated at high V_B with high gain, using a reset procedure to circumvent the decay in gain (explained in the following section); and a continuous mode where the APD is either operated at low V_B, or after the gain has stabilized over some time under a higher V_B.

4.4.4 Reset Procedure for Gated operation with High Gain

Despite the APD gain decreasing over time, it can be reset by the application of a forward bias voltage V_F. This likely causes the de-trapping of the charge carriers, allowing the device gain to recover to its original value. The procedure is illustrated in Figure 4.15(a). In between the sweeps of the reverse bias V_B used to characterize the APD, we apply V_F = -1 V for 1 s to the device cathode; a shorter duration might be sufficient, but we did not investigate this in detail. We note that our measurement instrument limitations result in a delay of $\sim$1 s when switching between V_B and V_F.

The reset procedure prevents the drift in the breakdown voltage over successive voltage sweeps (see Figure 4.15(b)), and also results in repeatable current-voltage characteristics after each reset. For the DC characterization results presented here, the reset procedure is carried out before each measurement.

Thus, we are able to periodically operate the APD in the high-gain regime with a gated mode, which would be compatible with applications where gating is used to reduce noise and enhance the signal. Such applications include time-of-flight imaging [117], low-light imaging [244], and Raman spectroscopy [245]. We also note that Geiger-mode infrared InGaAs APDs often employ gating techniques to suppress dark counts and afterpulsing [246].

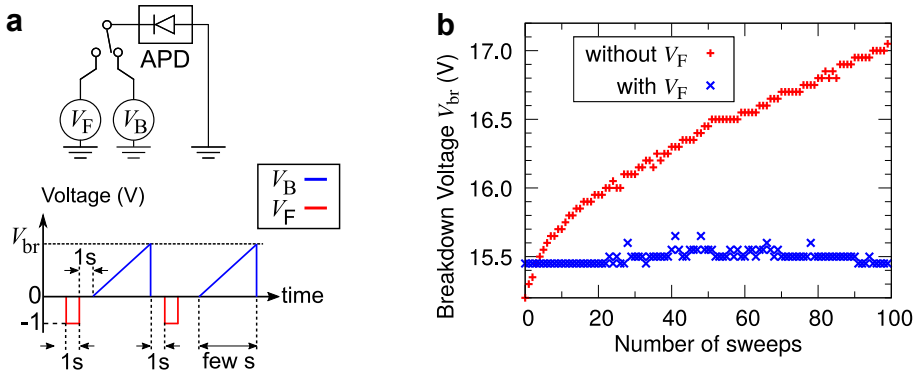

Figure 4.15: Reset procedure for high-gain operation. (a) Schematic of the procedure. Here, multiple sweeps of the reverse bias voltage V_B are applied to the APD. Prior to each sweep, a forward bias voltage of $V_F = -1$ V is applied to the APD cathode for 1 s. The time axis is not drawn to scale. (b) Comparing breakdown voltage V_{br} drifts for a $W = 900$ nm laterally doped device. By applying the forward bias V_F, the breakdown voltage V_{br} remains stable over successive sweeps of V_B. If V_F is not applied, we obtain the same results in Figure 4.14(b).

4.4.5 Benchmarking

Table 4.1 shows the benchmarking of our device performance with other recent reports of integrated APDs. Where possible, we report the performance of each device at the operating conditions where the maximum GBP is observed. For all the devices we benchmark against, we omit the uncertainty values, as only some of the literature reports include this information. We note that in the literature, the primary responsivity and unity gain are reported at varying bias voltages; where not explicitly defined, we have extracted the relevant values at a bias of $V_B = 1$ V, following ref. [235]. For our devices, we also note that the values for the dark current I_{dark} in Table 4.1 are measured in a different regime compared to Fig. 4.7(b), where the reset procedure is used (see § 4.4.4).

Our best-performing device is the $W = 900$ nm laterally doped APD, with a GBP of 234 GHz. Compared to other contemporary devices, this APD shows a strong, balanced performance in the performance metrics of dark current I_{dark}, primary responsivity R_p, gain, and bandwidth. With the exception of Ref. [235] which has a very high operating I_{dark} of 88 mA, the 234 GHz GBP of our APD is also comparable to the highest reported values of a few hundred GHz. Yet, our APD also exhibits a much lower I_{dark} of 0.12 µA at the operating bias V_B than other high-GBP devices; this would lead to decreased noise and power consumption.

These observations show that our devices are competitive and well-suited for visible-light applications requiring high bandwidth and high sensitivity.

Table 4.1: Benchmarking of device performance with other recent reports of integrated APDs. Results from this work are listed in the top section.

Type	**λ (nm)**	**V_B (V)**	**I_{dark} (μA)**	**R_p (A/W)**	**Gain**	**BW (GHz)**	**GBP (GHz)**	**Device/ Ref.**
Si, LD	685	20	0.12(1)	0.83(5)	12.3(8)	19.1(8)	234(25)	$W = 900$ nm
Si, LD	685	20	0.037(7)	0.48(2)	7.7(3)	18.7(1)	144(7)	$W = 750$ nm
Si, ID	685	18	0.31(4)	0.63(1)	2.25(6)	14.8(2)	33(1)	$W = 900$ nm
Si, ID	685	13	0.034(3)	0.56(1)	2.9(2)	16.44(8)	47.4(3)	$W = 750$ nm
Si	850	14	2	0.05	6	16.4	98.4 [a]	[247]
Si	850	20	0.016	0.071	2.2 [a]	13.1	28.8 [a]	[247]
Si	850	12	0.0004	0.133	1.2 [a]	15	18 [a]	[247]
Si	850	20	0.001	0.24	1.3 [a]	4.7	6.1 [a]	[247]
Si	850	20	0.075	0.2 [a]	1.45 [a]	14	20.3 [a]	[248]
InAs	1310	18.6	2000 [a]	0.13 [a]	45	5.3 [a]	240	[249]
InAs	1310	15.9	0.033	0.234	20	2.06	41 [a]	[250]
Ge/Si	1310	12	100	0.64	11	27	300	[251]
Ge/Si	1310	18 [a]	0.27	0.6 [a]	10	36	360 [a]	[252]
Si	1550	9	88000 [a]	0.0005 [a]	1080 [a]	26	28000	[235]
Ge/Si	1550	13	100	0.78	8.1 [a]	33.8 [a]	274 [a]	[251]
Ge/Si	1550	6	1000 [a]	0.48	15	18.9	284 [a]	[253]
Ge/Si	1550	10	1 [a]	1.25 [a]	17.8 [a]	25	445 [a]	[254]

[a] These values were not explicitly reported and were inferred from the figures or other values.

LD: lateral doping ID: interdigitated doping W: waveguide width
λ: operating wavelength V_B: reverse bias I_{dark}: dark current
R_p: primary responsivity BW: 3 dB bandwidth GBP: gain-bandwidth product

4.5 Conclusion

In conclusion, we report the first monolithically integrated APDs for visible light (685 nm). Our devices feature a small device footprint and are fabricated with a CMOS-compatible process. At a reverse bias of $V_B = 2$ V, a laterally doped APD of 900 nm width exhibited a highest primary responsivity of 0.83 ± 0.05 A/W over a dynamic range of > 50 dB, with dark current of ~ 1 pA. At higher V_B, laterally doped devices exhibit superior bandwidth, with a highest 3 dB bandwidth of 30.5 ± 0.2 GHz, and a highest gain-bandwidth product of 234 ± 25 GHz. APDs with an interdigitated doping profile require a lower bias to attain the same DC gain than lateral ones but have a higher dark current. Our devices perform strongly compared to other state-of-the-art integrated APDs operating at other wavelengths.

The addition of integrated visible-light APDs to the component toolbox of SiN photonics opens up many application possibilities, and greatly expands the versatility of silicon photonics platforms [105, 227, 228]. There is potential for further design optimizations, such as alternative doping profiles [235] which may enhance the APD gain and reduce the working bias.

In the next chapter, we will explore the operation of these devices in the Geiger mode for single-photon counting, which will play an important role in the development of integrated quantum photonics platforms, and for interfacing with single-photon sources operating at visible wavelengths.

Chapter 5

Characterization of Integrated APDs in Geiger-mode Operation

Following the device characterization in linear-mode operation, this chapter presents the experimental results on characterization of waveguide-integrated APDs in Geiger-mode operation to achieve single-photon sensitivity.

We first define characterization metrics for APDs when operated in Geiger mode and explain how these metrics change with operating conditions. Next, we review different types of quenching circuits which are used for Geiger-mode operation and describe how they affect device performance. We then introduce a passive-quenching circuit implementation and present characterization results of a commercial SPAD operated with this circuit. Finally, we report on experimental results obtained from characterization of our fabricated devices. Here, we measured avalanche breakdown voltage, avalanche pulse characteristics, dark count rate, and investigated their temperature and excess bias dependence. We discussed the physical mechanism behind excessive dark count rates that our devices exhibit and suggested various methods to prevent device saturation.

5.1 Introduction

APDs are reverse biased beyond their breakdown voltage in Geiger-mode operation[1]. Once an APD is biased in this way, the electric field in the depletion region is so high that a single charge carrier within a depletion region can trigger a self-sustaining avalanche of impact ionizations. The avalanche current pulse swiftly rises with its leading edge marking the

[1] In this chapter, we refer to the reverse bias voltage and breakdown voltage as positive values.

arrival time of the detected photon if the primary charge carrier is photogenerated. The self-sustaining avalanche is quenched by lowering its reverse bias voltage. Finally, the reverse bias voltage is restored to its initial value to prepare the device for subsequent detection events.

The electrical circuits that are used to handle these quenching and voltage recovery transitions are known as quenching circuits. These circuits are used to sense the leading edge of an avalanche pulse and subsequently provide a synchronized output pulse. Here, we first briefly define characterization metrics of SPADs and then introduce different types of quenching circuits.

5.1.1 SPAD Characterization Metrics

5.1.1.1 Breakdown voltage

The breakdown voltage V_{br} for semiconductor diodes is defined as the minimum reverse bias voltage that causes the diode to appreciably conduct current in reverse direction. In Geiger-mode operation, APDs are biased with a reverse bias voltage V_{B} that exceeds their breakdown voltage V_{br} by an amount called excess bias voltage V_{E}

$$V_{\mathrm{E}} \coloneqq V_{\mathrm{B}} - V_{\mathrm{br}}. \tag{5.1}$$

The excess bias voltage V_{E} is a significant factor on detector performance, and hence its value is determined according to the required performance metric. The breakdown voltage V_{br} of an APD operated in Geiger mode can be identified as the minimum reverse bias voltage at which an avalanche pulse is obtained from the device. The avalanche breakdown voltage has a positive temperature coefficient such that it increases with the device temperature.

5.1.1.2 Dark count rate

A dark count is defined as a detection event that occurs in the absence of incoming photons, and it consists of two types: primary and secondary. Primary dark counts originate from thermally-generated and tunneling charge carriers that trigger an avalanche event as if they were real photon detection events (see § 2.4.5 for details). Higher excess bias voltage V_{E} increases dark count rate because of the field-assisted enhancement of emission rates from generation centers and enhanced avalanche triggering probability [3].

Secondary dark counts stem from afterpulsing effect, which is discussed in more detail in § 5.1.1.4. Reducing junction temperature decreases primary dark counts; however, after-

pulsing effect gets stronger as lower temperature leads to slower release of trapped charge carriers [3]. Therefore, there is an optimum temperature to minimize total dark count rate, especially for devices which suffer from strong afterpulsing effect.

5.1.1.3 Photon detection efficiency

Once a photon is absorbed within the depletion region of the device, a photogenerated electron-hole pair is created. If these primary charge carriers trigger an avalanche of impact ionization events , then eventually a measurable current pulse can be generated such that the incident photon is detected.

If saturation effects are negligible, and the probability of having two incident photons within the dead time of a device is very low, then the photon detection efficiency (PDE) can be obtained as the ratio of the number of output pulses to the number of incident photons after correcting for the dark count rate of the device.

The photon detection efficiency generally rises with the excess bias voltage V_{E} as higher electric field increases the avalanche triggering probability. Enhanced avalanche triggering probability, however, also increases the dark count rate. Given this trade-off, there is usually an optimum excess bias voltage V_{E} for device operation.

5.1.1.4 Afterpulsing

Some charge carriers during an avalanche event can be trapped by the deep levels in the junction depletion layer. These trapped charge carriers are subsequently released with statistically fluctuating time delays whose mean value depends on the deep levels involved in the process [5]. Released charge carriers can cause avalanche pulses whose timings are correlated with the timing of previous pulses; these time-correlated events are known as afterpulsing.

The number of charge carriers captured during an avalanche event increases with the total number of carriers crossing the junction, i.e., the total charge contained in an avalanche pulse (see Eq. 5.6). Even though decreasing the excess bias voltage V_{E} reduces the total charge in an avalanche pulse, the excess bias voltage is usually selected based on the required performance metric.

Minimizing the parasitic capacitance and shortening the avalanche pulse duration reduce the number of charge carriers swept across the depletion region during an avalanche event, and subsequently lead to less trapped charge carriers and hence reduced afterpulsing effect. The parasitic capacitance can be minimized by having the quenching circuit close to the detector,

or more preferably, by monolithically integrating with the detector if possible. Avalanche pulse duration, on the other hand, can be kept short by using active-quenching circuits that quench the avalanche current during its build-up phase within a sub-ns time window [3]. Consequently, the total charge contained in an avalanche pulse with an active-quenching circuit would be much lower compared to that of obtained with a passive-quenching circuit.

Deliberately prolonging the dead time by keeping the reverse bias voltage at the quenching level can also be used to alleviate or totally mitigate afterpulsing effects. Extended dead time creates a time buffer during which the trapped charge carriers can be released without triggering any new avalanches. However, we note that this method comes with a trade-off: a prolonged dead time limits the count range of a device before its saturation.

5.1.1.5 Timing jitter

The timing jitter is a measure of degree of variations in the time delays between the arrival times of incident photons and the generated electrical output pulses. The timing jitter can be specified as the full-width-half-max (FWHM) and full-width-tenth-max (FWTM) of the statistical distribution of these time delays (see § 2.3.4.2). It is an important performance metric for applications such as quantum key distribution (QKD) and lifetime measurements of single-photon sources [195, 255]. For instance, the timing jitter can lead to intersymbol interference and increase the error rate of the key exchange process in QKD applications [256]; therefore, it should be minimized.

5.1.2 Avalanche Quenching Circuits

Geiger-mode avalanche photodiodes are operated with quenching circuits that

1. Sense the leading edge of the avalanche current pulses,
2. Provide a synchronized output signals upon triggering,
3. Quench the avalanche current by lowering its reverse bias voltage,
4. Restore its reverse bias voltage to reset the device for subsequent detections.

Depending on how they handle quenching and voltage recovery transitions, quenching mechanisms in the literature can be grouped into three main categories: passive, active and mixed.

The passive-quenching circuit is the simplest quenching mechanism, yet it bears some limitations due to its slow voltage recovery transition. Some applications may require more

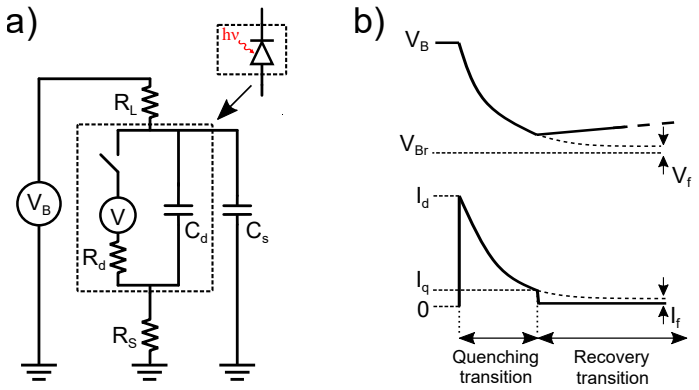

Figure 5.1: Passive-quenching circuit. a) A circuit model of a passively quenched SPAD. b) The corresponding diode voltage and diode current during an avalanche event. The image is based on [3].

elaborate quenching techniques to fully exploit inherent detector performance. Here, we give implementation details of a passive-quenching circuit following the description in [3], and then compare it with active and mixed implementations.

5.1.2.1 Passive-quenching circuits

The passive-quenching scheme is the simplest implementation of a quenching circuit as it only requires a large load resistor, which is connected in series with the device to limit the avalanche current flow. During an avalanche current build-up, the avalanche current starts to discharge the diode internal capacitance and parasitic capacitance. The excess bias voltage V_{E} then exponentially decreases towards zero with a time constant determined by the effective RC circuit at the device cathode.

Reverse bias voltage V_{B} never goes below the breakdown voltage V_{br}; however, the final value of avalanche current during discharging process approaches an asymptotic value. If this asymptotic value is less than some threshold current value, which is known as latching current, then the avalanche current flow is quenched [3]. Here, we describe the operation of a device with a passive-quenching circuit while referring to Fig. 5.1.

Quenching transition

Figure 5.1 shows a circuit model of an APD with a passive-quenching circuit. R_{L} denotes the large load resistor that is connected in series with the device. C_{d} and C_{s} represent the junction capacitance and parasitic stray capacitance, respectively. Diode series resistance R_{d} is given by the space-charge resistance of the diode junction and the resistance of the

neutral semiconductor crossed by the avalanche current. Triggering of an avalanche event corresponds to closing the switch in Fig. 5.1(a).

The relation between the transient current $I_{\mathrm{d}}(t)$ flowing through the device and the corresponding transient voltage $V_{\mathrm{d}}(t)$ across that device can be described by

$$I_{\mathrm{d}}(t) = \frac{V_{\mathrm{d}}(t) - V_{\mathrm{br}}}{R_{\mathrm{d}}} = \frac{V_{\mathrm{ex}}(t)}{R_{\mathrm{d}}}, \tag{5.2}$$

where $V_{\mathrm{ex}}(t)$ is the transient excess voltage. Once an avalanche event is triggered, $I_{\mathrm{d}}(t)$ and $V_{\mathrm{d}}(t)$ fall toward their asymptotic steady-state values of I_{f} and V_{f}

$$\begin{aligned} I_{\mathrm{f}} &= \frac{V_{\mathrm{B}} - V_{\mathrm{br}}}{R_{\mathrm{d}} + R_{\mathrm{L}}} \approx \frac{V_{\mathrm{E}}}{R_{\mathrm{L}}}, \\ V_{\mathrm{f}} &= V_{\mathrm{br}} + R_{\mathrm{d}} I_{\mathrm{f}}. \end{aligned} \tag{5.3}$$

The quenching time is given by the quenching time constant τ_{q}

$$\tau_{\mathrm{q}} = (C_{\mathrm{d}} + C_{\mathrm{s}}) \frac{R_{\mathrm{d}} R_{\mathrm{L}}}{R_{\mathrm{d}} + R_{\mathrm{L}}} \approx (C_{\mathrm{d}} + C_{\mathrm{s}}) R_{\mathrm{d}}. \tag{5.4}$$

The load resistor R_{L} is typically on the order of a few hundreds of kilo ohms in order to achieve passive-quenching, whereas the diode series resistance R_{d} is usually around a few kilo ohms. Therefore, the quenching time constant τ_{q} is effectively determined by the diode series resistance R_{d}.

The self-quenching mechanism works as follows: If the asymptotic steady-state diode current I_{f} is very small, then the asymptotic steady-state diode voltage V_{f} will be very close to V_{br}. Once an avalanche event is triggered, the transient diode voltage V_{d}(t) approaches the steady-state diode voltage V_{f}. Reduced transient current $I_{\mathrm{d}}(t)$ means that there are now less charge carriers traversing the high-field depletion region. Due to the statistical nature of avalanche process, it becomes probable that the impact ionizations fail to sustain the avalanche current flow. This probability becomes significant when the diode current I_{d} falls below a latching current I_{q} of around 100 µA [3, 257], and the avalanche current is eventually quenched. The latching current I_{q} can be obtained from

$$V_{\mathrm{q}} = V_{\mathrm{B}} + I_{\mathrm{q}} R_{\mathrm{d}}, \tag{5.5}$$

where V_{q} is the corresponding diode voltage at the onset of quenching.

Value of load resistor

The value of the load resistor R_L can be chosen by considering its relation to the asymptotic steady-state current I_f (see Eq. 5.3). In order to reduce the uncertainty on the time delay between a photon incidence and the corresponding quench onset, the transient current $I_d(t)$ should cross the latching current I_q with a steep slope in Fig. 5.1(b). Therefore, the asymptotic current I_f should be set to a value that is much lower than the latching current I_q. Otherwise, the quenching either does not occur at all and the avalanche sustains itself, or the quenching occurs with a longer time delay and degraded timing uncertainty. It is advised that the asymptotic current I_f should not exceed one-fifth of the corresponding latching current I_q [3]. This ratio suggests using a load resistor $R_L = 500\,\mathrm{k\Omega}$ for a latching current I_q of $100\,\mu\mathrm{A}$ when the excess bias voltage $V_E = 10\,\mathrm{V}$ (see Eq. (5.3)).

Total charge in an avalanche pulse

The total charge in an avalanche pulse also influences the dark count rate and afterpulsing performance through its effects on charge trapping. The total charge in an avalanche pulse Q_{pc} can be obtained from both quenching and voltage recovery transitions by

$$Q_{pc} = (V_B - V_q)(C_d + C_s) \approx V_E(C_d + C_s) \approx I_f T_r. \tag{5.6}$$

The number of charge carriers captured by the deep levels during an avalanche pulse increases with the total number of charge carriers crossing the junction. Therefore, the total charge in an avalanche pulse Q_{pc} should be minimized to reduce possible afterpulsing events. Minimizing the parasitic capacitance C_s by avoiding long electrical connections between a detector and its quenching circuit would reduce Q_{pc}.

Recovery transition

Once an avalanche current is quenched, the reverse bias voltage must be recovered to its initial value in order to reset the device for next detection events. The onset of the voltage recovery transition corresponds to opening the switch in Fig. 5.1 during which the diode capacitance and parasitic capacitance are charged by the current flowing through R_L. The time required for the full voltage recovery is given by the voltage recovery time constant τ_r

$$\tau_r = R_L(C_d + C_s). \tag{5.7}$$

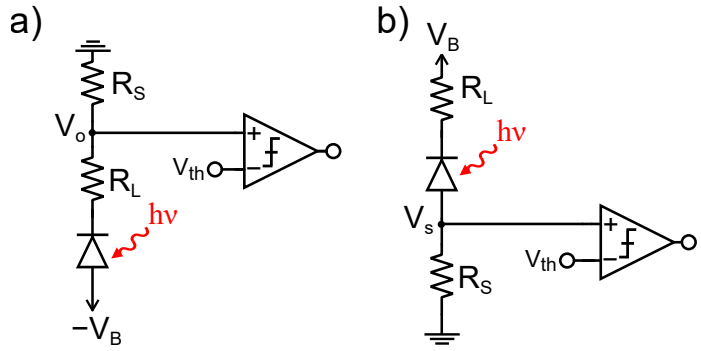

Figure 5.2: Output configurations in passive-quenching. (a) voltage-mode output and (b) current-mode output. Images are based on [3].

Since the value of the load resistor R_L required to achieve passive-quenching is considerably high, the resulting voltage recovery time constant τ_r would be high as well. For a typical commercial APD such as Perkin Elmer C30902SH, the diode capacitance C_d is around 1.6 pF. Assuming negligible parasitic stray capacitance, the diode capacitance leads to a voltage recovery time constant τ_r of 0.8 µs for a load resistor R_L of 500 kΩ. It takes approximately $5 \times \tau_r$ to recover the reverse bias voltage V_B within 1% of its initial value: the voltage recovery transition in this case takes about 4 µs. Here, we note that a parasitic capacitance C_s on the order of a few tens of pF or higher would dominate the voltage recovery time constant τ_r and lead to a voltage recovery transition that lasts tens of µs or higher.

Output pulse

The avalanche pulse can be sensed by connecting a low-value sense resistor R_s in series with the device. The avalanche current flowing through this sense resistor builds up a voltage drop, which can subsequently be discriminated by a voltage comparator. The configuration at which the sense resistor R_s is connected to the ground lead of the load resistor R_L (see Fig. 5.2(a)) is known as voltage-mode output [3], In this configuration, the peak amplitude of the avalanche voltage pulse V_o is read as

$$V_o = (V_B - V_{br} - I_q R_d)\frac{R_s}{R_L + R_s} \approx V_E \frac{R_s}{R_L} \approx I_f R_s. \tag{5.8}$$

The constraint imposed on the asymptotic steady-state diode current I_f to achieve a proper passive-quenching leads to very low values for the voltage pulse V_o. Moreover, the voltage pulse V_o is generated by the current that discharges the capacitances C_d and C_s through a highly resistive path formed by the large load resistor R_L. This effective low-pass filter acting

on the fast avalanche current pulse subsequently leads to a detector timing performance which is not fully exploited [3].

Therefore, it is a general practice to connect the sense resistor R_s on the ground lead of the photodiode from its anode terminal as shown in Fig. 5.2(b). Since the waveform of the pulse follows the diode current, this configuration is called current-mode output. The voltage V_s across the sense resistor in this case is given by

$$V_s \approx V_E \frac{R_s}{R_d(1+\frac{C_d}{C_s})} \approx I_f R_s \frac{R_L}{R_d(1+\frac{C_d}{C_s})} \approx V_o \frac{R_L}{R_d(1+\frac{C_d}{C_s})}. \tag{5.9}$$

Comparing Eqs. 5.8 and 5.9, it can be seen that V_s is much higher than V_o. The reason is that V_s is generated by the large current that is equal to V_E/R_d, whereas V_o is generated by the much smaller current that equals to V_E/R_L, i.e., I_f. In addition to output pulses with higher amplitudes, the output voltage waveform has the same rise time of the fast avalanche current in this configuration. The current-mode output, therefore, offers better photon-timing accuracy compared to that of voltage-mode output in the earlier example [3].

5.1.2.2 Active-quenching circuits

An active-quenching circuit uses active electronic components to reduce the reverse bias voltage once it detects the steep onset of an avalanche current. The voltage recovery transition is also expedited by actively restoring the excess bias voltage back to its initial value. This type of circuits mitigates the drawbacks associated with the slow voltage recovery of passive-quenching circuits. Moreover, such circuits offer short and well-defined durations for both avalanche current pulse width and device dead time; therefore, they provide improvements on afterpulsing and dark count rate performance.

5.1.2.3 Mixed-quenching circuits

The quenching and voltage recovery transitions can also be implemented by a hybrid approach where one transition is handled passively, whereas the other transition is managed using active components. One such circuit, a passive-quenching active-reset (PQAR) circuit, can use a large load resistor to passively quench the avalanche current in a way described in § 5.1.2.1, whereas active electronic components such as transistors can be utilized to accelerate the voltage recovery transition. Such mixed solutions can be useful for designing simple yet effective circuits to meet certain application needs.

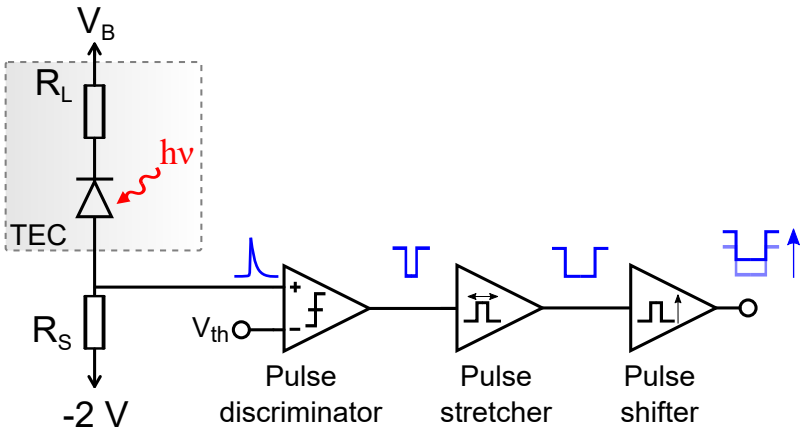

Figure 5.3: Block diagram of electronics circuit used for commercial APD characterization.

5.2 Experiment: Characterization of a Commercial APD

The avalanche output pulses are usually conditioned to make them compatible with the input signal standards of other instruments such as frequency counters and time-to-digital converters. Therefore, an electronic signal conditioning stage is usually implemented in addition to a quenching circuit. In this section, we first describe our passive-quenching circuit equipped with signal conditioning electronics, and then present our experimental results for its operation. This electronic circuit and our characterization testbed were verified by measuring the breakdown voltage, dark count rate, and photon detection efficiency of a commercial APD (Perkin Elmer C30902SH).

The block diagram of our electronics circuit is shown in Fig 5.3. In the first stage, this circuit performs passive-quenching as described in § 5.1.2.1. In subsequent stages, it uses electronic components to provide a standard output pulse that is synchronized to the leading edge of the avalanche pulses.

First, an avalanche output pulse is compared against a set threshold voltage V_{th} using a fast pulse discriminator. For other instruments that require a minimum pulse width for the input signal, a pulse stretcher is used to widen the pulse width of the discriminator output. Lastly, a pulse shifter is used to shift the signal level to a signal logic standard that is compatible with other instruments. The implementation details of this circuit are given in Appendix C.

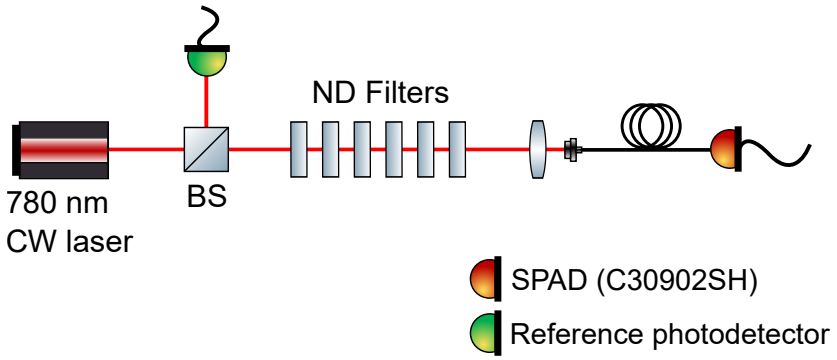

Figure 5.4: Setup to characterize the commercial APD (Perkin Elmer C30902SH).

5.2.1 Optical Setup

The number of photons incident on a SPAD should be far lower than the saturation limit of the device. Here, we used a 780 nm continuous wave (CW) laser that is attenuated down to the single-photon level with anti-reflective coated neutral density (ND) filters (see Fig. 5.4)[2].

The photon energy at 780 nm wavelength is approximately equal to 2.55×10^{-19} J. For a typical device saturation limit of around 10^6 cps [4], our aim is to attenuate the optical power down to sub-picowatt levels. Such low optical power levels are not measurable with typical silicon optical power sensors because their noise limits are usually around 100 pW. Therefore, we first separately characterized the attenuation factors of ND filters, and then combined the attenuation factor of each ND filter that is inserted into the optical path. Table 5.1 shows the transmitted power through each ND filter for an input optical power of 71.0 ± 0.1 µW together with the corresponding attenuation factor.

Table 5.1: Neutral density filter characterization.

Filter No.	Power (μW)	Attenuation (dB)
1	0.82 ± 0.01	-19.39 ± 0.05
2	0.76 ± 0.01	-19.71 ± 0.06
3	0.76 ± 0.01	-19.71 ± 0.06
4	3.75 ± 0.01	-12.77 ± 0.01
5	3.60 ± 0.01	-12.95 ± 0.01
6	3.50 ± 0.01	-13.07 ± 0.01

[2]The experimental setup also includes a reference photodetector to monitor any optical power drift during characterization; however, it was not deemed necessary in this preliminary study.

With all the ND filters inserted in the optical path, the total attenuation factor of -97.60 ± 0.05 dB[3] attenuates the input optical power down to 12.40 ± 0.14 fW. The corresponding photon flux is then read as

$$\psi_{in} = \frac{P_{\text{in}}}{h\nu} = \frac{12.40 \pm 0.14\,\text{fW}}{2.55 \times 10^{-19}\,\text{J}} \approx 48600 \pm 550\ s^{-1}, \tag{5.10}$$

which is two orders of magnitude lower than the saturation limit of the commercial device, and hence it is suitable for use during device characterization.

5.2.2 Characterization Results

Here, we report on the experimental results on commercial device characterization at various excess bias voltages and operating temperatures. In order to perform measurements at low temperatures, we used a hermetically sealed case and mounted the detector inside. The case contains a thermistor and a thermoelectric cooler for active temperature control, and it connects to our electronics circuit board. The design of the hermetically sealed case follows the one used in [4], and its photographs can be found in Appendix C. We gratefully acknowledge Prof. Christian Kurtsiefer for his assistance in providing the SPAD case as well as the circuit schematics of the quenching electronics that we used in this section.

5.2.2.1 Breakdown voltage

We determined the breakdown voltage V_{br} by slowly increasing the applied reverse bias voltage applied until an output pulse is seen on the oscilloscope. The breakdown voltage V_{br} is measured as 195 V at $-25\,^{\circ}$C.

5.2.2.2 Dark count rate

During the dark count rate (DCR) characterization, we turned off the laser and covered the setup by a black polyurethane-coated nylon fabric to have a light-tight environment. For a given reverse bias voltage and operating temperature, we measured number of pulses over a 1-second time interval using a universal counter (Agilent 53132A) and repeated this measurement for hundred times to obtain enough statistics.

The dark count rate first exponentially increases with the excess bias voltage V_{E} and then starts to saturate as shown in Fig. 5.5(a). The DCR is around 100k cps at room temperature,

[3]The uncertainty is obtained by root-sum-of-squares technique.

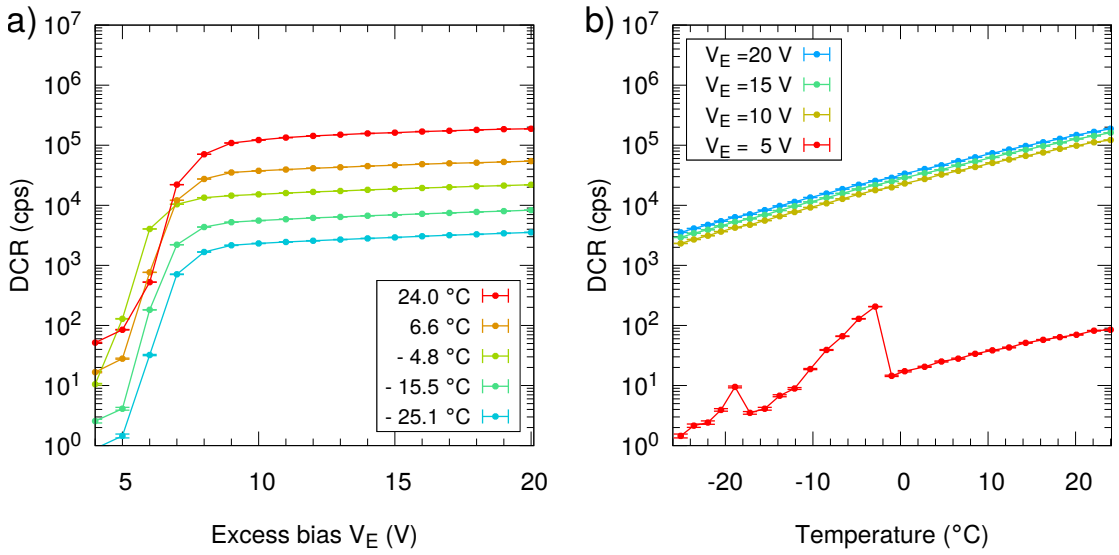

Figure 5.5: DCR measurements of the commercial APD. a) DCR vs. excess bias voltage V_{E}, b) DCR vs. temperature T.

whereas it decreases down to 3k cps at $-25.1\,^{\circ}\mathrm{C}$. The dark count rate, in general, decreases with reduced temperature for a given excess bias voltage V_{E}.

5.2.2.3 Photon detection efficiency

The strongly attenuated 780 nm CW laser is used as a photon source at the single-photon level for the photon detection efficiency (PDE) measurements. Similar to the DCR measurements, we counted the number of pulses over a 1-second time interval in a light-tight setup. We repeated this measurement for hundred times in both dark and illuminated conditions to obtain the number of dark counts N_{dark} and the number of device counts N_{device}, respectively. We subsequently calculated the photon detection efficiency by first subtracting the number of dark counts N_{dark} from the number of device counts N_{dev}, and then normalizing the result with the expected number of photons incident on the device

$$\mathrm{PDE} = \frac{N_{\mathrm{dev}} - N_{\mathrm{dark}}}{\psi_{\mathrm{in}}}. \tag{5.11}$$

Figure 5.6(a) shows that the photon detection efficiency, in general, increases with the excess bias voltage V_{E}. We did not observe PDE saturation over the range of excess bias voltages applied to the device. Figure 5.6(b) shows that the photon detection efficiency, in general, reduces with higher temperature for excess bias voltages beyond 10 V. The reason is that the number of avalanches due to thermally-generated charge carriers increases at higher

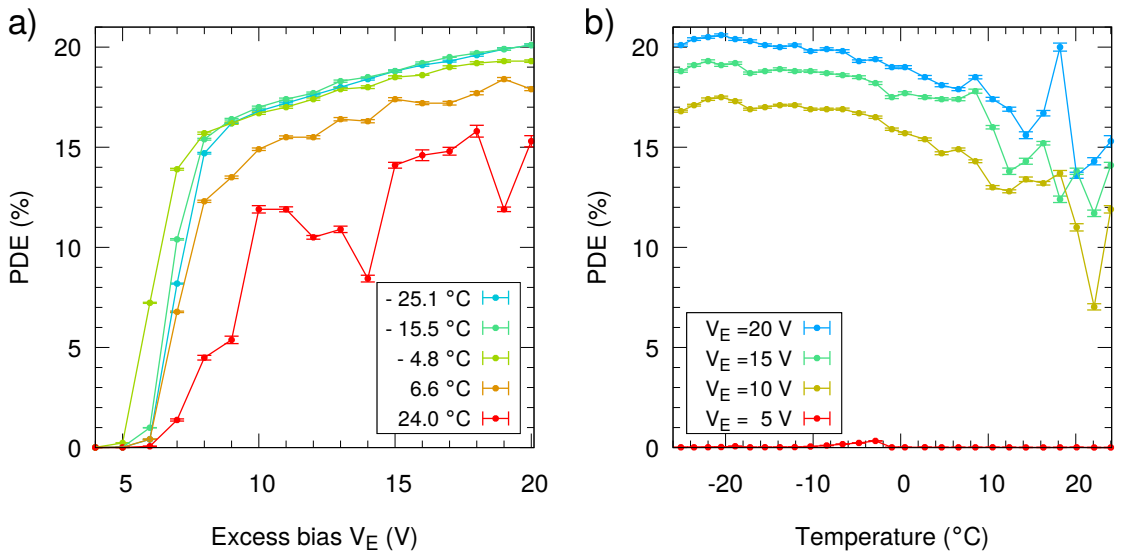

Figure 5.6: PDE measurements of the commercial APD. a) PDE vs. excess bias voltage V_{E}, b) PDE vs. temperature T.

temperatures, and this subsequently leads to inhibition of the device for next photon detection events. We note that the PDE traces do not show a consistent trend near room temperature operation most likely due to very high DCR at these temperatures.

5.2.2.4 Comparison of results

Here, we compared our measurement results with the device datasheet and other characterization studies performed for the same APD model (Perkin Elmer C30902SH).

Breakdown voltage

The datasheet of Perkin Elmer C30902SH APD specifies the breakdown voltage V_{br} as 225 V at 22 °C [258]. Using the specified breakdown voltage temperature coefficient of 0.7 V/°C, the breakdown voltage is calculated as 192 V at our operating temperature of −25.1 °C. This value agrees well with the measured breakdown voltage of 195 V at −25.1 °C.

Dark count rate

Figure 5.7(a) compares our DCR measurements with different studies. Our work and Ref-a ([4]) reports similar values, whereas the DCR values reported in Ref-b ([5]) is around one order of magnitude lower. It was specified that the device used in Ref-b ([5]) had been

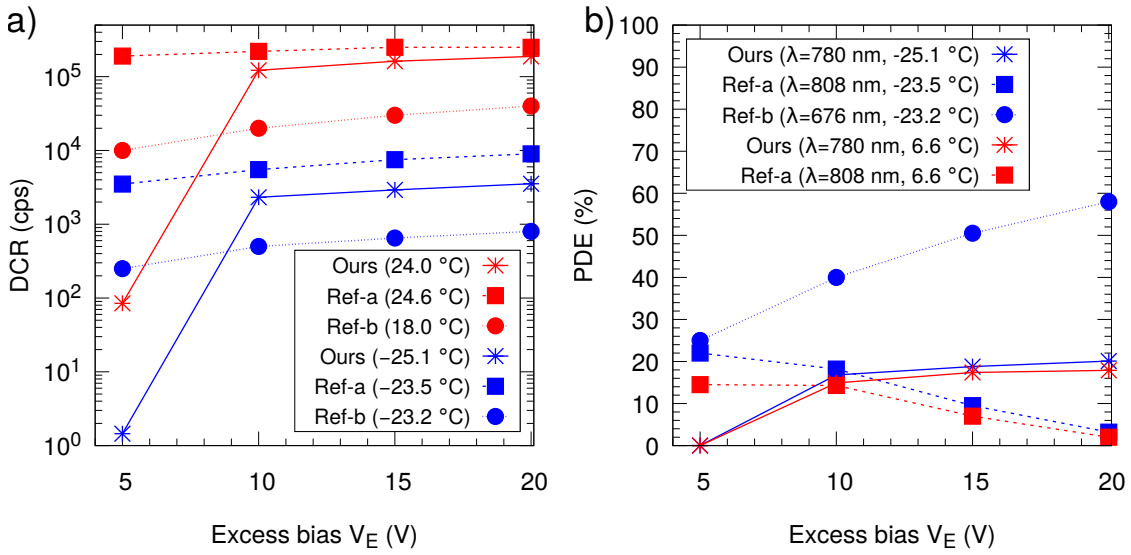

Figure 5.7: Comparison of characterization results for the commercial APD. a) Dark count rate and b) photon detection efficiency. Near room temperature measurements are shown in red, whereas measurements performed at temperatures below $<-23\,^{\circ}\mathrm{C}$ are shown in blue. Ref-a: [4], Ref-b: [5].

factory selected for its low noise; this might explain the reason why it shows better noise performance.

Photon detection efficiency

The comparison of photon detection efficiency measurements from the same studies are shown in Fig. 5.7(b). We note that different wavelengths of input light used in characterization studies render a direct comparison between these studies unfeasible. Nevertheless, we compared photon detection efficiencies for similar operating conditions of excess bias voltage and temperature.

The photon detection efficiency reported in Ref-b ([5]) is significantly higher than those reported here and in Ref-a ([4]), especially for excess bias voltages beyond 10 V. The measurements in Ref-a ([4]) are performed with an input light that has similar wavelength to ours, and it reports on similar yet not identical photon detection efficiencies at excess bias voltages of 10 V and 15 V. The photon detection efficiency in Ref-a ([4]) decays with increased excess bias voltage, whereas a similar trend is neither reported here nor in Ref-b ([5]). Lastly, the photon detection efficiencies reported here and in Ref-a ([4]) vary within few percent for similar temperature changes when the excess bias voltages are beyond 10 V.

Since Ref-b ([5]) does not report any data at near room temperature, the photon detection efficiency vs. temperature trends could not be compared.

We note that the device-to-device variability as well as a lack of absolute calibration standards for incoming photon rate might give rise to differences in the characterization results. Nevertheless, this study shows that our quenching electronics and test setup is suitable to characterize the fabricated waveguide-based APDs in the next sections.

5.3 Experiment: Symmetric Rib Waveguide p-n APDs

Here, we present the experimental results on characterization of our silicon waveguide-integrated APDs in Geiger-mode operation. Specifically, we measured breakdown voltage, avalanche pulse characteristics, and dark count rate of devices at different operating conditions. After studying how breakdown voltage V_{br} varies with temperature, we investigated dark count rate performance. When operated at a fixed reverse bias voltage, our devices showed DCR decay over time due to the breakdown voltage drift upon successive avalanche breakdowns. We proposed and implemented a method to prevent the DCR decay, and subsequently studied how DCR changes with excess bias voltage V_{E} and operating temperature.

5.3.1 Breakdown Voltage

Here, we report on the experimental results on breakdown voltage V_{br} measurements. Specifically, we investigated its temperature dependence and stability upon successive avalanches.

5.3.1.1 Temperature dependence

We used our custom light-tight temperature-controlled probe station to perform measurements at different operating temperatures (see § 4.3). In order to prevent water condensation on samples during low temperature operation, the entire setup is covered with a 3-mm-thick polycarbonate sheet and pumped with compressed dry air with a dew point of around $-40\,^{\circ}\mathrm{C}$ to substitute the humid air inside. The front cover was chosen to be transparent for visual access inside the station during probing[4]. The dew point inside the setup is measured via a hygrometer to ensure that the dew point is lower than the target temperature before cooling the sample.

[4]Similar to § 4.3, a black polyurethane-coated nylon fabric is used to cover the setup to prevent stray light leakage during data acquisition.

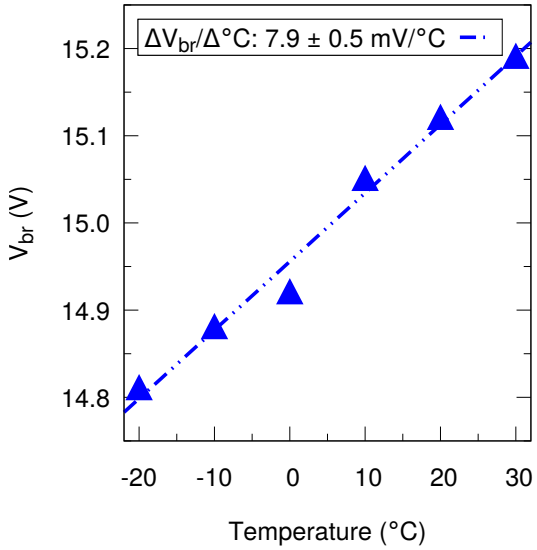

Figure 5.8: Breakdown voltage V_{br} vs. temperature measured for a 900-nm-wide p-n^{+} SPAD.

We placed our samples on top of a copper sample holder, which is soldered onto the top surface of a 3-stage thermoelectric cooler (TEC, Ferrotec 9530/228/060 M). A thermistor inside the sample holder is used to measure the device temperature, which is actively stabilized by a temperature controller. The bottom surface of the TEC is soldered onto the top surface of a copper heat sink to effectively dissipate the heat from the TEC, which would otherwise suffer from performance degradation.

The sample temperature could be reduced to $-30\,^{\circ}\mathrm{C}$. The lowest achievable temperature was limited by the effectiveness of the heat dissipation from the TEC. The cooling performance could further be improved by a more effective heat dissipation method such as chilled water cooling and by improving the isolation of the sample from its surroundings. The latter can be achieved by a hermetically sealed device packaging or by having the sample in a vacuum chamber.

In avalanche breakdown mechanism, a bunch of electrons knock out valence electrons from their bonded atoms and create secondary electron-hole pairs. At high temperatures, increased phonon scattering reduces the mean free path of charge carriers, and subsequently decreases the impact ionization probability. The device now requires higher electric field strengths to achieve avalanche breakdown; therefore, the avalanche breakdown voltage V_{br} has a positive temperature coefficient.

The temperature dependence of breakdown voltage is analyzed by measuring breakdown voltages at different operating temperatures as described in § 4.3.2. A temperature controller

is used to actively stabilize the device temperature to prevent possible breakdown voltage drift during measurements. The temperature is stabilized to within 0.1 °C for which the corresponding V_{br} fluctuation is less than 1 mV and hence negligible. The temperature coefficient of the breakdown voltage V_{br} is calculated to be 7.9 ± 0.5 mV/°C from the measurements results shown in Fig. 5.8.

In addition to the active stabilization of the device temperature, we note that the effects of temperature fluctuation can be prevented by generating a feedback response based upon avalanche pulse heights [259]. Such methods are more suitable to field-deployed systems such as LIDAR as well as airborne and spaceborne communication links, for which active temperature stabilization systems are impractical to be deployed due to power and volume constraints.

5.3.1.2 Breakdown voltage drift: decaying pulse amplitude

We report in § 4.3.2 that the breakdown voltage V_{br} increases upon successive avalanche breakdowns. One of our early hypotheses for the reason of such breakdown voltage walkout was the localized heating effects in the junction. The heating of the junction can originate from high current density during an avalanche event and elevated ambient temperature at which the device operates. As we actively stabilized the operation temperature to within 0.1 °C via a thermoelectric cooler, only high current density during an avalanche event could give rise to such heating effect in our case. Nevertheless, once the avalanche current is quenched and the device gets back to its idle state, the junction quickly thermalizes with its surroundings and V_{br} subsequently recovers back to its initial value. What we observed in our experiments, however, was that the V_{br} did not recover at all and remained at its last drifted value even days had been elapsed from the last device operation.

On the other hand, the drifted V_{br} did recover once we applied a forward bias voltage to the device (see § 4.4.3). It is well known that the application of a forward bias voltage across a p-n junction leads to charge injection, which is a process that does not decrease the junction temperature if not further increases it. We argue that applying a forward bias voltage to the device releases the trapped charge carriers such that the initial electric field for a given reverse bias voltage is restored with the elimination of the opposing electric field generated by these trapped charge carriers. Therefore, the breakdown voltage walkout did not originate from the localized heating of the junction, but most likely was caused by the charge trapping effects as we explained in § 4.4.3.

Regardless of the underlying mechanism, the breakdown voltage drift should be prevented if a continuous device operation with constant performance metrics is desired. Otherwise,

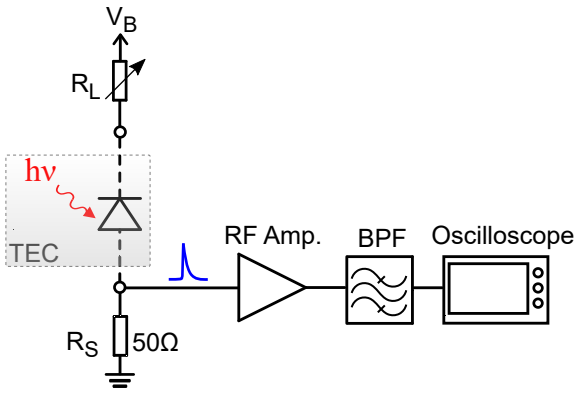

Figure 5.9: Schematic of our passive-quenching circuit with peripheral RF components. This circuit is used to perform avalanche pulse and DCR measurements for the waveguide-integrated SPADs.

the breakdown voltage drift leads to a decay of the excess bias voltage V_E for a fixed reverse bias voltage V_B as $V_E = V_B - V_{br}$. The reduced excess bias voltage V_E results in lower impact ionization probability, and subsequently decreases the avalanche gain G and hence avalanche pulse amplitude which are related by

$$G = \frac{1}{R_s e} \int_0^\infty V_t \, dt, \tag{5.12}$$

where R_s is the sense resistor of the passive-quenching circuit, e is the electron charge, and V_t is the voltage amplitude of the avalanche pulse that is generated across the R_s.

In order to check whether the avalanche pulse amplitudes of our devices decay over time when they are operated with a fixed reverse bias voltage V_B, we connected the output of a representative device to an oscilloscope (LeCroy WaveRunner 204MXi-A 2 GHz Oscilloscope (10 GS/s)) and monitored its avalanche pulses . Even though the oscilloscope could initially trigger on the avalanche pulses, after a few minutes of operation, the avalanche pulse height steadily decreased to a point that the oscilloscope stopped triggering. Therefore, the continuous operation in Geiger mode at a fixed reverse bias voltage was not possible as the performance would not have been predictable. The predictable and stable performance operation requires controlled gating of the applied bias voltage as explained in § 5.3.3.2

5.3.2 Avalanche Pulse Characteristics

Figure 5.9 shows the schematic of our passive-quenching circuit we used during avalanche pulse and DCR measurements. In our experiments, we examined different values for the

load resistor R_L and observed that the load resistors with resistance of less than 100 kΩ were failed to achieve passive quenching. After measuring avalanche pulses with different load resistors, we chose a load resistor R_L with resistance of 1 MΩ as it results in high enough avalanche pulse height with good signal-to-noise ratio.

For the characterization of avalanche pulses, we terminated the device output with the 50 Ω input impedance of the oscilloscope. The avalanche pulses directly obtained from the devices without any signal conditioning have pulse amplitude of around 2 mV with an FWHM pulse width of ≈ 1.5 ns as shown in Fig. 5.10(a).

In order to interface the avalanche pulses with a universal counter (Agilent 53132A), we amplified the avalanche pulses using an RF signal amplifier, and subsequently filtered them using RF filters. Here, we used a 30 dB RF amplifier together with a custom low pass filter and a high pass filter (see Appendix C for details).

Figure 5.10(b) shows the resulting avalanche pulses after amplification and filtering. The pulse amplitude was amplified by 20 times while FWHM pulse width was kept at around 1.5 ns. We note that the amplified pulses were accompanied by spurious signals whose pulse heights occasionally reach 30 mV. The pulse amplitudes of these spurious signals were lower than the trigger voltage $V_{\text{trig.}} = 40$ mV set on the oscilloscope such that they did not cause false counts. The distribution of avalanche pulse amplitudes after amplification and filtering are shown in Fig. 5.10(c). The pulses show an asymmetric distribution skewing towards higher values.

Next, we investigated how avalanche pulse amplitude and noise floor change with the reverse bias voltage V_{B}. Figure 5.11 shows subsequent avalanches that are captured by the oscilloscope operated in its persistence mode. The avalanche pulse amplitude increases with reverse bias voltage V_{B}, though the increase in pulse amplitude is not significant. The noise floor, on the other hand, significantly rises with V_{B}.

In order to use a fixed trigger voltage $V_{\text{trig.}}$ over the entire range of the applicable reverse bias voltages, the trigger voltage $V_{\text{trig.}}$ must be determined such that the oscilloscope is ensured not to trigger on false threshold crossings at none of the applicable reverse bias voltages. Since the probability of such false threshold crossings increases with higher reverse bias voltages due to the increased noise floor (see Fig. 5.11), we determined the trigger voltage $V_{\text{trig.}}$ at the maximum reverse bias voltage that is to be applied to the device. In this way, we ensured that the oscilloscope would not trigger on false threshold crossings over the entire V_{B} sweep range, albeit at a cost of some missed avalanche pulses at lower V_{B} depending on the distribution of pulse amplitudes.

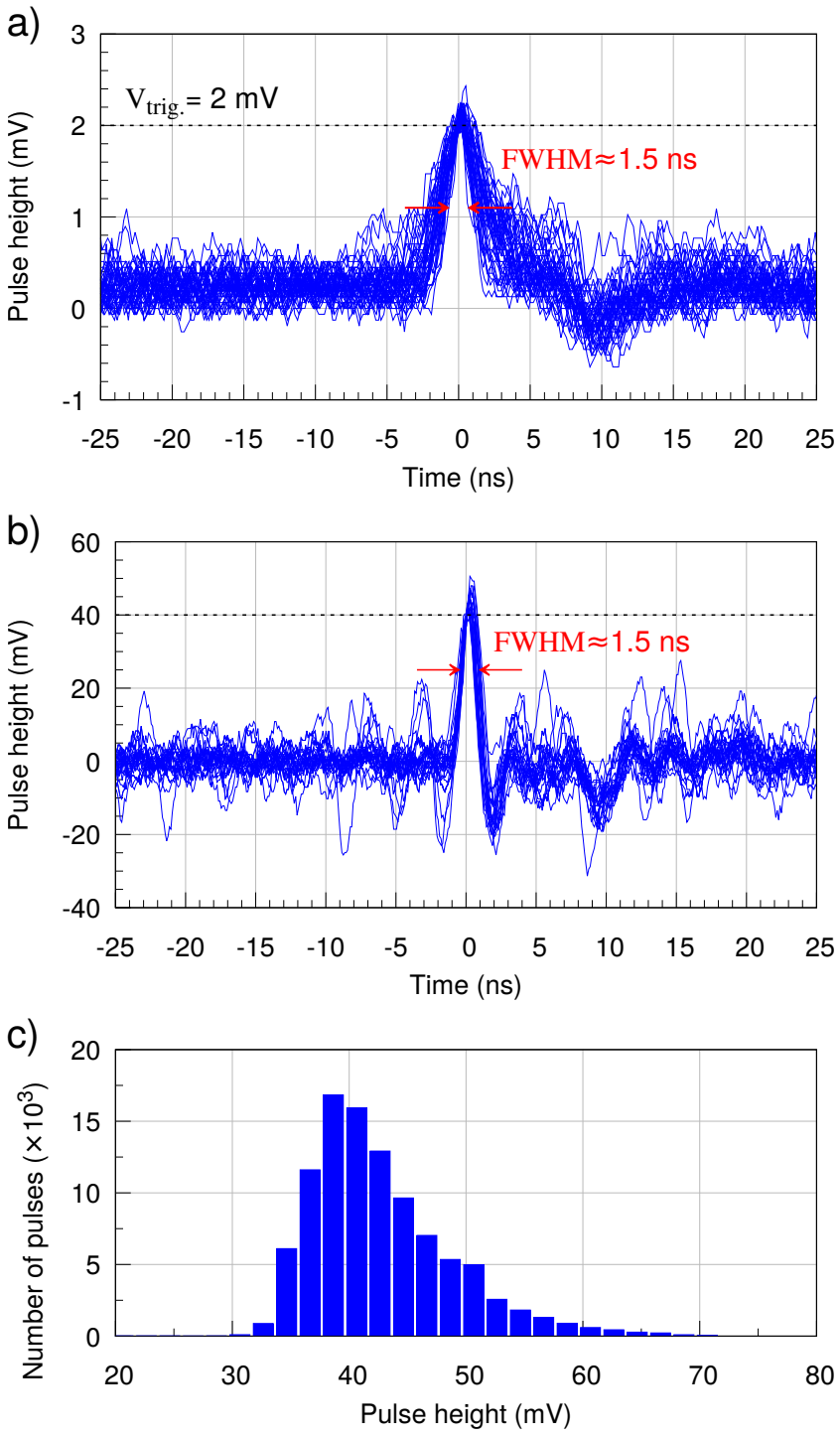

Figure 5.10: The avalanche pulse characteristics. a) The avalanche pulses that are directly obtained across the sense resistor R_S without any amplification or filtering. b) The amplified and filtered avalanche pulses, and c) the distribution of their pulse amplitudes.

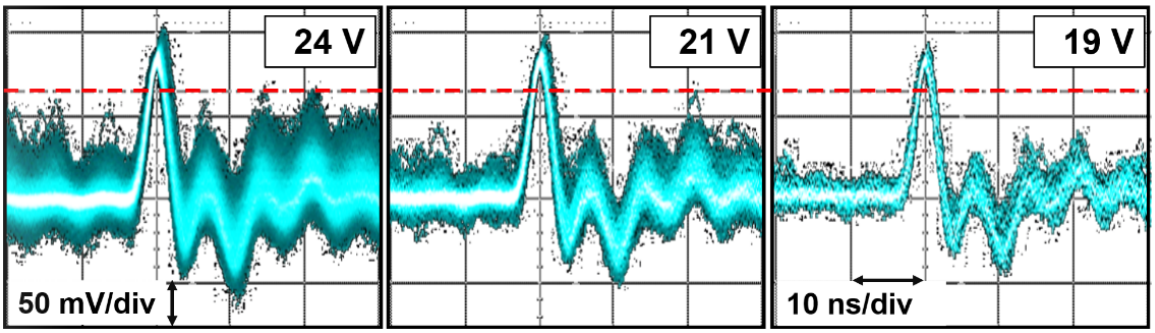

Figure 5.11: Representative plots of avalanche pulses at different V_B captured in persistence mode of the oscilloscope. Brighter regions correspond to higher signal concentrations. The red dashed line shows the trigger level $V_{trig.}$65 mV. The vertical and horizontal grids are 50 mV and 10 ns per division, respectively.

In our experiments, the maximum applicable reverse bias voltage V_B is initially set to be 1.5 times of the breakdown voltage V_{br}. We note that the maximum applicable V_B can vary depending on the noise performance of the device, and it might be necessary to limit the operating voltage to lower values.

5.3.3 Dark Count Rate

In order to measure the dark count rate (DCR), we fed the amplified and filtered avalanche pulses into the universal counter, which can count single-shot pulses up to 225 million counts per second. Specifically, we counted the number of threshold crossings within a specified time interval. Here, we first investigated the temporal behavior of DCR, and then investigated how DCR changes with operating temperature and excess bias voltage.

5.3.3.1 Dark count rate decay

The avalanche pulse amplitude reduction (see § 5.3.1.2)) manifested itself as a decay in the number of counts for a given time interval as shown in Fig. 5.12(a). In order to prevent the dark count rate decay over time, we applied a reset voltage $V_R = -V_B$ (i.e., forward bias polarity) as shown in Fig. 5.12(b). The pulse width of the reset voltage V_R was set to one-ninth of the pulse width of reverse bias voltage V_B. In the actual reset implementation, we used a programmable power supply (Rohde&Schwarz HMP2030) to act as a switch (see Fig. 5.12(c)).

After implementing this reset procedure, we measured the DCR over time at various excess bias voltages V_E at $-10\,^{\circ}$C as shown in Fig. 5.13(a). The use of the reset circuit

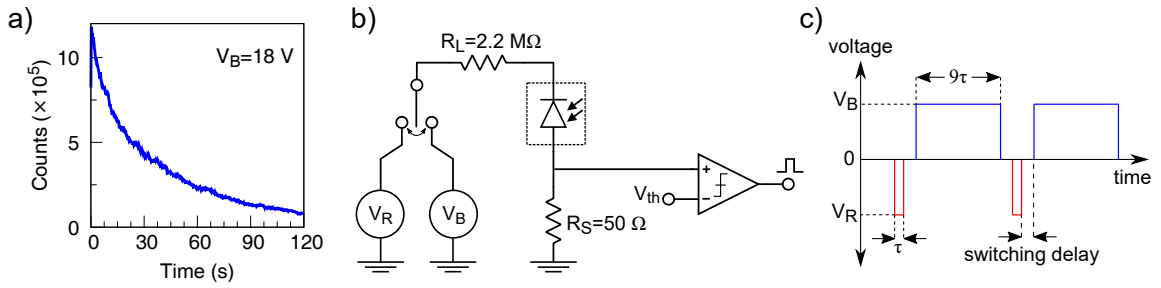

Figure 5.12: DCR decay over time due to V_{br} drift. a) Number of counts shown for a 450 nm wide p-n$^+$ SPAD biased at $V_{\text{B}} = 18$ V. Each data point is obtained with 0.2 seconds integration time. b) The reset circuit to stabilize DCR decay. c) The duty cycle of the bias voltages.

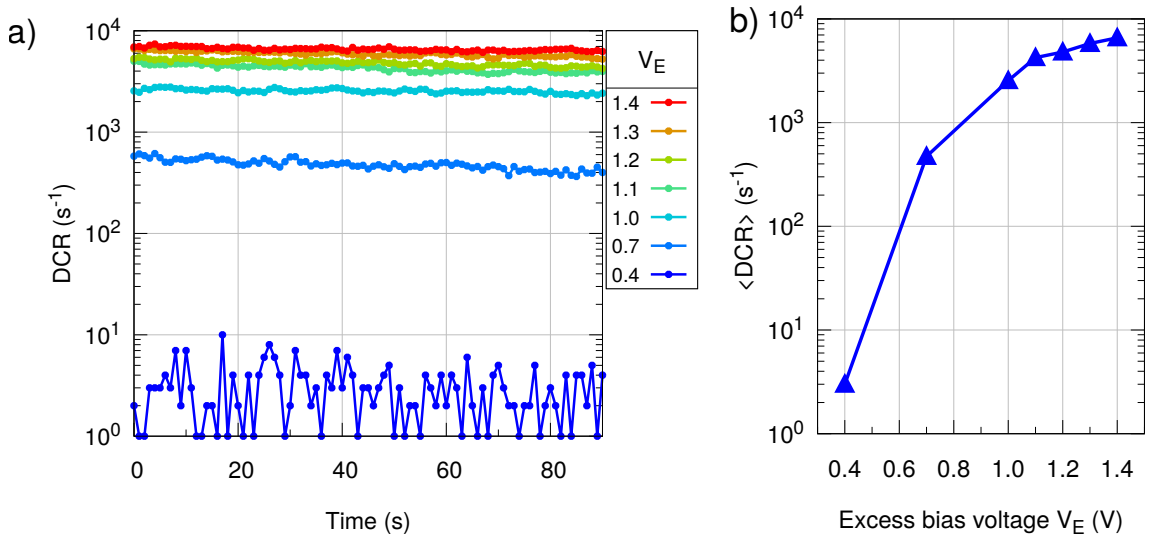

Figure 5.13: Temporal behavior of DCR at various excess bias voltages V_{E} at $-10\,^{\circ}$C. The data is obtained from a representative device that is comprised of a 900-nm-wide and 9-µm-long waveguide. b) The mean DCR values calculated from a).

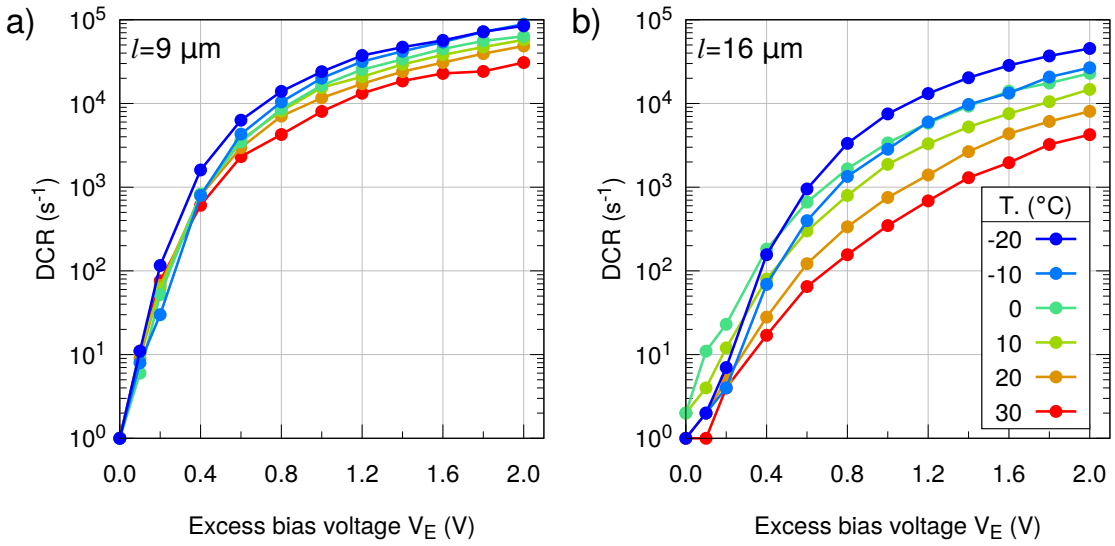

Figure 5.14: Temperature dependence of DCR at various excess bias voltages V_E. The data is shown for representative devices that have 900-nm-wide and a) 9-µm- and b) 16-µm-long waveguides.

reduced the pace of the DCR decay compared to Fig. 5.12(a); nonetheless, the complete stabilization could not be achieved over the time span of our measurements, and further modifications of the reset circuit might be needed for this purpose.

Figure 5.13(b) shows the mean DCR values calculated from Fig. 5.13(a). The dark count rate increases by more than 3 orders of magnitude when the excess bias voltage V_E is increased from 0.4 V to 1.4 V, and it reaches 6 k cps at $V_E = 1.4$ V.

5.3.3.2 Temperature dependence

The SPADs are usually operated at low temperatures in order to reduce the dark pulses originating from thermally-generated charge carriers. Here, we investigated how DCR performance of our devices changes at various operating temperatures. Figure 5.14 shows the DCR measurements for representative devices. The temperature was varied from $-20\,^{\circ}$C to $30\,^{\circ}$C, whereas V_E was increased up to 2 V. Our experimental results show that the dark count rate reduces when the operating temperature is lowered. This is in contrast with our expectations that a reduction in temperatures would lead to lower thermal generation of charge carriers and hence decrease the dark count rate.

Device Saturation

What gives rise to this counter-intuitive trend between DCR and temperature in our measurements is associated with the oversaturation of the device with the very high dark generation rate. Higher temperature does indeed increase the number of thermally generated charge carriers. However, if the generation rate is too high, most of these events occur prior to the full voltage recovery and lead to avalanche pulses with smaller amplitudes (see Eq. 5.9). This smaller avalanche pulses are subsequently missed by the counter as the pulse amplitudes are no longer high enough to exceed the trigger voltage $V_{\text{trig.}}$ set on the instrument.

Similar observations are also reported in the literature for a commercial Geiger-mode APD that is operated at its saturation regime with passive-quenching circuit [260]. The study models the recovery transition of a typical passively quenched Geiger-mode APD with a few high-level parameters. In the model, the combined probability of generating a digital signal (i.e., a count) upon a given charge carrier on the device is given by the joint probability of avalanche triggering probability P_{a} and the probability that an avalanche signal V_{s} is sensed by a comparator with a threshold voltage V_{th}. Since the voltage recovery transition of such devices are well known, and P_{a} and V_{s} can be modeled in terms of the excess bias voltage V_{E}, the observed behavior of such devices, even when they are operated deep into their saturation regimes, can be successfully modelled.

To verify our hypothesis that the increased number of thermal charge carriers at higher temperatures reduces the observed event rate as outlined in [260], we performed a numerical study to simulate the avalanche quenching and voltage recovery transitions for a device with typical device parameters. In our simulations, we assume that the SPAD has a series resistance R_{d} of 1 kΩ and a diode capacitance C_{d} of 10 fF. The parasitic stray capacitance C_{s} is assumed to be 1 pF, and the device is passively quenched with a load resistance R_{L} of 2.2 MΩ. The trigger voltage $V_{\text{trig.}}$ is set to 70% of the excess bias voltage V_{E}. Lastly, the latching current and breakdown voltage are assumed to be 100 µA and 16 V, respectively.

Once the avalanche current is quenched, the voltage across the diode V_{d} recovers to its initial value by [3]

$$V_{\text{d}}(t) = V_{\text{q}} + V_{\text{E}} \times (1 - \frac{e^{-(t-t_{\text{event}})}}{\tau_{\text{r}}}), \tag{5.13}$$

where V_{q} is the diode voltage when the diode current equals to the latching current (see Eq. 5.5), t_{event} is the timing of an avalanche breakdown event, and τ_{r} is the voltage recovery time constant (see Eq. 5.7).

In our simulations, we first set a mean event rate, and then determined the simulated event rate according to Poisson distribution. We assigned random timings to each of the events

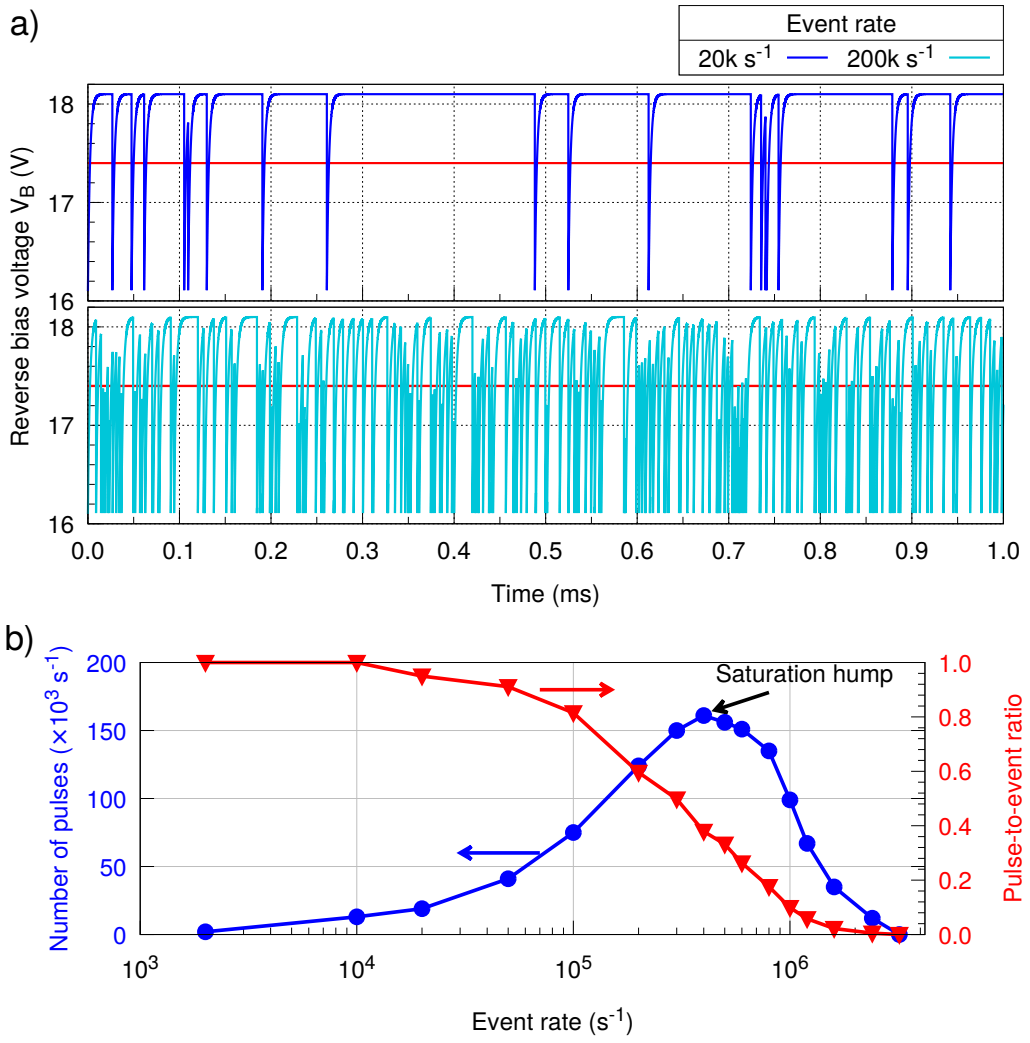

Figure 5.15: Simulation study to demonstrate device saturation under high event rates. Here, the diode voltage of a representative device is shown under different event rates. The red line denotes the detection threshold voltage. b) Simulated number of detected events, i.e., pulses, and pulse-to-event ratio at different event rates.

within a given time interval. The cathode voltage of the SPAD is calculated via capacitive discharging and charging equations during quenching and voltage recovery transitions, respectively. If the cathode voltage exceeds $V_{\text{trig.}}$, then the corresponding event results in a detection event, generating an output pulse. On the other hand, if the pulse amplitude fails to exceed $V_{\text{trig.}}$, then this event is not detected.

Figure 5.15 shows the cathode voltage of the simulated device with respect to time. At low event rates, most events occur after the device has fully restored its reverse bias voltage as shown in Fig. 5.15(a). At high event rates, however, most events occur during voltage recovery transitions as shown in Fig. 5.15(b) and lead to smaller pulse amplitudes that cannot be detected. As the event rate gets even higher, the device enters the heavy-saturation regime, where the reverse bias voltage cannot be recovered at all. At prohibitively high event rates, this eventually leads to no detected pulses and the effective duty cycle of the device becomes zero [260]. Such an extended dead time means the *paralysis* of the device [261], which we also confirmed by shining bright light onto one of the samples and getting zero counts in return.

This simulation study explains the trend between measured dark count rate and temperature. In our experimental results shown in Fig. 5.14, reducing the device temperature decreased the thermal generation rate of charge carriers. Consequently, there were less small-pulse events during voltage recovery transition, and the devices could recover their excess bias voltages to a larger extent such that the avalanche pulses with amplitudes exceeding the trigger voltage $V_{\text{trig.}}$ could be generated. Referring to Fig. 5.15(c), this trend corresponds to approaching the saturation hump from the high event rate region.

We note that the device saturation rendered the photon detection efficiency measurements inapplicable. Further reduction of the temperature may help to reduce thermal generation rate of charge carriers to a point that the measured dark count rate starts to decrease with lower temperature; in other words, the device may pass the saturation hump.

5.4 Experiment: Asymmetric Rib Waveguide p-i-n APDs

Here, we report the experimental results on characterization of p-i-n^+ junction-based devices in Geiger-mode operation. Similar to the devices introduced in § 2.4, the devices characterized here also utilize an asymmetric rib waveguide that is 250 nm thick with 70 nm etch depth. The doping profile of the device is shown in Fig. 2.15(b).

Here, we investigate the effect of intrinsic region width ΔW on breakdown voltage and dark count rate performance at different operating conditions such as excess bias voltage and

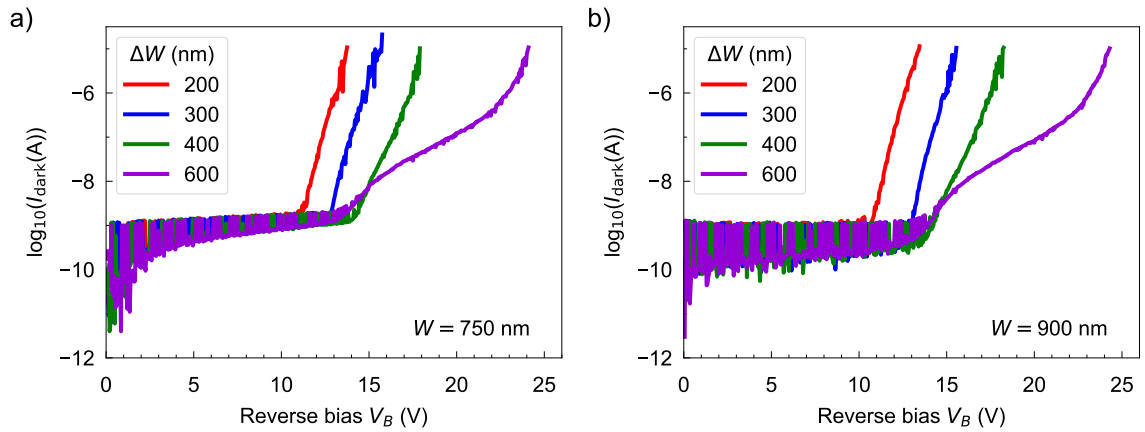

Figure 5.16: Current vs. voltage measurements to identify the breakdown voltage V_{br} of p-i-n$^+$ junction-based devices with rib waveguide width W of a) 750 nm and b) 900 nm. Each trace belongs to a device with different intrinsic region width ΔW.

temperature. Specifically, we investigated how utilizing an intrinsic region between p- and n$^+$-doped regions in an asymmetric rib waveguide structure helps to prevent oversaturation of the devices. We gratefully acknowledge Prithvi Gundlapalli, who is a member of our research group, for his assistance in acquiring measurement data presented in this section.

5.4.1 Breakdown Voltage

Figure 5.16 shows the current-voltage measurements of p-i-n$^+$ junction-based devices that have different intrinsic region widths ΔW. The breakdown voltage V_{br} is identified as the voltage at which the device current reaches to a current threshold level of 10 µA. The breakdown voltage V_{br} increases with larger depletion region width W: it is around 13.5 V for 200-nm-wide intrinsic region and increases up to 24.5 V for an intrinsic region width of 600 nm. The experimental results agree well with our simulation results presented in § 2.4.6.1. For instance, the simulated and measured breakdown voltage of a p-i-n$^+$ junction-based device that has 300-nm-wide intrinsic region are both around 16 V.

5.4.2 Dark Count Rate

The dark count rate of the devices is characterized similarly to those of p-n$^+$ junction-based devices. We note that the distribution of avalanche pulse amplitudes as well as the trigger level set on the pulse counter significantly affect the absolute values of count rates; small changes in the pulse heights significantly affect the number of counts obtained. This makes it challenging to directly compare the absolute values of DCR between different devices.

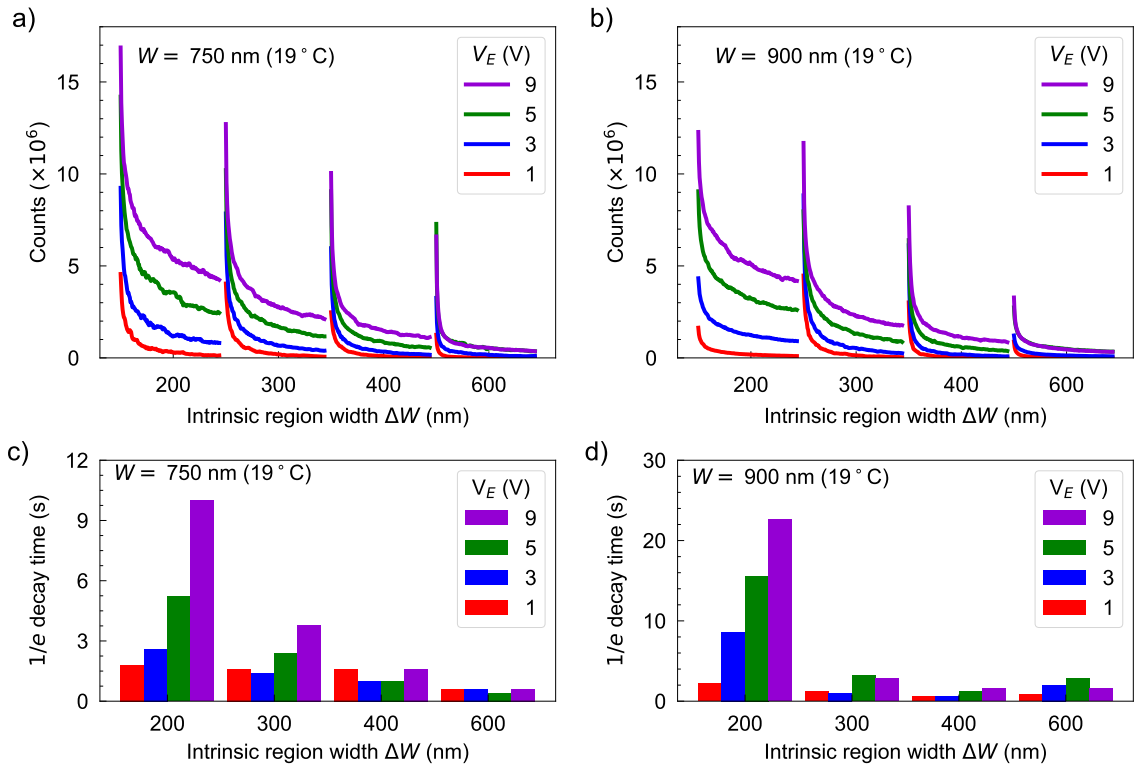

Figure 5.17: Dark count rate of p-i-n$^+$ junction-based APDs at different bias voltages. Dark count rate data is shown at various excess bias voltages V_E for p-i-n$^+$ devices with different intrinsic region width ΔW at 19 °C. The devices consist of a) 750-nm-wide and b) 900-nm-wide rib waveguides. Each trace corresponds to 30-seconds long sampling interval and each data point is obtained by integrating counts over 0.2 s. c) and d) shows 1/e decay times of count rates extracted from a) and b), respectively.

However, the comparison of how DCR changes with different operating conditions is still applicable because what is compared here is not the absolute values of count rates but the qualitative trend of the DCR change, which is independent of the pulse height and the trigger level used during a characterization. Here, we share the experimental data on how dark count rate of p-i-n$^+$ junction-based devices change with excess bias voltage V_E and operating temperature T, and thereafter compare the measurement results with that of p-n$^+$ counterparts.

Figure 5.17 shows how the dark count rate of p-i-n$^+$ junction-based APDs with different intrinsic region width ΔW changes with the excess bias voltage V_E. The dark count rates generally increase with higher excess bias voltage V_E because of more dark carriers generated at high electric field strengths. In general, a wider intrinsic region reduces the count rate for a given operation condition. This agrees well with our earlier simulations that a wider intrinsic

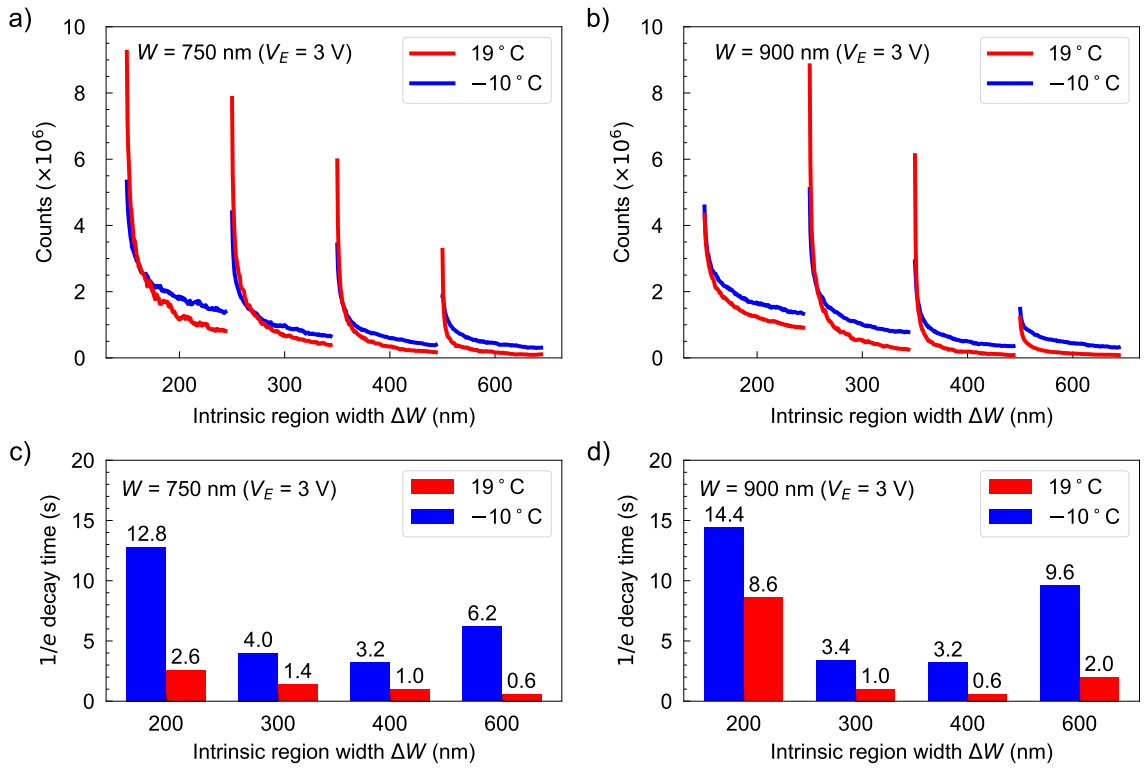

Figure 5.18: Dark count rate of p-i-n$^+$ junction-based APDs at different temperatures. Dark count rate vs. temperature T for $^+$ devices with different intrinsic region width ΔW at 3 V of excess bias voltage V_E. The devices consist of a) 750 nm and b) 900 nm wide rib waveguides. Each trace corresponds to 30-seconds long sampling interval and each data point is obtained by integrating counts over 0.2 s. c) and d) shows 1/e decay times of count rates extracted from a) and b), respectively.

region diminishes the peak electric field strength, which in turn, lowers the dark carriers generated by band-to-band tunneling and trap-assisted-tunneling mechanisms (see § 2.4.6.2).

In order to quantify how fast the count rates decay, we calculated the time durations during which the count rates decay from their initial values to $1/e$ times of those values (i.e., $\sim$36.7%), where e is the Euler's number. Figure 5.17(c) and 5.17(d) show that $1/e$ decay time, in general, increases with higher excess bias voltage V_E.

Next, we investigated how the dark count rate is influenced by the operating temperature T. Figure 5.18 shows our experimental results on dark count rate vs. temperature at the excess bias voltage V_E of 3 V. Reducing the operating temperature from 19 °C to −10 °C, in general, decreases the dark count rate. This is in contrast with the behavior observed in p-n$^+$ junction-based APDs where the dark count rate *increases* when the temperature is reduced because of the oversaturation effect (see § 5.3.3.2). Therefore, the asymmetric rib

waveguide geometry with p-i-n^+ doping profile indicates an improvement to prevent device oversaturation with excessive dark carrier generation.

Figure 5.18(c) and 5.18(c) show the calculated $1/e$ decays times of the count rates. The $1/e$ decay times of all the devices are higher at $-10\,^{\circ}$C compared to $19\,^{\circ}$C. One likely explanation is that the charge carrier trapping and subsequent breakdown voltage drift become more significant at higher operating temperatures since there would be more thermally-generated charge carriers that get captured at the interface trap levels. This subsequently would accelerate the weakening of the electric field inside the depletion region for a fixed reverse bias voltage, and hence the dark count rate would decay due to reduced avalanche triggering probability. The count rate decay time might also be affected from the local heating effects in the junction since such local heating effects modify the avalanche triggering probability as well and hence can modify the decay dynamics. Figure 5.18 shows that lower operating temperature T improves the stability of count rates, regardless of rib waveguide width W and intrinsic region width ΔW.

We note that p-i-n^+ junction-based devices have yet to attain dark count values that we predicted in our earlier simulation studies (see 2.4). This is most likely due to the charge trapping effects inside the oxide/silicon interface, whose secondary effects were observed as the breakdown voltage walkout and the dark count rate decay. Nonetheless, our new device design based on p-i-n^+ junction profile in an asymmetric rib waveguide structure, unlike their p-n^+ counterparts, mitigates the oversaturation of the devices.

5.4.2.1 Discussion: improving device performance

The device performance can further be improved by preventing the charge carrier injection and subsequent trapping at the interface. Different oxide deposition techniques and etching methods during the formation of the silicon rib waveguides may help to reduce the number of trap centers at the oxide/silicon interface. Annealing methods such as high-temperature forming gas anneal can also be explored to improve the oxide/silicon interface quality by lowering both the interface state density and the interface charges.

From the device design point of view, eliminating the silicon rib waveguide completely by zero etch depth and coupling the light from the silicon nitride input waveguide to directly into the resulting silicon slab may be beneficial to improve device performance as it eliminates possible charge carrier injection into the rib waveguide interface of the previous design. However, the trade-off would be that the spatial profile of the light inside the silicon slab would not be confined and hence well defined; therefore, the timing jitter performance would be degraded. The horizonal junction designs such as those introduced in § 2.4.1.1 might also

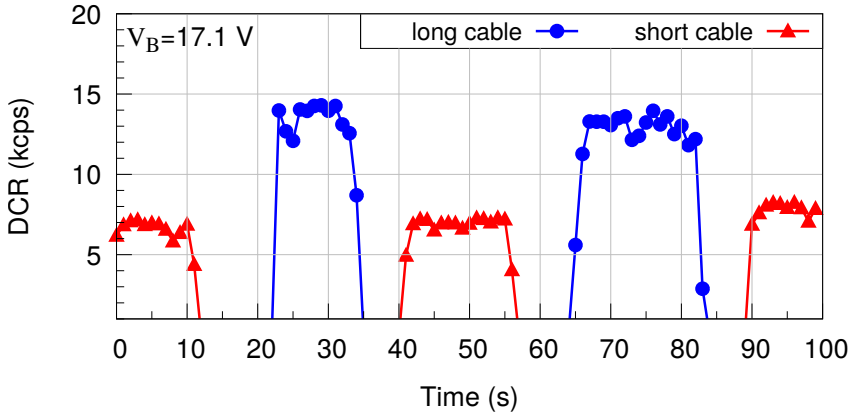

Figure 5.19: Dark count rate of p-n^+ junction-based device operated in 0 °C at V_B=17.1 V. The regions without data points correspond to the time intervals during which we change between short and long electrical connections. The length difference between cables is 5 meters.

improve the noise performance, albeit at the cost of small depletion region widths due to wafer thickness limitations. We note that thicker silicon wafers are commercially available and may be utilized to increase the depletion region thickness; however, an attention must be paid for the mechanical stress associated by such thick waveguide layers. Using field plates or guard ring structures at the proximity of the oxide/silicon interface can also be investigated to reduce the electric field strengths in such regions for the mitigation of premature edge breakdown and hot carrier injection.

In addition to these suggestions pertaining to the device design and fabrication improvements, the device saturation can also be prevented by improving the operating conditions. One such way would be to reduce the operating temperature even further to decrease the thermal generation of dark carriers. In addition, different quenching circuit types can also lead to better noise and saturation performance. Here, we describe our efforts to reduce parasitic capacitance and voltage recovery time by wire bonding devices and using passive-quenching active-reset circuit, respectively.

Wire bonding

A long electrical connection between the device cathode and electrical ground increases the parasitic capacitance. A higher capacitance increases the total charge in an avalanche pulse (see Eq. 5.6), and subsequently leads to more secondary dark count events. Here, we performed a simple experiment to gain more insight and checked if a longer electrical connection does indeed increase the measured count rates of the devices. Figure 5.19

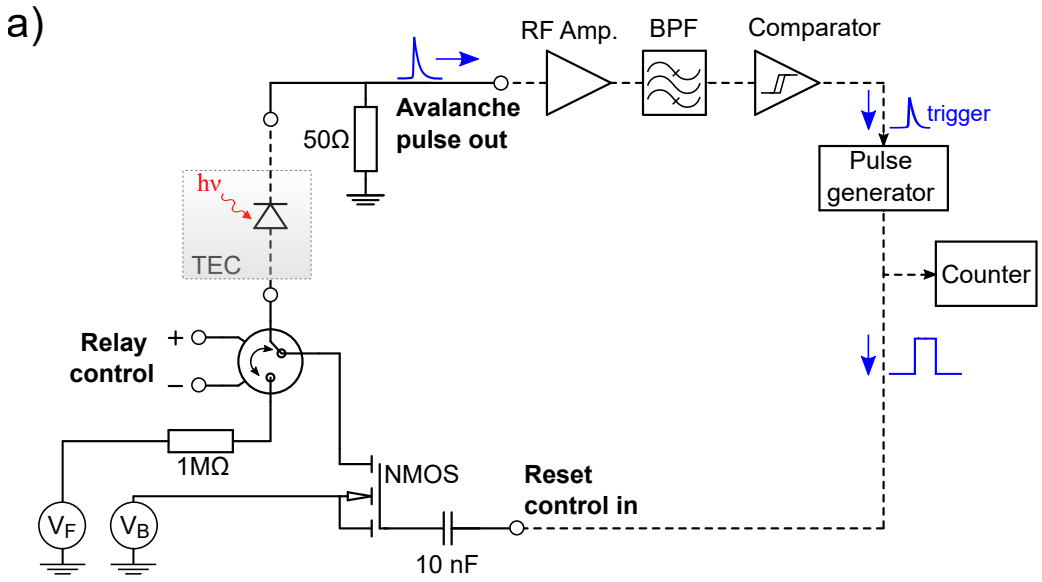

Figure 5.20: Schematic of the passive-quenching active-reset circuit.

shows the measurement results of the dark count rate for different electrical cable lengths between the device and the load resistor. The count rate clearly increases when the electrical connection is extended by 5 m.

Wirebonding devices may help to minimize such parasitic capacitance as it decreases the length of the electrical connection between a device and its quenching circuit. The design of our custom electronics board that accommodates wire bonded devices on a ceramic chip package with compatibility for light coupling from the edge is provided in Appendix C.

Passive-quenching active-reset circuit

Alternatively, the device saturation can be overcome by increasing the saturation threshold using a passive-quenching active-reset (PQAR) circuit. Compared to the slow recovery of a passive reset transition (see Eq. 5.1.2.1), such circuits can be used to achieve faster voltage recovery, and subsequently reduce the number of small pulse events. Figure 5.20 shows the schematic of our custom PQAR circuit, and the photographs of the implemented circuit are provided in Appendix C.

Here, we describe the operation of this circuit. The bias voltage applied to the device is controlled via a 1-form-C optocoupler relay (IXYS LCC120) configured as a single pole double throw switch. Controlled by the relay control signal, this part applies a forward bias voltage V_F to reset the breakdown voltage V_{br} that is drifted before reverse biasing the device with V_B (see § 5.3.3.1).

The avalanche current is passively quenched by the very large drain source resistance $R_{\mathrm{DS(off)}}$ of the n-MOSFET. The avalanche pulse is subsequently amplified and filtered before it is converted to a standard output pulse via a comparator. The output of the comparator is connected to a pulse generator which, upon triggering, provides an output pulse that is subsequently registered on a counter.

After a predefined time delay, the pulse generator outputs another pulse with a well-defined pulse width and amplitude. This second pulse is used as a feedback signal for active reset of the device. By switching the transistor on, the equivalent resistance of the electrical path of the avalanche current which charges the capacitances during voltage recovery transition decreases from R_{L}=1 MΩ to the equivalent resistance of the two resistors R_{L} and $R_{\mathrm{DS(on)}}$ connected in parallel. Since $R_{\mathrm{DS(on)}}$ of the n-MOSFET is very low compared to R_{L}[5], the equivalent resistance is effectively determined by $R_{\mathrm{DS(on)}}$. Consequently, the voltage recovery time constant τ_{r} decreases by a factor of $\sim R_{\mathrm{L}}/R_{\mathrm{DS(on)}}$ (see Eq. 5.7), and a faster voltage recovery can be achieved.

We note that the use of a PQAR circuit does not bring any advantage on improving the DCR performance compared to a passive-quenching circuit as it does not change the rate of dark carrier generation; nonetheless, this circuit can be used to measure the dark count rate without saturation effects as the dead time of the device can be significantly reduced.

5.5 Conclusion

In this chapter, we present the characterization results of our silicon waveguide-integrated APDs in Geiger-mode operation. We built a custom light-tight low-temperature probe station that is suitable for the characterization of bare dies of APD, and we developed necessary quenching and pulse conditioning electronics. We first verified the operation of our electronics and measurement testbed by characterizing a commercial APD in Geiger mode and comparing our results with prior studies. Next, we characterized our devices by measuring their breakdown voltage, avalanche pulse characteristics, and dark count rates. The dark count rate vs. temperature measurements clearly showed that APDs based on symmetric rib waveguides with p-n^+ junction profiles are oversaturated with very high dark carrier generation. On the other hand, we did not observe such oversaturation effects in general for the devices that have asymmetric rib waveguide structure with p-i-n^+ junction profile. Therefore, utilizing an asymmetric rib waveguide structure and incorporating an

[5]It is 50 mΩ for the Vishay SI4539ADY n-MOSFET we used here.

intrinsic region between p- and n-$^+$-doped regions to limit the peak electric field strength inside the depletion region improve the noise performance of the devices.

We note that our experimental results on device characterization show higher dark count rates than the simulated ones. This is most likely due to the material imperfections, especially at the oxide/silicon interface. We provided an in-depth analysis of the mechanism underlying the device saturation and suggested possible strategies for further research to mitigate this effect. The experimental results presented here provide insights on how device performance could further be improved to achieve on-chip single-photon sensitivity.

Part II

Single Photon Manipulations by Coherent Perfect Absorption

The achievement of on-chip single photon detection at visible wavelengths is an important pillar for our PIC concept introduced in Chapter 1. Targeting on-chip linear optical quantum computing (LOQC) applications with on-chip readout capability, the other key ingredient of our platform consists of interferometers with increased functionalities for single photon manipulation. Compared to a conventional MZI intensity modulator which redistributes light between its two output ports, interferometric modulator systems based on novel coherent perfect absorption (CPA) phenomenon allow for deterministic prevention of light propagation through coherent interactions with light. This is particularly useful for complex optical networks consisting of numerous cascaded interferometers, where residual photon propagation into other network arms could cause undesired interference or crosstalk if not prevented. Moreover, CPA interferometers can also be used to filter quantum states of light in an interferometric setup.

On the road towards an integrated CPA interferometer, we test our single photon manipulation concepts in a prototype platform comprising of an optical fiber interferometer with a CPA capability. Whether it is implemented in a photonic chip or in optical fiber, any interferometer is prone to phase noise, which must be eliminated to protect quantum coherence. The stabilization of interferometers while protecting the efficiency of quantum channels is of paramount importance for LOQC applications.

In Chapter 6, we introduce an active phase stabilization scheme for coherent optical networks operating at the single-photon level. Our method is based on single-photon counting, and it does not introduce any additional components for phase stabilization as conventional approaches do. Acquiring the phase information from single photon counts sampled directly from the quantum channel, the method prevents possible degradation of the quantum signal due to the introduction of other components into the quantum channel.

Chapter 7 presents experimental results where we demonstrated coherent perfect absorption at the single-photon level by using a plasmonic metamaterial in a phase-stabilized optical network. The coherent control of single-photon absorption probability allows us to demonstrate all-optical single-photon switching with high visibility.

In Chapter 8, we extended the application realm of the CPA interferometer. Using different optical responses of the coherent perfect absorber to symmetric and antisymmetric superpositions of input states, we showed that the CPA phenomenon can be used to filter quantum states of photons whose quantum information is encoded in superposition of spatial wave functions. This work might find use cases in quantum information processing such as dual-rail encoding protocols.

Our phase stabilization method enables us to perform successful single photon manipulation experiments in an interferometric setup containing coherent perfect absorbers. These demonstrations prove the applicability of our concepts and motivate their implementation in our hybrid quantum photonic platform. Merging integrated single-photon detectors with on-chip modulators equipped with added functionalities opens up new opportunities towards on-chip LOQC applications.

Chapter 6

Phase Stabilization of Coherent Networks by Single-photon Counting

6.1 Introduction

Coherent optical fiber networks provide an easily accessible testbed to verify photonic network concepts prior to their implementation in photonic chips. Leveraging on advanced telecommunication technologies, optical fiber networks are also indispensable for long-haul quantum light processing and quantum communication systems. Single-photon interference [6, 7], quantum computation based on dual-rail qubit encoding [89, 90], quantum key distribution [91, 92], entanglement swapping and distribution [92, 93], and high-dimensional quantum state transmission [94] have already been demonstrated in fiber environment proving the feasibility of fiber-based quantum optics.

Such demonstrations extensively use interferometers which are locked to specific phase offsets for minutes or even hours during their operation. To deal with the phase noise, these experiments usually employ resource demanding stabilization systems to set the required phase offset and to achieve long-term phase stability [6–8]. Most phase stabilization techniques use an additional classical control signal that is brighter than the quantum signal. When a quantum channel and a classical channel are combined into an interferometer, the bright control signal in the classical channel must be efficiently isolated from the quantum channel. The reason is that even small amounts of photons, which can be induced by Rayleigh and Raman light scattering in the classical channel, may lead to crosstalk and eventually degrade the quality of the quantum signal [262]. Efficient isolation of the control signal, however, is challenging and requires elaborate demultiplexing techniques with additional components.

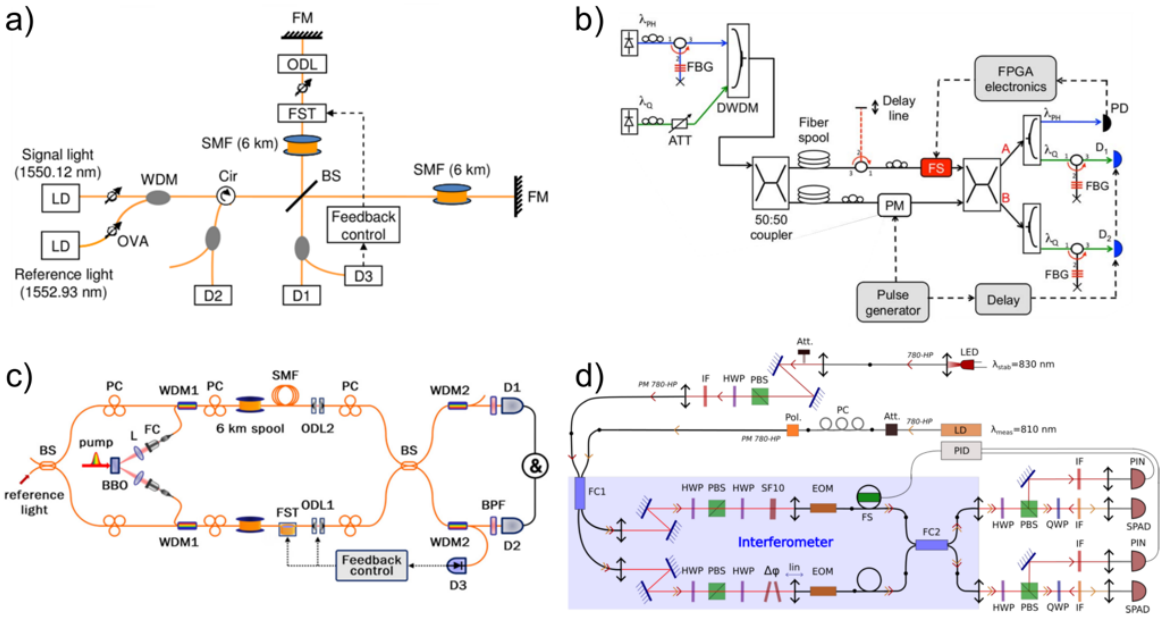

Figure 6.1: Examples of conventional phase stabilization schemes for fiber interferometers operating at the single-photon level. All these setups use an auxiliary light source, multiplexers, and additional photodetectors for phase stabilization, and they utilize demultiplexers to achieve good isolation between classical and quantum channels. The images of a, b, c, and d are from [6], [7], [8], and [9], respectively.

Figure 6.1 shows various conventional active phase stabilization schemes that are developed for fiber interferometers operating at the single-photon level. A common to all is to use an auxiliary laser signal, various (de)multiplexers, associated optical components, and additional photodetectors. The addition of these (de)multiplexers increases losses on the quantum channel due to added insertion losses, and it must be minimized especially for loss-sensitive networks.

In this chapter, we first propose a simple yet powerful technique for phase stabilization by single-photon counting. Next, we show the applicability of our method by implementing it in an optical network represented by a Mach-Zehnder interferometer (MZI). Our technique suppresses the phase noise with a phase stability that is comparable to that of conventional phase stabilization schemes. Moreover, it obviates the need for using a bright auxiliary laser with additional optical components required in conventional approaches, and hence it potentially increases the efficiency of the quantum channels.

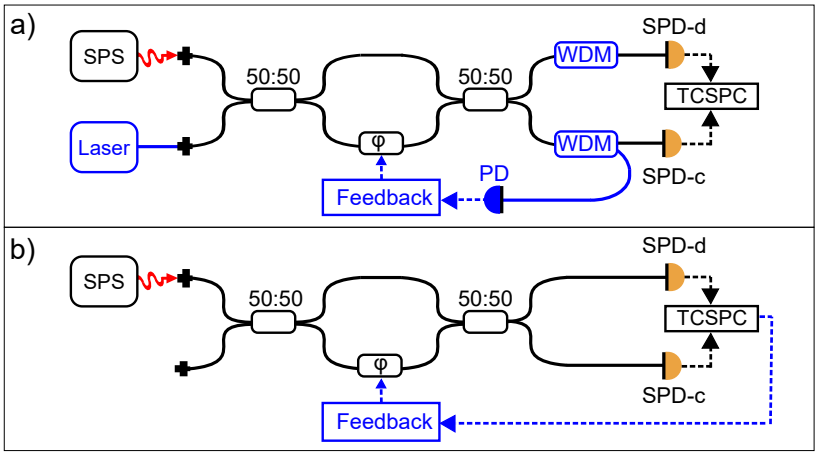

Figure 6.2: Stabilization of coherent optical fiber networks operating at the single-photon level. a) A Mach-Zehnder interferometer consisting of a single-photon source (SPS), 50:50 beamsplitters, and a phase modulator ϕ as an example network. In conventional stabilization schemes (highlighted in blue), a laser light sent through the coherent network is separated by a multiplexer (e.g., wavelength division multiplexer WDM) and measured by a photodetector PD. b) An optical fiber network stabilized by single-photon counting.

6.2 Phase Stabilization Method

6.2.1 Concept

The extreme sensitivity of optical fiber networks to thermal, mechanical, and acoustic noise [263] strongly affects the measurement of quantum light. One way to overcome this problem is to use a feedback loop for an active phase stabilization. The conventional approaches use a bright auxiliary laser with a distinct degree of freedom (e.g., wavelength, polarization, or temporal mode) probing the same optical path traversed by the quantum light [6–8]. Figure 6.2(a) shows an in-fiber Mach-Zehnder interferometer (MZI) operating at the single-photon level. The MZI consists of 50:50 beamsplitters and a phase modulator backbone together with an auxiliary phase stabilization loop. Phase fluctuations affect the intensity distribution of light detected at the MZI output ports. To compensate this effect, the intensity of the auxiliary laser beam traversing the same optical path is subsequently used to generate a feedback signal sent to the phase modulator. The dedicated multiplexers (e.g., wavelength division multiplexers, dichroic mirrors, and polarizers), filters, and photodetectors are used to isolate the feedback signal from the quantum channel. However, this subsequently degrades the quality of the quantum signal due to added insertion losses and nonideal isolation between channels.

Alternatively, single-photons themselves can be used to accomplish the same task (see Fig. 6.2(b)). In the single-photon regime, the photon wave function acquires different phases while passing through the different arms of the interferometer such that the photon distribution at the output ports is modified. The very same output of the single-photon detectors (SPDs) can be used to generate a feedback signal based on the expected photon count rate. The experiment can subsequently be performed within a time window that is shorter than the characteristic time of the phase fluctuation. The costs for this simplicity compared to conventional stabilization schemes based on auxiliary components are: (i) lower frequency of operation as single-photon counting requires comparatively long integration time, (ii) gated mode of operation since experimental measurements are interleaved with stabilization periods.

In our experimental setup shown in Fig. 6.2(b), the photon wave function is split after the first beamsplitter into a superposition of two spatial modes, corresponding to the upper and lower interferometer arm. Here, each arm is composed of $\sim$15 meters of polarization-maintaining single-mode optical fiber. The probabilities to a detect a single photon at output ports C and D depend on the phase delay ϕ between the two optical paths due to interference on the second beamsplitter. The corresponding detection probabilities p_{c} and p_{d} are equal to [141]

$$\begin{aligned} p_{\mathrm{c}}(\phi) &= (1+\sin(\phi))/2, \\ p_{\mathrm{d}}(\phi) &= (1-\sin(\phi))/2. \end{aligned} \tag{6.1}$$

To estimate these probabilities, the number of SPD counts N_{c} and N_{d} should be measured during a time interval Δt which is smaller than the characteristic time of the phase noise. Assuming N photons impinge on the second lossless beamsplitter during the time interval Δt, and single-photon detectors have unity photon detection efficiency, the numbers of counts are read as

$$\begin{aligned} N_{\mathrm{c}}(\phi) &= N \cdot p_{\mathrm{c}}(\phi), \\ N_{\mathrm{d}}(\phi) &= N \cdot p_{\mathrm{d}}(\phi). \end{aligned} \tag{6.2}$$

The most likely reasons for the phase noise in our experiments were thermal fluctuations affecting optical fibers [264] and electronic noise associated with single-photon counting unit [265]. The noise spectral density shown in Fig. 6.3 decreases by $1/f^{2.9}$ until 1 Hz and reaches a noise floor. Since the noise is present on a scale of $\Delta f_{\mathrm{N}} \approx$1 Hz without significant contributions above this frequency, we set the single-photon detector integration time window Δt to 24 ms such that $\Delta t \ll 1/\Delta f_{\mathrm{N}}$.

The phase delay ϕ is the only parameter that determines the detected photon numbers N_{c} and N_{d} in Eq. 6.2; therefore, we may monitor the phase stability of the network by measuring

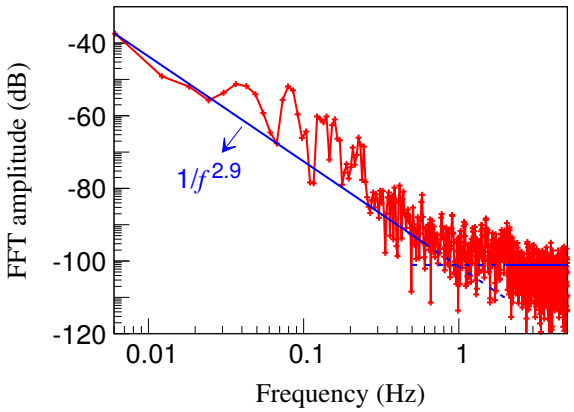

Figure 6.3: a) Noise spectral density of phase fluctuations of the unstabilized system, measured by sending a CW-laser of μW power through the same interferometer. The noise spectral density decreases by $1/f^{2.9}$ until 1 Hz before it reaches a noise floor.

single-photon detector counts variations. After scanning the phase to set N_c at approximately $N/2$ level, we start the stabilization procedure to keep N_c at the same level. If no significant phase fluctuations are present during Δt, then N_c does not change (more precisely, number of detected photons would be within the Poisson distribution centered at $N/2$, considering the random nature of the laser source), and no action is required. Conversely, if the noise causes significant phase fluctuations during Δt, and the difference $\Delta N = N_c - N/2$ becomes noticeable, then a feedback voltage proportional to $-\Delta N$ is generated to offset the phase modulator driving voltage and compensate for the fluctuations.

6.2.2 Development

Here, we introduce the implementation details of our digital feedback controller.

6.2.2.1 Working principle

Figure 6.4(a) shows the block diagram of the negative feedback loop of our active phase stabilization method. Here, the error signal ΔN is obtained by

$$\Delta N = \left| N_{sp} - N_{pv} \right|, \tag{6.3}$$

where N_{sp} is the set point at which we stabilize the network, and N_{pv} is the sampled SPD counts denoting the process variable of the feedback loop. We set $N_{sp} = N/2$ and generate a feedback voltage ΔV to offset the phase fluctuations if

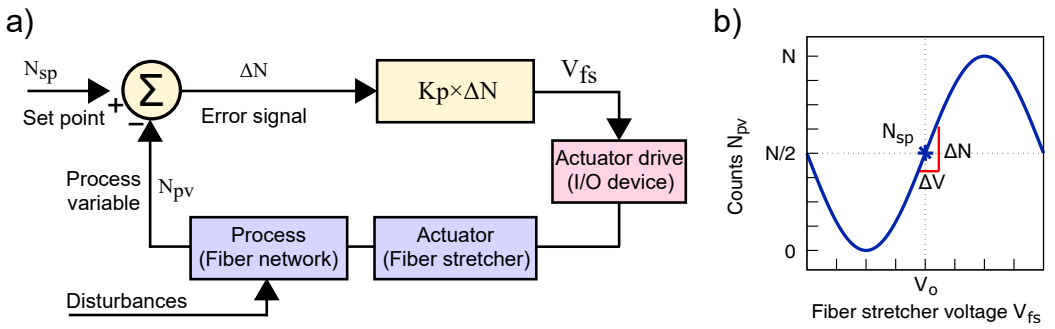

Figure 6.4: Feedback loop for active phase stabilization. a) The block diagram of the setup. b) A representative plot showing counts N_{pv} vs. fiber stretcher voltage V_{fs}. We set N_{sp} to $N/2$. The proportional gain K_p of the controller is equal to the reciprocal of the first derivative of N_{pv} vs V_{fs} curve at N_{sp}.

$$|\Delta N| - \sqrt{N_{\mathrm{sp}}} > 0, \tag{6.4}$$

where $\sqrt{N_{\mathrm{sp}}}$ is the photon shot noise centered at N_{sp}. A proportional controller generates ΔV according to

$$\Delta V = K_p \times \Delta N, \tag{6.5}$$

where K_p denotes the proportional gain of the controller. ΔV is added onto to the previously applied V_{fs} to compensate the phase fluctuation such that

$$V_{\mathrm{fs}}{}' = V_{\mathrm{fs}} - \Delta V. \tag{6.6}$$

Next, we describe how we determine the proportional gain K_p. In our interferometric setup, the number of detected counts $N_{\mathrm{pv}}(\phi)$ is a sinusoidal function of the phase difference $\Delta\phi$ between the interferometer arms (see Eqs. 6.1 and 6.2). The phase delay ϕ is linearly dependent on the relative optical path length (OPL) displacement Δl between interferometer arms

$$\Delta\phi = \Delta l/\lambda, \tag{6.7}$$

where λ is the photon wavelength inside the optical fiber. The OPL displacement Δl is controlled by a fiber stretcher that has a linear OPL displacement response of around $0.2\,\mu\mathrm{m}/V$ in our modulation frequency range. Therefore, the number of detected counts is a sinusoidal function of the fiber stretcher driver voltage V_{fs} due to linear input-output relations of the intermediate processes.

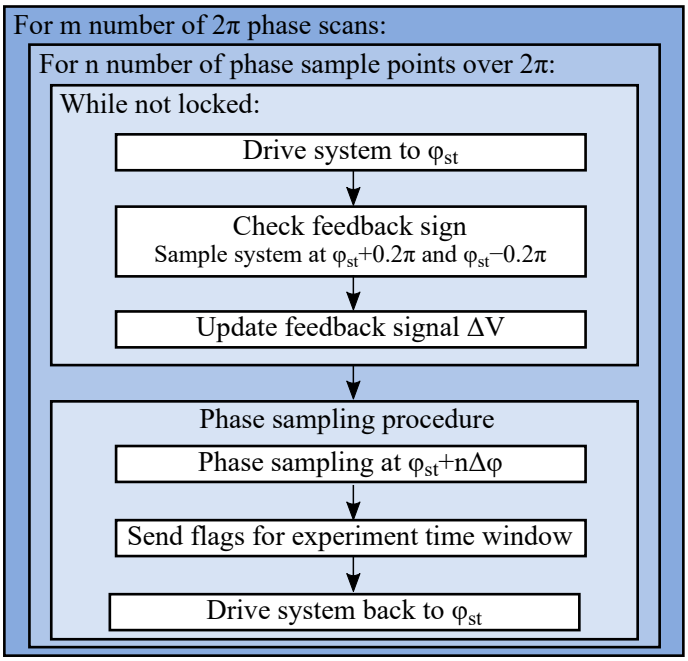

Figure 6.5: Flow chart of the algorithm.

Figure 6.4(b) shows a representative plot for the number of detected counts as a function of fiber stretcher driver voltage. The proportional gain K_p is set to the reciprocal of the slope of the tangent line at the set point N_{sp}; in other words, K_p is equal to the reciprocal of the first derivative of N_{pv} vs. V_{fs} curve at N_{sp}

$$K_p = \left(\frac{dN_{\mathrm{pv}}(V_{\mathrm{fs}})}{dV_{\mathrm{fs}}}\Big|_{V=V_o} \right)^{-1}, \tag{6.8}$$

where V_o is the voltage at which $N_{\mathrm{pv}}(V_o) = N_{\mathrm{sp}}$.

6.2.2.2 Algorithm

The flow chart of the algorithm is shown in Fig. 6.5. Here, we describe the main parts of the stabilization procedure.

Drive system to set point

The algorithm first attempts to drive the fiber stretcher to the set point ϕ_{sp} and samples N_{pv} during integration time Δt. To account for the optical power fluctuations of the input laser, we implement a section where N_{pv} counts can be normalized by the output voltage of a reference

linear photodetector monitoring the input light power (not shown for simplicity). However, it turns out that the power fluctuations are negligible so that this section is not critical to the implementation.

Check feedback sign

An attention must be paid to the sign of K_p in Fig. 6.4(b) when the generated feedback voltage is added onto the fiber stretcher voltage. If K_p is negative, ΔV should be summed with the previous fiber stretcher voltage V_{fs}; otherwise, the system would apply a positive feedback. We obtained the sign of the slope at N_{sp} point as follows: the system is perturbed with $\pm 0.2\pi$ phase delays and photon counts are subsequently sampled to check whether the counts are increased following the perturbation. It turns out that the sign of K_p does not flip once the system is locked, obviating the need for the slope check in the actual operation.

Update feedback signal

Next, we check whether the sampled count N_{pv} is within the associated Poisson fluctuation limits (see Eq. 6.4). If N_{pv} is outside of the photon shot noise range, then a feedback voltage is applied to compensate for the phase fluctuations. The algorithm does not proceed to the phase sampling block and iterates over the phase stabilization loop until it recovers the system back to the initial set point N_{sp} (see Fig. 6.5). The response time of the feedback loop is around a few ms[1].

Phase sampling procedure

Once the sampled count N_{pv} is within the boundaries of photon shot noise range, the algorithm proceeds to the phase sampling block. Here, single-photon interference fringes are sampled at different phase delays ranging from 0 to 2π radians by applying corresponding voltage steps to the fiber stretcher.

For each phase step, the algorithm sends one digital signal to an 8-channel time-correlated single-photon counting unit (TCSPC, IDQuantique ID800). This signal indicates the start of a data acquisition time window Δt, and it is followed by another signal indicating the termination of Δt. In our experiments with heralded single-photon source, the time correlations between single photons registered by the TCSPC unit are analyzed over the time interval

[1] We note that the speed of the digital controller was limited by the USB communication and the software execution time. It could be further increased if these bottlenecks are bypassed, for instance, by processing single-photon detector counts in a field-programmable gate-array (FPGA).

marked by these two signals. Finally, the system is driven back to its initial phase point once the sampling of photon counts is over.

6.2.2.3 Operation details

The fiber stretcher driving voltage V_{fs} is initialized in a way that the phase difference between interferometer arms leads to a count rate that is equal to the set point N_{sp}. This initialization procedure is similar to adding an offset voltage in conventional PID controllers to prevent overloading of the controller response.

Prior to the program execution, the fiber stretcher driving voltage that generates 2π phase retardation between the interferometer arms $V_{2\pi}$ is specified. This voltage value depends on the actuator response and the photon wavelength. In our experiments, $V_{2\pi}$ is approximately equal to 4 V for the operation wavelength of 810 nm.

This voltage is used to prevent the calculated V_{fs} from exceeding the output voltage limitations of ± 10 V of the analog I/O channels; otherwise, the voltage saturation would cause nonlinear feedback response. Such a case may occur if the network drifts in a way that the required V_{fs} to compensate for the phase drift monotonically increases. For this reason, before applying the calculated V_{fs} to the analog I/O channel driving the fiber stretcher, we performed a modulo operation and applied $V'_{\text{fs}} \equiv V_{\text{fs}} \pmod{V_{2\pi}}$ to the fiber stretcher.

Following the execution command of V_{fs}, a time buffer lasting a few ms is added before the data acquisition to ensure that the fiber stretcher completes its response. This additional time delay mitigates the effect of possible serial communication delays between the PC and I/O device driving the fiber stretcher.

Obtaining feedback parameters

We phase scanned the unstabilized interferometer with a ramp signal applied to the fiber stretcher. The amplitude of the ramp signal is set such that the phase delay ϕ between interferometer arms is scanned from 0 to 2π radians. The SPD-c counts N_c are sampled over an integration time Δt of 24 ms.

Figure 6.6(a) shows a representative phase scan plot for an unstabilized interferometer whose phase is scanned with a ramp voltage shown in Figure 6.6(b). The input parameters of set point N_{sp} and proportional gain K_p of the controller are obtained by fitting measured interference fringes to a sinusoidal function. The set point N_{sp} is determined to be the mean of the sinusoidal fit function, whereas the proportional gain is obtained according to Eq. 6.8 by substituting the fit parameters. For the representative phase scan shown in Fig. 6.6, the

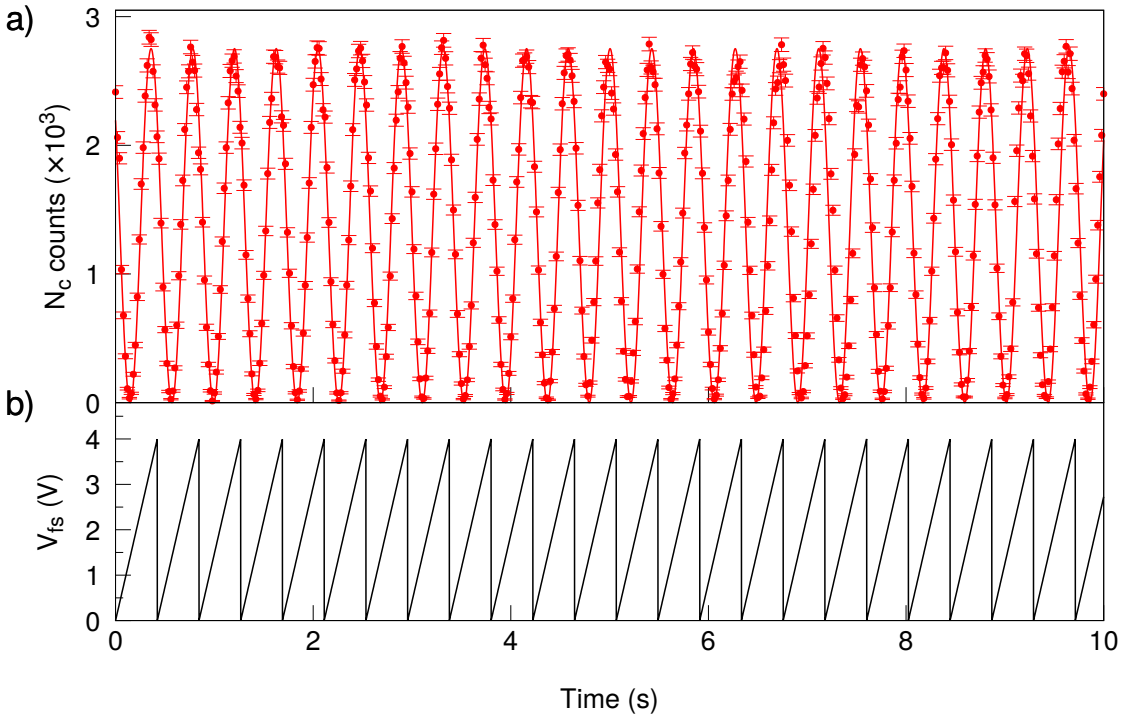

Figure 6.6: Phase scanning of the unstabilized interferometer to obtain feedback input parameters. a) The unstabilized interferometer is phase scanned by applying a ramp voltage to the fiber stretcher. Each data point corresponds to the SPD counts at output port C integrated over a time period Δt of 24 ms. The set point N_{sp} and proportional constant K_p are obtained by fitting measured interference fringes to a sinusoidal function. b) The corresponding ramp voltage.

controller locks into $N_{\mathrm{sp}} = 1360\,\mathrm{counts}/\Delta t$ with K_p being 2.44 mV/counts. Here, we consider the data measured up to 10 s in our fitting procedure because longer data acquisition times affect the evaluated fit parameters due to significant phase drift at longer time scales (see Fig. 6.3 for noise spectral density).

6.3 Experiment: Phase Stabilization

6.3.1 Single-photon Source

To assess the applicability of our phase stabilization technique by single-photon counting, we implemented our method in an optical network represented by a fully-fiberized Mach-Zehnder interferometer operating at the single-photon level (Fig. 6.2(b)). Here, we used a strongly-attenuated CW-laser as a single-photon source. The maximum number of detected photons was around $3\mathrm{k}\,\mathrm{counts}/\Delta t$ (see Fig. 6.6), indicating that the detected photon rate r was around $125\mathrm{k}\,\mathrm{counts}/s$ (hereinafter abbreviated as cps). Our single-photon detectors (Excelitas SPCM-AQRH-13 [266]) have a detection time window $\Delta\tau$ of around 30 ns, over which the mean number of detected photons is given by

$$\mu = r\Delta\tau. \tag{6.9}$$

The probability of finding n photons within detection time window $\Delta\tau$ follows Poisson statistics

$$P(n,\mu) = \frac{(\mu)^n e^{-\mu}}{n!}, \tag{6.10}$$

where e is the Euler's number. The probabilities of detecting 0 and 1 photon within $\Delta\tau$ are then read as

$$\begin{aligned} P(0,\mu) &= e^{-\mu}, \\ P(1,\mu) &= \mu\, e^{-\mu}. \end{aligned} \tag{6.11}$$

Similarly, the probability that a non-empty weak coherent state contains more than one photon equals to [267]

$$\begin{aligned} P(n>1|n>0,\mu) &= \frac{1-(P(0,\mu)+P(1,\mu))}{1-P(0,\mu)}, \\ &= \frac{1-e^{-\mu}(1+\mu)}{1-e^{-\mu}} \approx \frac{\mu}{2}, \end{aligned} \tag{6.12}$$

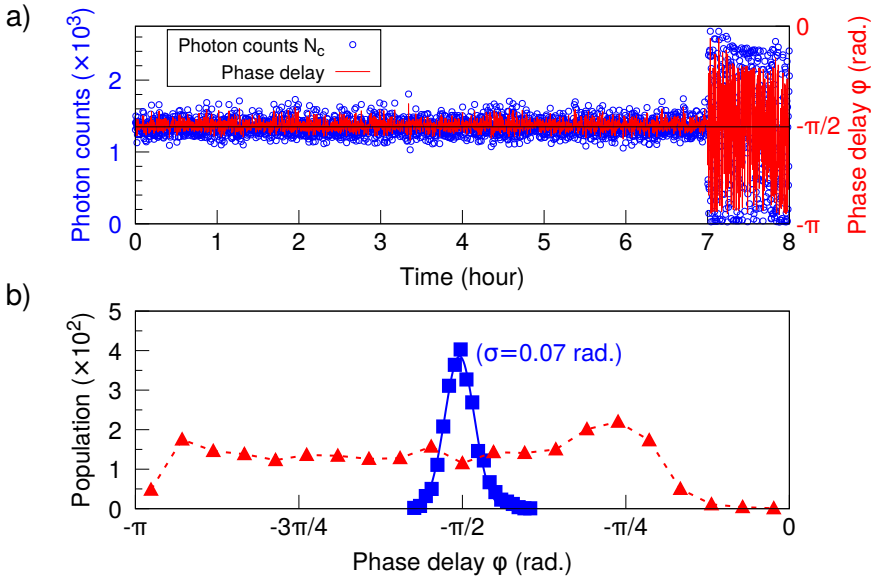

Figure 6.7: Long-term phase stabilization in a fully-fiberized MZI by single-photon counting. a) The system is stabilized for 7 hours, followed by another 7 hours without stabilization (only one hour is shown). Each blue circle corresponds to the number of single photon counts with the red line being the corresponding phase delay retrieved from these counts. The black line represents the stabilization point. b) The corresponding phase distributions, where the blue line is the Gaussian fit curve.

which was around 0.002 for our experiments; in other words, only one of ∼500 detection events was due to a multiphoton state. Consequently, a strongly-attenuated CW-laser source with these photon statistics is suitable for testing our stabilization method at the single-photon level.

6.3.2 Phase Stability

Figure 6.7(a) shows the continuous phase stabilization of the interferometer up to 7 hours. Each blue circle in Fig. 6.7(a) shows the number of single-photons detected by SPD-c over Δt, and the red line represents the phase delay retrieved from these counts. The sampling period was set to 10 s. The corresponding distribution of photon counts during stabilization and free-running regimes (i.e., unstabilized) are shown in Fig. 6.7(b) together with Gaussian fit-curves. The standard deviation of the Gaussian fit for the stabilized regime is $\sigma = 0.07$ radians. This implies that the length difference between interferometer arms is stabilized to within 10 nm range for 810 nm input photons, corresponding to a 9 orders of magnitude spatial resolution for 15 meters of fibers. This value is comparable to those demonstrated

in conventional stabilization schemes [6], and it proves the viability our method for phase stabilizing optical networks operating at the single-photon level by single-photon counting.

Figure 6.3 and 6.7 clearly show that the phase stabilization of the interferometer is necessary for its long-term operation beyond 1 second. We note that the stabilization of longer interferometers with enlarged noise bandwidth may require reduced integration time Δt or increased single-photon source brightness or both.

6.3.3 Operation Speed

The operation speed of our method is mainly limited by the photon integration time, which is required to be rather long in order to have a feedback signal with good signal-to-noise ratio. We note that the integration time window could be reduced if a bright single-photon source were used; nonetheless, the operation speed would eventually be limited by the response speed of the fiber stretcher. For instance, the fiber stretcher we used in the experiments (Optiphase PZ1-PM4-PC-E-850B) has a bandwidth of around 10 kHz, beyond which it has nonlinear frequency response including resonances.

With these limitations on mind, we tested the operation speed of our setup. We checked the unit step response of the system by inducing a step phase change in the interferometer. The fiber stretcher is driven by square modulation pulses having a period of 100 ms with 50% duty cycle, and subsequently the photon detection times are registered by a time-correlated single-photon counting (TCSPC) unit. Analyzing the timestamps of photon detection events, we calculated the second-order correlation function $g^{(2)}(\tau)$

$$g^{(2)}(\tau) = \frac{\langle n(t)n(t+\tau)\rangle}{\langle n(t)\rangle^2}, \tag{6.13}$$

where $\langle . \rangle$ denotes the time average, and τ is the time delay between detection events.

Figure 6.8 shows the corresponding $g^{(2)}(\tau)$ measurements. The exponential rise and decay fit functions indicate a time constant of around 3.5 ms. To convert this value to a comparable figure of merit in terms of operational bandwidth, we use the rise time vs. bandwidth relation of a simple RC low-pass filter model: $\tau_r \approx 0.35/B$ where τ_r represents 10%-90% rise time and B denotes the 3 dB bandwidth. A bandwidth of around 100 Hz is estimated for the stabilization system, which was mainly limited by the integration time Δt of the photon counts.

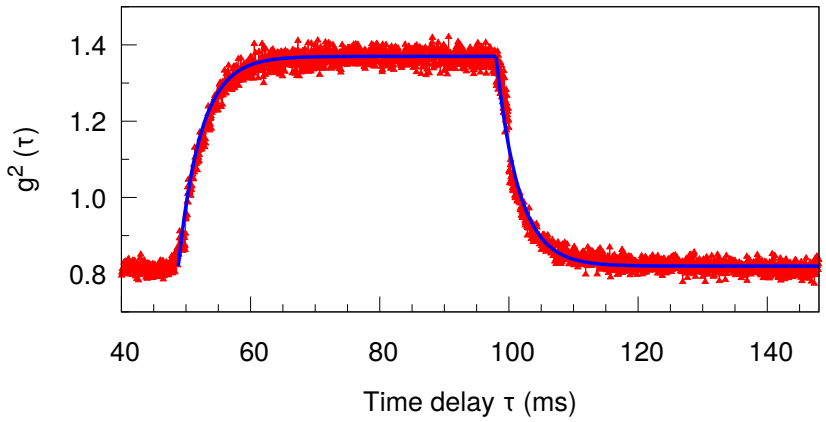

Figure 6.8: Operation speed of the phase stabilization. The system is modulated with a modulation signal of $T = 100$ ms and a duty cycle of 50%. Blue line shows the exponential rise and decay fit curves with a time constant of 3.5 ms.

6.3.4 Benchmarking

Table 6.1 benchmarks our phase stabilization technique with other contemporary methods developed for fiber interferometers operating at the single-photon level. All these methods use only a fiber stretcher as the feedback actuator component with the exception of [8], which additionally uses an optical delay line to achieve long-term stability and to have a wide range of optical path delays in their Hong-Ou-Mandel interference experiment.

The bandwidth of fiber stretchers is usually on the order of a few kHz because of large capacitance associated with the piezoelectric nature of the fiber stretcher; therefore, the operation speed of all these methods is limited to kHz range.

Long-term stability is demonstrated only in our work and in [8]. Since the experimental results for longer durations are not available in other works, a direct comparison on the long-term effectiveness of these methods is not applicable. Lastly, we achieved a phase stability that is comparable to that of [6].

Similar to [268], our method does not introduce additional insertion losses at the quantum channel due to (de)multiplexing. Moreover, since the system does not necessitate an auxiliary light source at a different wavelength, it inherently prevents possible crosstalk due to scattering-induced noise and insufficient isolation between channels and preserves the quality of the quantum signal. The drawbacks of our method are the interleaved operation and reduced operation speed. Nonetheless, for experiments that already operate in a gated regime, the cost of interleaved operation could be mitigated by generating the process variable signal during the inactive portions of the gate interval. Therefore, this method can be

Table 6.1: Benchmarking of our method with other phase stabilization schemes developed for fiber interferometers operating at the single-photon level.

Type	Length (m)	Phase stability [a]	BW (Hz)	Stabilized for (min.)	(De)mux items	Actuator	Ref.
MZ	15	0.07 rad.	100	420	Nil	FS	Ours
MZ	1k	N/A	1k	4.17	WDM, OC, FBG	FS	[7]
M	6k	0.06 rad.	1k	20	WDMs	FS	[6]
HOM	6k	N/A	1k	300	WDMs, BPF	FS, ODL	[8]
MZ	8.5	$50 \pm 0.1\%$ [b]	1k	15	OI, IF	FS	[9]
MZ	NA	1.6×10^{-3} [c]	10	0.17	Nil	FS	[268]

The "type" column indicates the interferometer configuration.
[a] The related information is included if the phase stability in radians is not available.
[b] This is the mean transmittance in a balanced MZI configuration.
[c] This is the estimated fundamental limit to the phase noise error.

MZ: Mach-Zehnder	HOM: Hong-Ou-Mandel	M: Michelson
FS: Fiber stretcher	WDM: Wavelength-division multiplexer	OI: Optical isolator
OC: Optical circulator	(De)mux: (De)multiplexer	BPF: Band-pass filter
ODL: Optical delay line	FBG: Fiber Bragg grating	IF: Interference filter

implemented in coherent optical networks operating at the single-photon level, where loss budget is prohibitively low and long-term stability is required.

6.4 Experiment: Single-photon Interference

Next, we implemented our phase stabilization technique in a coherent optical network represented by a fully-fiberized MZI and measured single-photon interference fringes to test the applicability of our method for quantum optics experiments. The schematic of our experimental setup is shown in Fig. 6.9.

Photons at the single-photon level is fed into the interferometer via a 50:50 beamsplitter. A delay line at the bottom arm is used to equal the lengths of the interferometer arms[2], and a variable optical attenuator at the upper arm is used to balance the optical losses in both arms.

The fiber stretcher serves both as a phase modulator and an actuator through which the feedback response is applied for phase stabilization. The output channels of the second

[2] We note that the coherence length of the laser beam is $\sim$30 meters, and the use of an optical delay line is not critical as optical fibers in both arms have almost the same length. Nonetheless, we decided to keep it in our experimental setup to make the setup compatible for different photon sources which might have significantly shorter coherence length and eventually require the use of an optical delay line.

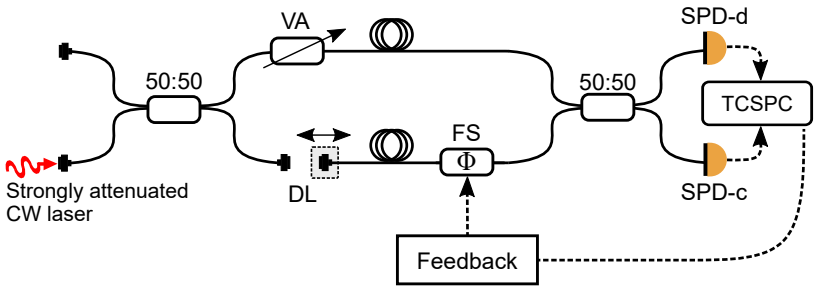

Figure 6.9: Schematic of the experimental setup to measure single-photon interference in a fully-fiberized MZI stabilized by our single-photon counting method. BS: beamsplitter, VA: variable attenuator, DL: delay line, FS: fiber stretcher, SPD: single-photon detector, TCSPC: time correlated single-photon counter.

50:50 beamsplitter are connected to single-photon detectors whose output signals fed into a TCSPC unit. The single-photon detector signals are also connected to a data acquisition card (National Instruments (NI), USB-6251) through a connector block (NI, BNC-2120) to retrieve the error signal during phase stabilization. These components are represented as the *Feedback* block in Fig. 6.9

The set point of the stabilization system N_{sp} is set in a way that SPD-c counts N_c locks into $N/2$, where N is the maximum count rate read by SPD-c. After stabilizing the interferometer, the phase retardation is shifted to one from a discrete set

$$\phi_{\mathrm{n}} = \phi_{\mathrm{st}} \pm n \cdot \Delta\phi, \tag{6.14}$$

where $\Delta\phi \approx 0.1\pi$ and n is an integer from 0 to 10. The photons are subsequently sampled by single-photon detectors at the output ports within a time interval Δt. Thereafter, the phase delay is reverted to its initial set point. The full 2π phase spectrum is sampled by repeating this procedure. In addition to this type of static stabilization in which the set point is fixed, we note that the proposed technique can be extended to dynamical type, where the stabilization is performed at any point of the SPD-c curve without any need to back to ϕ_{st} after each measurement, or to Pound–Drever–Hall type of phase control [269] by periodically modulating phase delay with an extra phase modulator.

The experimental data in Fig. 6.10(a) clearly demonstrates out-of-phase oscillations of N_{c} and N_{d} with near unity visibility, which agrees well with the theoretical predictions in Eqs. 6.1 and 6.2. In contrast to interference fringe measurements performed with an unstabilized interferometer (see Fig. 6.6), we are now able to set and retain any arbitrary phase delay in the interferometer. Out results show that phase stabilization by single-photon counting can

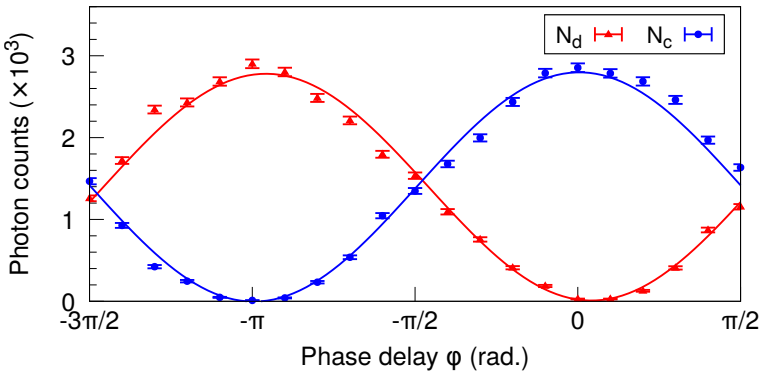

Figure 6.10: Single-photon interference in a fully-fiberized Mach-Zehnder interferometer stabilized by single-photon counting. Each data point shows the number of detected photons at the corresponding output ports. The error bars are given by the photon shot noise. Out-of-phase oscillations of N_c and N_d is in a good agreement with Eqs. 6.1 and 6.2.

be used to protect the coherence of single photons propagating through an optical network without complicating the setup for phase retrieval during stabilization.

6.5 Conclusion

In this chapter, we showed a simple yet powerful technique of phase stabilization by single-photon counting for coherent optical networks operating at the single-photon level. Our method can overcome phase noise with no need for auxiliary laser and additional optical components required in conventional approaches. Significant hardware simplification brought about by the proposed method is promising. We achieved a phase stability of 0.07 radians, which is comparable to those used in conventional stabilization schemes, while preserving the efficiency of the quantum channel.

The development of relevant quantum technologies such as single-photon detectors with decreased dead time and higher efficiency, bright sources of quantum light, and high-performance integrated optics at telecom wavelengths would allow real-world applications of this technique in quantum communication and computation systems.

In the next chapter, we applied our phase stabilization method to a coherent optical network which is configured as an interferometric intensity modulator with added functionalities enabled by coherent perfect absorption phenomenon. Such CPA interferometers can achieve complete light dissipation through coherent interactions with light even at the single-photon level. Therefore, any undesired interference or crosstalk in other network arms can be prevented by completely dissipating the residual photon.

Chapter 7

All-optical Single-photon Switch

7.1 Introduction

Controlling light-with-light at possible multi-THz bandwidth [270] without introducing signal distortion down to the single-photon level has allowed to extend coherent perfect absorption (CPA) phenomenon to quantum regimes[1]. Recent works include the experimental studies of CPA with single-photon Fock states [83], entangled states [84], and NOON states [85] as well as theoretical investigations of CPA for squeezed states [271]. Moreover, CPA has been demonstrated to control coupling of photons to other light-matter eigenstates such as exciton-polaritons [86], magnon-polaritons [87], and surface-plasmon-polaritons [88], extending its applicability to different realms.

Recent achievements in fabrication of fully-fiberized metamaterial packages have made it possible to manipulate quantum light in fiber environment [272]. For instance, quantum coherent perfect absorption (CPA) with plasmonic metamaterial absorber, first demonstrated in free space [85], was shown in an optical fiber network [141]. In the latter experiment, an elaborate data postselection technique was used to overcome the effects of phase noise in optical fibers. This data postselection method, however, prohibited to control absorption probability of single photons on demand.

In this chapter, we show that a phase stabilized coherent fiber network operating at CPA regime can be used to deterministically control single-photon absorption probability for coherent optical switching applications. Unlike conventional optical switches which are based on non-linear optical processes requiring high photon flux, interferometric switches can operate down to the single-photon level, and hence they are suitable for quantum

[1] The abbreviation CPA is used to indicate both coherent perfect absorption and coherent perfect absorber depending on the context.

optics applications. Compared to a standard Mach–Zehnder intensity modulator which only redistributes light between its two output ports, the optical switching via CPA has the added advantage of complete light dissipation. Therefore, CPA interferometers can be used in complex optical networks as they can prevent the propagation of residual photons into other network arms and eliminate undesired interference or crosstalk elsewhere. Moreover, CPA interferometers can be used to filter quantum states of photons as shown in the next chapter.

In the following sections, we first briefly describe the coherent perfect absorption phenomenon, and then introduce our fiberized plasmonic metamaterial absorber to achieve this effect. Next, we present experimental results where we control single-photon absorption probability on demand. The chapter concludes with the demonstration of all-optical single-photon switching through CPA.

7.2 Coherent Perfect Absorption

Coherent perfect absorption is a phenomenon where full absorption of light is achieved by a subwavelength thick absorber under coherent illumination. CPA was first introduced as a time-reversed laser at the lasing threshold in the original theoretical paper [273]; a coherent perfect absorber supports a purely incoming radiation pattern as opposed to lasers which support purely outgoing radiation pattern. Complete absorption and zero reflection of incoming coherent radiation is possible depending on material absorption for travelling waves and interference between transmitted and reflected fields. It has been shown that any arbitrary physical body can be made perfectly absorbing at discrete frequencies in the presence of specific amounts of dissipation and correctly chosen relative phase between incident coherent beams of equal intensity [273]. Coherent perfect absorbers can be used to control the incident radiation energy to a device through phase or amplitude modulation of the incoming beams; therefore, they act as linear and absorptive interferometric optical elements.

The first experimental demonstration of CPA was performed with two counter-propagating coherent beams incident on a silicon wafer of subwavelength thickness in a free-space Mach-Zehnder interferometer [274]. In this experiment, CPA occurred near the silicon band-edge; therefore, the wavelength at which CPA could take place was determined by the material properties. Nonetheless, it was emphasized that the operating wavelength could be engineered by fabricating devices where an additional parameter tunes the absorption coefficient independently of wavelength.

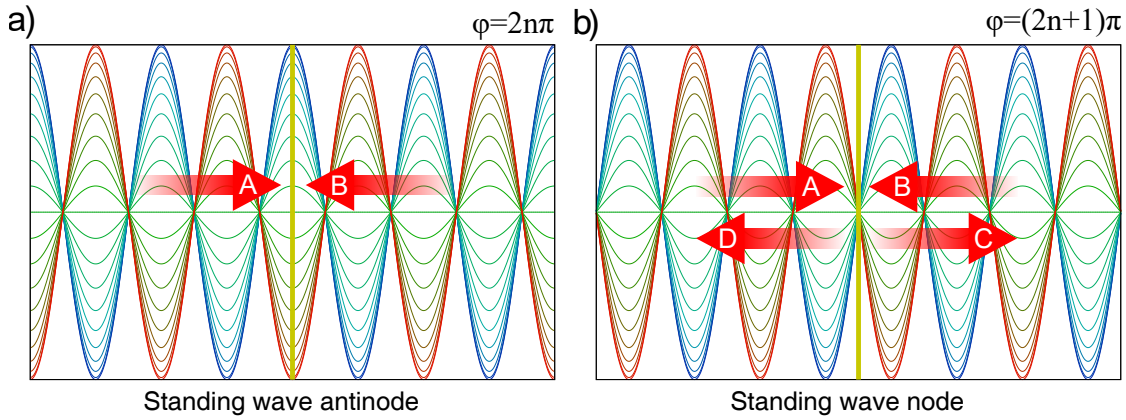

Figure 7.1: Concept of coherent perfect absorption (CPA). The plasmonic metasurface to achieve CPA is shown as a yellow stripe. Here, two counter-propagating coherent beams having the same amplitude interfere and form a standing wave. a) The configuration for coherent perfect absorption where an antinode of the standing wave is formed at the position of the metasurface. b) The other limiting case takes place once a node of the standing wave coincides with the metasurface.

Following this first demonstration with a silicon absorbing scatterer, CPA was reported with an artificial nanostructured material, a plasmonic metasurface [275]. To achieve the desired optical characteristics, resonant nanostructures were designed and fabricated at target wavelengths. The metamaterial was positioned along the path a standing wave formed by two counter-propagating coherent beams. Controlling the relative phase between the interferometer arms, coherent interaction of light with the metamaterial was altered. If the metamaterial absorption for travelling waves is 50%, then two limiting regimes of interaction are achievable depending on the relative position of the metasurface with respect to the standing wave as shown in Fig. 7.1. If an antinode of the standing wave coincides with the plasmonic metasurface, then the light strongly interacts with the absorber, and subsequently enhanced light absorption occurs (see § 7.2.1). The other limiting case happens once a node of the standing wave coincides with the metasurface. There is no interaction in this case since the total electric field within the subwavelength thick metasurface is equal to zero.

Alternatively, the interaction of light with the plasmonic metasurface can be modified through amplitude modulation of one beam. Given that the metasurface initially coincides with a node of the standing wave as shown in Fig. 7.1(b), blocking one of the beams destroys the standing wave pattern; consequently, the standing-wave regime of light-matter interaction is substituted by the travelling-wave regime for the other beam. It was shown that the combined output intensity of the light was reduced from 95% to 20% once the interaction with the metamaterial was switched from the travelling-wave regime to the standing-wave

regime [275]. These experiments show that plasmonic metasurfaces provide different ways of controlling light with light such as phase or amplitude modulation of the coherent light.

Coherent perfect absorbers have been used to design switching devices [270, 276], logic elements [272, 277], and interferometers [274]. Here, we demonstrate an all-optical single-photon switching device by using a plasmonic metasurface that is integrated within a fiberized Mach-Zehnder interferometer.

7.2.1 CPA at the Single-photon Level

The following quantum mechanical analysis briefly introduces the quantum regimes of coherent perfect absorption and transmission [141]. The quantum state of the photon in this analysis has the following path-entangled wave function

$$|\psi\rangle = \frac{1}{\sqrt{2}}\left(|1\rangle_A |0\rangle_B + e^{i\phi} |0\rangle_A |1\rangle_B\right), \tag{7.1}$$

where A and B denote the top and bottom incoming fields to the absorber in Fig. 7.2, respectively. Once this photon incidents upon a subwavelength thick lossy beamsplitter which induces a π phase shift between transmitted and reflected fields, then the following outcomes are possible depending on the phase shift ϕ defined at the absorber position:

- Destructive interference happens after the absorber if $\phi = 2n\pi$ (where $n \in \mathbb{Z}$) and reflected and transmitted fields extinguish each other (see Fig. 7.1(a)).
- Constructive interference happens after the absorber if $\phi = (2n+1)\pi$ and the field propagates through the absorber (see Fig. 7.1(b)).

In the case of $\phi = 2n\pi$, we note that the absorption probability under coherent illumination reaches unity if the travelling-wave absorption of the device is equal to 50%, a regime known as coherent perfect absorption. In Eq. 7.1, the input fields A and B relate to the annihilation operators $\hat{a}$ and $\hat{b}$ with the following commutation relations

$$\begin{aligned} [\hat{a}, \hat{a}^\dagger] = [\hat{b}, \hat{b}^\dagger] = 1, \\ [\hat{a}, \hat{b}^\dagger] = 0, \end{aligned} \tag{7.2}$$

where $[\ ,\ ]$ denotes the commutator. The coherent perfect absorber (hereinafter denoted as the absorber) mixes the input amplitudes and adds the Langevin noise operators $\hat{f}_c$ and $\hat{f}_d$,

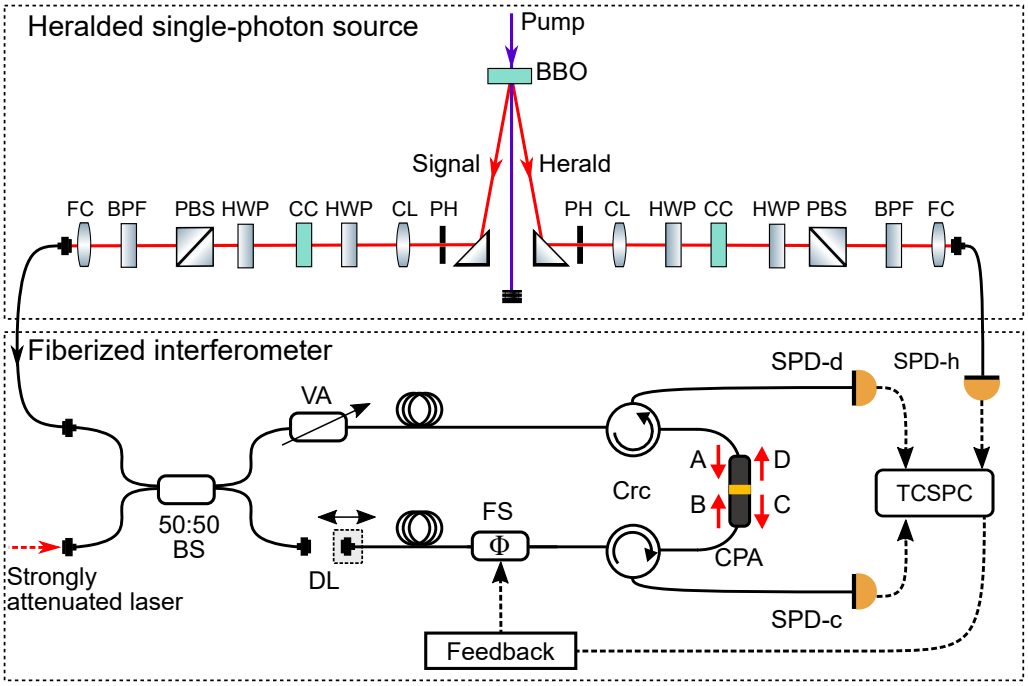

Figure 7.2: Schematic of the full setup for single-photon absorption control and all-optical single-photon switching experiments. The setup consists of a heralded single-photon source setup (top) and a fiberized interferometer with coherent perfect absorber (bottom). In each arm, a HWP and CC pair is used to compensate for spatial and temporal walk-off of down-converted photons due to birefringence of the first BBO crystal, whereas the following HWP and PBS pair is used to choose correlated photon polarizations. BBO: beta-barium borate, PH: pinhole, CL: collimator lens, HWP: half-wave plate, CC: compensating (BBO) crystal, BPF: band-pass filter, FC: fiber collimator, PBS: polarization beam splitter, DL: delay line, VA: variable attenuator, FS: fiber stretcher, Crc: circulator, CPA: (fiberized) coherent perfect absorber, SPD: single-photon detector, TCSPC: time-correlated single-photon counter.

which fulfil the commutation relation conversation [278, 279]

$$\begin{aligned} \hat{c} &= t\hat{a} + r\hat{b} + \hat{f}_c, \\ \hat{d} &= r\hat{a} + t\hat{b} + \hat{f}_d, \end{aligned} \tag{7.3}$$

where $\hat{c}$ and $\hat{d}$ are the annihilation operators related to the bottom and top outgoing fields from the absorber in Fig. 7.2, respectively, and t (r) is the amplitude transmission (reflection) coefficient for travelling waves. Given a single-photon input state and unity detection efficiency, the photon detection probabilities p_c and p_d at two output ports of the absorber equal to the expectation values of photon number operators associated with $\hat{c}$ and $\hat{d}$. The

mean values of photon number operators are then equal to

$$\begin{aligned} p_c &= \langle \hat{c}^\dagger \hat{c} \rangle = \Big(|t|^2 + |r|^2 + 2|t||r| \cos(\phi - \Delta_{tr}) \Big) /2, \\ p_d &= \langle \hat{d}^\dagger \hat{d} \rangle = \Big(|t|^2 + |r|^2 + 2|t||r| \cos(\phi + \Delta_{tr}) \Big) /2, \end{aligned} \tag{7.4}$$

where $t = |t|e^{i\theta_t}$, $r = |r|e^{i\theta_r}$, and $\Delta_{tr} = \theta_t - \theta_r$. Here, we performed quantum mechanical averaging with the initial state where the contributions due to noise operators average out to zero [278]. If $|t| = |r|$, Eq. 7.4 can be further simplified into

$$\begin{aligned} p_c &= |t|^2 \left(1 + \cos(\phi - \Delta_{tr})\right), \\ p_d &= |t|^2 \left(1 + \cos(\phi + \Delta_{tr})\right). \end{aligned} \tag{7.5}$$

Here, we performed two experiments in each of which single photons interact with a different material: (i) a lossless 50:50 beamsplitter with (see § 6.4)

$$|t| = |r| = 1/\sqrt{2}, \quad \Delta_{tr} = \pm\pi/2, \tag{7.6}$$

and (ii) a plasmonic metamaterial that was designed as an ideal lossy beamsplitter with

$$|t| = |r| = 1/2, \quad \Delta_{tr} = \pm\pi. \tag{7.7}$$

In the former case, the photon detection probabilities p_c and p_d oscillate out of phase (see § 6.2.1). In the case of the metamaterial , however, these probabilities oscillate in phase such that

$$p_c(\phi) = p_d(\phi) = (1 - \cos\phi)/4, \tag{7.8}$$

with the total detection probability p

$$p(\phi) \coloneqq p_c(\phi) + p_d(\phi) = (1 - \cos\phi)/2. \tag{7.9}$$

The total detection probability p, which also indicates the total probability of photons transmitted through the absorber, is equal to unity when $\phi = (2n+1)\pi$, whereas the probability becomes zero when $\phi = 2n\pi$ meaning that the photons are completely absorbed by the absorber.

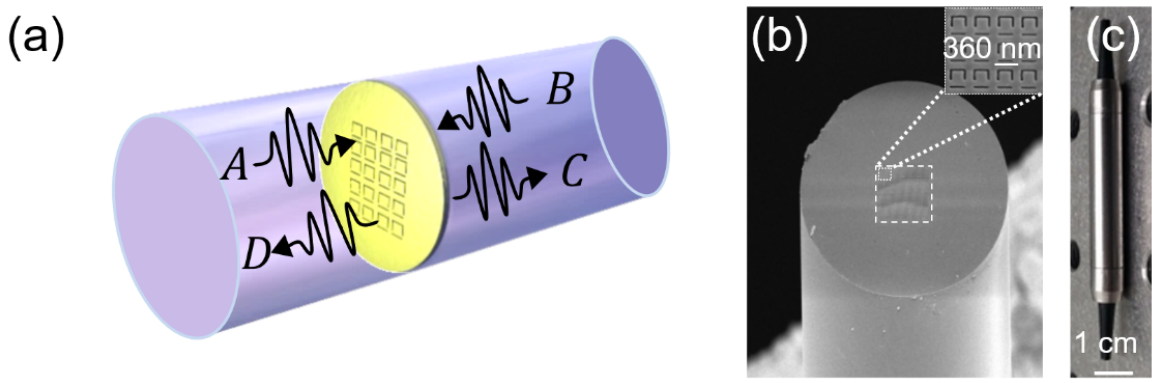

Figure 7.3: a) Concept of the fiberized plasmonic metamaterial. Coherent optical input fields *A* and *B* interact on the metasurface and generate output fields *C* and *D*. b) The SEM image of the plasmonic metamaterial absorber deposited on a fiber end facet. The inset shows the zoomed view SEM image of the engraved asymmetric split-ring resonator structures. c) The photograph of the packaged metadevice.

7.2.2 Fiberized Plasmonic Metamaterial Absorber

Coherent perfect absorbers in optical fiber environment have been fabricated by various methods including carving a plasmonic metasurface over a fiber tip [272, 276], depositing chromium thin film on a fiber cross-section [280], and defining a short-length erbium-doped-fiber cavity with fiber Bragg gratings [281].

Here, we followed the method described in [272] and fabricated a plasmonic metasurface on a fiber end facet (see Fig.7.3(a)). The metamaterial was fabricated on a 50-nm-thick gold film, which is thermally evaporated on the flat-cleaved facet of a polarization-maintaining (PM) single-mode optical fiber. The metamaterial consists of a 2D array of asymmetric split-ring resonator structures, which are engraved by focused ion beam (FIB) milling method on a 30×30 μm^2 area covering the fiber core. Figure7.3(b) shows the scanning electron microscope (SEM) image of the fabricated metamaterial.

The fiber with the patterned structure is mounted into a glass fiber ferrule and attached to a second bare fiber. The symmetry axis of the metamaterial is aligned with the slow axis of the PM fiber, and coupling is optimized by adjusting 3-axis kinematic stages. The fiber ferrule is mounted with a two-layer glass tubes, and then the device is encapsulated with a stainless steel housing for mechanical protection (see Fig.7.3(c)). The metadevice package is finally connected to standard FC/APC connectors on both sides.

The packaged device has 10% reflection, 20% transmission, and 70% absorption at the engraved side of the fiber at the operation wavelength of 810 nm. The corresponding figures for the bare side of the fiber are measured as 6% reflection, 20% transmission, and 74%

absorption. We note that these values also include the losses pertaining to the packaging and internal fiber-to-fiber coupling, and hence the actual reflection and transmission values of the device are higher.

7.3 Experiment: Single-photon Absorption Control via CPA

We used two different photon sources in our experiments: i) a strongly attenuated CW laser, and ii) a heralded single-photon source. The strongly attenuated CW laser at 810 nm was used to measure interference fringes, whereas the heralded single-photon source was used to demonstrate single-photon switching beyond the dark count noise.

Similar to the previous experiment with two 50:50 beamsplitters (see § 6.4), the coherent optical fiber network here was configured as a Mach-Zehnder interferometer with a modification that it now contains the metamaterial at the place of the second beamsplitter. A fiber stretcher was inserted in the bottom interferometer arm for phase stabilization and modulation, and a variable attenuator was placed in the upper arm to equal losses in both arms. An optical delay line in the lower arm was used to equal the 20-m-long interferometer arms to within 100 µm of the coherence length of heralded photons (see Appendix D). The circulators were added in both interferometer arms in order to separate photons propagating in different directions. After splitting on the first input 50:50 BS, the photon is recombined in the middle of the network where the absorber is positioned.

Since the phase noise was similar to the one shown in Fig. 6.3(a), we kept the SPD integration time Δt at 24 ms. The reference signal for phase stabilization was obtained from total photon counts of SPD-c and SPD-d as they oscillate in phase (see Eq. 7.8). Assuming N photons impinge on the metadevice, and single-photon detectors have unity detection efficiencies, the total counts are read as

$$N_{\mathrm{c}} + N_{\mathrm{d}} = N \cdot (1 - \cos\phi)/2, \tag{7.10}$$

where N_{c} and N_{d} represent the photon counts detected by SPD-c and SPD-d, respectively.

We measured the interference fringes after stabilizing the interferometer. Figure 7.4 shows that N_{c} and N_{d} oscillate almost in phase (with a shift of $\pi/3$), which is in a good agreement with the theoretical predictions from Eqs. 7.8 to 7.10. The phase shift stems from the imperfections in the device fabrication. In-phase behavior can be obtained by fabricating the metasurface symmetrically or using a matching gel inside the metadevice package.

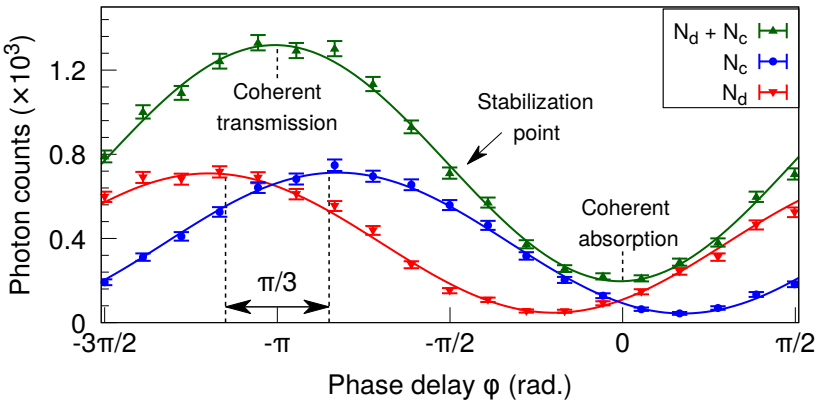

Figure 7.4: Single photon manipulation in coherent optical fiber networks stabilized by single photons. Single photon absorption control with a CPA. Each point corresponds to a single measurement; the dispersion is defined by the Poisson distribution.

During a 2π phase scan, the system passes the regimes of coherent absorption (i.e., the minimum of $N_c + N_d$ counts, N_{min}) and coherent transmission (i.e., the maximum of $N_c + N_d$, N_{max}) with the visibility of

$$(N_{max} - N_{min})/(N_{max} + N_{min}) = 73\%. \tag{7.11}$$

This visibility is lower than the visibilities of individual curves, which are equal to 89% for N_c and 86% for N_d). The unity system visibility is achievable if the device nonideality is mitigated. This result is close to the one demonstrated previously [141] with the exception that our phase stabilization method now enables us to control single-photon absorption probability on demand, which is crucial for utilizing the CPA phenomenon for quantum light processing. Next, we show how we used CPA for all-optical single-photon switching with a heralded single-photon source.

7.4 Experiment: All-optical Single-photon Switch via CPA

In order to demonstrate all-optical single-photon switching via CPA beyond the dark count noise, we use a heralded single-photon source instead of a strongly attenuated CW laser. First, we introduce our setup to generate heralded single photons.

7.4.1 Single-photon Source

The optical setup to generate heralded single photons is shown in Fig. 7.2. This setup is originally used to generate polarization-entangled photons, and more details can be found in [282]. Here, we used the same setup to generate heralded single photons and showed single-photon switching beyond the dark count noise.

Heralded single photons are generated via type-II spontaneous parametric down-conversion (SPDC) process in a 2-mm-thick beta-barium borate (BBO) crystal. A horizontally polarized 405 nm laser beam (Omicron LuxX compact 405-300) at 200 mW output power pumped the BBO crystal to generate photon pairs at 810 nm.

The light cones generated in the BBO crystal through SPDC process are imaged by a camera. The tilt and rotate angles of the crystal are adjusted such that the two light cones intersect each other at two points and satisfy the frequency degeneration condition. These two intersection points are separated into two paths after reflecting off two right angle mirrors. In order to have a symmetrical and aligned setup, all optical components are mounted on an optical rail that is positioned perpendicular to the direction of the pump beam. We aligned the reflected beams by obtaining their images along the optical rail by a camera equipping a pinhole. Beam divergence in each path is corrected with collimation lenses.

BBO is a negative uniaxial birefringent crystal. For this type of crystals, the extraordinary ray, which is polarized along the optic axis, has higher phase velocity than the ordinary ray, which is polarized perpendicular to the optic axis. This causes distinguishability of photons through time and position, and it gives rise to temporal and spatial walk-off, respectively. To prevent this distinguishability and achieve entanglement in polarization degree of freedom, the original setup incorporated a half-wave plate together with a 1-mm-thick compensating BBO crystal which has the same phase matching angle with the 2-mm-thick BBO crystals in each optical path [282]. Since we did not make use of polarization-entangled photons but rather generate only heralded single photons, these components are not strictly necessary for our experiments; nonetheless, we decided to keep the original setup intact.

These components are followed by a pair of half-wave plate and polarization beamsplitter for polarization adjustment. The heralded single-photon pairs are then coupled to single-mode fibers via fiber collimators after they are filtered with band-pass filters ($\lambda_{\text{center}} = 810$ nm and $\Delta\lambda_{\text{FWHM}} = 20$ nm). The idler photons are sent to a time-correlated single-photon counter (TCSPC) and herald the presence of signal photons within a coincidence time window $\Delta t_{\text{coinc.}}$, whereas the signal photons are sent into the interferometer through a 50:50 beamsplitter.

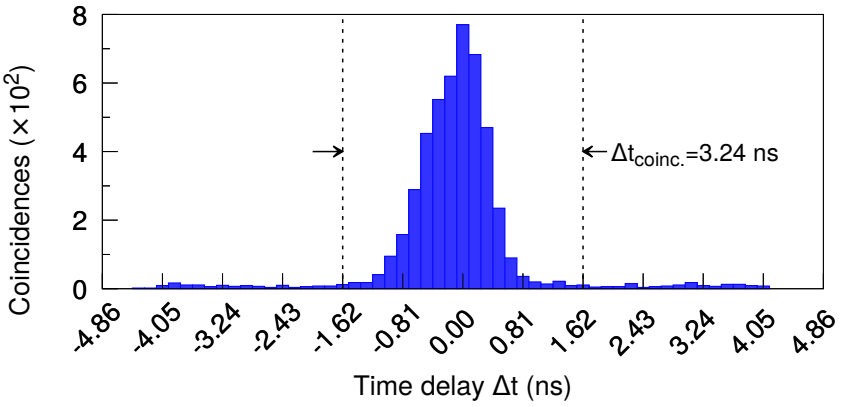

Figure 7.5: Timing statistics of heralded single photons. The width of histogram bins is set to 162 ps, which is twice the timing resolution of the TCSPC unit.

To determine the coincidence time window $\Delta t_{\text{coinc.}}$, we measured coincidence statistics of the heralded single-photon source as shown in Fig. 7.5. A coincidence time window $\Delta t_{\text{coinc.}} = 3.24$ ns is chosen to maximize the heralded single-photon flux rate while minimizing the false counts due to dark count rate of single-photon detectors. More details about the photon statistics of the heralded single-photon source can be found in Appendix D.

7.4.2 Results

Figure 7.6 shows the experimental results of all-optical single-photon switching. Here, the coherent optical network is driven to either coherent absorption or coherent transmission regime by modulating phase delay ϕ as shown in Fig. 7.6(a). The coincidence counts of SPD-c & SPD-h and SPD-d & SPD-h over $\Delta t_{\text{coinc.}}$ are accumulated over an integration time window Δt. Figure 7.6(b) shows the timestamps of these coincident detections registered by the TCSPC unit. The photons pass through the absorber at coherent transmission regime, whereas they are almost totally absorbed during coherent absorption regime. We obtain the distribution of photon counts that are accumulated over a detection time window Δt by accumulating statistics over 300 transmission and absorption cycles. Photon number distributions shown in Fig. 7.6(c) correspond to Poisson statistics of randomly generated heralded photons. The mean number of photons detected during transmission and absorption cycles were 8.0 with a standard deviation (s.d.) of 2.8 and 1.0 with a s.d. of 1.0, respectively. The average switching visibility of 78% is obtained, and the unity system visibility is achievable if the device nonidealities are mitigated (see § 7.3).

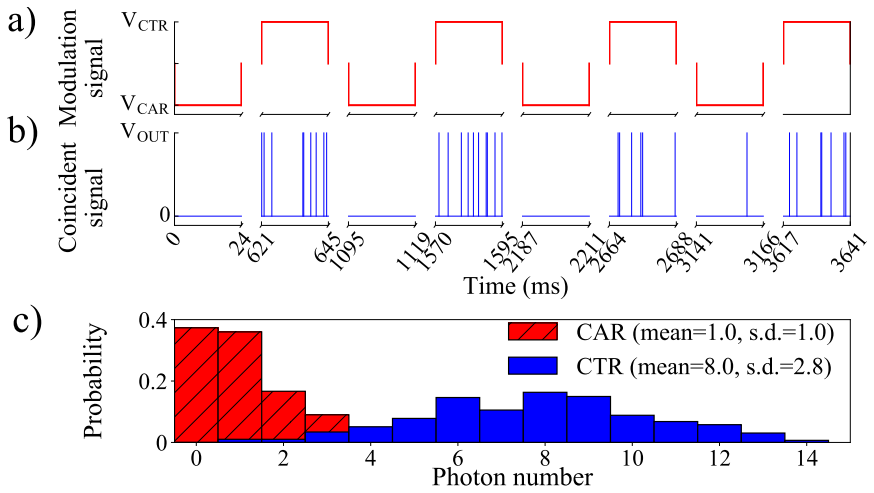

Figure 7.6: All-optical single-photon switching. a) The modulation signal driving the system between coherent absorption (CAR) and transmission regimes (CTR). b) The timestamps of coincidence detection events between SPD-c & SPD-h and SPD-d & SPD-h registered by TCSPC. The subplots a) and b) share the x-axis of which broken parts correspond to the phase stabilization periods. c) The distribution of coincident photon counts during coherent absorption (red) and transmission (blue) cycles.

7.5 Conclusion

In this chapter, we investigate the applicability of a coherent perfect absorber for coherent modulation of absorption probabilities of single photons propagating inside a fiber network. We demonstrate the coherent perfect absorption of single photons by integrating a plasmonic metasurface in a fully-fiberized phase-tunable Mach-Zehnder interferometer. Coherent control of single-photon absorption probability is achieved with the visibility of 73%, which was limited by the absorber nonidealities.

Compared to conventional all-optical switches based on non-linear optical processes requiring high light intensities, the interferometric switches can operate down to the single-photon level. Moreover, the interferometric modulators based on CPA possess the added advantage of deterministic, complete light dissipation compared to conventional Mach-Zehnder intensity modulators, which can only redistribute photons between its two output ports. Such a capability is particularly useful in complex coherent optical networks because the leakage of residual photons into other network arms can be prevented to eliminate any undesired interference or crosstalk. In this regard, as a proof of principle experiment, we demonstrated all-optical single-photon switching with a visibility close to 80% by using a

heralded single-photon source. Our demonstrations may find applications in linear optical quantum computing and quantum communication systems.

In the next chapter, we extended the applicability of our coherent optical network for quantum state manipulation and showed quantum states filtering of photons whose quantum information is encoded in superposition of spatial wave functions.

Chapter 8

Quantum State Filtering of Dual-rail Photons

8.1 Introduction

In the previous two chapters, we first phase stabilized a coherent optical network, and subsequently demonstrated all-optical single-photon switching via coherent perfect absorption phenomenon. Here, we show that a coherent perfect absorber in a phase-tunable optical network can be used to manipulate quantum states of light. Specifically, as a proof of principle, we modified the previous optical network into a cascaded Mach-Zehnder interferometer (MZI) to demonstrate that coherent perfect absorbers can be used to filter quantum states of photons whose quantum information is encoded in superposition of two spatial modes, i.e., dual-rail photons.

Here, we utilized the different optical responses of the absorber to symmetric and antisymmetric superposition of spatial wave functions, and measured the output state of photons after the absorber to verify the quantum state filtering action. Figure 8.1 shows the schematic of the cascaded MZI interferometer containing the metamaterial absorber. Here, we consider the following path-entangled wave function of a photon incident on the absorber

$$|\psi\rangle = \frac{1}{\sqrt{2}}\left(|1\rangle_A|0\rangle_B + e^{i\Phi}|0\rangle_A|1\rangle_B\right), \tag{8.1}$$

where indices A and B correspond to the input fields of the absorber. We note that Eq. 8.1 can also be described in the basis of symmetric $|\psi^{(S)}\rangle$ and antisymmetric $|\psi^{(AS)}\rangle$ states which

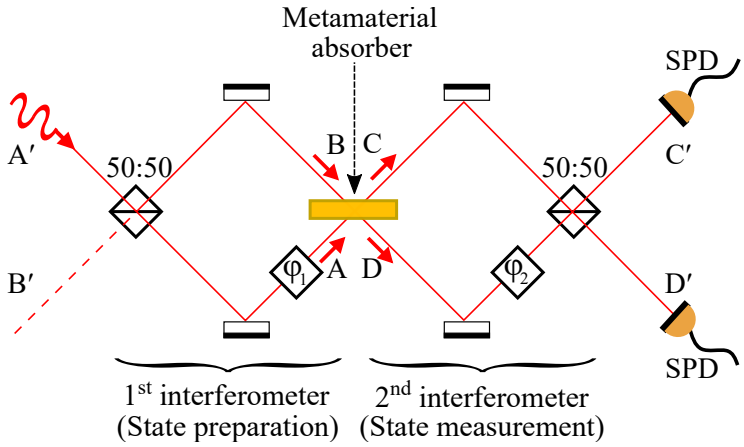

Figure 8.1: Schematic of the cascaded MZI configuration. ϕ_i: phase modulator, SPD: single-photon detector, 50/50: 50/50 beamsplitter.

are defined as

$$\begin{aligned} |\psi^{(S)}\rangle &:= \frac{1}{\sqrt{2}}\left(|1\rangle_A|0\rangle_B + |0\rangle_A|1\rangle_B\right), \\ |\psi^{(AS)}\rangle &:= \frac{1}{\sqrt{2}}\left(|1\rangle_A|0\rangle_B - |0\rangle_A|1\rangle_B\right). \end{aligned} \tag{8.2}$$

These states form a full orthonormal basis

$$\begin{aligned} \langle\psi^{(S)}|\psi^{(S)}\rangle &= \langle\psi^{(AS)}|\psi^{(AS)}\rangle = 1, \\ \langle\psi^{(S)}|\psi^{(AS)}\rangle &= 0. \end{aligned} \tag{8.3}$$

If we describe $|1\rangle_A|0\rangle_B$ and $|0\rangle_A|1\rangle_B$ in the basis of $|\psi^{(S)}\rangle$ and $|\psi^{(AS)}\rangle$ states, we then get

$$\begin{aligned} |1\rangle_A|0\rangle_B &= \frac{1}{\sqrt{2}}\left(|\psi^{(S)}\rangle + |\psi^{(AS)}\rangle\right), \\ |0\rangle_A|1\rangle_B &= \frac{1}{\sqrt{2}}\left(|\psi^{(S)}\rangle - |\psi^{(AS)}\rangle\right). \end{aligned} \tag{8.4}$$

By substituting Eq. 8.4 into Eq. 8.1, we obtain

$$|\psi\rangle = \frac{1}{2}\left(|\psi^{(S)}\rangle(1+e^{i\Phi}) + |\psi^{(AS)}\rangle(1-e^{i\Phi})\right), \tag{8.5}$$

which can also be described with respect to a common phase

$$|\psi\rangle = \cos\left(\frac{\Phi}{2}\right)|\psi^{(S)}\rangle - i\sin\left(\frac{\Phi}{2}\right)|\psi^{(AS)}\rangle. \tag{8.6}$$

In the previous chapter, we show that the amplitude transmission t and reflection r coefficients of the metamaterial for travelling waves result in complete absorption of the photons when $\Phi = 2n\pi$, $n \in \mathbb{Z}$. On the other hand, the transmission probability is equal to unity when $\Phi = (2n+1)\pi$ such that the photons pass through the absorber without losses (see Eq. 7.9). In other words, the symmetric state $|\psi^{(S)}\rangle$ that is obtained at $\Phi = 2n\pi$, is completely absorbed, whereas the antisymmetric state $|\psi^{(AS)}\rangle$ that is obtained at $\Phi = (2n+1)\pi$ is transmitted through the absorber without any losses (see Eq. 8.1). Since any path-entangled input state can be decomposed in the $\{|\psi^{(AS)}\rangle, |\psi^{(S)}\rangle\}$ basis, and the symmetric state $|\psi^{(S)}\rangle$ is completely absorbed, the output state of the photons after the absorber will be the antisymmetric state

$$|\psi_{\text{out}}\rangle = \frac{1}{\sqrt{2}}\left(|1\rangle_C|0\rangle_D - |0\rangle_C|1\rangle_D\right), \tag{8.7}$$

where C and D correspond to the output fields of the absorber. Consequently, the coherent perfect absorber functions as a quantum state filter by which dual-rail photons can leave the absorber only in antisymmetric state regardless of their input state[1].

The first MZI in Fig. 8.1 is used to prepare input states of single photons. The projective measurements on the output states of the photons leaving the absorbed are performed through the subsequent MZI. The phase delay between the two arms of the first MZI is controlled with a phase modulator denoted by ϕ_1. Following the photon-absorber interaction, the quantum state measurements are performed through the second MZI, where the phase delay between interferometer arms is controlled by a phase modulator ϕ_2 to sample the interference fringe at different phase points.

8.2 Theory

The metadevice acts as a lossy beamsplitter; the photon will end up in a statistical mixture of the vacuum state and the antisymmetric state once it interacts with the metadevice. The density matrix describing the *entire* output state after the absorber is read as

$$\rho = p_{AS}|\psi^{(AS)}\rangle\langle\psi^{(AS)}| + p_S|0\rangle\langle 0|, \tag{8.8}$$

[1] Similar to how a polarizer functions in a polarization degree of freedom, the coherent perfect absorber here operates in a spatial degree of freedom. In other words, the photons that pass through a polarizer would be in a well-defined polarization state, i.e., along the transmission axis of the polarizer. The coherent perfect absorber also behaves in a similar way that the photons after the absorber would be in the antisymmetric state.

where p_{AS} and p_S represent the probabilities of the input state to be in the antisymmetric state $|\psi^{(AS)}\rangle$ and the symmetric state $|\psi^{(S)}\rangle$, respectively, and they are normalized such that $p_{AS}+p_S=1$.

Here, we investigated the output state only for the cases where the photons are transmitted through the absorber. Our aim is to show that the quantum states of the *transmitted* photons are always in the antisymmetric state regardless of their input state. Since we are only interested in such cases, we can consider the metamaterial as a quantum state emitter that emits input states to the second interferometer with a probability depending on the quantum state of incoming photons. In our following mathematical treatment, we calculate the expectation values of the number operators at the output ports of the cascaded interferometer, and then verify our calculations by measuring the photon counts at the output ports.

8.2.1 Transformation Matrices

We first describe the transformation matrices of the 4-port optical components used in the experiment. The transformation matrix of a lossless 50:50 beamsplitter is read as

$$H_{\mathrm{BS}}=\frac{1}{\sqrt{2}}\begin{pmatrix}1 & i\\ i & 1\end{pmatrix}. \tag{8.9}$$

Since we assume a lossless device, the transformation matrix H_{BS} is unitary, i.e., $H_{\mathrm{BS}}^{\dagger}=H_{\mathrm{BS}}^{-1}$. The transformation matrix of a lossless phase shifter is given by

$$H_{\mathrm{PS}}=\begin{pmatrix}e^{i\phi} & 0\\ 0 & 1\end{pmatrix}. \tag{8.10}$$

Here, we introduce the annihilation and creation operators associated with the input and output fields of the absorber to describe the CPA transformation. The operator $\hat{a}$ is the annihilation operator and decreases the number of particles in a given state from $|n\rangle$ to $|n-1\rangle$

$$\begin{aligned}\hat{a}\,|n\rangle &= \sqrt{n}\,|n-1\rangle\,, \quad \hat{a}\,|0\rangle = 0,\\ (\hat{a}\,|n\rangle)^{\dagger} &= \langle n|\,\hat{a}^{\dagger} = \langle n-1|\,\sqrt{n},\end{aligned} \tag{8.11}$$

where $|n\rangle$ represents a number state or a Fock state, with $n \in \mathbb{N}^0$. The operator $\hat{a}^\dagger$ is the creation operator and increases the number of particles in a given state from $|n\rangle$ to $|n+1\rangle$

$$\begin{aligned} \hat{a}^\dagger |n\rangle &= \sqrt{n+1}\,|n+1\rangle\,, \quad \hat{a}^\dagger |0\rangle = |1\rangle\,, \\ (\hat{a}^\dagger |n\rangle)^\dagger &= \langle n|\,\hat{a} = \langle n+1|\,\sqrt{n+1}. \end{aligned} \tag{8.12}$$

These operators satisfy the following commutation relations of

$$\begin{aligned} [\hat{a}_i, \hat{a}_j^\dagger] &= \hat{a}_i \hat{a}_j^\dagger - \hat{a}_j^\dagger \hat{a}_i = \delta_{ij}, \\ [\hat{a}_i^\dagger, \hat{a}_j^\dagger] &= [\hat{a}_i, \hat{a}_j] = 0, \end{aligned} \tag{8.13}$$

where [,] denotes the commutator, and δ_{ij} is the Kronecker delta function.

The coherent perfect absorber in Fig. 8.1 mixes the input amplitudes and adds the Langevin noise operators $\hat{f}_C$ and $\hat{f}_D$ to preserve the commutation relations in Eq. 8.13. The resulting CPA transformation can be expressed as

$$\begin{pmatrix} \hat{a}_C \\ \hat{a}_D \end{pmatrix} = H_{\mathrm{CPA}} \begin{pmatrix} \hat{a}_A \\ \hat{a}_B \end{pmatrix} + \begin{pmatrix} \hat{f}_C \\ \hat{f}_D \end{pmatrix}, \tag{8.14}$$

where A and B (C and D) correspond to the input (output) fields of the absorber in Fig. 8.1 and non-unitary matrix H_{CPA} is defined as

$$H_{\mathrm{CPA}} = \frac{1}{2} \begin{pmatrix} 1 & -1 \\ -1 & 1 \end{pmatrix}, \tag{8.15}$$

as per its amplitude transmission and reflection coefficients for the travelling waves (see Eq. 7.7).

In our experiments, a photon is launched into the interferometer from input port A' with the vacuum state at input port B' (see Fig. 8.1). The photon subsequently propagates through a 50:50 beamsplitter, a phase shifter, the coherent perfect absorber, another phase shifter, and finally another 50:50 beamsplitter, respectively. The photon is finally detected by the single-photon detectors at the output ports C' and D'. If the phase delays induced by the phase modulators ϕ_1 and ϕ_2 are both set to ϕ, the complete transformation in a matrix form is read as

$$\begin{pmatrix} \hat{a}_{C'} \\ \hat{a}_{D'} \end{pmatrix} = H_{\mathrm{BS}}^{-1} \cdot H_{\mathrm{PS}}^{-1} \cdot \left[H_{\mathrm{CPA}} + \begin{pmatrix} \hat{f}_C \\ \hat{f}_D \end{pmatrix} \right] \cdot H_{\mathrm{PS}} \cdot H_{\mathrm{BS}} \begin{pmatrix} \hat{a}_{A'} \\ \hat{a}_{B'} \end{pmatrix}. \tag{8.16}$$

Equation 8.16 should be interpreted with caution. Here, the part of the equation that is in the right-hand side of the square bracket is not distributive. In other words, the column vector of the field operators after the multiplication with the beam splitter H_{BS} and phase shifter H_{PS} transfer matrices cannot be distributed over the CPA transfer matrix H_{CPA} and the column vector of the noise operators for multiplication operation since the multiplication of two column vectors is an invalid operation. The column vector of the field operators is multiplied with the CPA transfer matrix H_{CPA} only, and the noise operators at CPA output ports are added once the photon interacts with the metamaterial.

8.2.2 Expectation Values of Number Operators

Before proceeding to the calculations of the expectation values of the photon number at the output ports, we briefly introduce the particle number operator. The number of particles n in a given number state $|n\rangle$ can be obtained by the number operator $\hat{N}$ which is defined as

$$\hat{N} := \hat{a}^{\dagger}\hat{a}. \tag{8.17}$$

The number operator $\hat{N}$ is a Hermitian operator, i.e., $\hat{N} = \hat{N}^{\dagger}$. Acting on the Fock space, the number operator $\hat{N}$ counts the number of particles

$$\hat{N}\,|n\rangle = \hat{a}^{\dagger}\hat{a}\,|n\rangle = \hat{a}^{\dagger}\sqrt{n}\,|n-1\rangle = \sqrt{n}\hat{a}^{\dagger}\,|n-1\rangle = \sqrt{n}\sqrt{n}\,|n\rangle = n\,|n\rangle\,, \tag{8.18}$$

where $|n\rangle$ is the eigenfunction of the number operator $\hat{N}$ with the eigenvalue n. The expectation value of the number operator is then given by

$$\langle\hat{N}\rangle := \langle n|\hat{N}|n\rangle = n\,\langle n|n\rangle = n. \tag{8.19}$$

The expectation values of the number operators at the output ports are calculated by first evolving the field operators according to Eq. 8.16. The field operators evolve such that $\hat{a}_{C'}$ and $\hat{a}_{D'}$ are equal to

$$\begin{aligned} \hat{a}_{C'} &= \frac{1}{4}\left(M_1\hat{a}_{A'} + M_2\hat{a}_{B'}\right) + \cdots, \\ \hat{a}_{D'} &= \frac{1}{4}\left(M_3\hat{a}_{A'} + M_4\hat{a}_{B'}\right) + \cdots, \end{aligned} \tag{8.20}$$

where coefficients M_i are calculated from Eq. 8.16 as

$$
\begin{aligned}
M_1 &= -\left(e^{2i\phi} - 2ie^{i\phi} - 1\right), \\
M_2 &= -i\left(1 + e^{2i\phi}\right), \\
M_3 &= -i\left(1 + e^{2i\phi}\right), \\
M_4 &= e^{2i\phi} + 2ie^{i\phi} - 1.
\end{aligned}
\tag{8.21}
$$

In Eq. 8.20, "$\cdots$" symbols denote the contributions contained in the noise operators $\hat{f}_C$ and $\hat{f}_D$ (see Eq. 8.16), which later average out to zero and do not contribute to the final result [278].

By performing quantum mechanical averaging with the initial state $|1\rangle_{A'}|0\rangle_{B'}$ and using the relations in Eqs. 8.11 to 8.13, the expectation values of the number operators at the output ports C' and D' are calculated as

$$
\begin{aligned}
\langle \hat{N}_{C'} \rangle &= \langle \hat{a}^{\dagger}_{C'} \hat{a}_{C'} \rangle = \frac{1}{4}\left(1 - \sin(\phi)\right)^2, \\
\langle \hat{N}_{D'} \rangle &= \langle \hat{a}^{\dagger}_{D'} \hat{a}_{D'} \rangle = \frac{1}{8}\left(1 + \cos(2\phi)\right).
\end{aligned}
\tag{8.22}
$$

We note that the symmetric state is obtained when $\phi = (2n + 1/2)\pi$ because of the 50:50 beamsplitter that induces $\pi/2$ phase shift on the reflected field (see Fig. 8.1 and Eq. 8.9). In this phase delay, the expectation values of the number operators $\langle \hat{N}_{C'} \rangle$ and $\langle \hat{N}_{D'} \rangle$ are both equal to 0. On the other hand, for the antisymmetric state, which is obtained when $\phi = (2n - 1/2)\pi$, the expectation values of the number operators $\langle \hat{N}_{C'} \rangle$ and $\langle \hat{N}_{D'} \rangle$ are equal to 1 and 0, respectively. In other words, the expected mean photon number equals to 0 at both output ports when the input state is the symmetric superposition of the spatial wave functions, whereas the mean photon number becomes unity at the output port C' for the antisymmetric input state.

8.3 Experiment

We implemented the cascaded MZI configuration in Fig. 8.1 in a more compact way as shown in Fig. 8.2. This folded interferometer configuration brings the advantage of easier phase stabilization compared to an implementation with two separate interferometers. However, we note that the folded interferometer configuration does not allow us to scan the phase delays ϕ_1 and ϕ_2 in Fig. 8.1 independently; therefore, the same phase delay is applied during state preparation and state measurements cycles, i.e., $\phi_1 = \phi_2 = \phi$. The phase retardation between the interferometer arms is controlled via a fiber stretcher, which is denoted by ϕ in Fig. 8.2.

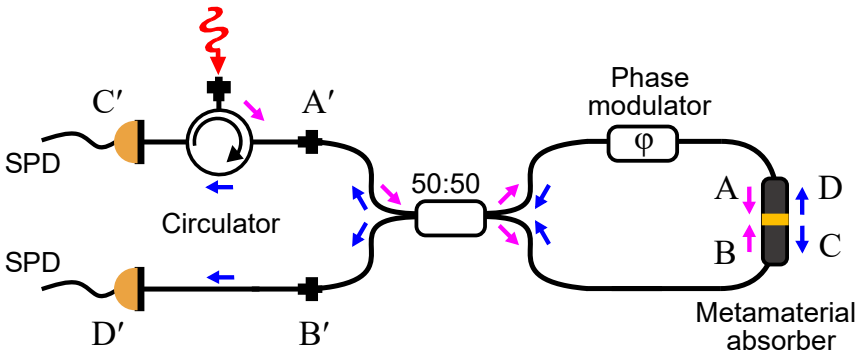

Figure 8.2: Experimental setup to implement the cascaded MZI configuration with optical fibers. The input ports A' and B' and output ports C' and D' correspond to the same port labels in Fig. 8.1. The arrows in magenta show the direction of the field incoming to the absorber, whereas the arrows in blue show the direction of the field after the absorber. The fiberized 50:50 beamsplitter induces $\pi/2$ phase shift on the cross port.

Here, an input photon launched into the setup from input port A' first traverses the interferometric path containing a beamsplitter, a phase modulator, and the coherent perfect absorber, respectively. Thereafter, the photon propagates through the second interferometric path containing the same phase modulator and the beamsplitter. The photon is finally detected by single-photon detectors located at output ports C' and D'.

A strongly attenuated CW laser at 810 nm is used as a photon source at the single-photon level (see § 6.3.1 for details.) Similar to the experimental setup shown in Fig. 7.2, an optical delay line is used to equal the lengths of interferometer arms. A variable attenuator is used to balance the optical losses in both arms (not shown in Fig. 8.2 for simplicity). We used our phase stabilization method to prevent any phase fluctuations. The quantum state measurements were subsequently performed by sampling single-photon detector counts at different phase points. Similar to § 6.2.1, the integration time window Δt is set to 24 ms.

Figure 8.3 shows the number of detected counts at each output port for different phase shift between the interferometer arms. The SPD counts at output port C' changes with $(1-\sin(\phi))^2/4$, whereas the SPD counts at output port D' varies with $(1+\cos(2\phi))/8$. Our experimental results show a good agreement with the calculated expectation values of number operators at the output ports in Eq. 8.22.

We note that each phase point in Fig. 8.3 corresponds to a different input state. Since we implemented the folded interferometer configuration, each input state is measured at the same phase delay ϕ that is used to generate that input state. For the antisymmetric input state, which only occurs at $\phi = 3\pi/2$ phase delay, the corresponding output state is only measured at this phase delay; $N_{C'}$ is at its maximum and $N_{D'}$ is almost zero at this point as Eq. 8.22

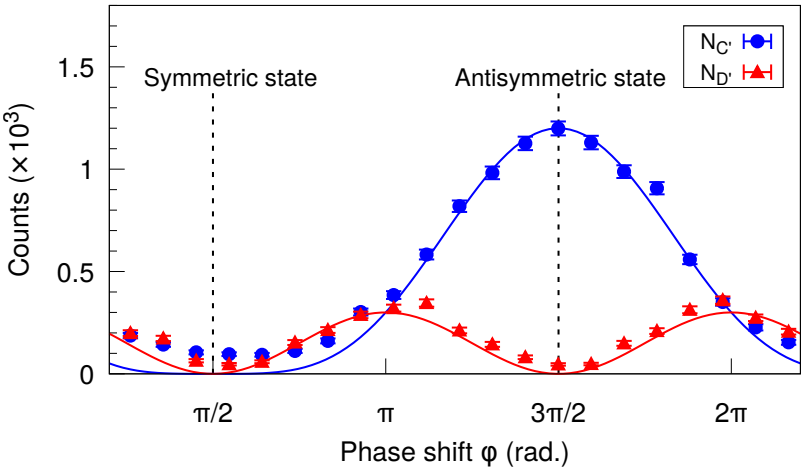

Figure 8.3: SPD counts at the output ports C' and D'. The counts are measured at different phase delays ϕ over an integration time window Δt of 24 ms. Error bars show the photon shot noise. The solid lines follow the expectation values of the number operators at the corresponding ports in Eq. 8.22.

predicted. Similarly, $\phi = \pi/2$ phase delay is the only point by which the symmetric input state is generated. At this phase delay, both $N_{C'}$ and $N_{D'}$ attain their minimum values, which were limited by single-photon detector dark counts and the metamaterial imperfections (see § 7.3).

The phase shift also modulates the probability amplitudes of the symmetric $|\psi^{(S)}\rangle$ and antisymmetric $|\psi^{(AS)}\rangle$ parts of the input wave function (see Eq. 8.6), and subsequently modulates the photon flux in the interferometer (Eq. 8.22). In order to account for this modulation, we normalized the number of counts detected at each port with the total number of detected counts (see Fig. 8.4). Here, the normalization is performed for the range of phase delays that result in high enough photon flux in the second interferometer. This region corresponds to the phase shifts from π to 2π radians in Fig. 8.3. The photon flux in the interferometer for the other half of the phase shift range (i.e., 0 to π radians) is so low that the effects of photon shot noise and single-photon detector dark counts become significant. This subsequently degrades the signal-to-noise ratio of the measured photon counts, and the uncertainty of the data is further increased once the normalization is performed due to the error propagation.

The experimental data shown in Fig. 8.4 indicates that the interference of the photons transmitted through the absorber generates the conventional single-photon interference fringe. We contrast this case with other scenarios for the sake of interpretation of the experimental results. If the output state after the absorber were incoherent, then the interference fringe

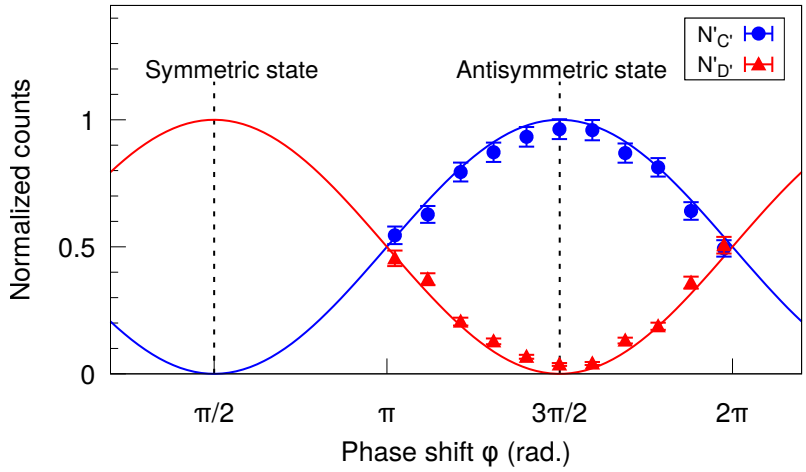

Figure 8.4: Normalized counts $N'_{C'}$ and $N'_{D'}$ at the output arms C' and D', respectively. The solid lines show the theoretical predictions. The error bars are calculated by propagating the photon shot noise.

would not have formed at all. Alternatively, if the output state after the metamaterial were coherent but varying with the input state, then the interference fringe would not have been a sinusoidal single-photon interference fringe as we obtained here. The experimental result obtained here is only possible if the output state of the photons after the metamaterial is always the same coherent state regardless of their input state.

The experimental results shown in Figs. 8.3 and 8.4 indicate that the metamaterial coherently transmits almost all the photons for a particular input state, whereas it almost totally absorbs all the photons when the input state is orthogonal to that particular input state. According to the designed reflection and transmission coefficients of the metamaterial for the travelling waves, these two states correspond to the antisymmetric state and symmetric state, respectively.

We note that the "symmetric" ("antisymmetric") label at $\pi/2$ ($3\pi/2$) radians phase shift in Figs. 8.3 and 8.4 represents the expected state based on the metamaterial design. The output state here was not explicitly measured through quantum state tomography, which requires measurements on all possible orthogonal basis states. Nevertheless, the metamaterial design ensures that the output state of the transmitted photons is always antisymmetric as per its transmission and reflection coefficients for the travelling waves (see Eq. 7.7). The absorber can also be designed in a way that it absorbs the antisymmetric input states and transmits only the symmetric input states. Such behavior can be obtained if the metamaterial is engineered to have $t = r = 1/2$.

8.4 Conclusion

In this chapter, we experimentally showed that a coherent perfect absorber in a phase-tunable coherent optical network can be used to manipulate quantum states of light. Here, we demonstrated filtering of quantum states of photons whose quantum information is encoded in superposition of two spatial modes. To achieve quantum state filtering action, we utilized the capability of our coherent perfect absorber to distinguish between the symmetric and antisymmetric superpositions of spatial wave functions. Our results agree well with the theoretical predictions. Such a filtering action can be useful in quantum information processing, for instance, in dual-rail encoding protocols.

In conclusion, utilizing coherent perfect absorption is a viable approach to extend the functionalities of optical networks for quantum light processing. Tailoring optical properties in designer metamaterials to accommodate target wavelengths can provide a universal processing platform for a variety of quantum states of light.

Chapter 9

Conclusion and Recommendations

Conclusion

In this thesis, we adopted a hybrid and modular approach for building an integrated photonics platform which comprises of on-chip quantum light sources, interferometric modulators equipped with coherent perfect absorbers, and single-photon detectors. On-chip detection of single photons at visible wavelengths and efficient phase stabilization of interferometers to enable coherent control of single photons are essential for our photonic integrated circuit design targeting on-chip LOQC applications.

In the first part of the thesis, we present our efforts towards development of waveguide-integrated single-photon avalanche diodes for visible wavelengths, which lacks in the literature. In this regard, we first developed a 2D Monte Carlo device simulator to optimize our device designs. Next, we fabricated and characterized our detectors. Operated in linear mode, we demonstrated a high gain-bandwidth product of 234 ± 14 GHz at 20 V reverse bias measured for 685 nm input light, with a low dark current of 0.12 μA. We also observe open eye diagrams at up to 56 Gbps. This performance is very competitive when benchmarked against other integrated APDs operating in the infrared range. With CMOS-compatible fabrication and integrability with silicon nitride platforms, our devices are attractive for visible-light photonics applications in sensing and communications.

Operated in Geiger-mode, the detectors are affected by high dark count rate. Our experimental results show that p-i-n^+ junction-based APDs with asymmetric rib waveguide structure, unlike p-n^+ junction-based devices, do not exhibit oversaturation by excessive dark counts. We provide an in-depth analysis about potential causes giving rise to such device saturation. The recommendations for improving the device performance are made, and they form the subject of the ongoing efforts in the lab.

In the second part of the thesis, we proposed single photon manipulation concepts utilizing coherent perfect absorption phenomenon, and then proved their applicability on a prototype coherent optical fiber network prior to their implementation in a photonic integrated circuit. The suppression of phase noise is of paramount importance to the coherent control of single photons through interferometric modulator systems. Here, we introduced and implemented an active phase stabilization scheme based on single-photon counting for coherent optical networks operating at the single-photon level. Our method can suppress the phase noise with a competitive phase stability of 0.07 radians with no need for auxiliary laser and additional optical components required in conventional approaches. By implementing our phase stabilization method to a coherent optical network containing a metamaterial-based coherent perfect absorber, we showed all-optical single-photon switching with a visibility close to 80%. We further extended our phase-stabilized coherent optical network into a cascaded Mach-Zehnder interferometer (MZI) in order to demonstrate that coherent perfect absorption can be utilized to filter quantum states of photons whose quantum information is encoded in superposition of two spatial modes, i.e., dual-rail photons.

These successful demonstrations verify that coherent perfect absorption is a viable approach to modulate quantum states of light in coherent optical networks, while providing flexibilities to engineer the optical properties to accommodate target wavelengths. Such extended functionalities can provide a universal processing platform for linear optical quantum computing with a variety of quantum states of light.

Recommendations for Further Research

In § 5.4.2.1, we recommended various methods to reduce high dark count rates observed in our waveguide-integrated APDs. Unlike p-n^+ junction-based devices with a symmetric rib waveguide structure, our experimental results show that p-i-n^+ junction-based devices with an asymmetric rib waveguide structure do not exhibit oversaturation by excessive dark counts. This improvement on DCR performance most likely originates from the reduced peak electric field strength enabled by the introduction of the intrinsic region between p- and n^+-doped regions as well as the reduced hot carrier injection into the oxide/silicon interface in the asymmetric rib waveguide geometry. Such hot carrier injection is also the likely reason for the breakdown voltage walkout observed in our devices. Therefore, we suggest that the future research should focus on the design ideas and fabrication methods outlined in § 5.4.2.1 to mitigate such adverse effects.

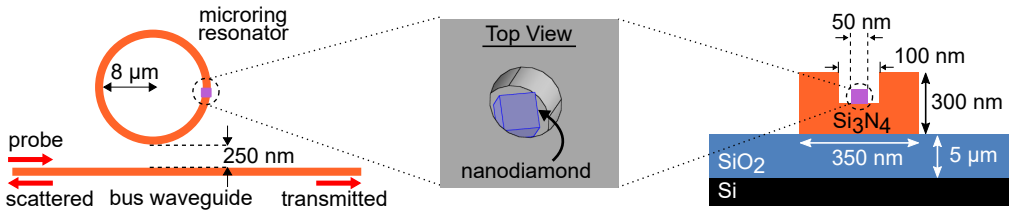

Figure 9.1: a) Our photonic integrated circuit will use nanodiamonds with silicon-vacancy (SiV) centers as single-photon sources. The nanodiamonds are positioned inside a high Q-factor SiN microring resonators, for which a typical set of device parameters is shown.

Quenching electronics and electrical connectivity significantly affect the Geiger-mode APD performance. In this regard, we suggested two methods to mitigate the device saturation: wire bonding and passive-quenching active-reset (PQAR) circuit. Wire bonding can be beneficial to reduce the parasitic capacitance and hence the dark count rate (see § 5.4.2.1). The PQAR circuit, on the other hand, can accelerate the slow voltage recovery transition of the conventional passive reset schemes, and consequently increase the saturation threshold of the device (see § 5.4.2.1). This might be useful for comparing the actual noise performance of different devices for future design optimization.

Following the achievement of Geiger-mode operation, the research effort will be geared towards integrating waveguide-integrated SPADs with single-photon sources, e.g., nanodiamonds with color centers, and other SiN photonic devices on a SOI photonic platform as introduced in Fig. 1.1.

The silicon-vacancy (SiV) center in diamond has attractive properties such as high brightness, nearly lifetime-limited optical linewidths, and insensitivity to environmental electrical noise [283]. In our hybrid integrated quantum photonics circuit concept, the nanodiamonds containing such SiV centers will be positioned inside the high-Q factor SiN microring photonic cavities in order to enhance the light-matter interaction (Fig. 9.1). Assuming a nanodiamond cube within a circular hole inside the microring resonator and a single dipole at the center of the nanodiamond, our FDTD simulations suggest a Purcell factor of 15, indicating an enhanced coupling between the color center and the high-Q factor resonator (Fig. 9.2). Single photons emitted from these SiV centers will evanescently couple to the SiN bus waveguides and then propagate into a SiN waveguide beamsplitter. The output ports of the interferometer are waveguide-coupled to the silicon waveguide-integrated SPADs on the same layer.

Here, the proof-of-principle demonstration of this platform is to observe Hong-Ou-Mandel (HOM) interference, which is a two-photon interference effect in quantum optics with no classical analogue [284]. The observation of HOM effect would indicate that

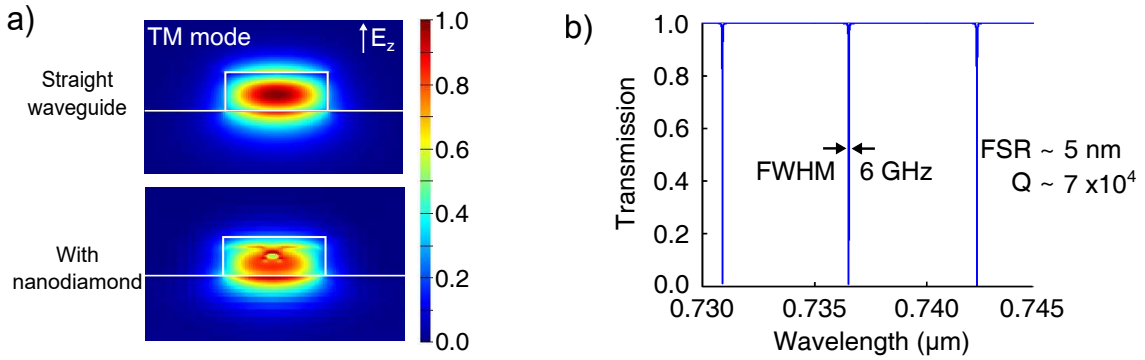

Figure 9.2: a) Cross-section electric field intensity profiles along the straight waveguide and at the position of the nanodiamond. b) Simulated transmission spectrum of the microring resonator device.

the photons emitted from two distinct SiV centers are indistinguishable. Such on-demand generation of indistinguishable photons, together with the entanglement between them, is prerequisite to realize quantum information processing.

The successful demonstration of on-chip two-photon interference will show the viability of our photonic chip to be used as a crucial building block for quantum networks [285]. In Appendix B, we present our experimental efforts to couple single photons from an alternative submicron-sized diamond with a color center to a SiN microring resonator. Specifically, we developed a photon coupling procedure for a diamond nanopillar with a nitrogen-vacancy (NV) center to study the coupling dynamics of a similar system.

In the second part of the thesis, we first developed a phase stabilization method for coherent optical networks operating at the single-photon level. Our phase stabilization method allowed us to demonstrate all-optical single-photon switching (Chapter 7) and quantum state filtering (Chapter 8) via interferometric modulators equipped with plasmonic coherent perfect absorbers. Having successfully proved the applicability of our concepts in a fiberized testbed, we recommend that the future research should focus on implementing these functionalities on a photonic integrated circuit to realize complete on-chip single-photon processing.

To explore the idea of on-chip coherent perfect absorber, we performed a preliminary numerical study on a simple waveguide model described in [1]. The approximate conditions for coherent perfect absorption at the telecommunication C-band were numerically shown to be achievable using realistic structures that consist of simple arrays of resonant gold and aluminum plasmonic nanoantennas on silicon-on-insulator (SOI) photonic waveguides [1].

For our preliminary investigation here, we studied a 400-nm-wide and 220-nm-thick silicon waveguide whose top surface is loaded with 3 rows of trimer gold nanoantennas with

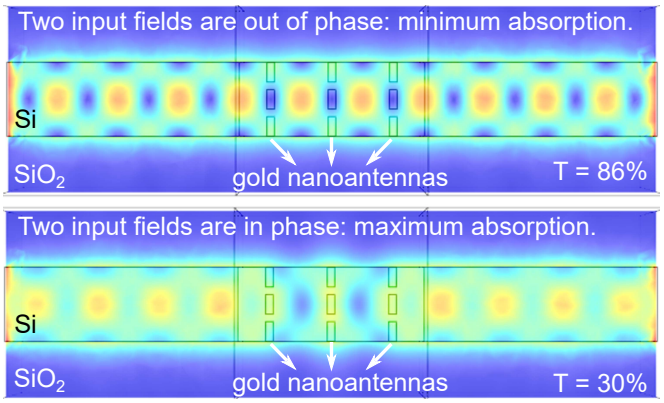

Figure 9.3: Preliminary FDTD simulations of plasmonic nanoantennas on top of silicon waveguides for integrated CPA interferometer.

optimized dimensions [1] at the center. By performing FDTD simulations at 1550 nm, we studied the transmission of the structure when the light is launched into the TE mode of the waveguide from both ends with different phase shifts in between (see Fig. 9.3).

When the two light fields are in phase such that they constructively interfere at the CPA location, the interaction of the light fields with the plasmonic nanoantennas is at its highest level so that the maximum absorption occurs. The other limiting case takes place when the two light fields are out of phase by π radians at the CPA location; the light fields minimally interact with the CPA, and subsequently the minimum absorption occurs. Figure 9.3 shows that the transmission reduces from 86% to 30% when the relative phase between the two light fields changes from π to 0 radians. The improved photon absorption enabled by the coherent interactions of the light with the plasmonic nanoantenna array indicates the viability of the on-chip coherent perfect absorption concept.

Tuning the design parameters of gold nanoantenna arrays and their positioning on the waveguides, the operation wavelength of such on-chip coherent perfect absorbers can further be extended to the visible spectrum where diamond color centers operate. Such a hybrid integration method provides opportunities to implement our previous in-fiber experiments in a scalable photonic integrated circuit, and it paves the way towards implementing on-chip linear optical quantum computing protocols with integrated quantum information readout capability.

Closing Remarks

We have shown significant progress in the engineering of individual photonic components such as waveguide-integrated APDs, microresonators, bus waveguides, and coherent perfect absorbers to achieve single photon manipulation and detection. Hybrid integration methods (e.g., transfer printing, die bonding, and pick-and-place transfer) can be used to integrate single-photon sources and plasmonic nanoantennas with our photonics platform. Besides, the quantum frequency conversion capability with nonlinear SiN nanophotonic cavities can further be utilized to create coherent optical interfaces between different physical systems.

Harnessing the functionality of each physical system for storage, processing, and readout of quantum information, such hybrid photonics approaches provide a viable path towards a scalable quantum information processing platform. Overcoming the device engineering and hybrid integration challenges as well as the compatibility requirements for different material systems and operating conditions would turn this vision into a reality.

Author's Publications

The main results of this thesis have been reported in the following articles:

1. **SALIH YANIKGONUL**, VICTOR LEONG, JUN RONG ONG, TING HU, SHAWN YOHANES SIEW, CHING ENG PNG, AND LEONID KRIVITSKY. Integrated Avalanche Photodetectors for Visible Light. *Nat. Commun* **12**, 1834 (2021).

2. **SALIH YANIKGONUL**, RUIXIANG GUO, ANGELOS XOMALIS, ANTON N. VETLUGIN, GIORGIO ADAMO, CESARE SOCI, AND NIKOLAY I. ZHELUDEV. Phase stabilization of a coherent fiber network by single-photon counting. *Opt. Lett.* **45**, 2740-2743 (2020).

3. **SALIH YANIKGONUL**, VICTOR LEONG, JUN RONG ONG, CHING ENG PNG, AND LEONID KRIVITSKY. Simulation of silicon waveguide-based single-photon avalanche detectors for integrated photonic applications. *IEEE J. Sel. Top. Quantum Electron* **26**, 2 (2020).

4. ANTON N. VETLUGIN, RUIXIANG GUO, ANGELOS XOMALIS, **SALIH YANIKGONUL**, GIORGIO ADAMO, CESARE SOCI, AND NIKOLAY I. ZHELUDEV. Coherent perfect absorption of single photons in a fiber network. *Appl. Phys. Lett* **115**, 191101 (2019).

5. **SALIH YANIKGONUL**, VICTOR LEONG, JUN RONG ONG, CHING ENG PNG, AND LEONID KRIVITSKY. 2D Monte Carlo simulation of a silicon waveguide-based single-photon avalanche diode for visible wavelengths. *Opt. Express* **26**, 15232-15246 (2018).

The results have also been presented at the following international conferences:

1. **[Invited Talk] SALIH YANIKGONUL**, VICTOR LEONG, JUN RONG ONG, LEONID KRIVITSKY. Silicon Waveguide Single-Photon Avalanche Detectors for Integrated Quantum Photonics. *Institute of Physics Singapore (IPS) Meeting*, Singapore (2020).

2. **[Poster] SALIH YANIKGONUL**, GUO RUIXIANG, ANGELOS XOMALIS, ANTON N. VETLUGIN, GIORGIO ADAMO, CESARE SOCI AND NIKOLAY I. ZHELUDEV Phase stabilization of a coherent fibre network by single-photon counting. *Institute of Physics Singapore (IPS) Meeting*, Singapore (2020).

3. **[Poster] SALIH YANIKGONUL**, VICTOR LEONG, JUN RONG ONG, LEONID KRIVITSKY. Single-photon Avalanche Diodes for Scalable Integrated Quantum Photonics. *Institute of Physics Singapore (IPS) Meeting*, Singapore (2020).

4. **[Poster] SALIH YANIKGONUL**, ANTON N. VETLUGIN, RUIXIANG GUO, ANGELOS XOMALIS, GIORGIO ADAMO, CESARE SOCI, AND NIKOLAY I. ZHELUDEV. Phase Stabilization of a Coherent Fibre Network by Single-photon Counting. *3rd International Workshop on Quantum and Topological Nanophotonics (QTN)*, Singapore (2019).

5. **[Talk]** ANTON N. VETLUGIN, ANGELOS XOMALIS, **SALIH YANIKGONUL**, RUIXIANG GUO, GIORGIO ADAMO, IOSIF DEMIRTZIOGLOU, YONGMIN JUNG, ERIC PLUM, COSIMO LACAVA, PERIKLIS PETROPOULOS, DAVID RICHARDSON, CESARE SOCI, AND NIKOLAY I. ZHELUDEV. Metamaterials for classical and quantum data processing in all-optical fiber information networks *13th International Congress on Artificial Materials for Novel Wave Phenomena*, Italy (2019).

6. **[Talk]** ANTON N. VETLUGIN, **SALIH YANIKGONUL**, ANGELOS XOMALIS, RUIXIANG GUO, GIORGIO ADAMO, CESARE SOCI, AND NIKOLAY I. ZHELUDEV. Filtering of quantum states with plasmonic metamaterial absorber. *Nanometa*, Seefeld, Austria (2019).

7. **[Invited Talk]** ANTON N. VETLUGIN, **SALIH YANIKGONUL**, RUIXIANG GUO, ANGELOS XOMALIS, GIORGIO ADAMO, CESARE SOCI, AND NIKOLAY I. ZHELUDEV. Quantum light manipulation with fiberized metamaterial perfect absorber *SPIE Optics and Photonics*, USA (2019).

8. **[Talk]** ANTON N. VETLUGIN, **SALIH YANIKGONUL**, RUIXIANG GUO, ANGELOS XOMALIS, CESARE SOCI, AND NIKOLAY I. ZHELUDEV. Coherent Processing of Quantum Light with Plasmonic Metamaterial *International Conference on. Materials for Advanced Technologies (ICMAT)*, Singapore (2019).

9. **[Talk] SALIH YANIKGONUL**, ANTON N. VETLUGIN, RUIXIANG GUO, ANGELOS XOMALIS, GIORGIO ADAMO, CESARE SOCI, AND NIKOLAY I. ZHELUDEV. Quantum State Filtering of Dual-rail Photons with Fiberized Plasmonic Metamaterial *Conference on Lasers and Electro - Optics (CLEO)*, San Jose, CA, USA (2019).

10. **[Talk]** ANTON N. VETLUGIN, **SALIH YANIKGONUL**, RUIXIANG GUO, ANGELOS XOMALIS, CESARE SOCI, AND NIKOLAY I. ZHELUDEV. Metamaterial absorber for dual-rail photonic qubit filtering *Institute of Physics Singapore (IPS) Meeting*, Singapore (2019).

11. **[Talk] SALIH YANIKGONUL**, ANTON N. VETLUGIN, RUIXIANG GUO, ANGELOS XOMALIS, CESARE SOCI, AND NIKOLAY I. ZHELUDEV. Coherent fibre network stabilized with single-photons *Institute of Physics Singapore (IPS) Meeting*, Singapore (2019).

12. **[Poster-Awarded] SALIH YANIKGONUL**, VICTOR LEONG, JUN RONG ONG, AND LEONID KRIVITSKY. 2D Monte Carlo Study of p-n+ and p-i-n+ Silicon Waveguide-based Single-photon Avalanche Diodes for Visible Wavelengths. *Institute of Physics Singapore (IPS) Meeting*, Singapore (2019).

13. **[Talk]** ANTON N. VETLUGIN, **SALIH YANIKGONUL**, ANGELOS XOMALIS, RUIXIANG GUO, GIORGIO ADAMO, CESARE SOCI, AND NIKOLAY I. ZHELUDEV. Plasmonic coherent perfect absorption and switching in a fiberized quantum network. *Quantum Technology International Conference (QTech)*, Paris, France, (2018).

14. **[Talk]** ANTON N. VETLUGIN, RUIXIANG GUO, ANGELOS XOMALIS, **SALIH YANIKGONUL**, GIORGIO ADAMO, CESARE SOCI, AND NIKOLAY I. ZHELUDEV. Coherent perfect absorption and switching in a fiberized quantum network with plasmonic metadevice. *12th International Congress on Artificial Materials for Novel Wave Phenomena*, Espoo, Finland (2018).

15. **[Talk] SALIH YANIKGONUL**, RUIXIANG GUO, ANGELOS XOMALIS, ANTON N. VETLUGIN, GIORGIO ADAMO, CESARE SOCI, AND NIKOLAY I. ZHELUDEV. Stabi-

lized dissipative single-photon switch for fiberized quantum networks. *1st Advances in Quantum Engineering International Meeting (AQE2018)*, Singapore (2018).

16. **[Invited Talk]** VICTOR LEONG, DMITRY KALASHNIKOV, SUMIN CHOI, JIBO DAI, **SALIH YANIKGONUL**, ALAGAPPAN GANDHI, JUNRONG ONG, TING HU, DORIS KT NG, LEONID KRIVITSKY. Towards a Quantum Nanophotonics Platform: Nanodiamond-on-chip Devices and Integrated Single-Photon Detectors. *1st Advances in Quantum Engineering International Meeting (AQE2018)*, Singapore (2018).

17. **[Poster]** **SALIH YANIKGONUL**, JUN RONG ONG, VICTOR LEONG, AND LEONID KRIVITSKY. Towards a Waveguide-based Single Photon Detector for Integrated Quantum Photonics Platforms. *Conference on Lasers and Electro - Optics (CLEO)*, San Jose, CA, USA (2018).

18. **[Poster]** **SALIH YANIKGONUL**, JUN RONG ONG, VICTOR LEONG, AND LEONID KRIVITSKY. 2D Monte Carlo simulation of CMOS-compatible waveguide-based single-photon avalanche diode for visible wavelengths. *2nd International Workshop on Quantum and Topological Nanophotonics (QTN)*, Singapore (2018).

19. **[Poster]** ANTON N. VETLUGIN, **SALIH YANIKGONUL**, ANGELOS XOMALIS, RUIXIANG GUO, CESARE SOCI, AND NIKOLAY I. ZHELUDEV. Fully fiberized dissipative single photon switch. *2nd International Workshop on Quantum and Topological Nanophotonics (QTN)*, Singapore (2018).

20. **[Talk]** RUIXIANG GUO, ANTON N. VETLUGIN, MIKHAIL V. SHESTAKOV, **SALIH YANIKGONUL**, VENKATRAM NALLA, CESARE SOCI AND NIKOLAY I. ZHELUDEV Nanophotonic Quantum Devices Realized in Fibers and on Chips. *Institute of Physics Singapore (IPS) Meeting*, Singapore (2018).

21. **[Poster]** **SALIH YANIKGONUL**, JUN RONG ONG, VICTOR LEONG, AND LEONID KRIVITSKY. 2D Monte Carlo simulation of CMOS-compatible waveguide-based single-photon avalanche diode for visible wavelengths. *Institute of Physics Singapore (IPS) Meeting*, Singapore (2018).

22. **[Poster]** **SALIH YANIKGONUL**, JUN RONG ONG, VICTOR LEONG, AND LEONID KRIVITSKY. Towards a Waveguide-based Single Photon Detector for Integrated Quantum Photonics Platforms. *Centre for Quantum Technologies 10th Anniversary Meeting*, Singapore (2017).

23. **[Poster] SALIH YANIKGONUL**, JUN RONG ONG, VICTOR LEONG, AND LEONID KRIVITSKY. Towards a Waveguide-based Single Photon Detector for Integrated Quantum Photonics Platforms. *Single Photon Workshop 2017*, Boulder, CO, USA (2017).

Bibliography

[1] R. Bruck and O. L. Muskens, "Plasmonic nanoantennas as integrated coherent perfect absorbers on soi waveguides for modulators and all-optical switches," *Opt. Express*, vol. 21, pp. 27652–27661, Nov 2013.

[2] C. M. Natarajan, M. G. Tanner, and R. H. Hadfield, "Superconducting nanowire single-photon detectors: physics and applications," *Superconductor Science and Technology*, vol. 25, p. 063001, Apr. 2012.

[3] S. Cova, M. Ghioni, A. Lacaita, C. Samori, and F. Zappa, "Avalanche photodiodes and quenching circuits for single-photon detection," *Appl. Opt.*, vol. 35, pp. 1956–1976, Apr 1996.

[4] L. Z. Jie and C. Kurtsiefer, "Characterisation of single photon avalanche detectors," 2016.

[5] M. Stipčević, H. Skenderović, and D. Gracin, "Characterization of a novel avalanche photodiode for single photon detection in vis-nir range," *Opt. Express*, vol. 18, pp. 17448–17459, Aug 2010.

[6] S.-B. Cho and T.-G. Noh, "Stabilization of a long-armed fiber-optic single-photon interferometer," *Opt. Express*, vol. 17, pp. 19027–19032, Oct 2009.

[7] G. B. Xavier and J. P. von der Weid, "Stable single-photon interference in a 1 km fiber-optic mach–zehnder interferometer with continuous phase adjustment," *Opt. Lett.*, vol. 36, pp. 1764–1766, May 2011.

[8] S.-B. Cho and H. Kim, "Active stabilization of a fiber-optic two-photon interferometer using continuous optical length control," *Opt. Express*, vol. 24, pp. 10980–10986, May 2016.

[9] V. ŠVARC, "Aktivní fázová stabilizace vláknových interferometrů pro měření na jednofotonové úrovni," Master's thesis, Katedra optiky, Univerzita Palackého, 2018. Diplomové práce.

[10] J. R. Ong, T. Y. L. Ang, G. Alagappan, C. H. Son, S. T. Lim, and C. E. Png, "Silicon nitride double-tip fiber-to-waveguide edge couplers at visible wavelengths," in *2017 Conference on Lasers and Electro-Optics Pacific Rim*, p. s1840, Optical Society of America, 2017.

[11] "Qzabre." qzabre.com, 2020. [Online; accessed 20-June-2020].

[12] P. W. Shor, "Polynomial-time algorithms for prime factorization and discrete logarithms on a quantum computer," *SIAM review*, vol. 41, no. 2, pp. 303–332, 1999.

[13] J. Preskill, "Quantum computing in the NISQ era and beyond," *Quantum*, vol. 2, p. 79, Aug. 2018.

[14] E. Martín-López, A. Laing, T. Lawson, R. Alvarez, X.-Q. Zhou, and J. L. O'Brien, "Experimental realization of shor's quantum factoring algorithm using qubit recycling," *Nature Photonics*, vol. 6, pp. 773–776, Oct. 2012.

[15] E. Lucero, R. Barends, Y. Chen, J. Kelly, M. Mariantoni, A. Megrant, P. O'Malley, D. Sank, A. Vainsencher, J. Wenner, T. White, Y. Yin, A. N. Cleland, and J. M. Martinis, "Computing prime factors with a josephson phase qubit quantum processor," *Nature Physics*, vol. 8, pp. 719–723, Aug. 2012.

[16] F. Arute, K. Arya, R. Babbush, D. Bacon, J. C. Bardin, R. Barends, R. Biswas, S. Boixo, F. G. S. L. Brandao, D. A. Buell, B. Burkett, Y. Chen, Z. Chen, B. Chiaro, R. Collins, W. Courtney, A. Dunsworth, E. Farhi, B. Foxen, A. Fowler, C. Gidney, M. Giustina, R. Graff, K. Guerin, S. Habegger, M. P. Harrigan, M. J. Hartmann, A. Ho, M. Hoffmann, T. Huang, T. S. Humble, S. V. Isakov, E. Jeffrey, Z. Jiang, D. Kafri, K. Kechedzhi, J. Kelly, P. V. Klimov, S. Knysh, A. Korotkov, F. Kostritsa, D. Landhuis, M. Lindmark, E. Lucero, D. Lyakh, S. Mandrà, J. R. McClean, M. McEwen, A. Megrant, X. Mi, K. Michielsen, M. Mohseni, J. Mutus, O. Naaman, M. Neeley, C. Neill, M. Y. Niu, E. Ostby, A. Petukhov, J. C. Platt, C. Quintana, E. G. Rieffel, P. Roushan, N. C. Rubin, D. Sank, K. J. Satzinger, V. Smelyanskiy, K. J. Sung, M. D. Trevithick, A. Vainsencher, B. Villalonga, T. White, Z. J. Yao, P. Yeh, A. Zalcman, H. Neven, and J. M. Martinis, "Quantum supremacy using a programmable superconducting processor," *Nature*, vol. 574, pp. 505–510, Oct. 2019.

[17] C. H. Bennett and G. Brassard, "Quantum cryptography: Public key distribution and coin tossing," *Theoretical Computer Science*, vol. 560, pp. 7–11, Dec. 2014.

[18] A. K. Ekert, "Quantum cryptography based on bell's theorem," *Phys. Rev. Lett.*, vol. 67, pp. 661–663, Aug 1991.

[19] C. H. Bennett, F. Bessette, G. Brassard, L. Salvail, and J. Smolin, "Experimental quantum cryptography," *Journal of Cryptology*, vol. 5, pp. 3–28, Jan. 1992.

[20] E. Waks, K. Inoue, C. Santori, D. Fattal, J. Vuckovic, G. S. Solomon, and Y. Yamamoto, "Secure communication: Quantum cryptography with a photon turnstile," *Nature*, vol. 420, no. 6917, pp. 762–762, 2002.

[21] M. Minder, M. Pittaluga, G. L. Roberts, M. Lucamarini, J. F. Dynes, Z. L. Yuan, and A. J. Shields, "Experimental quantum key distribution beyond the repeaterless secret key capacity," *Nature Photonics*, vol. 13, pp. 334–338, Mar. 2019.

[22] R. P. Feynman, "Simulating physics with computers," *International journal of theoretical physics*, vol. 21, no. 6, pp. 467–488, 1982.

[23] P. J. J. O'Malley, R. Babbush, I. D. Kivlichan, J. Romero, J. R. McClean, R. Barends, J. Kelly, P. Roushan, A. Tranter, N. Ding, B. Campbell, Y. Chen, Z. Chen, B. Chiaro, A. Dunsworth, A. G. Fowler, E. Jeffrey, E. Lucero, A. Megrant, J. Y. Mutus, M. Neeley, C. Neill, C. Quintana, D. Sank, A. Vainsencher, J. Wenner, T. C. White, P. V. Coveney, P. J. Love, H. Neven, A. Aspuru-Guzik, and J. M. Martinis, "Scalable quantum simulation of molecular energies," *Phys. Rev. X*, vol. 6, p. 031007, Jul 2016.

[24] G. H. Low and I. L. Chuang, "Optimal hamiltonian simulation by quantum signal processing," *Physical Review Letters*, vol. 118, Jan. 2017.

[25] A. M. Childs, D. Maslov, Y. Nam, N. J. Ross, and Y. Su, "Toward the first quantum simulation with quantum speedup," *Proceedings of the National Academy of Sciences*, vol. 115, no. 38, pp. 9456–9461, 2018.

[26] V. Giovannetti, S. Lloyd, and L. Maccone, "Quantum-enhanced measurements: beating the standard quantum limit," *Science*, vol. 306, no. 5700, pp. 1330–1336, 2004.

[27] C. L. Degen, F. Reinhard, and P. Cappellaro, "Quantum sensing," *Rev. Mod. Phys.*, vol. 89, p. 035002, Jul 2017.

[28] A. M. Wojciechowski, M. Karadas, C. Osterkamp, S. Jankuhn, J. Meijer, F. Jelezko, A. Huck, and U. L. Andersen, "Precision temperature sensing in the presence of magnetic field noise and vice-versa using nitrogen-vacancy centers in diamond," *Applied Physics Letters*, vol. 113, p. 013502, July 2018.

[29] J. Holzgrafe, Q. Gu, J. Beitner, D. M. Kara, H. S. Knowles, and M. Atatüre, "Nanoscale nmr spectroscopy using nanodiamond quantum sensors," *Phys. Rev. Applied*, vol. 13, p. 044004, Apr 2020.

[30] D. Castelvecchi, "Europe shows first cards in €1-billion quantum bet," *Nature*, vol. 563, pp. 14–15, Oct. 2018.

[31] C. Monroe, M. G. Raymer, and J. Taylor, "The u.s. national quantum initiative: From act to action," *Science*, vol. 364, no. 6439, pp. 440–442, 2019.

[32] Q. Schiermeier, "Russia joins race to make quantum dreams a reality," *Nature*, vol. 577, pp. 14–14, Dec. 2019.

[33] Q. Zhang, F. Xu, L. Li, N.-L. Liu, and J.-W. Pan, "Quantum information research in china," *Quantum Science and Technology*, vol. 4, p. 040503, nov 2019.

[34] T. V. Padma, "India bets big on quantum technology," *Nature*, Feb. 2020.

[35] J. Preskill, "Quantum computing and the entanglement frontier," 2012.

[36] D. Wecker, B. Bauer, B. K. Clark, M. B. Hastings, and M. Troyer, "Gate-count estimates for performing quantum chemistry on small quantum computers," *Phys. Rev. A*, vol. 90, p. 022305, Aug 2014.

[37] S. J. Devitt, W. J. Munro, and K. Nemoto, "Quantum error correction for beginners," *Reports on Progress in Physics*, vol. 76, no. 7, p. 076001, 2013.

[38] H. J. Kimble, "The quantum internet," *Nature*, vol. 453, no. 7198, p. 1023, 2008.

[39] C. Monroe, R. Raussendorf, A. Ruthven, K. R. Brown, P. Maunz, L.-M. Duan, and J. Kim, "Large-scale modular quantum-computer architecture with atomic memory and photonic interconnects," *Phys. Rev. A*, vol. 89, p. 022317, Feb 2014.

[40] S. Wehner, D. Elkouss, and R. Hanson, "Quantum internet: A vision for the road ahead," *Science*, vol. 362, no. 6412, 2018.

[41] J. Clarke and F. K. Wilhelm, "Superconducting quantum bits," *Nature*, vol. 453, no. 7198, pp. 1031–1042, 2008.

[42] J. M. Gambetta, J. M. Chow, and M. Steffen, "Building logical qubits in a superconducting quantum computing system," *npj Quantum Information*, vol. 3, Jan. 2017.

[43] P. Kurpiers, P. Magnard, T. Walter, B. Royer, M. Pechal, J. Heinsoo, Y. Salathé, A. Akin, S. Storz, J.-C. Besse, S. Gasparinetti, A. Blais, and A. Wallraff, "Deterministic quantum state transfer and remote entanglement using microwave photons," *Nature*, vol. 558, pp. 264–267, June 2018.

[44] G. J. Mooney, C. D. Hill, and L. C. L. Hollenberg, "Entanglement in a 20-qubit superconducting quantum computer," *Scientific Reports*, vol. 9, Sept. 2019.

[45] D. Loss and D. P. DiVincenzo, "Quantum computation with quantum dots," *Phys. Rev. A*, vol. 57, pp. 120–126, Jan 1998.

[46] J. Yoneda, K. Takeda, T. Otsuka, T. Nakajima, M. R. Delbecq, G. Allison, T. Honda, T. Kodera, S. Oda, Y. Hoshi, N. Usami, K. M. Itoh, and S. Tarucha, "A quantum-dot spin qubit with coherence limited by charge noise and fidelity higher than 99.9%," *Nature Nanotechnology*, vol. 13, pp. 102–106, Dec. 2017.

[47] T. F. Watson, S. G. J. Philips, E. Kawakami, D. R. Ward, P. Scarlino, M. Veldhorst, D. E. Savage, M. G. Lagally, M. Friesen, S. N. Coppersmith, M. A. Eriksson, and L. M. K. Vandersypen, "A programmable two-qubit quantum processor in silicon," *Nature*, vol. 555, pp. 633–637, Feb. 2018.

[48] P. Neumann, N. Mizuochi, F. Rempp, P. Hemmer, H. Watanabe, S. Yamasaki, V. Jacques, T. Gaebel, F. Jelezko, and J. Wrachtrup, "Multipartite entanglement among single spins in diamond," *Science*, vol. 320, no. 5881, pp. 1326–1329, 2008.

[49] A. Sipahigil, R. E. Evans, D. D. Sukachev, M. J. Burek, J. Borregaard, M. K. Bhaskar, C. T. Nguyen, J. L. Pacheco, H. A. Atikian, C. Meuwly, R. M. Camacho, F. Jelezko, E. Bielejec, H. Park, M. Lončar, and M. D. Lukin, "An integrated diamond nanophotonics platform for quantum-optical networks," *Science*, vol. 354, no. 6314, pp. 847–850, 2016.

[50] N. Kalb, A. A. Reiserer, P. C. Humphreys, J. J. W. Bakermans, S. J. Kamerling, N. H. Nickerson, S. C. Benjamin, D. J. Twitchen, M. Markham, and R. Hanson,

"Entanglement distillation between solid-state quantum network nodes," *Science*, vol. 356, no. 6341, pp. 928–932, 2017.

[51] J. I. Cirac and P. Zoller, "Quantum computations with cold trapped ions," *Phys. Rev. Lett.*, vol. 74, pp. 4091–4094, May 1995.

[52] H. Häffner, C. F. Roos, and R. Blatt, "Quantum computing with trapped ions," *Physics reports*, vol. 469, no. 4, pp. 155–203, 2008.

[53] C. Figgatt, A. Ostrander, N. M. Linke, K. A. Landsman, D. Zhu, D. Maslov, and C. Monroe, "Parallel entangling operations on a universal ion-trap quantum computer," *Nature*, vol. 572, pp. 368–372, July 2019.

[54] T. Zhong, J. M. Kindem, J. G. Bartholomew, J. Rochman, I. Craiciu, E. Miyazono, M. Bettinelli, E. Cavalli, V. Verma, S. W. Nam, F. Marsili, M. D. Shaw, A. D. Beyer, and A. Faraon, "Nanophotonic rare-earth quantum memory with optically controlled retrieval," *Science*, vol. 357, no. 6358, pp. 1392–1395, 2017.

[55] D. Serrano, J. Karlsson, A. Fossati, A. Ferrier, and P. Goldner, "All-optical control of long-lived nuclear spins in rare-earth doped nanoparticles," *Nature Communications*, vol. 9, May 2018.

[56] M. Saffman, "Quantum computing with atomic qubits and rydberg interactions: progress and challenges," *Journal of Physics B: Atomic, Molecular and Optical Physics*, vol. 49, no. 20, p. 202001, 2016.

[57] M. Saffman, "Quantum computing with neutral atoms," *National Science Review*, vol. 6, pp. 24–25, 09 2018.

[58] T. M. Graham, M. Kwon, B. Grinkemeyer, Z. Marra, X. Jiang, M. T. Lichtman, Y. Sun, M. Ebert, and M. Saffman, "Rydberg-mediated entanglement in a two-dimensional neutral atom qubit array," *Phys. Rev. Lett.*, vol. 123, p. 230501, Dec 2019.

[59] E. Knill, R. Laflamme, and G. J. Milburn, "A scheme for efficient quantum computation with linear optics," *Nature*, vol. 409, pp. 46–52, Jan. 2001.

[60] P. Kok, W. J. Munro, K. Nemoto, T. C. Ralph, J. P. Dowling, and G. J. Milburn, "Linear optical quantum computing with photonic qubits," *Rev. Mod. Phys.*, vol. 79, pp. 135–174, Jan 2007.

[61] S. Aaronson and A. Arkhipov, "The computational complexity of linear optics," *Theory of Computing*, vol. 9, no. 4, pp. 143–252, 2013.

[62] P. Sibson, C. Erven, M. Godfrey, S. Miki, T. Yamashita, M. Fujiwara, M. Sasaki, H. Terai, M. G. Tanner, C. M. Natarajan, R. H. Hadfield, J. L. O'Brien, and M. G. Thompson, "Chip-based quantum key distribution," *Nat. Commun.*, vol. 8, p. 13984, feb 2017.

[63] J. Wang, D. Bonneau, M. Villa, J. W. Silverstone, R. Santagati, S. Miki, T. Yamashita, M. Fujiwara, M. Sasaki, H. Terai, M. G. Tanner, C. M. Natarajan, R. H. Hadfield, J. L. O'Brien, and M. G. Thompson, "Chip-to-chip quantum photonic interconnect by path-polarization interconversion," *Optica*, vol. 3, pp. 407–413, Apr 2016.

[64] C. Ma, W. D. Sacher, Z. Tang, J. C. Mikkelsen, Y. Yang, F. Xu, T. Thiessen, H.-K. Lo, and J. K. S. Poon, "Silicon photonic transmitter for polarization-encoded quantum key distribution," *Optica*, vol. 3, pp. 1274–1278, Nov 2016.

[65] D. Bunandar, A. Lentine, C. Lee, H. Cai, C. M. Long, N. Boynton, N. Martinez, C. DeRose, C. Chen, M. Grein, D. Trotter, A. Starbuck, A. Pomerene, S. Hamilton, F. N. C. Wong, R. Camacho, P. Davids, J. Urayama, and D. Englund, "Metropolitan quantum key distribution with silicon photonics," *Phys. Rev. X*, vol. 8, p. 021009, Apr 2018.

[66] C. Abellan, W. Amaya, D. Domenech, P. M. noz, J. Capmany, S. Longhi, M. W. Mitchell, and V. Pruneri, "Quantum entropy source on an inp photonic integrated circuit for random number generation," *Optica*, vol. 3, pp. 989–994, Sep 2016.

[67] A. Politi, J. C. F. Matthews, and J. L. O'Brien, "Shor's quantum factoring algorithm on a photonic chip," *Science*, vol. 325, pp. 1221–1221, Sept. 2009.

[68] B. J. Metcalf, J. B. Spring, P. C. Humphreys, N. Thomas-Peter, M. Barbieri, W. S. Kolthammer, X.-M. Jin, N. K. Langford, D. Kundys, J. C. Gates, B. J. Smith, P. G. R. Smith, and I. A. Walmsley, "Quantum teleportation on a photonic chip," *Nature Photonics*, vol. 8, pp. 770–774, Sept. 2014.

[69] X. Qiang, X. Zhou, J. Wang, C. M. Wilkes, T. Loke, S. O'Gara, L. Kling, G. D. Marshall, R. Santagati, T. C. Ralph, J. B. Wang, J. L. O'Brien, M. G. Thompson, and J. C. F. Matthews, "Large-scale silicon quantum photonics implementing arbitrary two-qubit processing," *Nat. Photonics*, vol. 12, pp. 534–539, aug 2018.

[70] J. Carolan, C. Harrold, C. Sparrow, E. Martin-Lopez, N. J. Russell, J. W. Silverstone, P. J. Shadbolt, N. Matsuda, M. Oguma, M. Itoh, G. D. Marshall, M. G. Thompson, J. C. F. Matthews, T. Hashimoto, J. L. O'Brien, and A. Laing, "Universal linear optics," *Science*, vol. 349, pp. 711–716, July 2015.

[71] M. A. Ciampini, A. Orieux, S. Paesani, F. Sciarrino, G. Corrielli, A. Crespi, R. Ramponi, R. Osellame, and P. Mataloni, "Path-polarization hyperentangled and cluster states of photons on a chip," *Light: Science & Applications*, vol. 5, pp. e16064–e16064, Jan. 2016.

[72] J. C. Adcock, C. Vigliar, R. Santagati, J. W. Silverstone, and M. G. Thompson, "Programmable four-photon graph states on a silicon chip," *Nature Communications*, vol. 10, Aug. 2019.

[73] J. M. Arrazola, V. Bergholm, K. Brádler, T. R. Bromley, M. J. Collins, I. Dhand, A. Fumagalli, T. Gerrits, A. Goussev, L. G. Helt, J. Hundal, T. Isacsson, R. B. Israel, J. Izaac, S. Jahangiri, R. Janik, N. Killoran, S. P. Kumar, J. Lavoie, A. E. Lita, D. H. Mahler, M. Menotti, B. Morrison, S. W. Nam, L. Neuhaus, H. Y. Qi, N. Quesada, A. Repingon, K. K. Sabapathy, M. Schuld, D. Su, J. Swinarton, A. Száva, K. Tan, P. Tan, V. D. Vaidya, Z. Vernon, Z. Zabaneh, and Y. Zhang, "Quantum circuits with many photons on a programmable nanophotonic chip," *Nature*, vol. 591, pp. 54–60, Mar. 2021.

[74] M. Bentivegna, N. Spagnolo, C. Vitelli, F. Flamini, N. Viggianiello, L. Latmiral, P. Mataloni, D. J. Brod, E. F. Galvão, A. Crespi, R. Ramponi, R. Osellame, and F. Sciarrino, "Experimental scattershot boson sampling," *Science Advances*, vol. 1, p. e1400255, Apr. 2015.

[75] H. Wang, W. Li, X. Jiang, Y.-M. He, Y.-H. Li, X. Ding, M.-C. Chen, J. Qin, C.-Z. Peng, C. Schneider, M. Kamp, W.-J. Zhang, H. Li, L.-X. You, Z. Wang, J. P. Dowling, S. Höfling, C.-Y. Lu, and J.-W. Pan, "Toward scalable boson sampling with photon loss," *Phys. Rev. Lett.*, vol. 120, p. 230502, Jun 2018.

[76] A. Crespi, R. Osellame, R. Ramponi, V. Giovannetti, R. Fazio, L. Sansoni, F. D. Nicola, F. Sciarrino, and P. Mataloni, "Anderson localization of entangled photons in an integrated quantum walk," *Nature Photonics*, vol. 7, pp. 322–328, Mar. 2013.

[77] N. C. Harris, G. R. Steinbrecher, M. Prabhu, Y. Lahini, J. Mower, D. Bunandar, C. Chen, F. N. C. Wong, T. Baehr-Jones, M. Hochberg, S. Lloyd, and D. Englund,

"Quantum transport simulations in a programmable nanophotonic processor," *Nature Photonics*, vol. 11, pp. 447–452, June 2017.

[78] A. Peruzzo, J. McClean, P. Shadbolt, M.-H. Yung, X.-Q. Zhou, P. J. Love, A. Aspuru-Guzik, and J. L. O'Brien, "A variational eigenvalue solver on a photonic quantum processor," *Nature Communications*, vol. 5, July 2014.

[79] C. Sparrow, E. Martín-López, N. Maraviglia, A. Neville, C. Harrold, J. Carolan, Y. N. Joglekar, T. Hashimoto, N. Matsuda, J. L. O'Brien, D. P. Tew, and A. Laing, "Simulating the vibrational quantum dynamics of molecules using photonics," *Nature*, vol. 557, pp. 660–667, May 2018.

[80] J. Wang, S. Paesani, R. Santagati, S. Knauer, A. A. Gentile, N. Wiebe, M. Petruzzella, J. L. O'Brien, J. G. Rarity, A. Laing, and M. G. Thompson, "Experimental quantum hamiltonian learning," *Nature Physics*, vol. 13, pp. 551–555, Mar. 2017.

[81] A. Aspuru-Guzik and P. Walther, "Photonic quantum simulators," *Nature Physics*, vol. 8, pp. 285–291, Apr. 2012.

[82] E. Polino, M. Riva, M. Valeri, R. Silvestri, G. Corrielli, A. Crespi, N. Spagnolo, R. Osellame, and F. Sciarrino, "Experimental multiphase estimation on a chip," *Optica*, vol. 6, pp. 288–295, Mar 2019.

[83] T. Roger, S. Vezzoli, E. Bolduc, J. Valente, J. J. F. Heitz, J. Jeffers, C. Soci, J. Leach, C. Couteau, N. I. Zheludev, and D. Faccio, "Coherent perfect absorption in deeply subwavelength films in the single-photon regime," *Nature Communications*, vol. 6, may 2015.

[84] C. Altuzarra, S. Vezzoli, J. Valente, W. Gao, C. Soci, D. Faccio, and C. Couteau, "Coherent perfect absorption in metamaterials with entangled photons," *ACS Photonics*, vol. 4, no. 9, pp. 2124–2128, 2017.

[85] T. Roger, S. Restuccia, A. Lyons, D. Giovannini, J. Romero, J. Jeffers, M. Padgett, and D. Faccio, "Coherent absorption of n00n states," *Phys. Rev. Lett.*, vol. 117, p. 023601, Jul 2016.

[86] S. Zanotto, F. P. Mezzapesa, F. Bianco, G. Biasiol, L. Baldacci, M. S. Vitiello, L. Sorba, R. Colombelli, and A. Tredicucci, "Perfect energy-feeding into strongly coupled systems and interferometric control of polariton absorption," *Nature Physics*, vol. 10, no. 11, pp. 830–834, 2014.

[87] D. Zhang, X.-Q. Luo, Y.-P. Wang, T.-F. Li, and J. You, "Observation of the exceptional point in cavity magnon-polaritons," *Nature communications*, vol. 8, no. 1, pp. 1–6, 2017.

[88] B. Vest, M.-C. Dheur, É. Devaux, A. Baron, E. Rousseau, J.-P. Hugonin, J.-J. Greffet, G. Messin, and F. Marquier, "Anti-coalescence of bosons on a lossy beam splitter," *Science*, vol. 356, no. 6345, pp. 1373–1376, 2017.

[89] J. M. Lukens and P. Lougovski, "Frequency-encoded photonic qubits for scalable quantum information processing," *Optica*, vol. 4, pp. 8–16, Jan 2017.

[90] H.-H. Lu, J. M. Lukens, N. A. Peters, B. P. Williams, A. M. Weiner, and P. Lougovski, "Quantum interference and correlation control of frequency-bin qubits," *Optica*, vol. 5, pp. 1455–1460, Nov 2018.

[91] H. Liu, J. Wang, H. Ma, and S. Sun, "Polarization-multiplexing-based measurement-device-independent quantum key distribution without phase reference calibration," *Optica*, vol. 5, pp. 902–909, Aug 2018.

[92] G. B. Xavier and G. Lima, "Quantum information processing with space-division multiplexing optical fibres," *Communications Physics*, vol. 3, Jan. 2020.

[93] T. Ikuta and H. Takesue, "Four-dimensional entanglement distribution over 100 km," *Scientific Reports*, vol. 8, Jan. 2018.

[94] B. D. Lio, L. K. Oxenlowe, D. Bacco, D. Cozzolino, N. Biagi, T. N. Arge, E. Larsen, K. Rottwitt, Y. Ding, and A. Zavatta, "Stable transmission of high-dimensional quantum states over a 2-km multicore fiber," *IEEE Journal of Selected Topics in Quantum Electronics*, vol. 26, pp. 1–8, July 2020.

[95] J. W. Silverstone, R. Santagati, D. Bonneau, M. J. Strain, M. Sorel, J. L. O'Brien, and M. G. Thompson, "Qubit entanglement between ring-resonator photon-pair sources on a silicon chip," *Nat. Commun.*, vol. 6, p. 7948, 2015.

[96] J. Wang, D. Bonneau, M. Villa, J. W. Silverstone, R. Santagati, S. Miki, T. Yamashita, M. Fujiwara, M. Sasaki, H. Terai, M. G. Tanner, C. M. Natarajan, R. H. Hadfield, J. L. O'Brien, and M. G. Thompson, "Chip-to-chip quantum photonic interconnect by path-polarization interconversion," *Optica*, vol. 3, no. 4, pp. 407–413, 2016.

[97] P. Sibson, C. Erven, M. Godfrey, S. Miki, T. Yamashita, M. Fujiwara, M. Sasaki, H. Terai, M. G. Tanner, C. M. Natarajan, R. H. Hadfield, J. L. O'Brien, and M. G. Thompson, "Chip-based quantum key distribution," *Nat. Commun.*, vol. 8, p. 13984, 2017.

[98] J. L. O'Brien, A. Furusawa, and J. Vučković, "Photonic quantum technologies," *Nat. Photonics*, vol. 3, pp. 687–695, dec 2009.

[99] F. Najafi, J. Mower, N. C. Harris, F. Bellei, A. Dane, C. Lee, X. Hu, P. Kharel, F. Marsili, S. Assefa, K. K. Berggren, and D. Englund, "On-chip detection of non-classical light by scalable integration of single-photon detectors," *Nat. Commun.*, vol. 6, p. 5873, 2015.

[100] M. K. Akhlaghi, E. Schelew, and J. F. Young, "Waveguide integrated superconducting single-photon detectors implemented as near-perfect absorbers of coherent radiation," *Nat. Communications*, vol. 6, sep 2015.

[101] H. Shibata, T. Hiraki, T. Tsuchizawa, K. Yamada, Y. Tokura, and S. Matsuo, "A waveguide-integrated superconducting nanowire single-photon detector with a spot-size converter on a si photonics platform," *Superconductor Science and Technology*, vol. 32, p. 034001, jan 2019.

[102] R. E. Warburton, M. Itzler, and G. S. Buller, "Free-running, room temperature operation of an InGaAs/InP single-photon avalanche diode," *Appl. Phys. Lett.*, vol. 94, no. 7, p. 071116, 2009.

[103] Y. Liang, Y. Chen, Z. Huang, G. Bai, M. Yu, and H. Zeng, "Room-temperature single-photon detection with 1.5-ghz gated ingaas/inp avalanche photodiode," *IEEE Photonics Technology Letters*, vol. 29, no. 1, pp. 142–145, 2017.

[104] Y. Liang, Y. Chen, Z. Huang, G. Bai, M. Yu, and H. Zeng, "Room-temperature single-photon detection with 1.5-ghz gated InGaAs/InP avalanche photodiode," *IEEE Photon. Technol. Lett.*, vol. 29, no. 1, pp. 142–145, 2017.

[105] W. D. Sacher, Y. Huang, G.-Q. Lo, and J. K. Poon, "Multilayer silicon nitride-on-silicon integrated photonic platforms and devices," *J. Light. Technol.*, vol. 33, no. 4, pp. 901–910, 2015.

[106] M.-J. Lee, P. Sun, and E. Charbon, "A first single-photon avalanche diode fabricated in standard SOI CMOS technology with a full characterization of the device," *Optics Express*, vol. 23, p. 13200, may 2015.

[107] L. D. Huang, J. Y. Wu, J. P. Wang, C. M. Tsai, Y. H. Huang, D. R. Wu, and S. D. Lin, "Single-photon avalanche diodes in 0.18-μm high-voltage cmos technology," *Opt. Express*, vol. 25, pp. 13333–13339, Jun 2017.

[108] N. J. D. Martinez, C. T. Derose, R. W. Brock, A. L. Starbuck, A. T. Pomerene, A. L. Lentine, D. C. Trotter, and P. S. Davids, "High performance waveguide-coupled Ge-on-Si linear mode avalanche photodiodes," *Opt. Express*, vol. 24, pp. 19072–19081, Aug 2016.

[109] N. J. Martinez, M. Gehl, C. T. Derose, A. L. Starbuck, A. T. Pomerene, A. L. Lentine, D. C. Trotter, and P. S. Davids, "Single photon detection in a waveguide-coupled Ge-on-Si lateral avalanche photodiode," *Opt. Express*, vol. 25, no. 14, pp. 16130–16139, 2017.

[110] K. K. Mehta, C. D. Bruzewicz, R. McConnell, R. J. Ram, J. M. Sage, and J. Chiaverini, "Integrated optical addressing of an ion qubit," *Nat. Nanotechnol.*, vol. 11, no. 12, p. 1066, 2016.

[111] K. K. Mehta, G. N. West, and R. J. Ram, "Visible-wavelength photonic integrated circuits for trapped-ion quantum computing," in *2017 IEEE Photonics Society Summer Topical Meeting Series (SUM)*, IEEE, July 2017.

[112] J. Tao, Y. D. Lim, H. Y. Li, N. P. Chew, A. A. A. Apriyana, L. Bu, P. Zhao, L. Guidoni, and C. S. Tan, "3d integration of CMOS-compatible surface electrode ion trap and silicon photonics for scalable quantum computing," in *2019 IEEE 69th Electronic Components and Technology Conference (ECTC)*, IEEE, May 2019.

[113] R. E. Evans, M. K. Bhaskar, D. D. Sukachev, C. T. Nguyen, A. Sipahigil, M. J. Burek, B. Machielse, G. H. Zhang, A. S. Zibrov, E. Bielejec, H. Park, M. Lončar, and M. D. Lukin, "Photon-mediated interactions between quantum emitters in a diamond nanocavity," *Science*, vol. 362, no. 6415, pp. 662–665, 2018.

[114] M. Ren, X. Gu, Y. Liang, W. Kong, E. Wu, G. Wu, and H. Zeng, "Laser ranging at 1550 nm with 1-ghz sine-wave gated InGaAs/InP APD single-photon detector," *Opt. Express*, vol. 19, no. 14, pp. 13497–13502, 2011.

[115] A. Swatantran, H. Tang, T. Barrett, P. DeCola, and R. Dubayah, "Rapid, high-resolution forest structure and terrain mapping over large areas using single photon lidar," *Sci. Rep.*, vol. 6, p. 28277, 2016.

[116] M. Buttafava, J. Zeman, A. Tosi, K. Eliceiri, and A. Velten, "Non-line-of-sight imaging using a time-gated single photon avalanche diode," *Opt. Express*, vol. 23, no. 16, pp. 20997–21011, 2015.

[117] K. Morimoto, A. Ardelean, M.-L. Wu, A. C. Ulku, I. M. Antolovic, C. Bruschini, and E. Charbon, "Megapixel time-gated SPAD image sensor for 2D and 3D imaging applications," *Optica*, vol. 7, no. 4, pp. 346–354, 2020.

[118] M. A. Al-Rawhani, J. Beeley, and D. R. Cumming, "Wireless fluorescence capsule for endoscopy using single photon-based detection," *Sci. Rep.*, vol. 5, p. 18591, 2015.

[119] C. Bruschini, H. Homulle, I. M. Antolovic, S. Burri, and E. Charbon, "Single-photon avalanche diode imagers in biophotonics: review and outlook," *Light: Science & Applications*, vol. 8, no. 1, pp. 1–28, 2019.

[120] M. Wegmuller, F. Scholder, and N. Gisin, "Photon-counting otdr for local birefringence and fault analysis in the metro environment," *Journal of Lightwave Technology*, vol. 22, no. 2, pp. 390–400, 2004.

[121] P. Eraerds, M. Legre, J. Zhang, H. Zbinden, and N. Gisin, "Photon counting otdr: Advantages and limitations," *Journal of Lightwave Technology*, vol. 28, no. 6, pp. 952–964, 2010.

[122] I. C. Hernández, M. Buttafava, G. Boso, A. Diaspro, A. Tosi, and G. Vicidomini, "Gated STED microscopy with time-gated single-photon avalanche diode," *Biomed. Opt. Express*, vol. 6, no. 6, pp. 2258–2267, 2015.

[123] N. S. Nightingale, "A new silicon avalanche photodiode photon counting detector module for astronomy," *Experimental Astronomy*, vol. 1, no. 6, pp. 407–422, 1990.

[124] O. Ryan, M. Redfern, and A. Shearer, "An avalanche photodiode photon counting camera for high-resolution astronomy," *Experimental Astronomy*, vol. 21, pp. 23–30, Sept. 2006.

[125] D. Phelan and A. P. Morrison, "Geiger-mode avalanche photodiodes for high time resolution astrophysics," in *High Time Resolution Astrophysics*, pp. 291–310, Springer Netherlands.

[126] J. C. Campbell, "Recent advances in telecommunications avalanche photodiodes," *J. Lightwave Technol.*, vol. 25, pp. 109–121, Jan 2007.

[127] X. Li, N. Bamiedakis, X. Guo, J. McKendry, E. Xie, R. Ferreira, E. Gu, M. Dawson, R. Penty, and I. White, "Wireless visible light communications employing feed-forward pre-equalization and PAM-4 modulation," *Journal of Lightwave Technology*, vol. 34, no. 8, pp. 2049–2055, 2016.

[128] H. T. Chen, J. Verbist, P. Verheyen, P. D. Heyn, G. Lepage, J. D. Coster, P. Absil, X. Yin, J. Bauwelinck, J. V. Campenhout, and G. Roelkens, "High sensitivity 10gb/s si photonic receiver based on a low-voltage waveguide-coupled ge avalanche photodetector," *Optics Express*, vol. 23, p. 815, Jan. 2015.

[129] L. Virot, P. Crozat, J.-M. Fédéli, J.-M. Hartmann, D. Marris-Morini, E. Cassan, F. Boeuf, and L. Vivien, "Germanium avalanche receiver for low power interconnects," *Nature communications*, vol. 5, p. 4957, 2014.

[130] L. Zhang, D. Chitnis, H. Chun, S. Rajbhandari, G. Faulkner, D. O'Brien, and S. Collins, "A comparison of APD- and SPAD-based receivers for visible light communications," *Journal of Lightwave Technology*, vol. 36, pp. 2435–2442, June 2018.

[131] P. F. McManamon, P. Banks, J. Beck, D. G. Fried, A. S. Huntington, and E. A. Watson, "Comparison of flash lidar detector options," *Optical Engineering*, vol. 56, p. 031223, Mar. 2017.

[132] M. Ishino, T. Kitamura, A. Takamori, J. Kinoshita, N. Hasegawa, M. Nishikino, and K. Yamamoto, "Scanning 3d-LiDAR based on visible laser diode for sensor-integrated variable distribution lighting," *Optical Review*, vol. 26, pp. 213–220, Dec. 2018.

[133] A. Ingargiola, M. Segal, A. Gulinatti, I. Rech, I. Labanca, P. Maccagnani, M. Ghioni, S. Weiss, and X. Michalet, "48-spot single-molecule fret setup with periodic acceptor excitation," *The Journal of chemical physics*, vol. 148, no. 12, p. 123304, 2018.

[134] M. Moszyński, M. Szawlowski, M. Kapusta, and M. Balcerzyk, "Avalanche photodiodes in scintillation detection," *Nuclear Instruments and Methods in Physics Research Section A: Accelerators, Spectrometers, Detectors and Associated Equipment*, vol. 497, pp. 226–233, Jan. 2003.

[135] K. Inoue, Y. Kobayashi, Y. Yoda, M. Koshimizu, F. Nishikido, R. Haruki, and S. Kishimoto, "Measurement of nuclear resonant scattering on 61 ni with fast scintillation

detector using proportional-mode silicon avalanche photodiode," *Nuclear Instruments and Methods in Physics Research Section A: Accelerators, Spectrometers, Detectors and Associated Equipment*, vol. 880, pp. 87–91, Feb. 2018.

[136] S. Kishimoto, M. Koshimizu, F. Hiyama, R. Haruki, and F. Nishikido, "Measurements of 73-keV x-ray time spectrum with avalanche-photodiode scintillation detector using bi2o3-nanoparticle-doped plastic scintillator," *Nuclear Instruments and Methods in Physics Research Section A: Accelerators, Spectrometers, Detectors and Associated Equipment*, vol. 968, p. 163908, July 2020.

[137] T. Y. Liow, K. W. Ang, Q. Fang, J. F. Song, Y. Z. Xiong, M. B. Yu, G. Q. Lo, and D. L. Kwong, "Silicon modulators and germanium photodetectors on soi: Monolithic integration, compatibility, and performance optimization," *IEEE Journal of Selected Topics in Quantum Electronics*, vol. 16, pp. 307–315, Jan 2010.

[138] Y. Huang, J. Song, X. Luo, T.-Y. Liow, and G.-Q. Lo, "Cmos compatible monolithic multi-layer si3n4-on-soi platform for low-loss high performance silicon photonics dense integration," *Opt. Express*, vol. 22, pp. 21859–21865, Sep 2014.

[139] A. Singh, Q. Li, S. Liu, Y. Yu, X. Lu, C. Schneider, S. Höfling, J. Lawall, V. Verma, R. Mirin, S. W. Nam, J. Liu, and K. Srinivasan, "Quantum frequency conversion of a quantum dot single-photon source on a nanophotonic chip," *Optica*, vol. 6, pp. 563–569, May 2019.

[140] Q. Li, A. Singh, X. Lu, J. Lawall, V. Verma, R. Mirin, S. W. Nam, and K. Srinivasan, "Tunable quantum beat of single photons enabled by nonlinear nanophotonics," *Phys. Rev. Applied*, vol. 12, p. 054054, Nov 2019.

[141] A. N. Vetlugin, R. Guo, A. Xomalis, S. Yanikgonul, G. Adamo, C. Soci, and N. I. Zheludev, "Coherent perfect absorption of single photons in a fiber network," *Applied Physics Letters*, vol. 115, p. 191101, Nov. 2019.

[142] B. Du, C. Pang, D. Wu, Z. Li, H. Peng, Y. Tao, E. Wu, and G. Wu, "High-speed photon-counting laser ranging for broad range of distances," *Sci. Rep.*, vol. 8, mar 2018.

[143] M. O'Toole, D. B. Lindell, and G. Wetzstein, "Confocal non-line-of-sight imaging based on the light-cone transform," *Nature*, vol. 555, pp. 338–341, mar 2018.

[144] H. A. R. Homulle, F. Powolny, P. L. Stegehuis, J. Dijkstra, D.-U. Li, K. Homicsko, D. Rimoldi, K. Muehlethaler, J. O. Prior, R. Sinisi, E. Dubikovskaya, E. Charbon, and C. Bruschini, "Compact solid-state CMOS single-photon detector array for in vivo NIR fluorescence lifetime oncology measurements," *Biomed. Opt. Express*, vol. 7, p. 1797, apr 2016.

[145] K. D. Irwin, "An application of electrothermal feedback for high resolution cryogenic particle detection," *Applied Physics Letters*, vol. 66, no. 15, pp. 1998–2000, 1995.

[146] K. D. Irwin, S. W. Nam, B. Cabrera, B. Chugg, and B. A. Young, "A quasiparticle-trap-assisted transition-edge sensor for phonon-mediated particle detection," *Review of Scientific Instruments*, vol. 66, no. 11, pp. 5322–5326, 1995.

[147] J. P. Höpker, T. Gerrits, A. Lita, S. Krapick, H. Herrmann, R. Ricken, V. Quiring, R. Mirin, S. W. Nam, C. Silberhorn, and T. J. Bartley, "Integrated transition edge sensors on titanium in-diffused lithium niobate waveguides," *APL Photonics*, vol. 4, no. 5, p. 056103, 2019.

[148] T. Gerrits, N. Thomas-Peter, J. C. Gates, A. E. Lita, B. J. Metcalf, B. Calkins, N. A. Tomlin, A. E. Fox, A. L. Linares, J. B. Spring, N. K. Langford, R. P. Mirin, P. G. R. Smith, I. A. Walmsley, and S. W. Nam, "On-chip, photon-number-resolving, telecommunication-band detectors for scalable photonic information processing," *Phys. Rev. A*, vol. 84, p. 060301, Dec 2011.

[149] B. Calkins, P. L. Mennea, A. E. Lita, B. J. Metcalf, W. S. Kolthammer, A. Lamas-Linares, J. B. Spring, P. C. Humphreys, R. P. Mirin, J. C. Gates, P. G. R. Smith, I. A. Walmsley, T. Gerrits, and S. W. Nam, "High quantum-efficiency photon-number-resolving detector for photonic on-chip information processing," *Opt. Express*, vol. 21, pp. 22657–22670, Sep 2013.

[150] D. Rosenberg, A. E. Lita, A. J. Miller, and S. W. Nam, "Noise-free high-efficiency photon-number-resolving detectors," *Phys. Rev. A*, vol. 71, p. 061803, Jun 2005.

[151] M. E. Huber, P. A. Neil, R. G. Benson, D. A. Burns, A. M. Corey, C. S. Flynn, Y. Kitaygorodskaya, O. Massihzadeh, J. M. Martinis, and G. C. Hilton, "Dc squid series array amplifiers with 120 mhz bandwidth," *IEEE Transactions on Applied Superconductivity*, vol. 11, no. 1, pp. 1251–1256, 2001.

[152] K. Irwin and G. Hilton, "Transition-edge sensors," in *Topics in Applied Physics*, pp. 63–150, Springer Berlin Heidelberg, July 2005.

[153] A. E. Lita, A. J. Miller, and S. W. Nam, "Counting near-infrared single-photons with 95% efficiency," *Opt. Express*, vol. 16, pp. 3032–3040, Mar 2008.

[154] P. A. Hiskett, D. Rosenberg, C. G. Peterson, R. J. Hughes, S. Nam, A. E. Lita, A. J. Miller, and J. E. Nordholt, "Long-distance quantum key distribution in optical fibre," *New Journal of Physics*, vol. 8, pp. 193–193, Sept. 2006.

[155] R. Radenbaugh, "Refrigeration for superconductors," *Proceedings of the IEEE*, vol. 92, no. 10, pp. 1719–1734, 2004.

[156] V. Zwiller, I. E. Zadeh, J. Los, R. Gourgues, V. Steinmetz, S. Dobrovolskiy, and S. N. Dorenbos, "Single-photon detection with near unity efficiency, ultra-high detection-rates, and ultra-high time resolution," in *Conference on Lasers and Electro-Optics*, p. FF1E.1, Optical Society of America, 2017.

[157] W. H. Pernice, C. Schuck, O. Minaeva, M. Li, G. Goltsman, A. Sergienko, and H. Tang, "High-speed and high-efficiency travelling wave single-photon detectors embedded in nanophotonic circuits," *Nat. Commun.*, vol. 3, p. 1325, 2012.

[158] J. P. Sprengers, A. Gaggero, D. Sahin, S. Jahanmirinejad, G. Frucci, F. Mattioli, R. Leoni, J. Beetz, M. Lermer, M. Kamp, S. Höfling, R. Sanjines, and A. Fiore, "Waveguide superconducting single-photon detectors for integrated quantum photonic circuits," *Applied Physics Letters*, vol. 99, no. 18, p. 181110, 2011.

[159] M. A. Karami, M. Gersbach, H.-J. Yoon, and E. Charbon, "A new single-photon avalanche diode in 90nm standard cmos technology," *Opt. Express*, vol. 18, pp. 22158–22166, Oct 2010.

[160] M.-J. Lee, P. Sun, and E. Charbon, "A first single-photon avalanche diode fabricated in standard SOI CMOS technology with a full characterization of the device," *Opt. Express*, vol. 23, pp. 13200–13209, May 2015.

[161] L. D. Huang, J. Y. Wu, J. P. Wang, C. M. Tsai, Y. H. Huang, D. R. Wu, and S. D. Lin, "Single-photon avalanche diodes in 0.18 μm high-voltage cmos technology," *Opt. Express*, vol. 25, pp. 13333–13339, Jun 2017.

[162] F.-Z. Hsu, J.-Y. Wu, and S.-D. Lin, "Low-noise single-photon avalanche diodes in 0.25 μm high-voltage CMOS technology," *Optics Letters*, vol. 38, p. 55, Dec. 2012.

[163] L. C. Kimerling, D. Ahn, A. B. Apsel, M. Beals, D. Carothers, Y.-K. Chen, T. Conway, D. M. Gill, M. Grove, C.-Y. Hong, M. Lipson, J. Liu, J. Michel, D. Pan, S. S. Patel, A. T. Pomerene, M. Rasras, D. K. Sparacin, K.-Y. Tu, A. E. White, and C. W. Wong, "Electronic-photonic integrated circuits on the CMOS platform," in *Silicon Photonics* (J. A. Kubby and G. T. Reed, eds.), SPIE, Feb. 2006.

[164] J. Wang, W. Y. Loh, K. T. Chua, H. Zang, Y. Z. Xiong, T. H. Loh, M. B. Yu, S. J. Lee, G. Lo, and D. . Kwong, "Evanescent-coupled ge p-i-n photodetectors on si-waveguide with seg-ge and comparative study of lateral and vertical p-i-n configurations," *IEEE Electron Device Letters*, vol. 29, no. 5, pp. 445–448, 2008.

[165] L. Li, H. Lin, Y. Huang, R.-J. Shiue, A. Yadav, J. Li, J. Michon, D. Englund, K. Richardson, T. Gu, and J. Hu, "High-performance flexible waveguide-integrated photodetectors," *Optica*, vol. 5, pp. 44–51, Jan 2018.

[166] Z. Huang, C. Li, D. Liang, K. Yu, C. Santori, M. Fiorentino, W. Sorin, S. Palermo, and R. G. Beausoleil, "25 Gbps low-voltage waveguide Si–Ge avalanche photodiode," *Optica*, vol. 3, no. 8, pp. 793–798, 2016.

[167] S. Subramanian, H.-Y. Wu, T. Constant, J. Xavier, and F. Vollmer, "Label-free optical single-molecule micro-and nanosensors," *Advanced Materials*, vol. 30, no. 51, p. 1801246, 2018.

[168] A. Maccarone, F. M. Della Rocca, A. McCarthy, R. Henderson, and G. S. Buller, "Three-dimensional imaging of stationary and moving targets in turbid underwater environments using a single-photon detector array," *Optics express*, vol. 27, no. 20, pp. 28437–28456, 2019.

[169] C. V. Poulton, M. J. Byrd, M. Raval, Z. Su, N. Li, E. Timurdogan, D. Coolbaugh, D. Vermeulen, and M. R. Watts, "Large-scale silicon nitride nanophotonic phased arrays at infrared and visible wavelengths," *Optics letters*, vol. 42, no. 1, pp. 21–24, 2017.

[170] C. V. Poulton, M. J. Byrd, P. Russo, E. Timurdogan, M. Khandaker, D. Vermeulen, and M. R. Watts, "Long-range LiDAR and free-space data communication with high-

performance optical phased arrays," *IEEE Journal of Selected Topics in Quantum Electronics*, vol. 25, no. 5, pp. 1–8, 2019.

[171] M. Karbalayghareh, F. Miramirkhani, M. Safari, and M. Uysal, "Vehicular visible light communications with SPAD receivers," in *2019 IEEE Wireless Communications and Networking Conference (WCNC)*, pp. 1–5, IEEE, 2019.

[172] C.-K. Wang and W. D. Philpot, "Using airborne bathymetric lidar to detect bottom type variation in shallow waters," *Remote Sensing of Environment*, vol. 106, no. 1, pp. 123–135, 2007.

[173] H.-S. Zhong, H. Wang, Y.-H. Deng, M.-C. Chen, L.-C. Peng, Y.-H. Luo, J. Qin, D. Wu, X. Ding, Y. Hu, *et al.*, "Quantum computational advantage using photons," *Science*, vol. 370, no. 6523, pp. 1460–1463, 2020.

[174] J. Lee, V. Leong, D. Kalashnikov, J. Dai, A. Gandhi, and L. A. Krivitsky, "Integrated single photon emitters," *AVS Quantum Science*, vol. 2, no. 3, p. 031701, 2020.

[175] "C30902sh - si apd, 0.5mm, to-18, photon counting." https://www.excelitas.com/file-download/download/public/61601?filename=Excellitas_Si_APD_C30902_C30921_Series_datasheet.pdf, 2021. Accessed: 2021-03-18.

[176] "Avalanche photodiode a user guide - perkinelmer." http://www.perkinelmer.com/CMSResources/Images/44-3430APP_APD_a_user_guide.pdf, 2021. Accessed: 2021-03-19.

[177] N. J. D. Martinez, M. Gehl, C. T. Derose, A. L. Starbuck, A. T. Pomerene, A. L. Lentine, D. C. Trotter, and P. S. Davids, "Single photon detection in a waveguide-coupled Ge-on-Si lateral avalanche photodiode," *Opt. Express*, vol. 25, no. 14, pp. 16130–16139, 2017.

[178] T.-Y. Liow, K.-W. Ang, Q. Fang, J.-F. Song, Y.-Z. Xiong, M.-B. Yu, G.-Q. Lo, and D.-L. Kwong, "Silicon modulators and germanium photodetectors on SOI: Monolithic integration, compatibility, and performance optimization," *IEEE J. Sel. Topics Quantum Electron.*, vol. 16, no. 1, pp. 307–315, 2010.

[179] Y. Huang, J. Song, X. Luo, T.-Y. Liow, and G.-Q. Lo, "CMOS compatible monolithic multi-layer Si3N4-on-SOI platform for low-loss high performance silicon photonics dense integration," *Opt. Express*, vol. 22, no. 18, pp. 21859–21865, 2014.

[180] D. S. Ong, K. F. Li, G. J. Rees, J. P. David, and P. N. Robson, "A simple model to determine multiplication and noise in avalanche photodiodes," *J. Appl. Phys.*, vol. 83, no. 6, pp. 3426–3428, 1998.

[181] S. L. Tan, D. S. Ong, and H. K. Yow, "Theoretical analysis of breakdown probabilities and jitter in single-photon avalanche diodes," *J. Appl. Phys.*, vol. 102, no. 4, 2007.

[182] A. Ingargiola, M. Assanelli, A. Gallivanoni, I. Rech, M. Ghioni, and S. Cova, "Avalanche buildup and propagation effects on photon-timing jitter in Si-SPAD with non-uniform electric field," *Proc. SPIE*, vol. 7320, p. 73200K, 2009.

[183] J. Ma, M. Zhou, Z. Yu, X. Jiang, Y. Huo, K. Zang, J. Zhang, J. S. Harris, G. Jin, Q. Zhang, and J.-W. Pan, "Simulation of a high-efficiency and low-jitter nanostructured silicon single-photon avalanche diode," *Optica*, vol. 2, no. 11, p. 974, 2015.

[184] S. Mandai, M. W. Fishburn, Y. Maruyama, and E. Charbon, "A wide spectral range single-photon avalanche diode fabricated in an advanced 180 nm CMOS technology," *Opt. Express*, vol. 20, no. 6, pp. 5849–5857, 2012.

[185] K. Zang, X. Jiang, Y. Huo, X. Ding, M. Morea, X. Chen, C.-Y. Lu, J. Ma, M. Zhou, Z. Xia, Z. Yu, T. I. Kamins, Q. Zhang, and J. S. Harris, "Silicon single-photon avalanche diodes with nano-structured light trapping," *Nat. Commun.*, vol. 8, no. 1, p. 628, 2017.

[186] W. G. Oldham, R. R. Samuelson, and P. Antognetti, "Tiggering phenomena in avalanche diodes," *IEEE Trans. Electron Devices*, vol. 19, no. 9, p. 1056, 1972.

[187] J. J. Ackert, A. S. Karar, D. J. Paez, P. E. Jessop, J. C. Cartledge, and A. P. Knights, "10 gbps silicon waveguide-integrated infrared avalanche photodiode," *Opt. Express*, vol. 21, no. 17, pp. 19530–19537, 2013.

[188] H. Chen, M. Galili, P. Verheyen, P. D. Heyn, G. Lepage, J. D. Coster, S. Balakrishnan, P. Absil, L. Oxenlowe, J. V. Campenhout, and G. Roelkens, "100-Gbps RZ Data Reception in 67-GHz Si-Contacted Germanium Waveguide p-i-n Photodetectors," *J. Lightwave Technol.*, vol. 35, pp. 722–726, Feb 2017.

[189] C. T. DeRose, D. C. Trotter, W. A. Zortman, A. L. Starbuck, M. Fisher, M. R. Watts, and P. S. Davids, "Ultra compact 45 ghz CMOS compatible germanium waveguide photodiode with low dark current," *Opt. Express*, vol. 19, no. 25, pp. 24897–24904, 2011.

[190] M. M. P. Fard, G. Cowan, and O. Liboiron-Ladouceur, "Responsivity optimization of a high-speed germanium-on-silicon photodetector," *Opt. Express*, vol. 24, no. 24, pp. 27738–27752, 2016.

[191] G. Masetti, M. Severi, and S. Solmi, "Modeling of carrier mobility against carrier concentration in arsenic-, phosphorus-, and boron-doped silicon," *IEEE Trans. Electron Devices*, vol. 30, pp. 764–769, Jul 1983.

[192] C. Canali, G. Majni, R. Minder, and G. Ottaviani, "Electron and hole drift velocity measurements in silicon and their empirical relation to electric field and temperature," *IEEE Trans. Electron Devices*, vol. 22, pp. 1045–1047, Nov 1975.

[193] S. Selberherr, *Analysis and simulation of semiconductor devices*. Springer-Verlag, 1984.

[194] Silvaco, Inc., "Atlas user's manual," 2006.

[195] J. Bienfang, A. Restelli, D. Rogers, A. Mink, B. Hershman, A. Nakassis, X. Tang, L. Ma, H. Xu, D. Su, C. W. Clark, and C. J. Williams, "High-repetition rate quantum key distribution," *Proc. SPIE*, vol. 6780, p. 67800C, 2007.

[196] G. Buller and A. Wallace, "Ranging and three-dimensional imaging using time-correlated single-photon counting and point-by-point acquisition," *IEEE Journal of selected topics in quantum electronics*, vol. 13, no. 4, pp. 1006–1015, 2007.

[197] M. J. Stevens, R. H. Hadfield, R. E. Schwall, S. W. Nam, R. P. Mirin, and J. A. Gupta, "Fast lifetime measurements of infrared emitters using a low-jitter superconducting single-photon detector," *Appl. Phys. Lett.*, vol. 89, no. 3, p. 031109, 2006.

[198] A. Gulinatti, I. Rech, S. Fumagalli, M. Assanelli, M. Ghioni, and S. D. Cova, "Modeling photon detection efficiency and temporal response of single photon avalanche diodes," *Proc. SPIE*, vol. 7355, p. 73550X, 2009.

[199] C. A. Lee, R. L. Batdorf, W. Wiegmann, and G. Kaminsky, "Time dependence of avalanche processes in silicon," *J. Appl. Phys.*, vol. 38, no. 7, pp. 2787–2796, 1967.

[200] I. Wêgrzecka, M. Wêgrzecki, M. Grynglas, J. Bar, A. Uszyñski, R. Grodecki, P. Grabiec, S. Krzemiñski, and T. Budzyñski, "Design and properties of silicon avalanche photodiodes," *Opto-Electronics Review*, vol. 12, pp. 95 – 104, 03 2004.

[201] G. Ripamonti and S. Cova, "Carrier diffusion effects in the time-response of a fast photodiode," *Solid State Electron.*, vol. 28, no. 9, pp. 925–931, 1985.

[202] A. Spinelli and A. L. Lacaita, "Mean gain of avalanche photodiodes in a dead space model," *IEEE Trans. Electron Devices*, vol. 43, no. 1, pp. 23–30, 1996.

[203] Y. Kamakura, H. Mizuno, M. Yamaji, M. Morifuji, K. Taniguchi, C. Hamaguchi, T. Kunikiyo, and M. Takenaka, "Impact ionization model for full band monte carlo simulation," *J. Appl. Phys.*, vol. 75, pp. 3500–3506, apr 1994.

[204] T. Kunikiyo, M. Takenaka, M. Morifuji, K. Taniguchi, and C. Hamaguchi, "A model of impact ionization due to the primary hole in silicon for a full band Monte Carlo simulation," *J. Appl. Phys.*, vol. 79, no. 10, pp. 7718–7725, 1996.

[205] A. Spinelli and A. Lacaita, "Physics and numerical simulation of single photon avalanche diodes," *IEEE Trans. Electron Devices*, vol. 44, no. 11, pp. 1931–1943, 1997.

[206] D. Schroder, "Carrier lifetimes in silicon," *IEEE Trans. Electron Devices*, vol. 44, no. 1, pp. 160–170, 1997.

[207] S. Ramo, "Currents induced by electron motion," *Proc. IRE*, vol. 27, pp. 584–585, Sept 1939.

[208] T. Cao, Y. Fei, L. Zhang, Y. Cao, and S. Chen, "Design of a silicon mach–zehnder modulator with a u-type pn junction," *Appl. Opt.*, vol. 52, no. 24, pp. 5941–5948, 2013.

[209] Z. Yong, W. D. Sacher, Y. Huang, J. C. Mikkelsen, Y. Yang, X. Luo, P. Dumais, D. Goodwill, H. Bahrami, P. G.-Q. Lo, E. Bernier, and J. K. S. Poon, "U-shaped pn junctions for efficient silicon mach-zehnder and microring modulators in the o-band," *Opt. Express*, vol. 25, no. 7, pp. 8425–8439, 2017.

[210] T. Y. Ang, C. E. Png, S. T. Lim, and J. R. Ong, "Silicon modulators with optimized vertical pn junctions for high-modulation-efficiency in the o-band," in *Silicon Photonics XIII*, vol. 10537, p. 105370H, International Society for Optics and Photonics, 2018.

[211] M. Ghioni, A. Gulinatti, I. Rech, P. Maccagnani, and S. Cova, "Large-area low-jitter silicon single photon avalanche diodes," *Proc. SPIE*, vol. 6900, p. 69001D, 2008.

[212] T. Bendib, L. Pancheri, F. Djeffal, and G. Dalla Betta, "Impact of temperature and doping concentration on avalanche photodiode characteristics," *Proc. of the World Congress on Engineering*, vol. 1, 2014.

[213] M. S. Tyagi, "Zener and avalanche breakdown in silicon alloyed p-n junctions —I," *Solid-State Electron.*, vol. 11, pp. 99–115, jan 1968.

[214] M. Eisaman, J. Fan, A. Migdall, and S. V. Polyakov, "Invited review article: Single-photon sources and detectors," *Rev. Sci. Instr.*, vol. 82, no. 7, p. 071101, 2011.

[215] W. Shockley, "Currents to conductors induced by a moving point charge," *J. Appl. Phys.*, vol. 9, pp. 635–636, oct 1938.

[216] Z. He, "Review of the shockley–ramo theorem and its application in semiconductor gamma-ray detectors," *Nucl. Instrum. Methods Phys. Res., Sect. A*, vol. 463, pp. 250–267, may 2001.

[217] Y. Xu, P. Xiang, X. Xie, and Y. Huang, "A new modeling and simulation method for important statistical performance prediction of single photon avalanche diode detectors," *Semicond. Sci. Technol.*, vol. 31, no. 6, p. 065024, 2016.

[218] W. Kindt and H. V. Zeijl, "Modelling and fabrication of geiger mode avalanche photodiodes," *IEEE Trans. Nucl. Sci.*, vol. 45, pp. 715–719, jun 1998.

[219] G. Hurkx, H. de Graaff, W. Kloosterman, and M. Knuvers, "A new analytical diode model including tunneling and avalanche breakdown," *IEEE Trans. on Electron Devices*, vol. 39, no. 9, pp. 2090–2098, 1992.

[220] C. H. Ling and Z. Y. Cheng, "An improved analysis for the determination of trap levels in silicon from laser microwave photoconductive decay measurements," *Appl. Phys. Lett.*, vol. 71, pp. 3218–3220, dec 1997.

[221] G. Hurkx, D. Klaassen, and M. Knuvers, "A new recombination model for device simulation including tunneling," *IEEE Trans. on Electron Devices*, vol. 39, no. 2, pp. 331–338, 1992.

[222] K. Misiakos and D. Tsamakis, "Accurate measurements of the silicon intrinsic carrier density from 78 to 340 k," *J. Appl. Phys.*, vol. 74, pp. 3293–3297, sep 1993.

[223] S. Park, K. Yamada, T. Tsuchizawa, T. Watanabe, H. Shinojima, H. Nishi, R. Kou, and S. ichi Itabashi, "Influence of carrier lifetime on performance of silicon p-i-n variable optical attenuators fabricated on submicrometer rib waveguides," *Opt. Express*, vol. 18, p. 11282, may 2010.

[224] D. Garetto, Y. M. Randriamihaja, A. Zaka, D. Rideau, A. Schmid, H. Jaouen, and Y. Leblebici, "Analysis of defect capture cross sections using non-radiative multiphonon-assisted trapping model," *Solid-State Electron.*, vol. 71, pp. 74–79, may 2012.

[225] W. Bludau, A. Onton, and W. Heinke, "Temperature dependence of the band gap of silicon," *J. Appl. Phys.*, vol. 45, pp. 1846–1848, apr 1974.

[226] I. Takai, H. Matsubara, M. Soga, M. Ohta, M. Ogawa, and T. Yamashita, "Single-photon avalanche diode with enhanced nir-sensitivity for automotive lidar systems," *Sensors*, vol. 16, no. 4, p. 459, 2016.

[227] Q. Wilmart, H. El Dirani, N. Tyler, D. Fowler, S. Malhouitre, S. Garcia, M. Casale, S. Kerdiles, K. Hassan, C. Monat, *et al.*, "A versatile silicon-silicon nitride photonics platform for enhanced functionalities and applications," *Applied Sciences*, vol. 9, no. 2, p. 255, 2019.

[228] M. A. Porcel, A. Hinojosa, H. Jans, A. Stassen, J. Goyvaerts, D. Geuzebroek, M. Geiselmann, C. Dominguez, and I. Artundo, "Silicon nitride photonic integration for visible light applications," *Optics & Laser Technology*, vol. 112, pp. 299–306, 2019.

[229] H. Yu, M. Pantouvaki, J. Van Campenhout, D. Korn, K. Komorowska, P. Dumon, Y. Li, P. Verheyen, P. Absil, L. Alloatti, *et al.*, "Performance tradeoff between lateral and interdigitated doping patterns for high speed carrier-depletion based silicon modulators," *Optics express*, vol. 20, no. 12, pp. 12926–12938, 2012.

[230] M. Passoni, D. Gerace, L. O'Faolain, and L. C. Andreani, "Optimizing an interleaved pn junction to reduce energy dissipation in silicon slow-light modulators," *Photonics Research*, vol. 8, no. 4, pp. 457–467, 2020.

[231] Y. Kang, H.-D. Liu, M. Morse, M. J. Paniccia, M. Zadka, S. Litski, G. Sarid, A. Pauchard, Y.-H. Kuo, H.-W. Chen, W. S. Zaoui, J. E. Bowers, A. Beling, D. C. McIntosh, X. Zheng, and J. C. Campbell, "Monolithic germanium/silicon avalanche

photodiodes with 340 GHz gain–bandwidth product," *Nature Photonics*, vol. 3, pp. 59–63, Dec. 2008.

[232] M.-J. Lee and W.-Y. Choi, "A silicon avalanche photodetector fabricated with standard cmos technology with over 1 thz gain-bandwidth product," *Opt. Express*, vol. 18, pp. 24189–24194, Nov 2010.

[233] H. Zhu, L. Zhou, X. Sun, Y. Zhou, X. Li, and J. Chen, "On-chip optical power monitor using periodically interleaved PN junctions integrated on a silicon waveguide," *IEEE Journal of Selected Topics in Quantum Electronics*, vol. 20, no. 4, pp. 56–63, 2014.

[234] M.-J. Lee, H. Rücker, and W.-Y. Choi, "Optical-power dependence of gain, noise, and bandwidth characteristics for 850-nm cmos silicon avalanche photodetectors," *IEEE Journal of Selected Topics in Quantum Electronics*, vol. 20, no. 6, pp. 211–217, 2014.

[235] H. Zhu, K. Goi, and K. Ogawa, "All-silicon waveguide photodetection for low-bias power monitoring and 20-km 28-gb/s NRZ-OOK signal transmission," *IEEE Journal of Selected Topics in Quantum Electronics*, vol. 24, pp. 1–7, Mar. 2018.

[236] H. T. Chen, J. Verbist, P. Verheyen, P. D. Heyn, G. Lepage, J. D. Coster, P. Absil, X. Yin, J. Bauwelinck, J. V. Campenhout, and G. Roelkens, "High sensitivity 10Gb/s Si photonic receiver based on a low-voltage waveguide-coupled Ge avalanche photodetector," *Optics Express*, vol. 23, p. 815, Jan. 2015.

[237] H. T. Chen, J. Verbist, P. Verheyen, P. D. Heyn, G. Lepage, J. D. Coster, P. Absil, B. Moeneclaey, X. Yin, J. Bauwelinck, J. V. Campenhout, and G. Roelkens, "25-Gb/s 1310-nm optical receiver based on a Sub-5-V waveguide-coupled germanium avalanche photodiode," *IEEE Photonics Journal*, vol. 7, pp. 1–9, Aug. 2015.

[238] H. T. J. Meier, *Design, characterization and simulation of avalanche photodiodes*. PhD thesis, ETH Zurich, 2011.

[239] Lumerical, "Avalanche photodetector." https://support.lumerical.com/hc/en-us/articles/360042454814-Avalanche-photodetector. Accessed: 2020-12-24.

[240] S. Liu, C. Yang, W. Sun, Q. Qian, Y. Huang, X. Wu, M. Wu, Q. Yang, and L. Sun, "Repetitive-avalanche-induced electrical parameters shift for 4h-sic junction barrier schottky diode," *IEEE Transactions on Electron Devices*, vol. 62, pp. 601–605, Feb 2015.

[241] M.-J. Lee, H. Rucker, and W.-Y. Choi, "Effects of guard-ring structures on the performance of silicon avalanche photodetectors fabricated with standard CMOS technology," *IEEE Electron Device Letters*, vol. 33, no. 1, pp. 80–82, 2011.

[242] J. Verwey, A. Heringa, R. de Werdt, and W. v.d. Hofstad, "Drift of the breakdown voltage in p-n junctions in silicon (walk-out)," *Solid-State Electronics*, vol. 20, pp. 689–695, Aug. 1977.

[243] C. Neugebauer, J. Burgess, R. Joynson, and J. Mundy, "Electron trapping in thin SiO2 films due to avalanche currents," *Thin Solid Films*, vol. 13, pp. 5–9, Nov. 1972.

[244] T. Resetar, K. De Munck, L. Haspeslagh, M. Rosmeulen, A. Süss, R. Puers, and C. Van Hoof, "Development of gated pinned avalanche photodiode pixels for high-speed low-light imaging," *Sensors*, vol. 16, no. 8, p. 1294, 2016.

[245] J. Kostamovaara, J. Tenhunen, M. Kögler, I. Nissinen, J. Nissinen, and P. Keränen, "Fluorescence suppression in raman spectroscopy using a time-gated CMOS SPAD," *Optics express*, vol. 21, no. 25, pp. 31632–31645, 2013.

[246] Y. Liang, Q. Fei, Z. Liu, K. Huang, and H. Zeng, "Low-noise InGaAs/InP single-photon detector with widely tunable repetition rates," *Photonics Research*, vol. 7, no. 3, pp. A1–A6, 2019.

[247] M. M. P. Fard, C. Williams, G. Cowan, and O. Liboiron-Ladouceur, "High-speed grating-assisted all-silicon photodetectors for 850 nm applications," *Optics express*, vol. 25, no. 5, pp. 5107–5118, 2017.

[248] A. Chatterjee, S. K. Sikdar, S. K. Selvaraja, *et al.*, "High-speed waveguide integrated silicon photodetector on a SiN-SOI platform for short reach datacom," *Optics letters*, vol. 44, no. 7, pp. 1682–1685, 2019.

[249] B. Tossoun, G. Kurczveil, C. Zhang, A. Descos, Z. Huang, A. Beling, J. C. Campbell, D. Liang, and R. G. Beausoleil, "Indium arsenide quantum dot waveguide photodiodes heterogeneously integrated on silicon," *Optica*, vol. 6, no. 10, pp. 1277–1281, 2019.

[250] B. Chen, Y. Wan, Z. Xie, J. Huang, N. Zhang, C. Shang, J. Norman, Q. Li, Y. Tong, K. M. Lau, *et al.*, "Low dark current high gain InAs quantum dot avalanche photodetectors monolithically grown on Si," *ACS Photonics*, 2020.

[251] S. A. Srinivasan, M. Berciano, P. De Heyn, S. Lardenois, M. Pantouvaki, and J. Van Campenhout, "27 ghz silicon-contacted waveguide-coupled ge/si avalanche photodiode," *Journal of Lightwave Technology*, 2020.

[252] M. Huang, P. Cai, S. Li, G. Hou, N. Zhang, T.-I. Su, C.-y. Hong, and D. Pan, "56GHz waveguide Ge/Si avalanche photodiode," in *2018 Optical Fiber Communications Conference and Exposition (OFC)*, pp. 1–3, IEEE, 2018.

[253] X. Zeng, Z. Huang, B. Wang, D. Liang, M. Fiorentino, and R. G. Beausoleil, "Silicon–germanium avalanche photodiodes with direct control of electric field in charge multiplication region," *Optica*, vol. 6, no. 6, pp. 772–777, 2019.

[254] B. Wang, Z. Huang, Y. Yuan, D. Liang, X. Zeng, M. Fiorentino, and R. G. Beausoleil, "64 Gb/s low-voltage waveguide SiGe avalanche photodiodes with distributed Bragg reflectors," *Photonics Research*, vol. 8, pp. 1118–1123, Jul 2020.

[255] R. J. Collins, R. Hadfield, V. Fernandez, S. W. Nam, and G. S. Buller, "Low timing jitter detector for gigahertz quantum key distribution," *Electron. Lett.*, vol. 43, no. 3, pp. 180–182, 2007.

[256] R. J. Collins, R. H. Hadfield, V. Fernández, S. W. Nam, and G. S. Buller, "Low Timing Jitter Detector for Gigahertz Quantum Key Distribution," *Electron. Lett.*, vol. 43, pp. 180–182. 11 p, Feb 2007.

[257] R. H. Haitz, "Model for the electrical behavior of a microplasma," *Journal of Applied Physics*, vol. 35, no. 5, pp. 1370–1376, 1964.

[258] "Silicon avalanche photodiodes c30902 series." https://www.perkinelmer.com/CMSResources/Images/44-3477DTS_C30902.pdf, 2020. Accessed: 2020-07-06.

[259] R. Chandrasekara, Z. Tang, Y. Tan, C. Cheng, C. Wildfeuer, and A. Ling, "Single photon counting for space based quantum experiments," in *Advanced Photon Counting Techniques IX* (M. A. Itzler and J. C. Campbell, eds.), SPIE, may 2015.

[260] J. A. Grieve, R. Chandrasekara, Z. Tang, C. Cheng, and A. Ling, "Correcting for accidental correlations in saturated avalanche photodiodes," *Opt. Express*, vol. 24, pp. 3592–3600, Feb 2016.

[261] K. Schätzel, "Dead time correction of photon correlation functions," *Applied Physics B Photophysics and Laser Chemistry*, vol. 41, pp. 95–102, oct 1986.

[262] D. Subacius, A. Zavriyev, and A. Trifonov, "Backscattering limitation for fiber-optic quantum key distribution systems," *Applied Physics Letters*, vol. 86, no. 1, p. 011103, 2005.

[263] T. Musha, J. ichi Kamimura, and M. Nakazawa, "Optical phase fluctuations thermally induced in a single-mode optical fiber," *Appl. Opt.*, vol. 21, pp. 694–698, Feb 1982.

[264] J. Dong, J. Huang, T. Li, and L. Liu, "Observation of fundamental thermal noise in optical fibers down to infrasonic frequencies," *Applied Physics Letters*, vol. 108, p. 021108, Jan. 2016.

[265] N. Dutton, I. Gyongy, L. Parmesan, and R. Henderson, "Single photon counting performance and noise analysis of CMOS SPAD-based image sensors," *Sensors*, vol. 16, p. 1122, July 2016.

[266] "Spcm-aqrh." https://www.excelitas.com/file-download/download/public/60241?filename=Excelitas_SPCM-AQRH_Family_datasheet.pdf, 2021. Accessed: 2021-03-19.

[267] N. Gisin, G. Ribordy, W. Tittel, and H. Zbinden, "Quantum cryptography," *Rev. Mod. Phys.*, vol. 74, pp. 145–195, Mar 2002.

[268] D. Pulford, C. Robillard, and E. Huntington, "Single photon locking of an all-fiber interferometer," *Review of Scientific Instruments*, vol. 76, no. 6, p. 063114, 2005.

[269] E. D. Black, "An introduction to pound–drever–hall laser frequency stabilization," *American Journal of Physics*, vol. 69, no. 1, pp. 79–87, 2001.

[270] X. Fang, M. Lun Tseng, J.-Y. Ou, K. F. MacDonald, D. Ping Tsai, and N. I. Zheludev, "Ultrafast all-optical switching via coherent modulation of metamaterial absorption," *Applied Physics Letters*, vol. 104, no. 14, p. 141102, 2014.

[271] A. Ü. Hardal and M. Wubs, "Quantum coherent absorption of squeezed light," *Optica*, vol. 6, no. 2, pp. 181–189, 2019.

[272] A. Xomalis, I. Demirtzioglou, E. Plum, Y. Jung, V. Nalla, C. Lacava, K. F. MacDonald, P. Petropoulos, D. J. Richardson, and N. I. Zheludev, "Fibre-optic metadevice for all-optical signal modulation based on coherent absorption," *Nature Communications*, vol. 9, Jan. 2018.

[273] Y. D. Chong, L. Ge, H. Cao, and A. D. Stone, "Coherent perfect absorbers: Time-reversed lasers," *Phys. Rev. Lett.*, vol. 105, p. 053901, Jul 2010.

[274] W. Wan, Y. Chong, L. Ge, H. Noh, A. D. Stone, and H. Cao, "Time-reversed lasing and interferometric control of absorption," *Science*, vol. 331, no. 6019, pp. 889–892, 2011.

[275] J. Zhang, K. F. MacDonald, and N. I. Zheludev, "Controlling light-with-light without nonlinearity," *Light: Science & Applications*, vol. 1, pp. e18–e18, July 2012.

[276] A. Xomalis, I. Demirtzioglou, Y. Jung, E. Plum, C. Lacava, P. Petropoulos, D. J. Richardson, and N. I. Zheludev, "Picosecond all-optical switching and dark pulse generation in a fibre-optic network using a plasmonic metamaterial absorber," *Applied Physics Letters*, vol. 113, no. 5, p. 051103, 2018.

[277] M. Papaioannou, E. Plum, J. Valente, E. T. Rogers, and N. I. Zheludev, "All-optical multichannel logic based on coherent perfect absorption in a plasmonic metamaterial," *APL Photonics*, vol. 1, no. 9, p. 090801, 2016.

[278] S. M. Barnett, J. Jeffers, A. Gatti, and R. Loudon, "Quantum optics of lossy beam splitters," *Phys. Rev. A*, vol. 57, pp. 2134–2145, Mar 1998.

[279] J. Jeffers, "Interference and the lossless lossy beam splitter," *Journal of Modern Optics*, vol. 47, no. 11, pp. 1819–1824, 2000.

[280] A. Goodarzi, M. Ghanaatshoar, and M. Mozafari, "All-optical fiber optic coherent amplifier," *Scientific reports*, vol. 8, no. 1, pp. 1–6, 2018.

[281] A. K. Jahromi, A. Van Newkirk, and A. F. Abouraddy, "Coherent perfect absorption in a weakly absorbing fiber," *IEEE Photonics Journal*, vol. 10, no. 4, pp. 1–10, 2018.

[282] C. Altuzarra, *Quantum interferences with nanostructured metamaterials*. PhD thesis, 2018.

[283] A. Sipahigil, K. D. Jahnke, L. J. Rogers, T. Teraji, J. Isoya, A. S. Zibrov, F. Jelezko, and M. D. Lukin, "Indistinguishable photons from separated silicon-vacancy centers in diamond," *Phys. Rev. Lett.*, vol. 113, p. 113602, Sep 2014.

[284] C. K. Hong, Z. Y. Ou, and L. Mandel, "Measurement of subpicosecond time intervals between two photons by interference," *Phys. Rev. Lett.*, vol. 59, pp. 2044–2046, Nov 1987.

[285] H. J. Briegel, W. Dür, J. Cirac, and P. Zoller, "Quantum repeaters: The role of imperfect local operations in quantum communication," *Phys. Rev. Lett.*, vol. 81, pp. 5932–5935, Dec. 1998.

[286] Y. Zhang, S. Yang, A. E.-J. Lim, G.-Q. Lo, C. Galland, T. Baehr-Jones, and M. Hochberg, "A compact and low loss y-junction for submicron silicon waveguide," *Opt. Express*, vol. 21, pp. 1310–1316, Jan 2013.

[287] "Si-apd visible single-photon detector." https://s-fifteen.com/collections/single-photon-detectors-1/products/si-apd-single-photon-counting-module. Accessed: 2021-03-18.

Appendix A

Characterization of SiN Fiber-to-waveguide Edge Couplers

Introduction

Improving the fiber-to-waveguide coupling efficiency is crucial for loss-sensitive integrated quantum photonics applications. The large mode size mismatch between an optical fiber and a typical SiN waveguides of sub-micron dimensions imposes a challenge to achieve fiber-to-waveguide coupling with high efficiency.

In our APD characterizations, the light is coupled into the chip via SiN single-tip fiber-to-waveguide edge couplers with a minimum taper width of 180 nm (see §4.2.3). Recent simulation studies have shown that the fiber-to-waveguide coupling efficiency at visible wavelengths can further be improved using double-tip tapers together with a multimode interference (MMI) coupler [10]. The use of such higher efficiency tapers would subsequently increase the external responsivity of the waveguide-integrated detectors.

In this chapter, we present the characterization results of double-tip SiN fiber-to-waveguide edge couplers equipped with MMI combiners whose design and simulation study were previously reported by Dr. Jun Rong Ong in [10]. Specifically, here we measured the transmission of the fabricated couplers at 685 nm input light for both H and V polarizations, and then compared their performance to that of single-tip edge couplers.

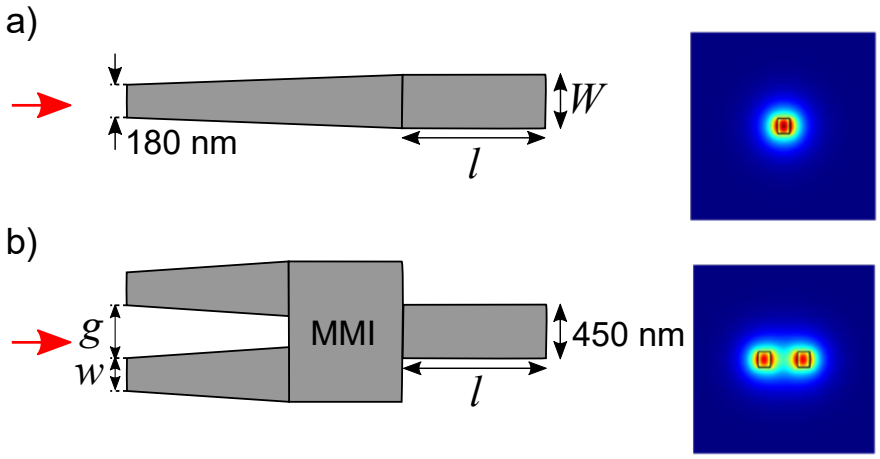

Figure A.1: Design parameters of the taper structures. a) Single-tip taper has a minimum taper width w of 180 nm, which widens to the various waveguide widths W ranging from 450 to 900 nm to achieve adiabatic coupling. b) Double-tip tapers coupled to a multimode interference coupler. The structures have different taper widths w and tip gaps g. The simulated optical mode profiles are shown on the right.

SiN edge coupler designs

Figure A.1 shows the design of SiN fiber-to-waveguide edge couplers together with the simulated optical mode profiles. The SiN waveguide thickness is 250 nm, and the waveguides are fully embedded in SiO_2, with a 3 µm top cladding and 3 µm bottom oxide (BOX) layer. The single-tip inverse tapers have minimum taper width w of 180 nm, and they are adiabatically coupled to SiN waveguides of various widths W between 450 - 900 nm (Fig. A.1(a)). The double-tip inverse tapers have various taper widths w of 140, 160, and 180 nm with corresponding gaps g of 520, 540 and 560 nm between the tips (Fig. A.1(b)).

The fiber-to-waveguide coupling efficiency of these designs are studied by calculating the mode matching efficiency. The mode overlap integral between the mode at the input side of the coupler and a Gaussian beam of corresponding polarization is read as

$$\eta = \frac{\left\| \int E_1 E_0 dA \right\|^2}{\int \left\| E_1^2 \right\| dA \int \left\| E_0^2 \right\| dA}. \tag{A.1}$$

The calculations are done for 638 nm and 738 nm, which are the typical photon emission wavelengths of nitrogen-vacancy (NV) and silicon-vacancy (SiV) centers in nano-diamonds, respectively. The mode matching efficiencies are calculated for a Gaussian beam with $1/e^2$

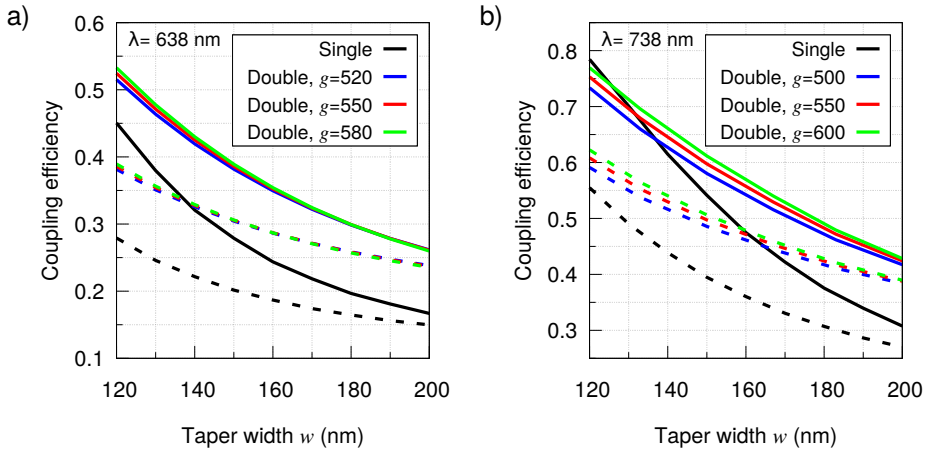

Figure A.2: Calculated mode matching efficiencies for single-tip and double-tip tapers with various taper widths at w a) 638 nm and b) 738 nm. For double-tip structures, the plots show results for various gap g (in nm) between the tips. The solid and dashed lines show data for TE and TM mode, respectively.

diameter of 2.5 µm. Figure A.2 shows the calculated mode matching efficiencies for various double-tip taper designs together with a single-tip taper for comparison [10].

For a taper width w of 180 nm, which is the typical minimum feature size for 248 nm DUV lithography, the calculations suggest that the double-tip tapers are more efficient than the single-tip taper, with the difference being more significant at 638 nm.

MMI beam combiner designs

In double-tip inverse tapers, the dual waveguide mode is converted to a single channel waveguide mode of 450 nm wide waveguides via MMI beam combiners. In addition to the mode matching efficiency between optical fiber and double-tip tapers (Fig. A.2), the MMI beam combiner may introduce additional insertion losses. Therefore, the MMI combiner designs with ultra-low losses are desired for double-tip taper structures to be advantageous compared to single-tip tapers. Figure A.3(a) and A.3(b) show two MMI beam combiners that are designed for 638 nm (MMI-1) and 738 nm (MMI-2) operation [10]. The designs are optimized for the transmitted power of the TE mode through the device via the particle swarm optimization method used in [286]. Figure A.3(c) shows their simulated transmission spectrum. For the optimized TE mode structures, a transmission of > 0.97 is obtained for both designs at their corresponding target wavelengths. For our characterization wavelength of 685 nm, both MMI designs show > 0.95 transmission for both TE and TM mode.

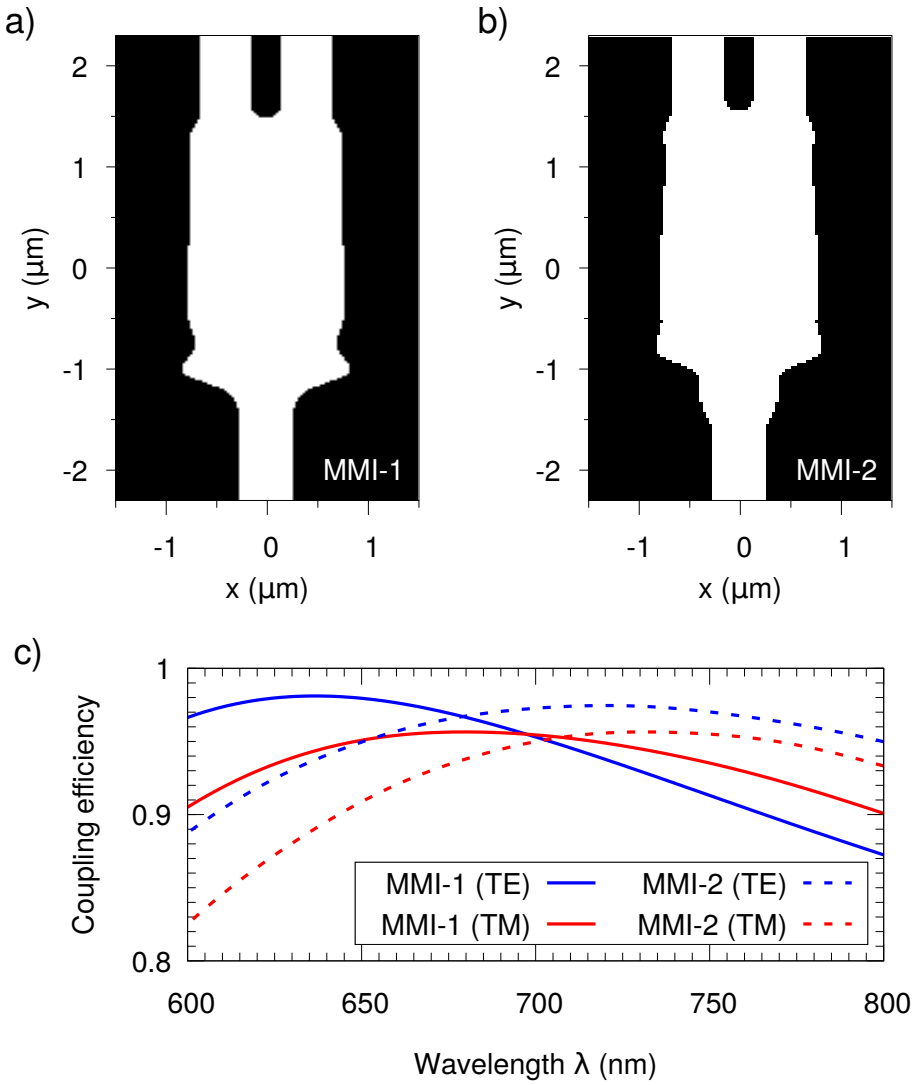

Figure A.3: MMI beam combiner designs at operating wavelength of a) 638 nm and b) 738 nm [10]. c) The corresponding coupling efficiencies for both TM and TE mode.

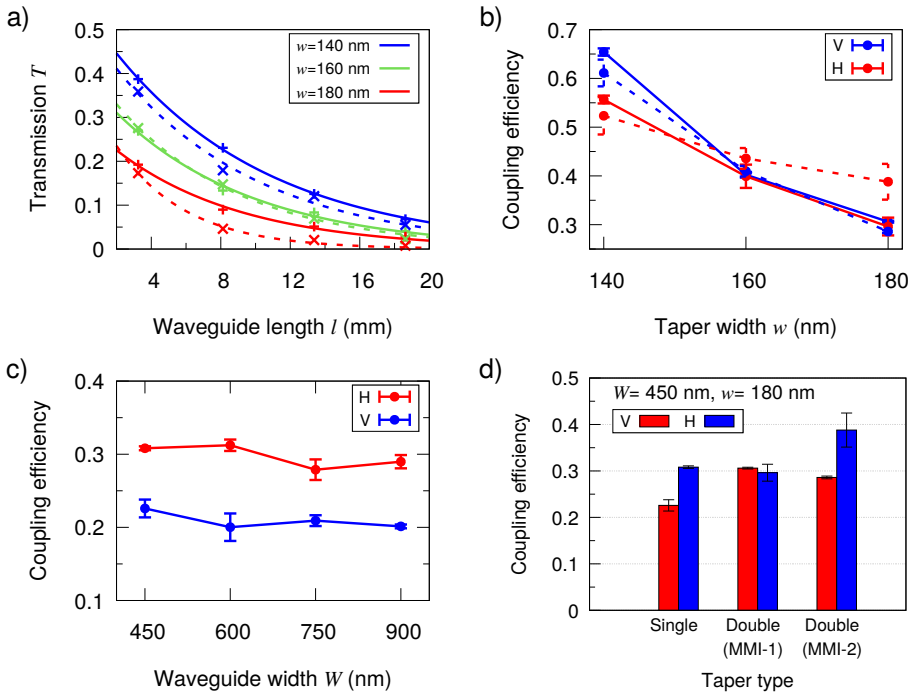

Figure A.4: Characterization of SiN fiber-to-waveguide edge couplers. a) Optical transmission of double-tip tapers of various taper widths w and waveguide lengths l at 685 nm input light with H polarization. b) Fiber-to-waveguide coupling efficiencies of double-tip tapers of various taper widths w for both polarization states. Solid (dashed) line denotes the edge coupler with MMI-1 (MMI-2) beam combiner. c) Fiber-to-waveguide coupling efficiency of single-tip edge couplers with $w = 180$ nm that are tapered to $W = 450$ nm. d) Comparison of double-tip and single-tip edge couplers with $w = 180$ nm that are tapered to $W = 450$ nm. The parameter w denotes the *design* widths.

Experiment

In our experiments, the fabricated edge couplers are adiabatically coupled from a minimum taper width w to various waveguide widths W along a 200-µm-long taper. In order to characterize the coupling efficiency of the fabricated edge couplers, we first measured the optical transmission T of SiN waveguides of various lengths l at 685 nm input light for both H and V polarizations using cutback method. The optical transmission of double-tip edge couplers at H polarization is shown in Fig. A.4(a) as a representative measurement. We note that parameter w in Fig. A.4 denotes the *designed* widths, and the actual values may deviate, especially for dimensions which are below the typical minimum feature size of 180 nm.

After accounting for the propagation loss, we extracted the fiber-to-waveguide coupling efficiency of these structures as shown in Fig. A.4(b). A lower minimum taper width w

yields higher coupling efficiency for both polarizations, and it agrees well with the simulation results shown in Fig. A.2(a).

Similar transmission measurements are performed for single-tip edge couplers with $w = 180$ nm that are tapered to SiN channel waveguides of various waveguide widths W, and Fig. A.4(c) shows their coupling efficiency. The coupling efficiency for H polarization is higher than that for V polarization. The fiber-to-waveguide coupling efficiency is uncorrelated with the waveguide width W as expected. We note that we could not check the dependence of the coupling efficiency of single-tip edge couplers on the minimum taper width w as we lacked those test structures.

Figure A.4(d) compares the performance of double-tip and single-tip edge couplers all of which have a minimum taper width w of 180 nm and couple to 450-nm-wide SiN channel waveguides. The double-tip edge coupler has higher coupling efficiency than the single-tip counterpart for V polarization. For H polarization, the coupling efficiency of double-tip edge coupler with MMI-2 combiner is higher than that of the single-tip edge coupler, whereas the coupling efficiencies of single-tip edge coupler and double with edge coupler with MMI-1 combiner are within their error bars. Also, we note that the polarization dependence of the double-tip edge coupler with MMI-2 combiner is larger than that of with MMI-1 combiner. This trend agrees well with the larger difference in the simulated transmission of MMI-2 combiner at 685 nm as shown in Fig. A.3(c).

Conclusion

In conclusion, we performed a comparative characterization study of various SiN edge couplers in terms of their fiber-to-waveguide coupling efficiency. Our measurement results showed that the double-tip edge couplers yield higher fiber-to-waveguide coupling efficiency than the single-tip edge coupler at 685 nm input light with V polarization. The corresponding coupling efficiency for H polarization is higher for double-tip edge coupler with MMI-2 combiner compared to that of single-tip edge couplers, whereas there is no significant difference for the other double-tip edge couplers with MMI-1 combiner. The performance can further be improved with the use of MMI beam combiners that are optimized for the operation wavelength, though an attention must be paid for the bandwidth limitation that might be imposed by MMI beam combiners. The use such fiber-to-waveguide edge couplers with improved coupling efficiency can increase the external responsivity of waveguide-integrated APDs (see 4.2.3).

Appendix B

Towards Interfacing Nanodiamonds with Integrated APDs

We aim to integrate a nanodiamond containing a color center inside a high-Q factor microring resonator in order to have an on-chip single-photon source (see § 9). In addition to such nanodiamond particles, the diamond nanopillars fabricated in the form of a scanning microscope probe provide alternative platforms where we explore the coupling of single photons emitted from a diamond of similar submicron sizes.

Here, we present our experimental efforts to couple single photons emitted from a diamond nanopillar with a nitrogen-vacancy (NV) center into a microring resonator in a combined atomic force microscope (AFM) and confocal microscope (CFM) setup. The purpose of this experiment is to understand the emission dynamics of a diamond nanopillar with an NV color center and to develop new techniques to interface such an emitter with our photonics platform.

Concept

The diamond nanopillar is attached to the tip of the cantilever of an AFM probe. These combined probes are commercially available and extensively used for quantum-enhanced scanning magnetometry through optically detected magnetic resonance (ODMR) of NV color centers.

We loaded one such probe into our combined scanning atomic force and confocal microscope (Attocube attoAFM/CFM), and then performed experiments at room temperature. Figure B.1 depicts the concept of the experiment. The diamond nanopillar is 200 nm wide and 2 µm long. It hosts a single NV center that is centrally located about 20 nm from the bottom

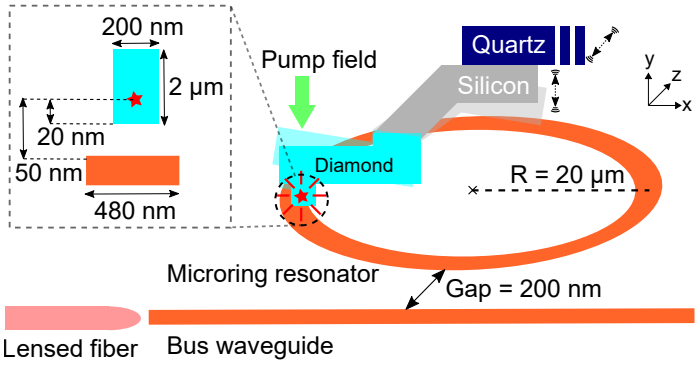

Figure B.1: Concept of coupling single photons emitted from a diamond color center into a microring resonator. A diamond nanopillar containing an NV center is positioned in close proximity to the microring resonator. The pump field from the top excites the NV center to emit single photons. The light field is enhanced by the resonator, and evanescently couples to a bus waveguide. A lensed fiber is positioned next to the bus waveguide at the edge of the chip to outcouple single photons for optical spectrum measurements. The oscillation direction of the AFM tip during AFM measurements is shown by vibrating arrow symbols. The image is not drawn to scale.

of the nanopillar as per specifications provided by the supplier, QZabre LLC. Our objective is to approach the NV center to a SiN microring resonator within 50 nm by using an AFM probe, and then couple single photons emitted from the NV center into the SiN microring resonator that has a waveguide width of 480 nm and a radius of 20 µm. The photons are then evanescently coupled from the SiN microring resonator to a bus waveguide that is placed 200 nm away. Finally, a lensed fiber is coupled to a SiN bus waveguide at the edge of the chip in order to collect the photons for optical spectrum measurements.

Experiment

AFM tip with a diamond nanopillar

Our AFM probe is of Akiyama type. This type of probes uses a quartz tuning fork combined with a micromachined cantilever for distance control and topography readout through force-feedback sensor (see Fig. B.2). While approaching, the quartz tuning fork is electrically excited at one of its resonance frequencies. The motion of its prongs on the horizontal (xz) plane causes a small vibration at the glued ends of the cantilever in the vertical (xy) plane as shown in Fig. B.1. As the probe approaches the sample underneath, the phase change of the

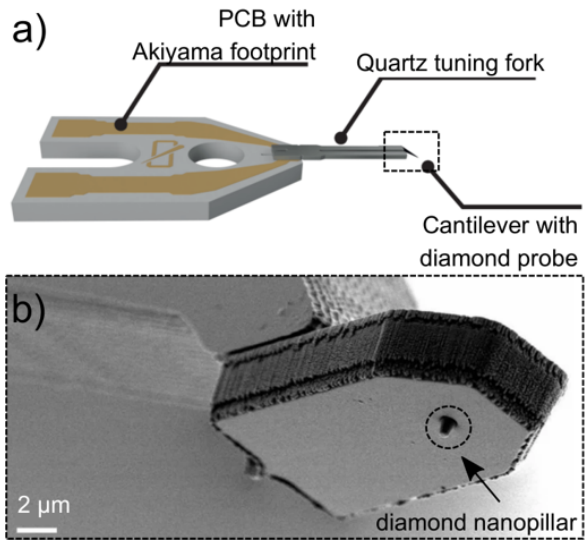

Figure B.2: AFM diamond tips. a) The AFM tip with Akiyama probe footprint has a cantilever to its quartz tuning fork. b) The cantilever has a diamond nanopillar underneath of the tip of the cantilever. The nanodiamond nanopillar contains single NV color center. Images are adapted from [11].

resonance frequency and the resonance amplitude are used to measure the distance between the probe and the sample.

The photographs of the experimental setup are shown in Fig. B.3. The excitation of the NV center is performed by a pump laser at 532 nm located inside of the AFM/CFM optical head (Fig. B.3(a)). A beamsplitter diverting some light to a camera was used to image the sample during positioning and coupling adjustments. A lensed fiber is coupled to the SiN bus waveguide at the edge of the chip via 3-axis motorized piezo (Sutter instrument) stage as shown in Fig. B.3(b). The sample stage is located at the bottom of the microscope stick with two sets of 3-axis piezo stages for the AFM tip and sample positioning control. Figure B.3(c) shows the lensed fiber together with the sample and the AFM probe underneath the objective lens of the attoAFM/CFM. The green scattering from the AFM tip in Fig. B.3(c) is due to the 532 nm pump laser.

Alignment procedure

In order to outcouple single photons emitted from an NV center via a lensed fiber, a precise alignment between the pump field, NV center, microring resonator, and lensed fiber is required as shown in Fig. B.1. Here, we listed the main steps of the alignment process and showed each of them in Fig. B.4:

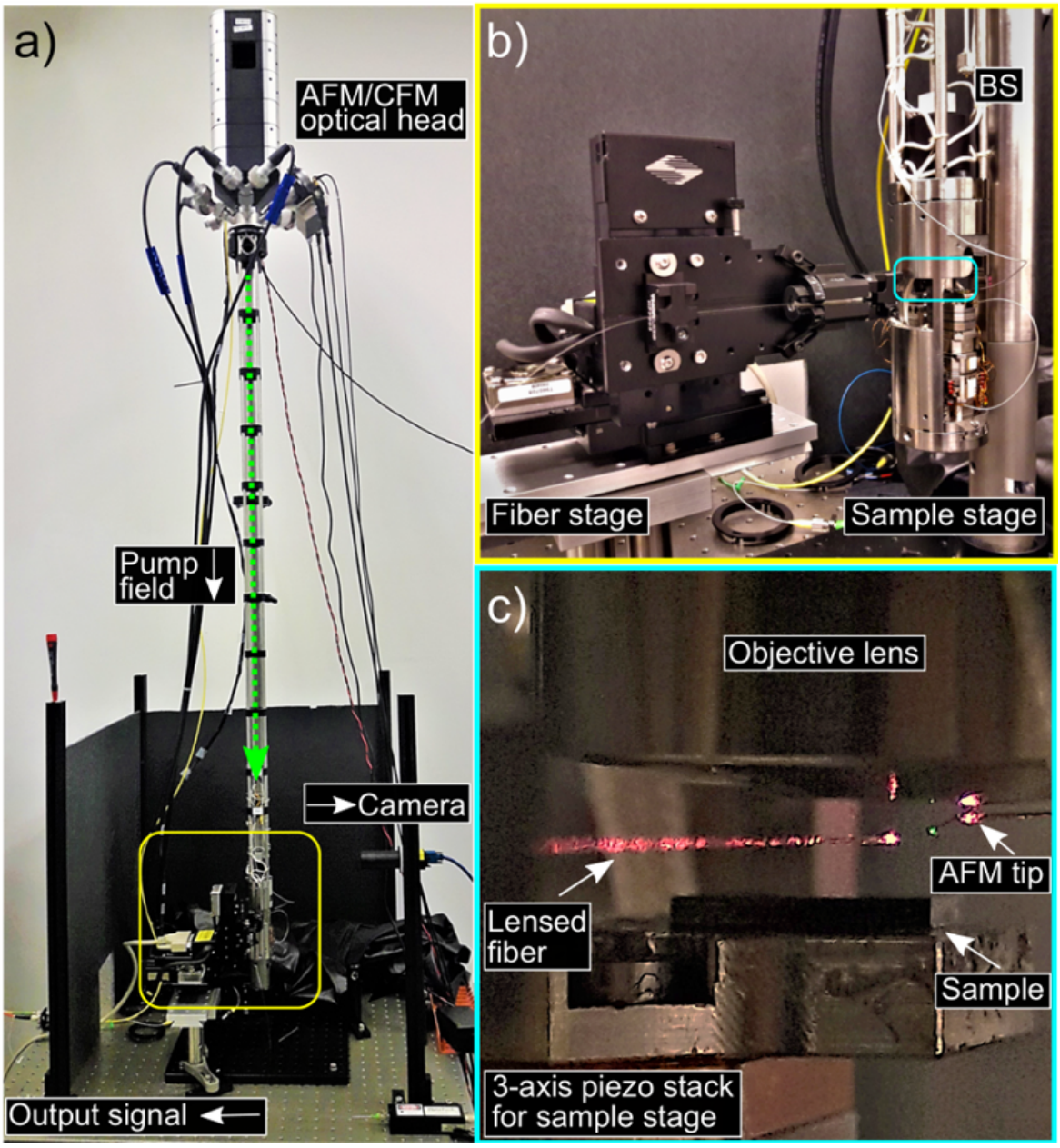

Figure B.3: Photographs of the experimental setup for nanodiamond coupling. a) 532 nm pump field coming from the top excites the AFM tip located at the bottom of the microscope stick. b) The bus waveguide is coupled to a lensed fiber via a 3-axis motorized stage from the edge of the chip. An NPBS diverting some light to camera was used adjust image the AFM tip and the sample during initial positionings. Two independent stacks of 3-axis piezoelectric stages are used to align the microring and the diamond nanopillar with respect to the pump field. c) 660 nm CW light coupled from the lensed fiber into the chip is used to optimize the fiber coupling. The bright green scattering at the tip of the AFM probe is due to the pump field coming from the top.

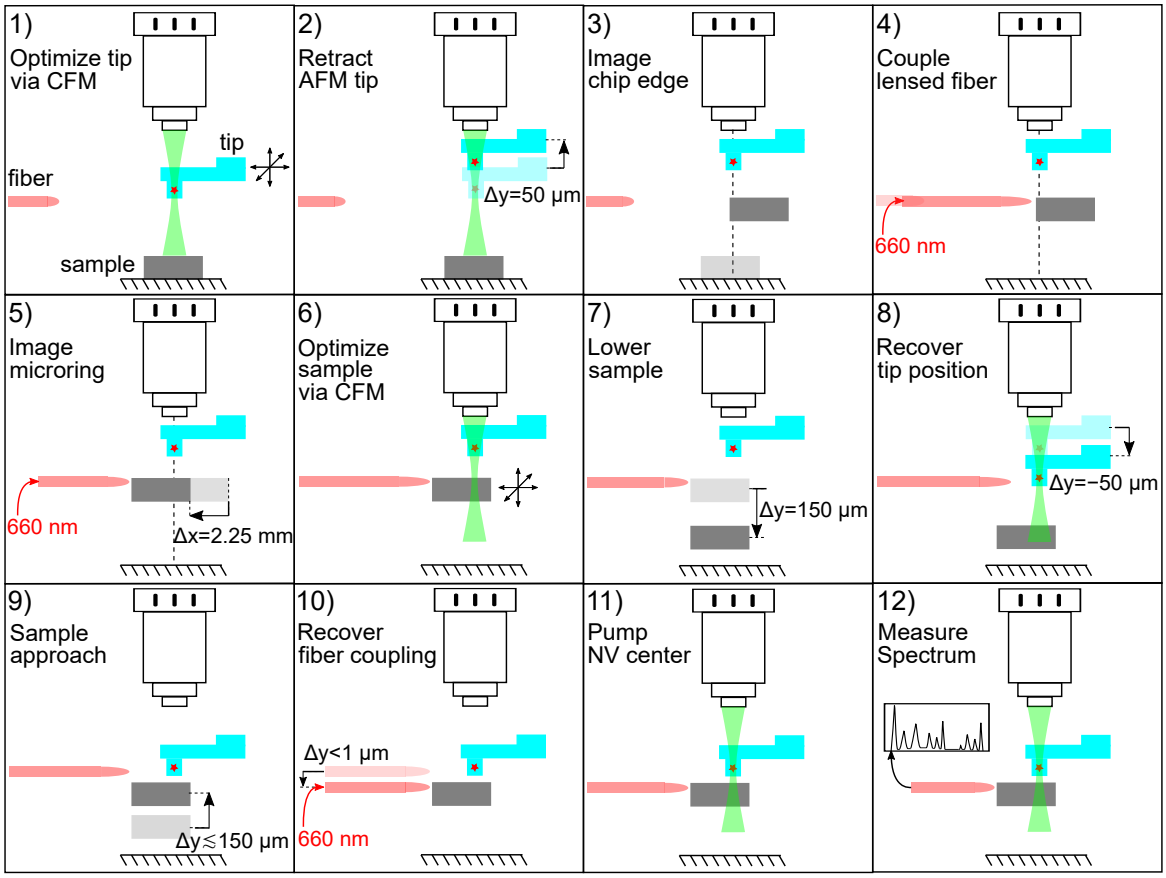

Figure B.4: Main steps of the experiment for the demonstration of coupling of single photons from a NV center in a diamond nanopillar into a SiN microring resonator.

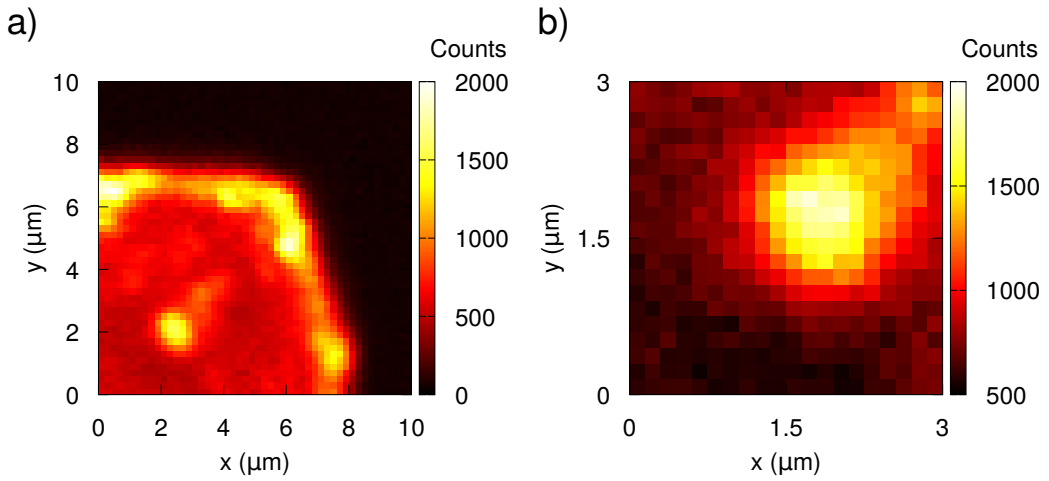

Figure B.5: a) CFM image of the diamond cantilever tip. Each pixel shows number of photon counts per 50 ms. b) CFM image of the diamond nanopillar region once the y-position of the tip is optimized.

1. Image the AFM tip and optimize its position under the pump field via CFM scan.
2. Move the AFM tip upwards by $\Delta y = 50\,\mu$m.
3. Move the sample upwards from the bottom and image the edge of the chip.
4. Couple the lensed fiber from the edge of the chip.
5. Image the microring resonator and bus waveguide while retaining the fiber coupling.
6. Optimize the position of the microring resonator under the pump field via CFM scan.
7. Lower the sample by $\Delta y = 150\,\mu$m.
8. Move the AFM tip back to the focal plane of the pump field by $\Delta y = -50\,\mu$m and optimize its position.
9. Move the sample towards the AFM tip by $\Delta y \leq 150\,\mu$m with auto-approach procedure.
10. Recover the fiber coupling by accounting for the net vertical displacement $\Delta y < 1\,\mu$m.
11. Pump the NV center.
12. Measure the optical spectrum of the outcoupled photons.

In step-1, we located the cantilever of the AFM tip with the camera, and then optimized the tip position under the pump field by maximizing the photon counts from the diamond nanopillar region. Figure B.5(a) shows a CFM image of the edge of the AFM tip with the diamond nanopillar region located at the lower left corner. We adjusted the height of the tip to optimize the coupling of the pump field into the diamond nanopillar as shown in Fig. B.5(b). Since we could only image one structure at a time in the focal plane, we had to moved tip upwards by 50 µm (step-2) to prevent any collision with the sample, and then proceeded to the adjustment of sample position. We moved the sample until we could image the edge of the chip (step-3), and then we coupled the lensed fiber into the SiN bus waveguide by launching 660 nm CW light (step-4).

In step-5, we moved the sample such that we could image both the microring resonator and the bus waveguide while still retaining the lensed fiber coupling; though, this was not an easy task. The reason is that the microring resonator was 2.25 mm away from the edge of the chip where it is coupled to the lensed fiber, whereas the camera imaging area of 320 µm$\times$200 µm[1] was not wide enough to capture the lensed fiber and the microring resonator at once. Moreover, we could not change the position of this imaging area as the imaging optics inside the microscope were fixed.

Therefore, in step-5 we performed the fiber coupling procedure shown in Fig. B.6. First, we imaged the lensed fiber and the bus waveguide on the edge of the chip. Next, we launched a 660 nm CW light from the lensed fiber, and then achieved coupling by maximizing the scattering signal from the bus waveguide (see Fig.B.7(a)). Thereafter, we retracted the lensed fiber from the edge of the chip by 10 µm; the fiber-waveguide coupling decreased but remained sufficient to provide a visible scattering signal. Subsequently, we moved the chip towards the retracted fiber by $<$10 µm, and subsequently re-optimized the coupling. By repeating these steps, we could get the microring resonator and bus waveguide into our imaging area while maintaining the fiber coupling to the chip. A micrograph of the fiber that is coupled to the microring resonator is shown in Fig. B.7(b).

Thereafter, we proceeded to positioning of the microring resonator and the bus waveguide under the pump field via CFM scan as shown in Fig. B.8 (step-6). Once we positioned the microring resonator under the pump field, we lowered the sample by 150 µm (step-7). Subsequently, we moved the previously retracted AFM tip back to the focal plane of the pump field (step-8). In doing so, we keep the NV center at its optimal position along the focal plane of the pump beam.

[1] We obtained these dimensions by proportioning the microring resonator diameter to the edges of the camera image.

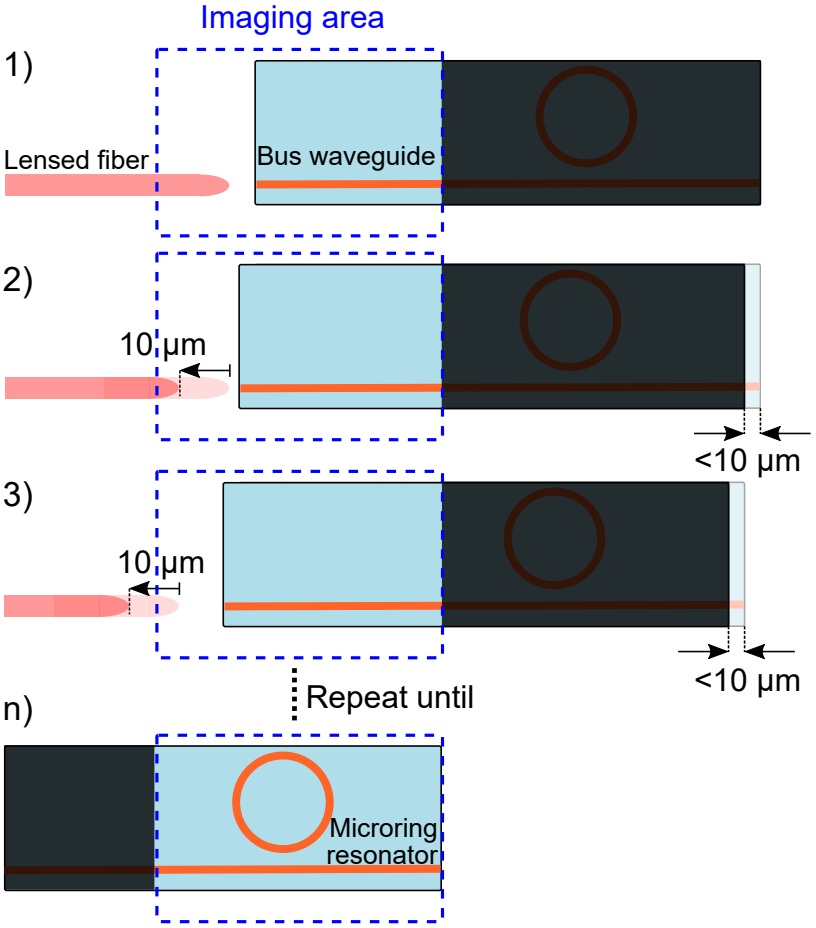

Figure B.6: Lensed fiber coupling procedure in step-5. First, we imaged the fiber and the bus waveguide at the edge of the chip and achieved coupling by maximizing the scattering signal from the bus waveguide. In subsequent steps, we retracted the lensed fiber by 10 µm, moved the chip towards the fiber, and then re-coupled the fiber. While retaining the fiber coupling, these steps are repeated until we could image the microring resonator and the bus waveguide at once. The dashed blue line denotes the fixed imaging region, and the portions of the chip that could not be imaged are shaded.

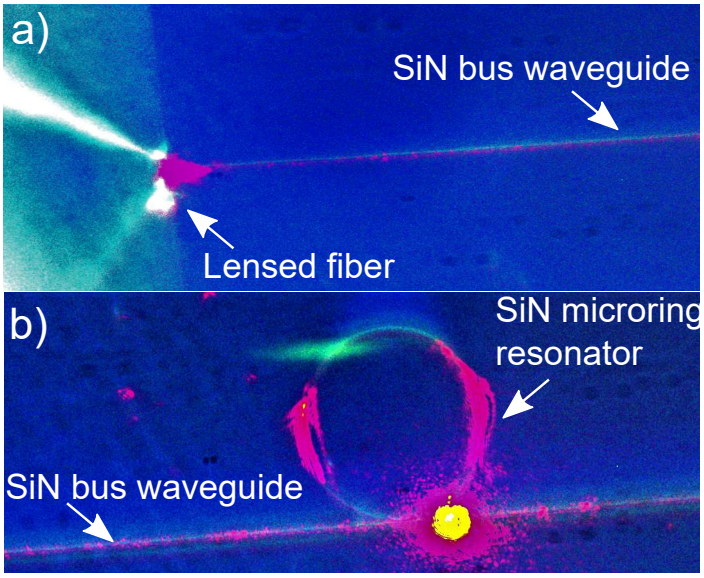

Figure B.7: Fiber coupling to the microring resonator. a) A lensed fiber is coupled to a SiN bus waveguide. b) The light evanescently couples from the bus waveguide to the SiN microring resonator. The bright red spot is due to the scattering along the waveguide, whereas the green light seen at the top left of the microring resonator is due to the reflection of the illumination LED of the imaging system.

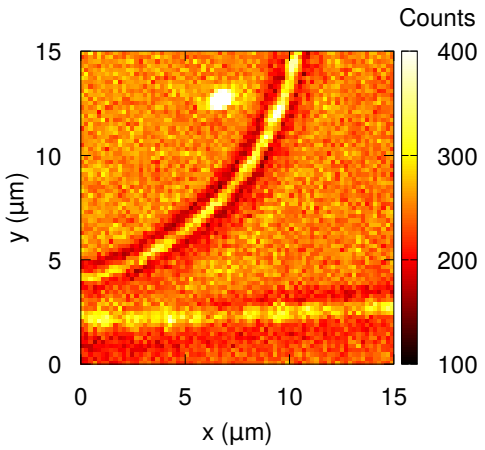

Figure B.8: CFM image of the microring resonator and the bus waveguide. Each pixel shows the number of photon counts integrated over 50 ms.

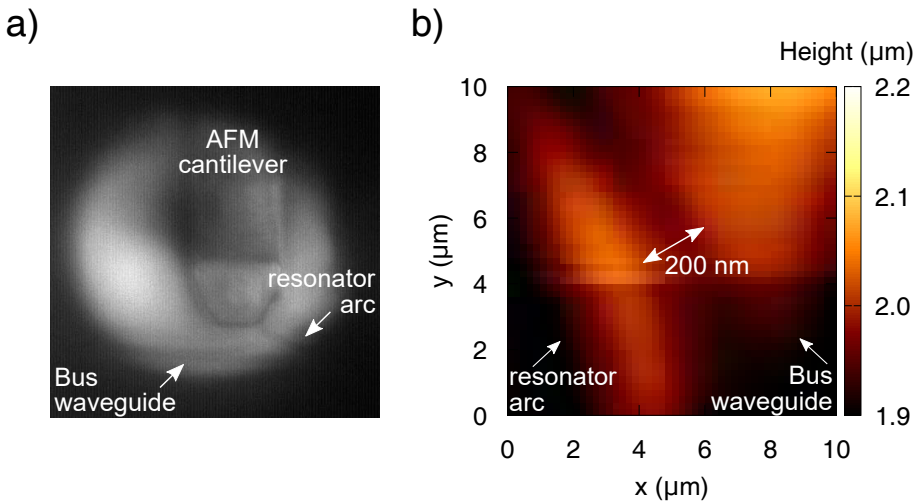

Figure B.9: a) Micrograph of the diamond tip on top of the microring resonator arc. b) Atomic force microscope image of the microring resonator and the bus waveguide.

After independently adjusting the positions of both the microring resonator and the diamond nanopillar on the xz-plane, we kept the tip position under the pump field fixed, and then moved the previously lowered sample plate towards the tip along the y-axis (step-9). We performed the auto-approach procedure of the attoAFM/CFM setup. This procedure uses the resonant tuning fork principle to sense the distance between the sample and the probe tip. After bringing the chip and the tip closer, the coupling to the chip is recovered by reoptimizing the position of the lensed fiber (step-10). Here, the lensed fiber is moved upwards by the net vertical displacement between step-7 and step-9, i.e., $\Delta y < 1$ μm.

A micrograph of the tip on top of the sample is shown in Fig. B.9(a). Figure B.9(b) shows the AFM image of the microring resonator and the bus waveguide. Although we could not finely resolve the topography, Fig. B.9(b) shows a contrast between the lower left and the upper right portions of the scanned area. The reason for not being able to finely resolve the topography is that the diamond nanopillar was not as sharp as the conventional AFM probe tips. Nevertheless, since the lower left feature seems like an arc that bends towards left, we think that this arc-like structure belongs to the microring resonator, whereas the other feature was a part of the bus waveguide. Moreover, the slightly shallower region between these two portions possibly corresponds to the region between the resonator structure and the bus waveguide. For reference, we put an arrow corresponding to the length of 200 nm, which is the designed gap between these two structures.

After aligning the AFM tip on top the microring resonator arc, we excited the diamond nanopillar with a pump field at 1.5 mW output power (step-11), and then, checked the

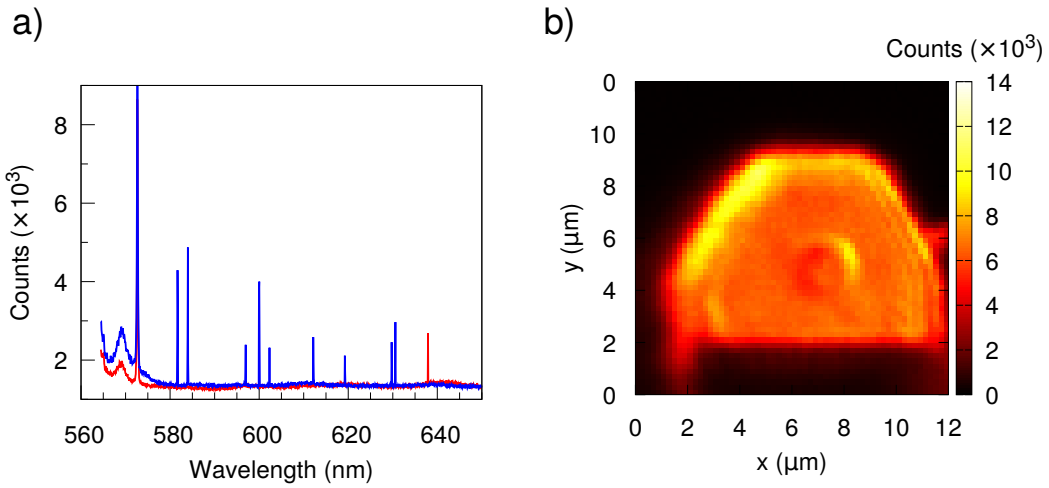

Figure B.10: a) Optical spectrum of photons collected from the diamond nanopillar region. b) CFM image of the diamond cantilever just after the spectrum measurements.

optical spectrum of the coupled photons via a spectrometer (Princeton Instruments Lightfield Spectrometer) with an exposure time of 60 seconds (step-12).

Optical Spectrum Measurements

In our optical spectrum measurements, we used a notch filter with a center wavelength of 532 nm and a bandwidth of 25 nm at the output stage to block the pump field. Figure B.10(a) shows the two optical spectrum measurements of the diamond nanopillar region. There are some sharp spectral lines which are not manifested in both scans; thus, we think that they are artefact spectral lines due to the spectrometer. On the other hand, there is a spectral line at 572 nm which persists at both scans. This may first suggest a zero-phonon line of a NV^0 charge state; however, it lacks a more pronounced phonon side band until 700 nm. Therefore, it does not belong to the NV^0 charge state, and it is most likely a Raman line.

In a subsequent CFM scan of the diamond cantilever as shown in Fig. B.10(b), we observed a circular feature at the location of the diamond nanopillar instead of a bright spot at that location similar to Fig. B.5(a). We argue that this circular feature in Fig. B.10(b) corresponds to the remains of the broken diamond nanopillar. While performing the auto-approach procedure in step-9, the tip probably crashed into the sample, and then it was broken. Therefore, what we observed in Fig. B.10(a) is not the optical spectrum of the diamond nanopillar with NV center but just the diamond cantilever slab.

Conclusion

The coupling of single photons emitted from a single NV center embedded in a diamond nanopillar into a SiN microring resonator was not shown during the time frame of our experimental efforts. Relying on Fig. B.10(b), we think that the diamond nanopillar was broken while moving the sample towards the tip. A scanning electron microscopy image would have been useful to further verify that this was indeed the case.

Nonetheless, with the arrival of new tips and the development of custom scripts for 3-axis piezo stages for more precise tip and sample position control, our group has succeeded in demonstrating the coupling of photons from the NV center into a fiber by observing the spectral signature of the NV center in diamond, showing the viability of our approach.

Appendix C

Electronic Circuits for APDs in Geiger-mode Operation

Commercial SPAD characterization

We verified our characterization testbed by characterizing a commercial APD (Perkin Elmer C30902SH) operated in Geiger mode. We gratefully acknowledge Prof. Christian Kurtsiefer for providing us with this APD detector module we used in the verification of our characterization testbed. These APD detector modules are now commercially available [287], and the more details about the module can be found in [4]. Here, we briefly describe this module and explain the operation of its avalanche pulse conditioner electronics.

The fiber-pigtailed APD detector is mounted inside a hermetically sealed case (see [287] for its photographs). The device temperature is controlled by an electronic temperature controller consisting of a thermistor and a thermoelectric cooler inside the case as feedback elements. An electronics circuit, which consists of an analog temperature controller, a high voltage amplifier, and avalanche pulse conditioner, is connected to the case.

The commercial APD has a latching current I_q of around 50 µA. We selected the load resistor $R_L = 390\,\mathrm{k}\Omega$ so that the asymptotic steady state current I_f is 25 µA for an excess bias voltage V_E of 10 V (see Eq. 5.3). Higher resistance values of R_L could also be chosen in order to achieve faster quenching transition and lower timing uncertainty; however, this would have increased the voltage recovery time constant (see Eq. 5.7). The voltage recovery time constant was around 0.6 µs for our chosen R_L value for an effective capacitance of 1.6 pF.

Here, we briefly describe the avalanche pulse conditioner part of the electronics circuit. Figure C.1 shows the schematic of the quenching and avalanche pulse conditioning circuit. Following an avalanche breakdown, the avalanche current pulse flows through the sense

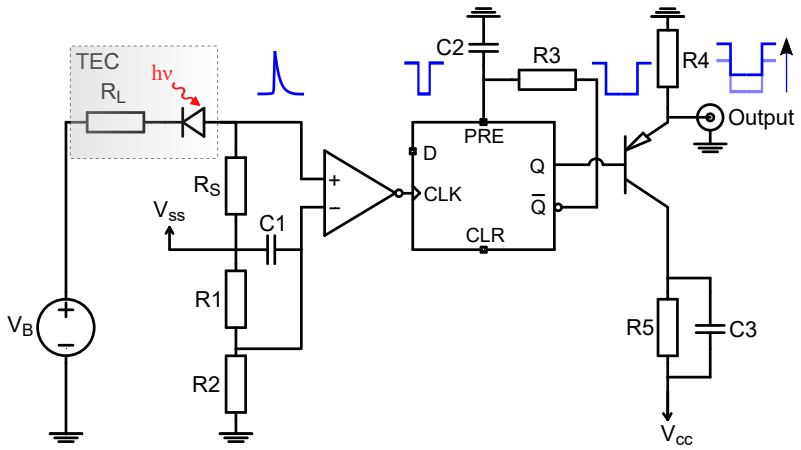

Figure C.1: Simplified schematic of the pulse conditioning circuit.

resistor R_s and generates a voltage drop across it. This voltage drop is then compared with a threshold voltage V_{th}, which is set at the other input port the comparator by a resistive network divider composed of R_1 and R_2. The comparator output signal is subsequently fed into a latch block to widen the pulse width by a duration determined by the time constant set by C_2 and R_3. The latch block consists of a D flip-flop that is configured as a monostable multivibrator. At the final stage, the widened pulse is fed into a transistor to convert the logic level of the pulse to a fast logic standard for transmission to other instruments.

RF filters in waveguide-integrated SPAD characterization

In our waveguide-integrated APD characterization in § 5.3, the avalanche pulses directly obtained from the devices had a pulse height of 2 mV with a rise time of around 2 ns. The pulse amplitude was not high enough to reliably transmit the avalanche pulses to other instruments. Therefore, we first amplified the avalanche pulses with a wideband RF amplifier (RF BAY, LPA-7-25) that operates within a frequency range from 0.1 MHz to 7 GHz with around 35 dB power gain.

The amplified pulses were filtered by a custom high-pass filter and low-pass filter. When they are cascaded, these filters function as a band-pass filter with a lower and upper cutoff frequency of 5 and 157 MHz, respectively (see Fig.C.2). The filtering and amplification of stages allowed us to amplify avalanche pulse amplitudes to around 50 mV, which was high enough for subsequent electrical interfacing.

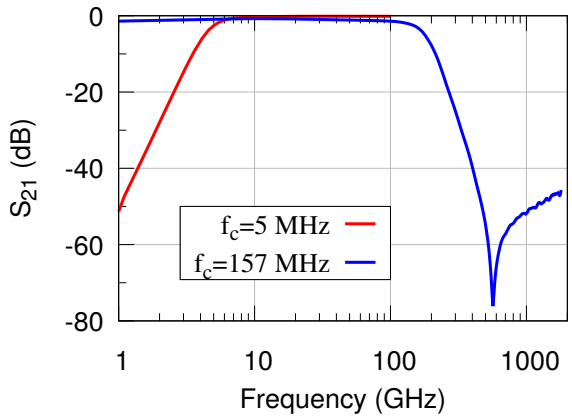

Figure C.2: Frequency response of home-built RF filters.

Wire Bonded APDs

Minimizing the parasitic capacitance associated with long electrical connections improve the noise performance of devices (see § 5.4.2.1). Figure C.3(a) shows the photograph of devices that are wire bonded onto a ceramic dual in-line (CDIP) package for reducing the electrical connection between the devices and the quenching circuit. Figure C.3(b) shows the electronic circuit board accommodating these wire bonded devices. The circuit consists of a double-pole six-throw switch (DP6T) and two opto-relays for two different regimes of operation, namely, gated and continuous operation. DP6T switch allows us to choose amongst 6 different devices, where each throw of the switch allows us to connect the common electrical ports of the switch to the cathode and anode of one device.

Figure C.3(c) shows an alternative design which is more suitable for the characterization of wire bonded devices at low temperatures. Unlike the previous design where the heat transfer between a thermoelectric cooler and the wire bonded devices may be impeded by the ceramic package, the devices in this design are directly mountable onto the top surface of the circuit board through a glue with a good thermal conductivity. The top and bottom copper layers of the attachment region are exposed and connected to each other with vias to facilitate good thermal conduction between them. A thermoelectric cooler can be soldered onto the exposed bottom layer of the circuit board for cooling the device.

The APDs are wire bondable to the exposed contact pads on the top surface of the PCB. Compared to the previous circuit board design, this design uses two 6PDT switches for switching between 12 different devices on a single board.

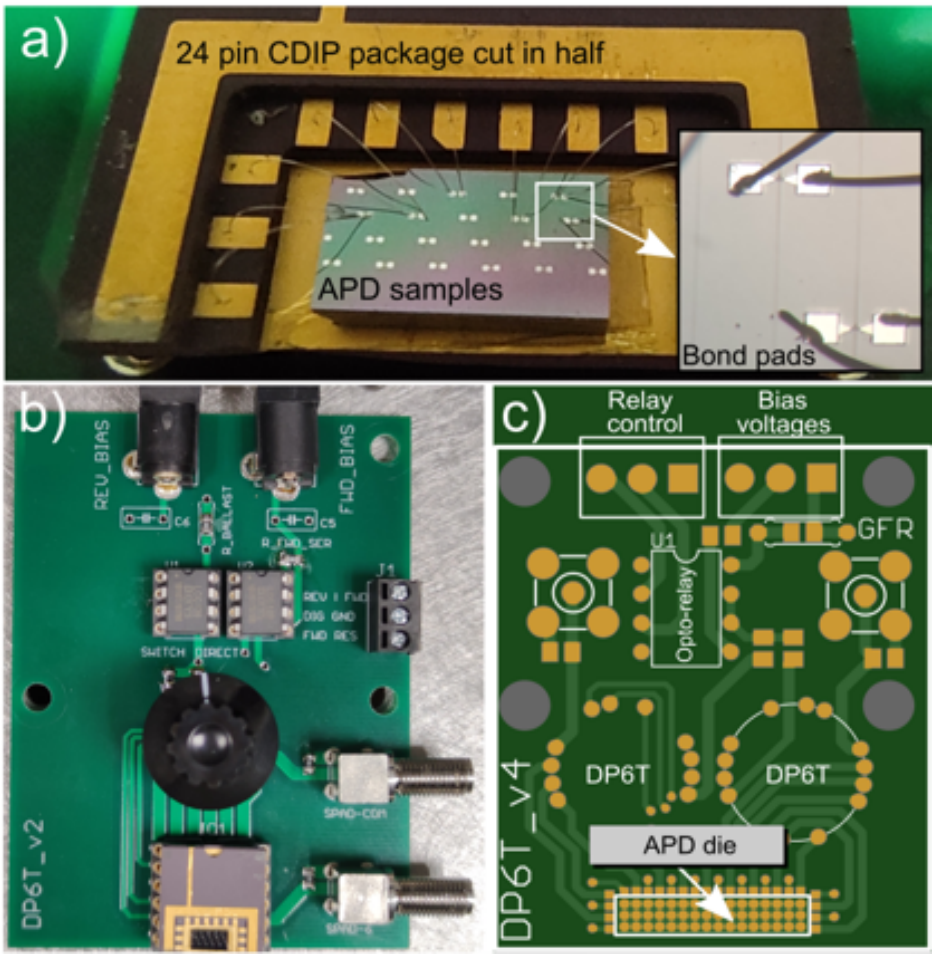

Figure C.3: Quenching circuit board designs for wirebonded APDs. a) The devices are wire bonded to the pins of a 24-pin ceramic dual in-line package (CDIP) that is cut in half. The inset shows the zoomed view of the wire bonded contact pads. a) The photograph of the custom electronics board accommodating the wire bonded devices on a CDIP package. c) The alternative board design for low temperature operation. Here, the devices are directly wire bonded onto the exposed pads of the printed circuit board.

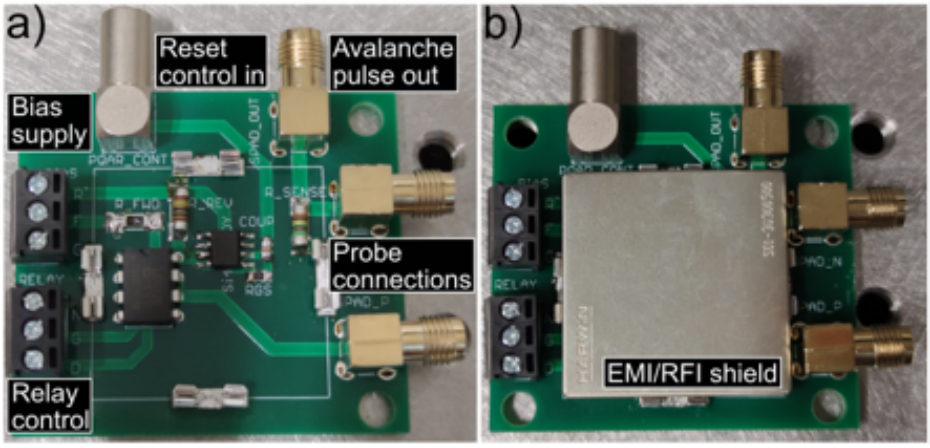

Figure C.4: Photographs of passive-quenching active-reset circuit a) with and b) without an EMI/RF shielding.

Given their benefits of reduced electrical connections and suitability for lower temperature operation, the circuit board designs provided here can be utilized in future studies.

Passive-quenching Active-reset circuit

Figure C.4 shows the photographs of the passive-quenching active-reset circuit board (see § 5.4.2.1). Such circuits can be useful in future studies to prevent device saturation by actively expediting the slow voltage recovery of a passive transition.

Appendix D

Heralded Single-photon Source

Here, we provide more details about the photon statistics of the heralded single-photon source.

Coincidence-to-accidental ratio

The coincidence time window $\Delta t_{\text{coinc.}}$ in our experiments with heralded single-photon source was set to 3.24 ns (see 7.4). The count rate of the heralding photons N_h and the total coincidence rate N_{tot} were 1.25×10^5 counts per seconds (cps) and 192 cps, respectively. The total coincidence rate N_{tot} was calculated from the single-photon detector timestamps. The half of these timestamps were obtained when the interferometer was driven to its coherent absorption regime (CAR), whereas the other half were obtained during the coherent transmission regime (CTR). Since the corresponding total photon detection probabilities for these two regimes were $p_{\text{CAR}} = 0.05$ and $p_{\text{CTR}} = 0.46$, respectively, the total coincidence rate N_{tot} was calculated for a system where the average total probability of single-photon detection $\overline{p}$ was around 0.25. The heralding efficiency of our single-photon source is then read as

$$\eta = \frac{N_{\text{tot}} \pm \sqrt{N_{\text{tot}}}}{N_h \pm \sqrt{N_h}}, \tag{D.1}$$

which was equal to $1.53 \pm 0.11 \times 10^{-3}$ in our experiment. We note that N_{tot} was not high enough to have a feedback control signal with good signal-to-noise ratio (SNR), which is given by

$$SNR = \frac{N}{\sqrt{N}} = \sqrt{N}, \tag{D.2}$$

where N is the number of events integrated over Δt, and $\sqrt{N}$ is the associated shot noise. For instance, even if the integration time window Δt were 100 ms instead of 24 ms, the SNR of the feedback control signal solely consisting of N_{tot} would have been around 4.4 due to the associated Poisson fluctuations. This would have subsequently degraded the performance of the feedback loop. Therefore, for our proof-of-concept demonstration, we also engaged a CW laser in all-optical switching demonstration. We adjusted the photon flux N_{CW} such that the photon rate at the phase stabilization set point was equal to 850 counts/Δt. This allowed us to improve the SNR of the feedback signal by around 7 times.

The probability of accidental coincidence counts due to weak 810 nm CW laser during $\Delta t_{\text{coinc.}}$ is given by

$$n = \frac{N_{\text{CW}} \pm \sqrt{N_{\text{CW}}}}{\Delta t} \times \Delta t_{\text{coinc.}}, \tag{D.3}$$

which equals to $2.75 \pm 0.09 \times 10^{-5}$ in our case. The coincidence-to-accidental ratio CAR (i.e., n/η) is then equal to 55.6 ± 0.04. Therefore, the noise contribution from weak CW laser was insignificant compared to the photon number fluctuations of the heralded single-photons.

The expected mean photon numbers at coherent transmission and absorption regime are given by

$$\begin{aligned} \mu_{\text{CTR}} &= N_{\text{tot}} \times \frac{p_{\text{CTR}}}{\overline{p}} \times \Delta t, \\ \mu_{\text{CAR}} &= N_{\text{tot}} \times \frac{p_{\text{CAR}}}{\overline{p}} \times \Delta t. \end{aligned} \tag{D.4}$$

The expected mean photon numbers μ_{CTR} and μ_{CAR} are calculated as 8.3 and 0.9, showing a good agreement with the measured mean photon numbers of 8.0 and 1.0 at coherent transmission and absorption regimes, respectively (see § 7.4.2).

We note that reduction of the of p_c and p_d compared to free-space experiments with similar metamaterials is mainly attributed to fiber-to-fiber coupling losses inside the metamaterial package. Nonetheless, this does not give rise to any difference in the interference fringe visibilities of the in-fiber and free-space experiments [83, 84].

Balancing the interferometer

In order to balance the lengths of the interferometer arms to within the coherence length of around 100 µm of the heralded single photons, we used an 810-nm LED light that has a shorter coherence length of around 20 µm, and then varied the length of one interferometer arm using an optical delay line until we observed an interference fringe. Figure D.1 shows

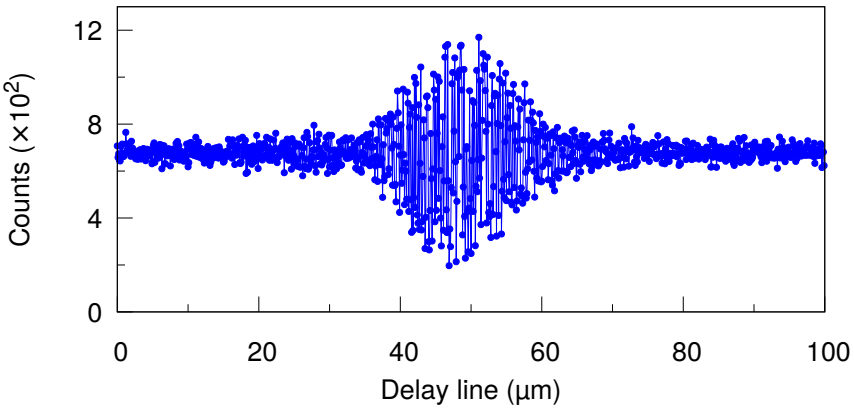

Figure D.1: The interference fringe obtained by an 810-nm LED light launched into the interferometer. Each data point shows the measured single-photon detector counts integrated over 10 ms. Here, the corresponding coherence length is around 20 μm.

that the interferometer arms are balanced to within the coherence length of the LED light so that the heralded single photons can be used in the interferometer as well.